École polytechnique de Louvain

Institute of Mechanics, Materials and Civil Engineering (IMMC)

Institute of Information and Communication Technologies,
Electronics and Applied Mathematics (ICTEAM)

Experimental mechanics of suspended and supported graphene-based systems

Farzaneh Bahrami

Dissertation Submitted for the Degree of Doctor of Philosophy in engineering sciences

Thesis committee

Prof. Thomas Pardoen	Université catholique de Louvain, Belgium
Prof. Jean-Pierre Raskin	Université catholique de Louvain, Belgium
Prof. Bernard Nysten	Université catholique de Louvain, Belgium
Prof. Jean-Christophe Charlier	Université catholique de Louvain, Belgium
Prof. Joris Everaerts	KU Leuven, Belgium
Dr. Marc Verdier	Grenoble INP, France

Acknowledgement

Writing acknowledgement to show how blessed I am to share the moments of my life with an amazing group of people is not an easy task to do. Words cannot be enough expressive while talking about people who spend their time, energy and life to make us happy and help us grow. However, I am going to use this opportunity to express a small part of my gratitude and delightedness to know these people and have them in my life as supervisors, advisors, colleagues, friends and family.

First and most, I am extremely thankful to my supervisors ***Prof.*** **Thomas Pardoen** and ***Prof.*** **Jean-Pierre Raskin** who without their presence, advice, ideas, and commitments, this journey didn't exist let alone reach this stage. Not only did they guide me in every step of the thesis also they teach me how to live a better life. Their ambition, enthusiasm and passion for science and research motivate me in progressing on this path and their knowledge and experience help me to grow professionally and personally. Working with them is one of the best experiences in my life and I am hugely grateful for that.

I would like to thank all the members of my jury, ***Prof.*** **Bernard Nysten**, ***Prof.*** **Jean-Christophe Charlier**, ***Prof.*** **Joris Everaerts** and ***Dr.*** **Marc Verdier** who spent the time to read the manuscript and help me to improve my thesis with their precious remarks, comments and suggestions. I need to thank ***Prof.*** **Nysten** also for his presence, help, and ideas during these four years as well as his time and patience in teaching me the different technical and theoretical subjects.

A special thank you to my colleagues who were always supportive and made a friendly and joyful atmosphere in ***IMAP***. Working and having good times with ***IMAP*** and ***IMMC*** teams make my days in UCLouvain unrepeatable. I would like to have a very big thanks to our secretary **Catherine Bauwens** and our accountant **Rania Sakkal** who do whatever they can to make the process of PhD easier for us. I have worked with two amazing technical teams during my PhD, the ***LACAMI*** team and ***WINFAB*** team, and without their help and knowledge, sure nothing worked properly. I am grateful for working with them and being very good friends with a lot of them. I like to especially thank **Marc**, **Luc**, **Laurence**, **Sophie**, **Alban**, **Jonathan** and **Bruno** for helping me not only with experimental procedures but also for learning Belgian culture. Besides that thanks for the time you spend with us playing babyfoot, it was the best moment in the last months. I am extremely thankful to **Michael**,

Benjamin, **Romain**, **Hamid**, **Christian**, **Sebastian**, **Miloud** and **Ester** who have always been there when facing a problem or needing any kind of help.

I have friends who thank to them I laugh much louder, cry a little less and smile a lot more. Therefore, I am very thankful for their presence in my life. I think that I am very lucky that I am always surrounded by very good friends in all stages of my life but at this stage, I would like to have a special thanks to **Vincent, Natalia** and **Vida** and who were there always for me in my happy and sad days, so I never felt alone. Thanks to **Khaled**, **Nasim**, **Ali** and **Maryam** whom I know later, and we had a lot of fun together. I thank **Patricia's group** to accept me into their group and for letting me be a part of all their gathering and good times. Also a big thanks to **Mar** and **Mohamed** for sharing the office with me and having a lot of fun together.

They say family is an important thing but I don't believe in that, for me family is not an important thing, family is everything. Having a supportive family, whom you can feel their presence in each moment of your life even if there are thousands of kilometres distance between you, who do whatever they can to make you happy and see you succeed is the most precious blessing that someone can have in their life and I am so proud for having them present in my life. **My mother** and **my brother** are the hearts of my life, so I cannot say any word to thank them because I am who I am and I have whatever I have because of them. I just want to thank God for blessing me with their presence. **My father** gave life to me but we couldn't live long together and I've lost him in one of the difficult moments of my life (last days of my PhD) and I couldn't be there even to say goodbye. I want to say thank you to my father many times. I hope that I can make you proud and I just want you to know that I love you. I want to thank **Ramin** as he is more than a relative or friend, he is one of the most supportive people in my life who was there always for me and support me in all conditions.

Thank you all, Thanks a lot.

Abstract

The high-quality two-dimensional (2D) crystals possess remarkable mechanical behaviour which offers exciting opportunities for new material selection and design, like the combination of extremely high in-plane stiffness and bending flexibility. For this reason, nanomechanical testing of 2D layers and their 3D heterostructures is vital in order to prove that they can be practical and useful in different applications. In this work, different nanomechanical testing including membrane deflection, nanoindentation and tensile tests have been performed with various techniques such as atomic force microscopy, nanoindentation and lab-on-chip developed in UCLouvain, respectively. The elastic and plastic behaviour of graphene as well as its effect on the mechanical response of copper thin film have been investigated by using these methods. For each technique, some challenges are required to be faced and some uncertainties needed to be considered in order to extract the mechanical response precisely. Membrane deflection on single and bilayer graphene has been performed in order to extract Young's modulus and fracture strength of these layers by considering the uncertainties and errors that can occur regarding the device calibration and experimental procedure. The effect of CVD-graphene on the plastic behaviour of Cu thin film in two different configurations has been investigated by nanoindentation in two different modes which are complementary to each other limitations. In this configuration, graphene acted as a perfect barrier against the movement and propagation of dislocations underneath the indent. In the last part, lab-on-chip (LOC) technique has been used to evaluate the effect of graphene on the fracture and creep behaviour of thin film of copper. Although convincing and reliable experimental data could not be generated, a well-defined, adapted process for Cu/Gr specimens with Ni actuators has been proposed and the solutions for most of the challenges in each step have been provided opening perspectives for future research actions.

Acronyms and symbols

A ..... Projected contact area

A_H ..... Hamaker coefficient

a ..... Membrane radius (µm)

A_m ..... Oscillation amplitude of m^{th} mode

A_{m0}..... Free amplitude of m^{th} mode

A_0 ..... Free cantilever vibration amplitude (nm)

A_{sp} ..... Cantilever vibration amplitude setpoint (nm)

α ..... half-opening angle

b ..... Burgers vector

c ..... Speed of light

CTF..... Contrast transfer function

d ..... Cantilever vertical deflection (nm)

d_H ..... Tip-sample separation distance (Hamaker equation)

δ ..... Membrane deflection (nm)

E ..... Young's modulus

E_r ..... Reduced elastic modulus

E_0 ..... Young's modulus of indenter

E^{2D}..... Membrane stiffness (N/m)

ε_a ..... Relative uncertainty on the membrane radius

ε_d ..... Relative uncertainty on the cantilever deflection

ε_δ ..... Relative uncertainty on the membrane deflection

ε_F ..... Relative uncertainty on the load

ε_{kc} ..... Relative uncertainty on the cantilever spring constant

ε^{mech} ..... Mechanical strain in actuator

ε^{mis} ..... Mismatch strain in actuator

ε^{t} ..... Total strain

ε_x ..... Relative uncertainty on the scanner lateral displacement in *x*-direction

ε_x ..... Relative uncertainty on the scanner lateral displacement in *y*-direction

ε_z ..... Relative uncertainty on the scanner vertical displacement

e ..... Electron charge

ξ ..... Unit vector of the line direction

F ..... Load

F_{max}..... Maximum applied load

H ..... Hardness

h ..... Plank constant

h_c ..... Contact depth

h_i ..... Penetration depth

k_B ..... Boltzmann's constant ($1.381\ 10^{-23}$ J/K)

k_c ..... Cantilever spring constant (N/m)

L_0 ..... Initial actuator length

m_0 ..... Residual mass of electrons

PSPD..... Position-sensitive photodetector

Q_m ..... Quality factor

R ..... Tip radius

R_{sp} ..... Setpoint amplitude ratio

S ..... Unloading stiffness

S_a ..... Cross-sectional of actuator after release

S_{PSPD} ..... PSPD vertical sensitivity (nm/V)

S_x, S_y, *Sz*..... Scanner sensitivities in *x*-, *y*- and *z*-directions (nm/V)

σ_a ..... True stress of actuator

σ_{int} ..... Internal stress

σ_{app}..... Applied stress

σ_f ..... Maximum mamebrane stress

t ..... Membrane thickness (nm)

T ..... Temperature (K)

u ..... Displacement in cursors

V ..... Potential difference

V_{PSPD}..... Vertical voltage signal on the PSPD (V)

v ..... Poisson's ratio of test material

v_0 ..... Poisson's ratio of indenter

z ..... Probe (scanner) vertical displacement (nm)

Table of Content

4. Extraction of accurate elastic mechanical properties of graphene via membrane deflection

5. Single-layer graphene controlled surface and bulk indentation plasticity in copper

Chapter 1

Introduction and general overview

1.1 General context and motivations

Even though single-layer graphene (SLGr) was explored theoretically by P. R. Wallace in 1947, a new chapter of science opened with the experimental discovery of graphene when Novoselov and Geim first isolated two-dimensional (2D) graphene sheets from graphite in 2004 (K. S. Novoselov, Jiang, et al., 2005). Graphene has been formalized as an atomically flat and thin carbon material with electronic and mechanical properties unprecedented in the world of bulk or even thin-film materials (Geim, 2009). Graphene properties have been derived from a perfect covalent sp^2 carbon bond matrix which makes graphene extraordinary under different aspects; from the electrical point of view like mobility (~ 200000 cm^2/Vs) (Abergel et al., 2010; Soldano et al., 2010), down to mechanical aspect with the reported elastic modulus of 1 TPa and outstanding fracture strength (Akinwande et al., 2017a). Besides the unique properties of graphene, the discovery of graphene opened the field of 2D materials (Mas-Ballesté et al., 2011). The group of 2D materials offers a full spectrum of physical properties, from conducting graphene to semiconducting MoS_2 and insulating h-BN (hexagonal-Boron Nitride) (Bhimanapati et al., 2015). Moreover, the 2D crystal structures render a unique combination of mechanical properties, with high in-plane stiffness and strength but extremely low flexural rigidity (the resistance offered by a structure while undergoing bending) (Akinwande et al., 2017a). To overcome the shortage that existed in each individual 2D layer, the architecturing of 2D stacks to form a 3D structure is an effective solution (Hong Wang et al., 2014).

In order to fabricate the 3D structure of 2D layers, the combination of the same 2D layers, called homostructure, or of different ones which create heterostructures can be utilized. By combining different 2D crystals in a perpendicular way or by in-plane stitching, specific properties can arise due to nonlinear mechanical interactions between them. Van der Waals forces between perpendicularly stacked crystals give rise to a wide range of useful phenomena such as layer-number dependent friction, superlubricity, and spatial modulation of elastic properties through Moiré structures (Androulidakis et al., 2018). Not only the homostructures of graphene (such as bilayer graphene) are attractive for electronic and optical applications but also, among the discovered 2D layers, h-BN and the family of TMDs (transition metal dichalcogenides) occupy a prominent position owing to their technological importance (Solís-Fernández et al., 2017). Their properties need to be investigated individually and combined with other layers to utilize these

3D structures in different types of applications, their properties need to be investigated individually and while combined with other layers.

The mechanical properties not only affect many physical properties of 2D materials, but they also have a significant effect on their functionality in the fabrication of various devices such as next-generation of micro and nanoelectromechanical systems. However, the lack of extensive knowledge of the mechanical properties of such systems makes their functionality arguable in different applications (Jiang et al., 2020). On the other hand, decreasing the dimensions of the materials makes the probing of their mechanical properties more complicated.

Even though there are plenty of challenges in probing the mechanical properties of these structures, a lot of efforts have been done to fabricate compatible approaches for this purpose. Several well-known techniques can be used to measure the mechanical properties of 2D materials such as nanoindentation (Yupeng Zhang & Pan, 2012b), deflection test (Xing Li et al., 2018) or tensile test (Koskinen et al., 1993). Each method has some advantages and limitations as well as uncertainties which are necessary to be considered while extracting the mechanical response of the target material. Some of these challenges come from the parameters related to testing, characterisation, and analysing methods which have a strong effect on the extracted mechanical properties of 2D materials (G. Cao, 2014a; G. Cao & Gao, 2019; Q. Y. Lin et al., 2013a; Zhou, Wang, et al., 2013). By facing these challenges and considering the uncertainties, these techniques can provide the opportunity to probe the 2D layers in different forms such as supported on another substrate and freestanding. Various types of mechanical or even electromechanical properties can be investigated by using these techniques on different forms of 2D layers.

Many nanoindentation studies have been performed on graphene-based systems (S. W. Chang et al., 2013; Gao et al., 2015), including nanoscratching in order to investigate the graphene's tribological properties (Z. Deng et al., 2012; C. Lee et al., 2009). This includes:

- probing the adhesion interaction of graphene on SiO_2 by nanoindentation for mono, bi and trilayer graphene (Suk et al., 2016);
- the investigation of the mechanical properties and the determination of the number of layers by using instrumented nanoindenter (Yupeng Zhang & Pan, 2012b).

Despite the series of studies by nanoindentation for extracting the properties of graphene/substrate systems, the effect of graphene or other 2D materials on the response of the indented material, and on the atomistic processes involved in modifying the mechanical contact has not been extensively analysed. From the viewpoint of elasticity, the stiffer response of Gr-coated Cu has been demonstrated through experimental and theoretical studies (Hammad et al., 2017). There are some discrepancies regarding the length of the pop-ins and their onset while investigating the plastic response of Cu/Gr system under indentation when compared to bare Cu (Park et al., 2019; X. Zhu et al., 2019). These discrepancies will lead us to investigate the effect of graphene on the plastic behaviour of Cu substrate and the movement of dislocations. In addition, to study the effect of graphene on plasticity based on its position in the structure, two different systems will be considered where graphene acts as a coating and an interlayer, respectively. Aside from addressing the extrinsic effect of Gr on Gr-including systems, it is important to consolidate the knowledge of its intrinsic mechanical properties. It necessitates the study of graphene properties in freestanding form.

Freestanding testing of 2D layers can be divided into two categories: deflection test by atomic force microscopy (AFM) (C. Lee et al., 2008a; Rasool et al., 2013) and uniaxial tensile testing (Mohiuddin et al., 2009; Z. H. Ni et al., 2008a) of 2D layer suspended on a patterned substrate.

AFM has been used by numerous groups to measure different properties of suspended 2D layers such as the effective spring constant of the stack of graphene sheets (less than 5 layers) suspended on the defined trenches in SiO_2 (Frank et al., 2007), the elastic modulus of CVD monolayer MoS_2 and WS_2 as well as, the stiffness of their bilayer heterostructures which are lower than the sum of stiffness of each layer (K. Liu et al., 2014a). In addition, deflection tests have been performed on monolayer graphene to measure the 2D stiffness and fracture strength (C. Lee et al., 2008a). Despite the measurements of different properties of 2D layers in the form of a single layer or heterostructure by AFM, there is a range of parameters affecting the extracted mechanical behaviour of freestanding 2D layer while performing deflection test by AFM. These parameters result from the production method (Bonaccorso et al., 2012), transferring process (L. P. Ma et al., 2019), natural defects in 2D layers such as grain boundaries and edges (S. Deng & Berry, 2016) as well as data processing (G. Cao & Gao, 2019) and instrumental uncertainties (Legleiter, 2009). For instance, CVD-grown graphene follows all the traces of grain boundaries or ripples on the donner substrate which can modify the mechanical behaviour of graphene (K. Lee & Ye, 2016). Preparing the sample

for the deflection test requires transferring graphene on pre-patterned substrates which increases the complexities and defects in graphene. Moreover, the area around the AFM tip is under a huge stress concentration compared to the other areas of the membrane. Besides all these investigations, there are sample preparation parameters and instrumental and data processing factors that are effective on the mechanical results and have not been investigated sufficiently. We will investigate and secure the AFM-based deflection method to extract reliable elastic and strength data on Gr and hBN. Besides that, uniaxial tensile testing will be used as it provides some opportunities to overcome the uncertainties and limitations regarding the extraction of mechanical properties in the nanoscale.

Among the techniques for characterisation of mechanical properties of thin films, uniaxial tensile testing provides the most straightforward data to extract both elastic and plastic properties. It is necessary to make the available uniaxial tensile testing compatible with very low dimension materials. Several techniques have been reported to measure the mechanical properties of thin films by tensile testing. In these techniques, efforts have been made to improve the gripping system, actuation system, the technique of applying load as well as fabricating the actuators and sample beams on the same wafer. An electrostatic gripper and a piezoelectric actuator have been designed for the specimen that is uniaxially loaded (Tsuchiya et al., 1996). A stage was fabricated by single-crystal silicon containing the actuator and specimen to integrate both specimen and actuator beams on the same wafer (Haque & Saif, 2002). Despite all these efforts, there are critical challenges in each tensile testing in nano-scale which requires to be dealt with. The UCLouvain lab-on-chip testing method has been developed to overcome the challenges and issues that existed in the previous methods (André et al., 2007; Boé et al., 2009; Fabrègue et al., 2007; Gravier et al., 2009). In this technique, the gripping issue has been solved by using the adhesion between the layers to connect the different beams and the internal stress present in the actuator material is used to impose the load on another film which acts as the specimen. In addition, one of the greatest advantages of microfabrication technology is the easy production of large numbers of elementary patterns. Due to this advantage, thousands of elementary testing stages can be processed on a single silicon wafer with the potential to replicate the tensile testing processes. Despite the advantage of the lab on chip testing systems, each step (sample preparation, patterning and releasing of the structures) needs to be compatible with the material that is used as a specimen or an actuator in order to make sure that the structures are in good condition till the end of the process. The material

that is chosen as the actuator needs to possess high internal stress in order to apply enough load to displace the specimen. To investigate the properties of 2D materials with lab-on-chip tensile testing technique, a range of parameters required to be considered and be adapted to maintain reliable and reproducible data. In this work, we will investigate the effect of graphene on the fracture and relaxation behaviour of Cu thin film by using UCLouvain lab on chip technique. Ni will be used as an actuator and the results and challenges will be discussed in detail.

1.2 Objectives of the thesis and organization

The general objective of this thesis is to investigate experimental techniques to strain graphene, to determine several mechanical properties of interest, and from there unravel fundamental effects/mechanisms. Different forms of graphene systems (supported and freestanding) have been fabricated and several mechanical probing techniques were used depending on the system being studied.

Chapter 2 proposes an in-depth coverage of the key elements of the state of art.

Chapter 3 presents materials and test procedures which have been utilised for the experimental processes and simulation analysis in this work.

Chapter 4 presents the deflection test by AFM. For this test, graphene has been fabricated in the suspended form. PMMA-wet transfer method has been modified and imaging of the samples has been performed by scanning electron microscopy (SEM) as well as AFM to check the quality of the suspension of graphene layers on the cavities. As the final step in the experimental procedure, deflection tests have been performed by AFM to extract the mechanical properties of CVD-grown graphene (single or bilayer). The effect of different parameters on the mechanical response of 2D layers coming from samples preparation and deflection test has been probed simultaneously. This investigation considers the impact of various uncertainties in mechanical testing and helps to extract reliable values for the elastic modulus of single and bilayer Gr. In addition, elastic simulations have been performed to prove the accuracy of the equation used to determine Young's modulus based on force-displacement curves as well as the investigation of the effect of some uncertainties on the mechanical response of graphene. For these simulations, ABAQUS and COMSOL finite element codes have been used, as discussed in more detail in chapter 3.

Chapter 5 addresses the effect of graphene on a metal substrate during plastic deformation which is investigated by nanoindentation and using four different systems to verify the effect of graphene on the movement of dislocations in Cu substrate. The behaviour of Cu substrate coated with CVD graphene has been investigated in comparison to pure copper. In addition, Gr was placed between two films of copper and the effect on the plastic response has been reported and compared with a system of two films of copper with no graphene in between. After performing nanoindentation test on each sample, the effect has been investigated by analysing the force-displacement curves, AFM and TEM images. The effect of graphene is more significant when it is sandwiched between two films of copper. Besides the experimental work, discrete dislocation dynamics (DDD) simulations prove the effect of graphene on the propagation and the movement of the dislocations in Cu substrate. The details of the DDD computational method will be described in chapter 3.

Chapter 6 describes the use of the so-called on chip nanomechanical test method developed at UCLouvain [Gravier et al., 2009; Fabrège et al., 2007] to deform Cu/Gr thin freestanding layers. The lab-on-chip of graphene as a specimen with Ni actuator has been already done at UCLouvain and the results have been available. This technique has been adapted to apply uniaxial tensile loading on Cu/Gr compared to pure copper in order to study the effect of graphene on the fracture strength and creep behaviour of copper. Cu/Gr has been considered as the specimen and the material which has been used as an actuator was Ni. This method contains different steps for specimen and actuator parts and each step needs to be compatible with graphene and Cu. It is necessary to be sure that the quality of graphene has not been degraded while performing the process. As the system is complicated, in this work the compatibility of the testing structures with different steps of the process has been investigated, some issues have been dealt with and some parameters have been modified. However, to make the lab-on-chip with Cu/Gr as a specimen work reliably, more modifications of the process are necessary.

The thesis ends with the conclusion and perspectives.

Chapter 2

Background and literature review

2.1 2D materials

One of the most defining and most effective characteristics of materials is dimensionality. Even though, for a long time scientists believed that intrinsic properties of materials can be defined independent of size, these properties have been formed to change significantly based on whether it is categorised as zero-dimensional (0D), one-dimensional (1D), two-dimensional (2D), or three-dimensional (3D) (K. S. Novoselov, Jiang, et al., 2005). Both physical and mechanical properties are known to change when at least one dimension is reduced to the nanoscale. Among the materials with reduced dimensions, 2D materials attract significant attention. Graphene is the first discovered 2D material and it is the mother of most allotropes of carbon (Geim, 2009; Castro Neto et al. 2009) and Figure 2.1 shows this fact clearly.

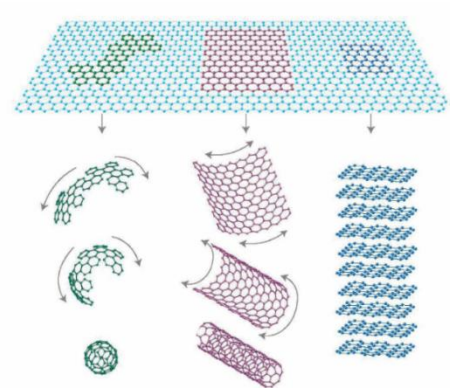

Fig. 2.1. *Graphene is a basic building block of graphitic materials. It can be wrapped up into 0D buckyballs, rolled into 1D nanotubes, or stacked into 3D graphite (taken from Geim et al, 2009).*

However, it is not only graphite that responds to the idea of pulling out one layer from a 3D material with strong covalent in-plane bonds and weak Van der Waals coupling between layers (Mas-Ballesté et al., 2011). Consequently, the most important benefit of graphene discovery besides its unique properties is paving the way for the discovery of a huge range of 2D materials (Akinwande et al., 2017b; Kostya S. Novoselov et al., 2019; Papageorgiou et al., 2017). Monolayers of BN, MoS_2, and $NbSe_2$ have been prepared by rubbing a fresh surface of a layered crystal against another surface, leaving a variety of flakes attached to it (K. S. Novoselov, Geim, et al., 2005). In recent years, single-layer graphene (SLGr), bilayer graphene (BLGr), and hexagonal boron nitride (hBN) are the most attractive ones among 2D materials rooting in their unique properties which in some cases are complementary to each

other (Barrios-Vargas et al., 2017). In order to use 2D materials in modern technologies, knowing their properties is of utmost importance.

2.1.1 Single-layer graphene and mechanical properties

Graphene shows outstanding electrical, thermal, and mechanical properties such as the highest room-temperature carrier mobility, high thermal conductivity, extremely high in-plane stiffness (Young's modulus), and superior strength (Geim, 2009; Sreeprasad & Berry, 2013). A full understanding of the mechanical properties of graphene is necessary in order to deal with its promises. The elastic modulus *E*, Poisson ratio *v* and intrinsic strength σ_{int} are known as the most fundamental phenomenological mechanical properties of graphene. To measure the elastic modulus of graphene, different experimental attempts have been employed.

One of the first studies has been done experimentally by Lee et al. and reported the value of Young's modulus (*E)* of SLGr around 1.02 TPa by performing deflection tests (C. Lee et al., 2008a). In other work, Young's modulus and 2D stiffness (E^{2D}) of SLGr have been measured as equal to 1.12 TPa and 375 N/m, respectively by using the same method as the one used by Lee et al (Annamalai et al., 2012). The in-plane stiffness (E^{2D}) is also an important property of graphene and owing to the 2D nature of graphene, the 2D elastic stiffness (E^{2D}) has the dimensionality of surface tension (N/m). Furthermore, instrumented nanoindentation has been used to investigate the elastic modulus of single and bilayer graphene which was estimated to be 0.89 TPa and 0.39 TPa, respectively. Different methods have been used to measure the elastic properties of graphene and other 2D layers and the extracted results can be seen in Table 2.1.

Table 2.1. *Mechanical properties of 2D materials obtained from freestanding indentation (taken from Cao et al, 2019).*

2D materials	Approach	*E* (TPa)	σ_t (GPa)
Bi-layer Graphene	MD	0.8	
Monolayer graphene	MD	0.501–1	
Monolayer graphene	FEM		108.5
Monolayer graphene	MD		105
Monolayer graphene	Experiment	1.0 ± 0.1	130 ± 10
Graphene (n < 5)	Experiment	0.5	
Monolayer graphene	Experiment	1.12	
Polycrystalline graphene	Experiment	0.967–1.01	98.5–118
Monolayer MoS_2	MD	0.149–0.159	13–58
Monolayer MoS_2	Experiment	0.27 ± 0.1	23
Monolayer MoS_2	Experiment	0.264 ± 0.018	
MoS_2 (n = 5–25)	Experiment	0.21–0.37	
Multiple-layer BP	Experiment	0.0586 ± 0.0117(zz) 0.0272 ± 0.0041(ac)	4.79 ± 1.43(zz) 2.31 ± 0.71(ac)
Multiple-layer BP	Experiment	0.276 ± 0.0324	25
Multiple-layer WSe_2	Experiment	0.1673 ± 0.0067	12.4

Despite the different experimental approaches that have been used to extract the Young's modulus of graphene, the value of the Poisson ratio v is determined from numerical simulations as it cannot be directly measured with experimental approaches (G. Cao, 2014b). By using an atomistic simulation approach the bending stiffness, the effective elastic modulus and Poisson ratio of graphene have been determined. The intrinsic strength of single-layer graphene is approximately 130 GPa as it is estimated by using numerical simulations from the inverse analysis of the deflection test performed by Lee et al (C. Lee et al., 2008a). Mechanical studies on 2D layers are challenging and in some cases are not in good agreement.

There are several sorts of discrepancies in the extracted mechanical properties of graphene or other 2D layers (G. Cao & Gao, 2019). However, most of the possible reasons which cause discrepancies and the root of the differences/deviations in the extracted results have not been investigated, precisely. There is a range of studies that focus on the effect of defects and intrinsic characteristics of graphene on its elastic and plastic mechanical response. The presence of out-of-plane ripples would effectively lower the in-plane stiffness of graphene as it demonstrated in recent studies (Ruiz-Vargas et al., 2011). These out of plane ripples can occur during CVD or post-processing of CVD-grown graphene. On the other hand, it has been reported that E^{2D} of graphene is similar to pristine graphene at a high density of sp^3-type defects and the fracture strength of defective graphene reduces to around 14% smaller in comparison to its pristine counterpart in the sp^3-defect regime (Zandiatashbar et al., 2014a). By using molecular dynamic (MD) simulations, the effect of defects (vacancy and Stone–Wales (SW)) on Young's modulus of graphene sheet has been investigated. The Young's modulus of graphene sheets decreases in the presence of defects and by increasing the degree of defects the decrease of the Young's modulus gets larger (Jing et al., 2012). In general, the experiments at the nanoscale are full of challenges. Although the mentioned studies clarify some sources of the deviations, there are very limited analyses on the influence of the parameters related to testing procedure, sample preparation, and instrumental and analytical uncertainties.

In the mechanical characterisation of 2D layers, the range of applied mechanical load is effective (G. Cao & Gao, 2019). Under sufficiently large load which leads to large deformation (e.g., $\varepsilon > 5\%$) an anisotropic nonlinear behaviour is dominant whereas, under very small deformation, graphene exhibits the isotropic linear behaviour (G. Cao, 2014b; Wei et al., 2009). Pretension in suspended graphene has been discussed by different researchers. It can result from the Van der Waals interaction between graphene and the

walls of the cavities which can be released after applying small loads (C. Lee et al., 2008a). It mentioned that pretension results from the growth of graphene by chemical vapour deposition and can be released easily by flatting out the wrinkles (Q. Y. Lin et al., 2013b). In most cases, the prestress is determined by fitting the measured force-deflection relationship with the existing indentation models such as clamped beam and clamped circular thin plate (G. Cao & Gao, 2019). To achieve reliable and reproducible data on the mechanical properties of 2D layers and to make the 2D layers practical in various applications, a more precise and broad investigation of these uncertainties is necessary while mechanical testing

Furthermore, the use of graphene in applications requires knowledge of its mechanical properties in order to ensure structural integrity. The mechanical properties of graphene are important, (i) to exploit graphene as a super strong structural material; (ii) to understand and control the durability of graphene used in electronics and energy storage;(iii) to form curved graphene specimens for electronics and structural applications; (iv) to exploit nanocomposites with graphene inclusions as structural and/or practical materials. In addition, understanding the micro mechanisms of unique deformation and fracture processes in graphene is of crucial significance for the progress of fundamental science (Mahmoud et al., 2015; Ovid'ko, 2013). Not only knowing the mentioned properties is important for graphene itself also the effect of graphene on other materials such as metals (AbuShanab et al., 2020; Moustafa & Taha, 2020), polymers (Tang et al., 2013) and ceramics (W. Kim et al., 2015) is of utmost importance. The effect of graphene on the mechanical properties of another substrate will be discussed more in chapter 5.

2.1.2 Bilayer graphene and mechanical properties

Despite all the outstanding properties of SLGr, the lack of an energy gap in its electronic structure seems like a deficiency for electronic applications (Das et al., 2008). However, the stacking of two layers of graphene and the fabrication of bilayer makes graphene more attractive as by applying an electric field across the bilayer graphene a tunable bandgap can be generated (Fang et al., 2015). This phenomenon can be seen in Figs. 2.2a to 2.2c. Figures 2.2a and 2.2b represent SLGr and BLGr with no bandgap, respectively. On the other hand, Fig. 2.2c shows the opening of the bandgap in bilayer graphene as a result of the applied electric field. The BLGr has been formed when two

layers of SLGr are held together by Van der Waals (VdW) interaction. This stacking does not lead to a flawless stacking order (AB stacking), as frequently small twisting of a SLGr is observed relative to the other (Nimbalkar & Kim, 2020) which is called "twisted bilayer graphene" (tBLGr) (L. Liao et al., 2015). In general, BLGr can be ordered in an AB, AA, or a twisted orientation (C. Y. Lin et al., 2014). Figure 2.3a illustrates the local AA, AB, and twisted stackings, and 2.3b shows the lattice configuration of different stackings (Abbas et al., 2020).

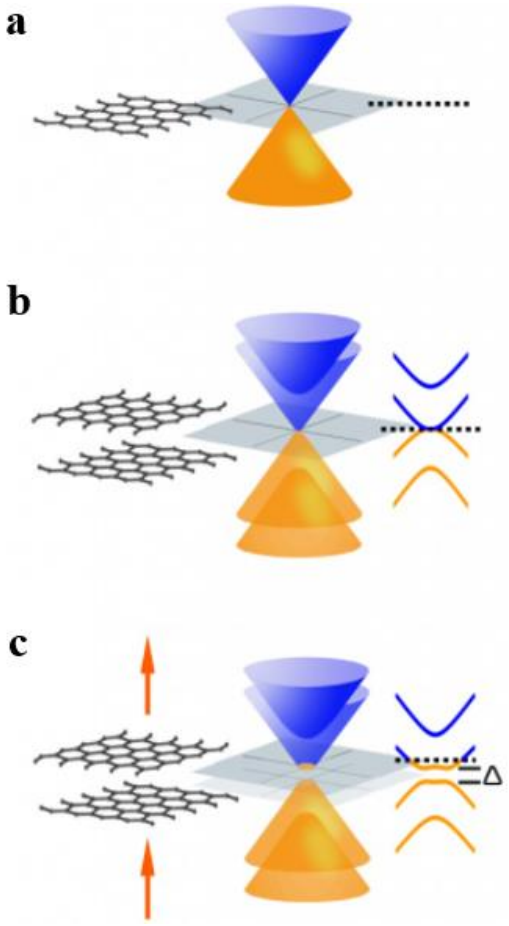

Fig. 2.2. *(a) Single-layer graphene with its conical conduction and valence bands meet at a point (it has no bandgap); (b) symmetrical bilayer graphene also lacks a bandgap; (c) electrical fields (arrows) introduce asymmetry into the bilayer structure, yielding a bandgap (Δ) that can be selectively tuned.*

The intensity ratio of the *2D/G* peak can change for different angles between the layers, hence Raman spectroscopy can be useful in the prediction

of the behaviour of BLGr (Xing et al., 2013). Figures 2.4a and 2.4b illustrate the optical images of bilayer graphene with different angles between the layers and corresponding Raman spectra can be seen in Fig 2.4c. By comparison, the Raman spectrum of AB stacked and 23° rotated bilayer graphene, it can be recognised that the intensity ratio of *2D/G* changed and it is different from the one for SLGr. It is explained that by increasing the number of layers *2D* peak intensity decreases and the peak becomes wider. On the other side, the intensity of the *G* peak increases. However, based on the angle between the layers, the intensity ratio of these two peaks can change. It has been shown that this variation of the angle between the layers can influence to some extent on the extracted mechanical properties of bilayer graphene. Recently, some simulations and first-principles calculations have been performed to investigate the mechanical behaviour of BLGr such as intrinsic strength, fracture strength and Young's modulus as well as the effect of the angle between the layers on these properties.

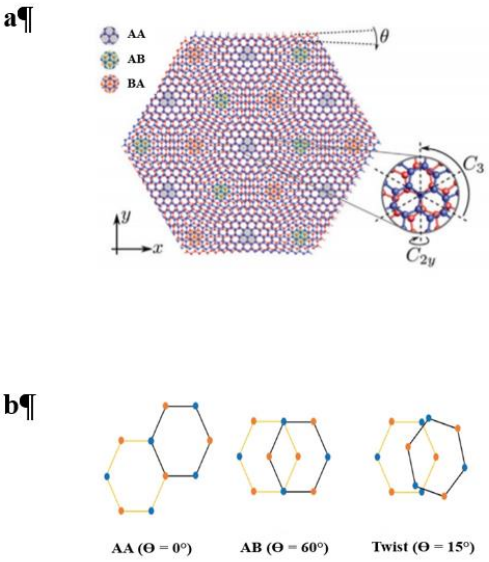

Fig. 2.3. *(a) Illustration of local AA, AB, and BA highlighted in gray, green, and orange, respectively; (b) lattice configuration of AA-stacking, AB-stacking, and twisted BLGr (taken from Abbas et al, 2020).*

Zheng et al. studied the mechanical properties of tBLGr with different twist angles. The tensile tests have been simulated by molecular dynamic simulations in-plane and perpendicular to the plane. The conclusion is that the in-plane properties are dominated by graphene orientation and twist angle

affects the perpendicular properties. They have mentioned that the intrinsic strength increases by increasing the twist angle (Zheng et al., 2018). The nanoindentation of bilayer graphene has been studied using molecular dynamic simulations and Young's modulus of BLGr has been estimated to be 0.8 TPa (Neek-Amal & Peeters, 2010a). Also, it was reported that under different loading histories, the BLGr shows quite different mechanical responses such as initial elastic deformation and fracture strain. The effect of the twist angle and grain boundaries on the mechanical properties of BLGr have been studied under uniaxial tension. In addition, the effect of different grain boundaries and intrinsic defects on the strength of BLGr have been investigated by simulation (L. Wang & Zhang, 2012).

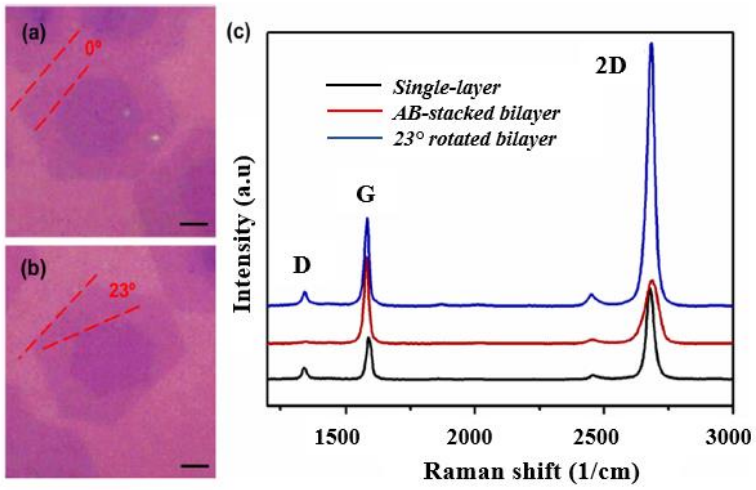

Fig. 2.4. *Optical images of transferred bilayer graphene grains on SiO_2/Si; (a) oriented bilayer and; (b) bilayer with an angle of 23°. The substrate surface, single layer and bilayer regions of the grains can be well identified by the colour contrast in the images, (the scale bars are 2 μm); (c) Raman spectra of the bilayer grains. The laser excitation wavelength is 532 nm. (taken from Xing et al., 2013).*

Figures 2.5a and b show armchair and zigzag grain boundaries to make the difference between them clearer (Du, 2021). In addition, the effect of the mentioned grain boundaries with different angles on the stress-strain curve in bilayer graphene is represented in Fig. 2.6.

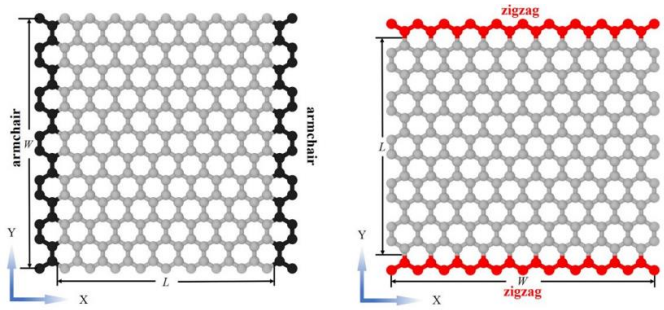

Fig. 2.5. *The schematics of the armchair and zigzag monolayer pristine graphene (taken from Du et al., 2021).*

It has been shown that by increasing the angle between the layers, the bilayer graphene can withstand higher strain (J. Zhang & Zhao, 2013b). Molecular dynamics simulations have shown the enhancement of the strength of BLGr sheets while coupling by sp^3 bonding because of the boosted interlayer interaction and smaller interlayer distance (Y. Y. Zhang et al., 2011). There are not many experimental studies on the mechanical properties of BLGr.

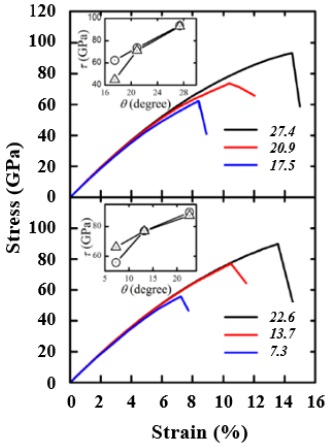

Fig. 2.6 *Stress-strain curves of BLGr with armchair orientated (upper) and zigzag-orientated grain boundaries (lower) in one layer. To make it clearer, the intrinsic strengths of graphene grain boundaries in SLGr (shown in triangles) and bilayer (shown in circles) as a function of misorientation angle (h) are plotted in the insets (taken from Zhang et al., 2013).*

2.1.3 h-BN and mechanical properties

2D hexagonal boron nitride (hBN) or white graphene, an isomorph of graphene with a very similar layered structure, is being attractive because of its incredible optoelectrical properties, high mechanical robustness, good thermal stability, and chemical inertness (M. Xu et al., 2013; K. Zhang et al., 2017). hBN shows remarkable mechanical properties which make it a good candidate in different applications such as reinforcement phase in different composites, polymer-based (Andrew et al., 2012), ceramic-based (Kovalčíková et al., 2014), and metal-based (Tyagi et al., 2010) as well as a substrate in electronic devices (C. Dean et al., 2012).

hBN nanosheets introduced into polymers lead to the improvement of the elastic modulus by 22% (Zhi et al., 2009). The elastic modulus and microhardness improved and wear loss decreased significantly in the presence of hBN in a Ni-based composite (Tozar & Karahan, 2019). In-plane tensile and shear rigidity of hBN have been calculated to be 0.328 TPa nm and 0.171 TPa nm by using the force field model. Both the thickness and size can impact strongly the mechanical response (Boldrin et al., 2011). A three-point bending test has been conducted to extract the bending modulus of hBN nanosheets and the bending modulus was found to increase with decreasing of the layer thickness, and for the thickness less than 50 nm, the value approaches the theoretical one (C. Li et al., 2009). The non-contact mode of atomic force microscopy (AFM) has been used to evaluate the elastic constant of freestanding hBN with 1-2 nm thickness and the value has been evaluated between 220-510 N/m (Song et al., 2010a). The latter value has been estimated at 270 N/m by theoretical computation for single-layer hBN (Kudin et al., 2001). The fracture strength has been measured in Song's research as equal to ~ 8.8 N/m (Song et al., 2010a). Young's modulus of multilayer hBN with a thickness of 15 nm has been measured by nanoindentation using AFM and it was found to be approximately equal to 1.16 TPa (S. M. Kim et al., 2015).

2.2 2D-heterostructures

Composites and heterostructures (artificial assembly of materials in a specific sequence like building blocks) have revolutionized many aspects of our lives and the idea of combining different materials to achieve the best of different properties is very appealing but it is quite hard to accomplish especially in the case of 2D materials (K. S. Novoselov et al., 2016). Therefore, facing the

challenges of mixing or superposing different crystals with different properties and creating combinations with improved properties are necessary (K. S. Novoselov et al., 2016). There are several challenges when combining different materials, and various parameters need to be considered in order to achieve the composites or heterostructures with the target properties (Ahmad & Mohamed, 2014; Borkar & Harimkar, 2011). Despite these difficulties, the fabrication of the heterostructures of the 2D layers is the most efficient solution to overcome their deficiencies (Su et al., 2020). Figure 2.7 represents a schematic for creating heterostructure of different 2D materials (Geim & Grigorieva, 2013). The good selection of the 2D layers and precise designing of the elements in fabricating the heterostructure can open up countless opportunities to create new materials and systems aimed at high-performance device applications (Yuan Liu et al., 2016). For instance, it has been shown that the electronic structure of graphene could evolve rapidly by increasing the number of layers (close to the 3D limit of graphite) (G. Yang et al., 2018). From a physical point of view, investigating the coupling between elementary layers in different heterostructures can provide useful information regarding the properties of the heterostructures (K. S. Novoselov et al., 2016). In addition, the approach of assembling the heterostructure has a significant effect on the final achieved properties.

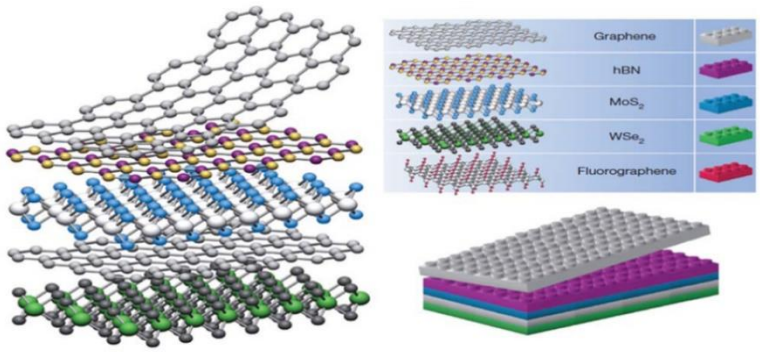

Fig. 2.7. *The creation of the heterostructure with different 2D materials (taken from Geim et al., 2013).*

In general, there are two types of heterostructures from an assembling point of view. The first category is when 2D materials are stacked perpendicular to their planes to make multilayers together with weak interaction (Van der Waals interaction) and the second one is assembling the 2D materials laterally by joining them seamlessly on the same plane mostly by covalent bonds (Cai

et al., 2018a). The difference between the perpendicular/vertical and lateral assembly has been shown in Figs. 2.8a and b (D. Singh et al., 2021). Up to this time, different heterostructured 2D materials have been made and novel properties of these structures have been discovered (Yanping Liu et al., 2019).

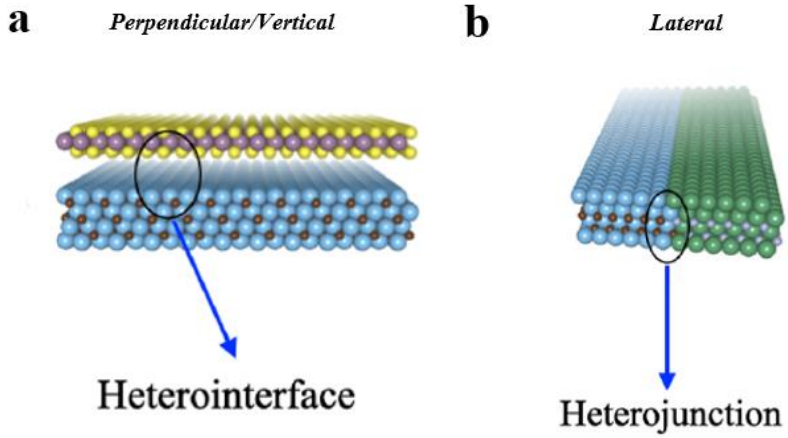

Fig. 2.8. *(a) 2D materials assembled in a perpendicular way; (b) 2D materials assembled laterally (taken from Singh et al., 2021).*

The quality of Gr on SiO_2 substrate is influenced by scattering from charged surface states (at the surface of thin silicon oxide films grown on silicon, oxide ions provide a layer of negative charge; an equal positive charge (usually sodium ions) is concentrated in the oxide within about 200 Å of the surface) and impurities (sodium oxide impurities are the dominant electron-donors; these supply the electrons for the negative surface and interfacial layers). In order to mitigate this limitation, hBN has been used as the substrate and gate dielectric for graphene electronics (C. R. Dean et al., 2010). Gr-based devices on single-crystal hBN substrates demonstrate almost an order of magnitude better mobilities and carrier inhomogeneities than devices on SiO_2 (C. Dean et al., 2012). Recently, a field-effect transistor has been fabricated with MoS_2 channels, hBN dielectric, and graphene gate electrodes. The flow of the fabrication process for the complete device (flake of MoS_2 channel, flake of hBN dielectric and few layers graphene gate) is shown in Figure 2.9. The transfer has been performed by dry-PDMS-transfer. For patterning source, drain and gate electrodes, e-beam lithography has been used. The field-effect mobilities of the device improved up to 45 cm^2/Vs and operating gate voltage was below 10 V, with a significant reduction of hysteresis.

Furthermore, the good mechanical strength and flexibility of these heterostructures open a new route toward flexible and transparent electronics (G. H. Lee et al., 2013).

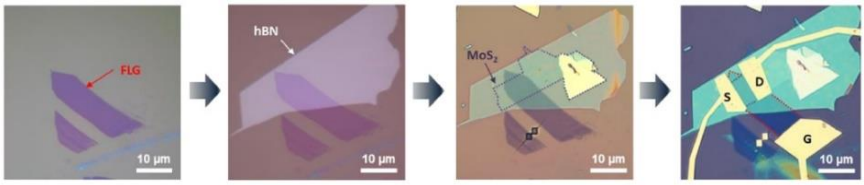

Fig. 2.9. *Optical micrographs of the corresponding samples in each fabrication step (taken from Lee et al., 2013).*

2D materials such as MoS_2 show promising properties for flexible electronics and piezoelectric applications. However, the low mechanical strength of these layers acts as a barrier in these applications. Liu et al. used the nanoindentation process to probe the elastic stiffness of 2D bilayer heterostructures. The results revealed that the values of E^{2D} of bilayer heterostructures are always lower than the sum of E^{2D} of each layer resulting from an interlayer sliding that depends on the interlayer interaction. By considering this effect, the measured stiffness of a 2D bilayer described with a phenomenological equation defined as:

$$E_t^{2D} = E_{bot}^{2D} + \alpha * E_{top}^{2D} \tag{2.1}$$

where E_t^{2D}, is the total 2D stiffnness of the heterostructure. E_{bot}^{2D}, and E_{top}^{2D} are the 2D stiffness of bilayer heterostructure, of the bottom layer and of the top layer, respectively. α is an interaction coefficient and it ranges from 0 to 1 (K. Liu et al., 2014b). The illustration of the elastic properties of 2D heterostructures and the values considered for α of each structure are shown in Fig 2.10a and b. In addition, it has been recently investigated that the combination of MoS_2 with graphene can significantly improve the mechanical properties of 2D structures (Elder et al., 2015)

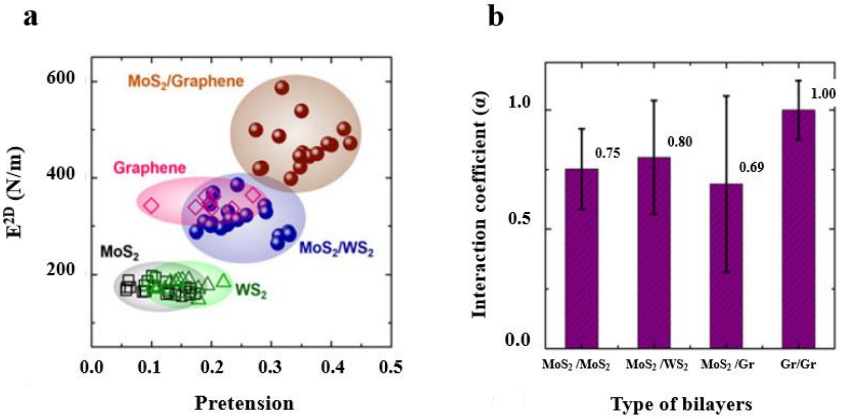

Fig. 2.10 *(a) Elastic properties of 2D heterostructures; (b) interaction coefficient between the layers of bilayer heterostructure (taken from Liu et al., 2015).*

2.3 Transfer of 2D materials

One of the determining steps in the processing of 2D layers is the transferring step which has a significant effect on the quality of 2D sheets. To take advantage of the exceptional properties of 2D materials and make them practical for different kinds of applications, the availability of 2D materials with high quality is of utmost importance (Z. Chen et al., 2019; L. P. Ma et al., 2019). High-quality 2D layers entail single crystalline material without contamination, wrinkle, cracks, or other defects. Despite the considerable advancement in the synthesis method of graphene, the transferring methods are not fully satisfying. For instance, chemical vapour deposition (CVD) is a versatile method for the production of 2D films with high structural integrity on transition metal substrates (Cu is commonly used), however, such substrates are not suitable for most applications (Deokar et al., 2015; Muñoz & Gómez-Aleixandre, 2013; G. X. Ni et al., 2012). Therefore, employing 2D materials in many applications requires specific substrates, such as semiconductors and metal oxides. Consequently, a subsequent process is often necessary to transfer the layers to the target substrates (Huaping Wang & Yu, 2016; X. Yang & Yan, 2020). To transfer 2D materials produced by CVD, several steps need to be followed: first a support/protective layer (often organic polymers such as camphor) coats on 2D layer to minimize wrinkles, cracks, and other mechanical damages. Then, the substrate on which 2D material has grown needs to be etched away by dissolution in a liquid etchant,

bubble delamination, or thermal peel off (Qu et al., 2019; Y. Wang et al., 2011; Mafra et al., 2015). Finally, the stack of polymer and 2D layer transfers on a target substrate and then the polymer is removed (M. Chen et al., 2017; Y. Chen et al., 2016). After the production of 2D layers, the most challenging step is the transfer itself. To deal with this challenge, different transfer techniques have been developed and evaluated. In general, transfer methods are classified into two main categories: wet transfer and dry transfer (C. Kim et al., 2020). The type of polymer used to protect the 2D layer is playing an important role hence both small- and large-molecular polymers have been used to improve the transfer technique (M. Chen et al., 2017).

2.3.1 Wet transfer

In wet transfer, ionic etchants are used to dissolve the growth substrate then the 2D layer is transferred from the liquid cleaning solvent (often water) to the target substrate without drying.

Among wet transfer methods, using polymethyl methacrylate (PMMA) as a protective film is the most common approach (J. S. Lee et al., 2018; Kosmider et al., 2013). Fig. 2.11 represents a schematic of different steps of the PMMA-transfer method. In the process, firstly, PMMA is spin-coated onto 2D material synthesized on donor substrate (in the case of CVD mostly transition metals) then the stack of PMMA/2D layer/substrate is floated on an etchant to get rid of the donor substrate. For the newt step, PMMA/2D layer stack is rinsed by deionized (DI) water several times, and the floated stack of the PMMA/2D layer is scooped by a host substrate. Finally, the stack of PMMA/2D layer/substrate is dipped in a solvent to dissolve the PMMA. The advantage of this approach is the free selection of a target substrate and the small range of mechanical damages of 2D material during the transfer process (C. Kim et al., 2020). This approach makes the transfer of 2D material with the size of 4-inch (wafer size) possible (Shinde et al., 2018; Li Wang et al., 2019). However, PMMA is difficult to be completely removed from the 2D layer surface. The PMMA residues cause the degradation of the electrical and optical properties of the flexible electronics fabricated with 2D materials (Pirkle et al., 2011). Although, it is difficult to remove PMMA residues completely even for the most established method which is dissolving PMMA in acetone as a solvent; PMMA is well known as a soft polymer and it is not supposed to have a significant effect on the mechanical properties of strong and brittle graphene (P. Zhang et al., 2014).

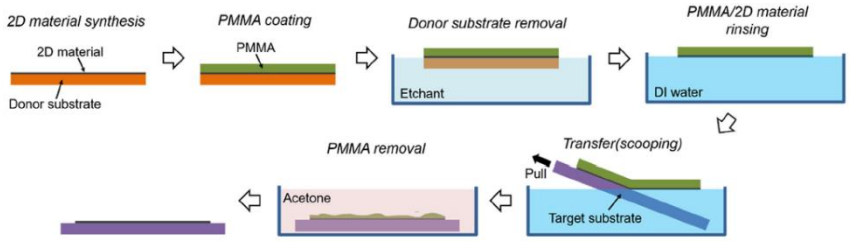

Fig. 2.11. *Schematic of the conventional wet transfer process of two-dimensional material using Poly(methyl methacrylate) as a transfer film (taken from Kim et al., 2020).*

2.3.2 Dry transfer

In the dry-transfer technique, no ionic etchant is involved and delamination methods have been used to make a transfer. In this transfer process, the adhesion difference of support layer/2D material and 2D material/target substrate plays an important role. In other words, greater adhesion between 2D material and a target substrate is required for transferring them without damage. On the other hand, the adhesion between a support film/2D layer should be large enough to support the layer from damages by external forces, but less than the adhesion of 2D material/target substrate (C. Kim et al., 2020). This makes the use of dry transfer more challenging for different substrates. Polydimethylsiloxane (PDMS) is the most well-known polymer for dry transfer. It is a viscoelastic material with a water contact angle of 100° to 110° (Allen et al., 2009; K. S. Kim et al., 2009; Y. Lee et al., 2010). Figure 2.12 shows a schematic of different steps of PDMS transfer. There are some other limitations regarding this method; first, the 2D material might not come into good contact with PDMS. This can result from the non-flat surface of the donor substrate where 2D material has been grown due to the grain boundaries as well as the ripple patterns formed on a donor substrate during the synthesis process of 2D layer resulting from the high temperature of CVD process (Y. Kim et al., 2013; G. X. Ni et al., 2012). Second, PDMS supports 2D material with a weak Van der Waals force (VdW) which can lead to mechanical damages on these layers during etching and rinsing processes, resulting in degraded electrical and mechanical properties of 2D material (C. Kim et al., 2020).

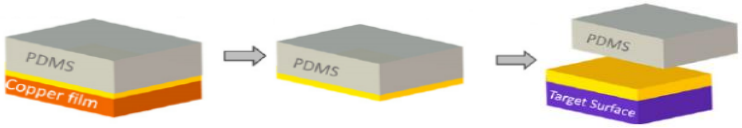

Fig. 2.12. *Schematic of the dry transfer process for CVD-grown graphene (taken from Feng et al., 2014).*

2.4 Van der Waals interaction between layers

The force that keeps the structure together when transferring the 2D layers either on another 2D layer or on another substrate material is Van der Waals (VdW) force. The Van der Waals force is a distance-dependent interaction between atoms or molecules. Unlike ionic or covalent bonds, these attractions do not result from a chemical electronic bond; they are comparatively weak electrostatic forces that attract neutral molecules to one another. π-π interaction is a particular type of dispersion force from Van der Waals forces and graphene sheets are stacking together with this interaction (X. J. Zhao et al., 2019). The advantage of π-π stacking and other non-covalent modification methods is that these interactions do not disrupt the conjugation of graphene. Furthermore, the bonding strength of this interaction can approach the strength of covalent modifications (X. Zhang, 2017). This bonding strength has been proved to play a dominant role in the functionality of the VdW structures (K. S. Novoselov et al., 2016).

An important factor in the characterisation of 2D materials is the impact of VdW strength while 2D layers lay on the surface. As mechanical structures enter the nanoscale regime, the influence of VdW forces increases (Koren et al., 2015). Graphene is attractive for nanomechanical systems because its Young's modulus and strength are both intrinsically high, but the mechanical behaviour of graphene can also change by the strength of Van der Waals forces (Koenig et al., 2011).

As a result, having knowledge of the strength of VdW forces when graphene or other 2D layers are placed on a surface is necessary. In recent studies, the Hamaker coefficient has been introduced to measure the strength of VdW forces when 2D layers are in the form of supported or suspended on another surface. Hamaker demonstrated that the VdW force strength between two bodies could be split into a purely geometrical component and a coefficient that depends solely on material chemistry i.e. polarizabilities and number densities of the atoms in the two interacting bodies (Hamaker, 1937).

Hamaker coefficient offers a more general picture of the surface characteristics than the measurement of a particular physical quantity such as adhesion or surface energy. The measurements of Hamaker coefficient of graphene on a variety of substrates have been performed to evaluate the impact of the substrate on the VdW strength of the graphene surfaces. They have investigated three different systems including as-grown graphene on Cu substrate, transferred Gr on SiO_2 in supported and suspended form. After measuring the Hamaker coefficient, it has been observed that the substrate has a significant effect on the VdW strength of graphene surfaces (Chiou et al., 2018). Table 2.2 shows the comparison between Hamaker coefficient for different substrates.

Table 2.2. *comparison of effective Hamaker constants between experiment and theoretical prediction when graphene is on different substrates (taken from Chiou et al., 2018).*

Method	Substrate	Monolayer e^{-20} J	Bilayer e^{-20} J	TriLayer e^{-20} J
Experiment	Suspended	7.2	17.99	24.7
	Cu	16	23.03	30
	SiO_2	5.4	6.34	12
Calculation	Cu	15.22	21.71	26.87
	SiO_2	4.16	16.58	23.92

The Hamaker coefficient can be defined as (Chiou et al., 2018; Hamaker, 1937):

$$A_H = -\frac{3\pi k_c A_{m0}\cos(\varphi_m)}{0.83RQ_mA_m}\sqrt{d_H^5 A_1} \qquad (2.2)$$

where R is the tip radius. k_c and Q_m are spring constant and quality factor, respectively. d is the tip-sample separation distance. The oscillation amplitude of the m^{th} mode and the free amplitude of the m^{th} mode are defined with A_m and A_{m0}, respectively, and φ_m is the phase of the m^{th} mode.

Based on the study that has been performed by Chiou et al, the measured Hamaker for graphene on SiO_2 is lower than that for the suspended graphene on perforated SiO_2 substrate. In their research, the highest value was for as-grown graphene on Cu substrate (Chiou et al., 2018). This value certainly decreases in the case of transferred graphene on Cu substrate.

2.5 Mechanical testing of 2D materials

2D materials have been scaled up to fabricate nanocomposites, energy storage devices, flexible electronics, etc. The goal of mechanical testing of 2D layers is to extract the mechanical properties, which play a significant role in both fundamental science and practical engineering (Al-Quraishi et al., 2020). The mechanical properties involve elastic coefficient, yield strength, fracture stress, fracture toughness, creep resistance, fatigue resistance and etc. In the context of this thesis, we essentially focus on the elastic properties (Young's modulus and 2D stiffness) and fracture strength. The mechanical testing of 2D materials can be divided into two different approaches: a) supported 2D layers on a substrate, b) freestanding/suspended 2D layers above a gap in the substrate. The mechanical characterisation with each of the mentioned methods can be performed in an ex-situ or in-situ way.

2.5.1 Nanoindentation using nanoindenter equipment (supported mechanical testing)

Among the methods that have been used for supported films involving 2D materials, nanoindentation is one of the most common methods (Yupeng Zhang & Pan, 2012b). Nanoindentation is a method widely used in the characterisation of small scale mechanical behaviours of materials (Xiaodong Li & Bhushan, 2002; Oliver & Pharr, 2004). With this method, load and displacement as small as 1 nN and 0.1 nm can continuously be measured. Hardness and elastic modulus can be determined from the load-displacement data. In addition, the instrumented nanoindentation adopts the continuous stiffness measurement (CSM) technique to collect continuous data with thickness. CSM is achieved by imposing a small, sinusoidal varying signal on top of a DC signal that drives the motion of the indenter. This allows the measurement of contact stiffness at any point along the loading curve and obtains the hardness and elastic modulus at exceedingly small penetration depths. Thus, this technique provides an ideal approach for measuring nano-films upon a substrate (Yupeng Zhang & Pan, 2012a) and provides meaningful insight into the material's elastic and plastic response as well as surface properties. Recently, the mechanical behaviour of 2D materials on different substrates has been investigated by instrumented nanoindentation (J. Chen et al., 2013; Niu et al., 2016). Hammad has used nanoindentation to investigate the effect of graphene on the tribological behaviour of Cu thin film. In the

presence of graphene, the modification of the elastic contact behaviour between the indenter and the surface in the presence of graphene has been confirmed due to the elimination of adhesion (Hammad et al., 2017) but not due to the stiff nature of graphene. On the other hand, Cu coated graphene has demonstrated a higher effective elastic modulus compared to pure Cu resulting from the ultra-high elastic modulus of graphene layer under indentation (Park et al., 2019). This method provides valid data on the effect of 2D layers on other materials' behaviour from elastic and plastic points of view.

Not only, nanoindentation can provide solid information on the material's elastic and plastic behaviour, also its procedure is quite straightforward. The procedure of nanoindentation experiments is followed by the approaching of a sharp tip to the surface of the target material. After the tip contact with the surface, the load starts to increase and the tip can go deeper into the material until a maximum predetermined depth, followed by unloading. At the loading part, the material undergoes elastic as well as plastic deformations. In the unloading part, only the elastic deformation is reversed with some non-linearity due to reserve plasticity upon unloading. Figure 2.13 shows the procedure of nanoindentation experiments while loading and unloading. Based on the mechanism of the device, the nanoindentation can be controlled by load or displacement.

Therefore, there are two modes to perform nanoindentation tests:

1. Load-controlled nanoindentation: the load is applied and the corresponding displacement is measured.

2. Displacement-controlled nanoindentation: the displacement is set and the load corresponding to this indentation depth is measured.

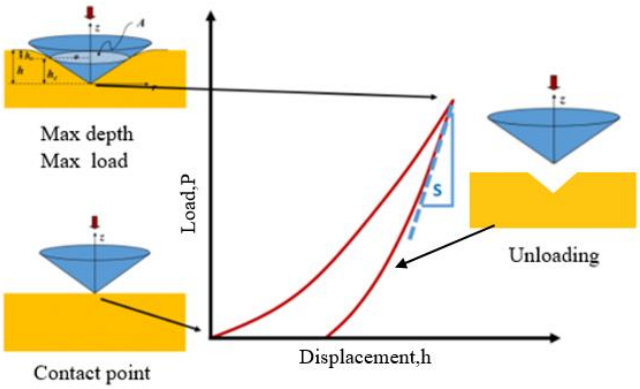

Fig. 2.13. *The schematic of the procedure of nanoindentation experiments.*

The values of hardness and Young's modulus are extracted from the load-displacement data, following the procedure explained next.

The applied load divided by the contact area presents the hardness of the test material. The contact depth can be determined using the method by Doerner and Nix (Doerner, 1986), improved by Oliver and Pharr (Pharr & Oliver, 1992). The hardness is defined as:

$$H = \frac{F_{max}}{A}, \tag{2.3}$$

where H is the hardness and F_{max} is the maximum applied load that can be directly measured during the test. A is the projected contact area. The area of contact at peak load is determined by the geometry of the indenter and the depth of the contact, h_c. For example, in the case of a tip with Berkovich geometry, it is approximated by a cone of equivalent contact area as a function of indentation depth defined by the half-included angle θ. The contact depth h_c can be calculated from the penetration depth h_i, applied load F_{max} and the unloading stiffness S using the Oliver and Pharr model (Oliver & Pharr, 1992) to account for the contact geometry as:

$$h_c = h_i - 0.75\,\frac{F_{max}}{S}\,. \tag{2.4}$$

The Young's modulus can also be extracted by using a relationship including the contact area and the unloading stiffness as:

$$S = \frac{\partial P}{\partial h} = \beta \frac{2}{\sqrt{\pi}} E_r \sqrt{A}, \tag{2.5}$$

where *S* is the unloading stiffness given by $\frac{dP}{dh}$, β equals to unity in most cases and it is a geometrical dimensionless parameter, and E_r is the reduced effective modulus given by

$$\frac{1}{E_r} = \frac{1-\vartheta^2}{E} + \frac{1-\vartheta_0^2}{E_0}. \tag{2.6}$$

E_r is dependent on Young's modulus of the test material (*E)* and the Young's modulus of the indenter (E_0), as well as of ϑ and ϑ_0 which are the Poisson ratio of the test material and the indenter, respectively.

The loading curves can also be used to analyse the behaviour of the material in the elastic and plastic regime during the indentation test. While conducting indentation onto a defect-free surface at small loads, the initial indentation response is purely elastic until a critical load is reached to trigger an onset of plasticity (referred to as the 'pop-in' phenomenon). The Hertz linear elastic theory can be used to describe the load-displacement before the occurrence of pop-in (Bahr et al., 1998; Xiaodong Li & Bhushan, 2002; Van Vliet et al., 2003). The Hertzian elastic theory leads to:

$$F = \frac{4}{3} E_r \sqrt{R h^3}, \tag{2.7}$$

where *F* is the load, *R* is the radius of the tip, *h* is the depth, and E_r is the reduced modulus as defined by equation (2.6). The quantities that are used in nanoindentation analysis are represented in Fig. 2.14.

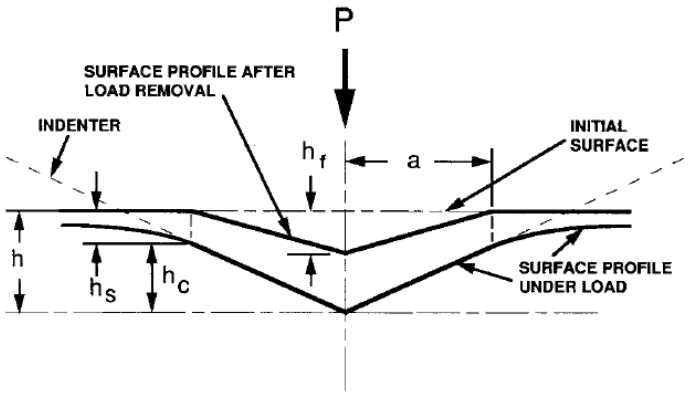

Fig. 2.14. *A schematic representation of a section through an indentation showing various quantities used in analysis, in this image P is applied load (F) (taken from Oliver et al., 1992).*

At the onset of plasticity in the loading curve of each crystal, an obvious pop-in phenomenon occurs during the nanoindentation test. The collective dislocation activities at critical load or displacement may lead to the formation of pop-in as the resolved shear stress approaches its shear strength (Bahr et al., 1998; Xiaodong Li & Bhushan, 2002). The unloading curve overlaps with the loading one before the appearance of pop-in which indicates that loading is fully elastic before pop-in occurs (Hong Wang et al., 2014).

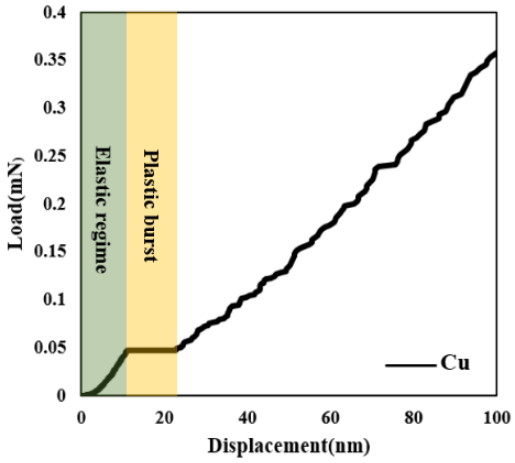

Fig. 2.15. *The typical load-displacement curve of a copper thin film.*

Figure 2.15 shows a typical loading curve for pure copper, a ductile material. As it is shown, the initial part of a load-displacement loading curve is dominated by the elastic properties of the material. After appearing of the

pop-in (called plastic burst), the plastic behaviour of the material reveals. The pop-in phenomenon and different regions of the load-displacement curve extracted from nanoindentation test will be discussed more in chapter 5.

2.5.2 Atomic force microscopy (AFM)

Dynamic atomic force microscopy (AFM) methods are powerful and versatile techniques used to characterise and manipulate atomic and nanometer-scale surfaces with a wide variety. Four main factors make the dynamic AFM interesting and sophisticated including (i) routine nanometer-scale spatial resolution of semiconductors, polymers and biomolecules as well as atomic-resolution images of insulator surfaces in ultra-high vacuum (UHV), (ii) the existence of several parameters sensitive to the tip-sample interactions (amplitude, frequency, phase shift and cantilever deflection), (iii) the challenging features of the motion of a vibrating tip interacting with a surface and (iv) the potential to develop quantitative methods to characterise material properties at the nanometer scale. The amplitude, the resonance frequency and the phase shift of the oscillation link the dynamics of a vibrating tip to the tip-surface interactions. Any of them could be used as a feedback parameter to track the topography of a surface (García & Pérez, 2002). Presently, two major dynamic AFM modes, amplitude modulation atomic force microscopy (AM-AFM) (Martin et al., 1987), and frequency modulation atomic force microscopy (FM-AFM) (Albrecht et al., 1991) are being developed to measure the topography of a sample surface. Most of the experiments in air or liquid are performed by AM-AFM which is also known as tapping mode and is one of the most common modes for tracking the topography of 2D materials. In AM-AFM, a stiff microlever with a sharp tip at its free end is excited at or near its free frequency. The oscillation amplitude is used as a feedback parameter to measure the topography of the sample surface. In addition, the mapping of the phase shift between the driving force and the tip oscillation can be used to record the material properties variations (García & Pérez, 2002).

AFM probe scans across the target surface while collecting data about its properties. An AFM probe is composed of a substrate, a cantilever, and a sharp tip. The high-resolution imaging by AFM probe resulted from a combination of efficient piezoelectric actuation that is used to precisely drive the tip or the sample and a fast feedback control loop for maintaining the user-defined tip-sample interaction, the so-called setpoint. The feedback system responsible

for the achievement of such high resolution is based on precisely sensing the interaction between the tip and sample using a laser-bouncing optical-lever technique that utilizes a fast position-sensitive photodetector (PSPD) (H. Zhang et al., 2018).

AFM based methods have been widely used to measure the mechanical properties of nanomaterials. According to the geometry of the prepared samples, AFM indentation and AFM deflection tests can be utilized.

2.5.3 Nanoindentation by atomic force microscopy

The ability to conduct nanoindentation studies with nanometer depth, and sub-nanonewton force resolution is also possible using a standard AFM setup. The AFM allows for nanomechanical studies to be conducted alongside topographic analyses, without the use of dedicated instruments. Performing nanoindentation with AFM requires an applied static load with a probe and the penetration depth of the tip is calculated. Load-penetration (displacement) is thus obtained and analysed with contact mechanics models. It is equivalent to (nano)-indentation without CSM (without oscillation). Load-displacement curves can be collected similarly for a variety of materials and mechanical properties can be directly calculated from these curves (Kurland et al., 2012). The fundamental tribological characteristics of graphene have been studied by AFM indentation in order to recognise its mechanical behaviour under sliding contact conditions (Filleter et al., 2009; L. Y. Lin et al., 2011). MoS_2 layers were also transferred on a soft poly-dimethylsiloxane (PDMS) substrate and the mechanical behaviour has been investigated via applying a point load by AFM. The elastic behaviour of MoS_2 layers has been studied based on the indentation deformation of the MoS_2/PDMS substrate (Jiang et al., 2020). Figures 2.16a and b represent the schematic of AFM and tip-sample interaction for quantitative nanomechanics study, respectively. The mechanical properties of the CVD-grown h-BN films transferred on Si substrate have been measured by nanoindentation. The large area of h-BN films consisting of two to five atomic layers shows the 2D elastic modulus in the range of 200-500 N/m (Song et al., 2010a).

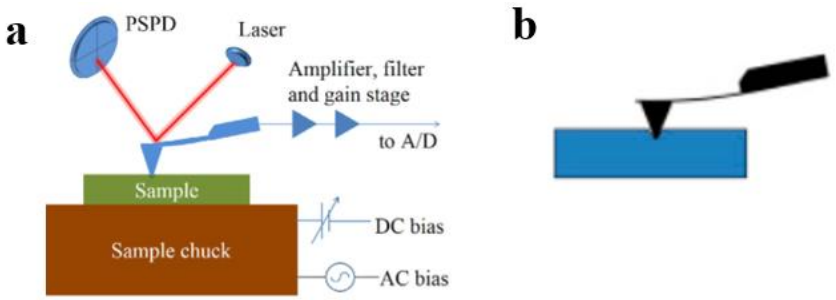

Fig. 2.16. *(a) Schematic representation of an AFM; (b) tip-sample interaction for quantitative nanomechanics study (taken from Zhang et al., 2018).*

2.5.4 Membrane deflection by atomic force microscopy (suspended mechanical testing)

In the case of suspended 2D films transferred on the patterned trenches, AFM deflection method is usually applied. The AFM deflection method is a simple, direct and non-destructive approach to obtain the elastic properties of atomically thin membranes. By pressing the centre of the suspended 2D sheets with calibrated AFM tips, their Young's modulus can be successfully extracted (Frank et al., 2007; Gómez-Navarro et al., 2008). Figure 2.17 shows a schematic of probing the mechanical properties of 2D layers by AFM deflection test. The width, length, and thickness of 2D materials can be precisely measured with AFM and Raman spectroscopy.

Young's modulus and strength of single-layer graphene have been determined by AFM, and the value of the 2D stiffness (E^{2D}) has been recorded 342 N/m (C. Lee et al., 2008a). Bertolazzi et al. have used AFM deflection to determine the mechanical properties of the exfoliated mono and bilayer MoS_2 (Bertolazzi et al., 2011). A deflection test by AFM has been performed to measure the elastic properties of freely suspended MoS_2 nanosheets, with thicknesses ranging from 5 to 25 layers. These measurements give the possibility to simultaneously measure Young's modulus (E) and the initial pre-tension (T) of the MoS_2 nanosheets (Castellanos-Gomez et al., 2012).

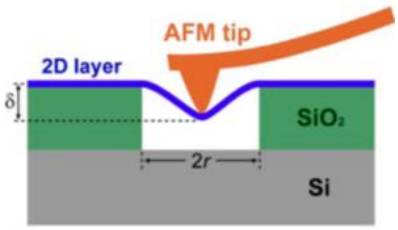

Fig. 2.17. *Illustration of probing mechanical properties of 2D materials by AFM deflection test (taken from Liu et al., 2014).*

The value of E^{2D} and the average fracture strength have been recorded to be 270±100 GPa and 23 GPa, respectively which are several times less than the values for graphene but yet much stronger than the one for steel (Bertolazzi et al., 2011). WSe_2 layers have been isolated by mechanical exfoliation from bulk WSe_2 then a flake of multilayer WSe_2 has been transferred onto a pre-patterned Si/SiO_2 substrate. It was reported that the decreas of the number of layers results in decreasing the prestress which cause the linear enhancement of E^{2D} (R. Zhang et al., 2016). 2D stiffness of MoS_2, WS_2, and the heterostructure of them (MoS_2/WS_2), as well as the heterostructure of MoS_2/Gr, has been determined by AFM. The 2D stiffness are 171±11 N/m and 177±12 N/m for MoS_2 and WS_2, respectively. The E^{2D} of MoS_2/WS_2 heterostructure is measured to be 314 ± 41 N/m and for MoS_2/Gr is calculated to be 467± 48 N/m (K. Liu et al., 2014a). Although, extracting the mechanical response of 2D layers with a deflection test is one of the most common methods, there are different sources of uncertainties that can definitely affect the results. There are not enough studies on these uncertainties while performing deflection tests by AFM on 2D layers. The challenges and uncertainties resulting from this method as well as the extracted mechanical properties of single and bilayer graphene with using this method will be discussed further in the chapter dealing with deflection testing

2.5.5 Lab on chip (suspended mechanical testing)

In addition to the AFM based methods, various microelectromechanical systems (MEMS) have been developed to realize the accurate measurement of the elastic properties and simultaneous visualization of the fracture behaviours of 2D materials. Lab-on-Chip (LoC) technology is a technique that

brings various laboratory operations on a miniaturized scale. In other words, LoC is a device that can apply single or multiple laboratory functions on a chip format by scaling them down (Gupta et al., 2016). This technology enables the development of the next generation of portable and implantable microelectromechanical (MEMS) and nanoelectromechanical (NEMS) systems (Giannitsis, 2011). By increasing the applications of nano-scale thin film materials, the demand for the miniaturization of mechanical and electronic systems has surged. On the other hand, the mechanical properties of thin films play a significant role in the functionality and efficiency of small-scale systems (Haque & Saif, 2002). Mechanical testing of thin films with a few nano to microns thick requires novel techniques and advanced procedures for preparation, handling, and loading (Sharpe et al., 1997).

Several techniques have been reported to evaluate the mechanical properties of thin films, such as biaxial bulge tests (Vlassak & Nix, 1992), hardness tests (Stone et al., 1988), uniaxial tensile tests that record cross-head speed to determine strain (Koskinen et al., 1993), and bending experiments including the measurement of deflection or resonant frequencies of microcantilever beams (X. Ding et al., 1990; Weihs et al., 1988). However, each method has its limitations and performing a mechanical test on samples in the micro or nanoscale is extremely challenging. These challenges result from fabrication techniques, handling of micro or nanoscale samples, applying load, and data processing. On the other hand, the constraints regarding microstructure (grain size) and dimension (specimen thickness) can change or even reverse conventional size laws in materials behaviour (Arzt et al., 1998).

For instance, the Hall-Petch phenomenon for different materials represents three regions including i) when grain sizes are above 1 μm and the conventional Hall-Petch relationship works, ii) when grain sizes are from 30 nm to 1 μm and deviation from the classical Hall-Petch relationship is observed, and finally (iii) when grain sizes are below 30 nm, where no further strengthening or even reverse Hall-Petch behaviour is observed (Gutkin et al., 2001). Despite the reports of the observation of reverse Hall-Petch behaviour for nano-crystalline materials in indentation experiments (Chokshi et al., 1989) and simulation (Schiøtz et al., 1998), no investigation report this behaviour for tensile testing experiments. Among all known techniques for mechanical properties characterisation, the most functional one for thin films is uniaxial tensile testing which provides the most straightforward data to extract both elastic and plastic properties.

In tensile testing machines, four main elements must be considered. These are the actuator, the load and the strain sensors as well as the mechanical frame

and the grips. All parts of the tensile testing machine need to be adapted for small-scale testing. While using the tensile testing in nano-scale, there are some critical challenges such as (a) preparation of freestanding structures (b) gripping of the specimen, (c) measurement of prestress in the specimen, (d) accurate alignment in the structure, and (e) generation and measurement of small-scale forces and displacements in the specimen (Haque & Saif, 2002).

Several techniques and devices have been proposed to perform such tests on thin films. The works of Tsuchiya (Tsuchiya et al., 1998) and Sharpe (Sharpe et al., 1997) were the starting point on uniaxial tensile testing techniques on freestanding films. An electrostatic force gripping system has been reported by Tsuchiya et al, to load the thin films. Figure 2.18 represents a schematic of tensile testing developed by Tsuchiya. The structure contains a thin film specimen that acts as a beam fixed at one end to the silicon substrate and with a large pad at the other end. In order to perform the tensile testing of the cantilever beam, a probe is in contact with the free end pad. By applying a voltage between two surfaces an electrostatic attractive force is generated. Tensile testing is achieved by piezoelectric actuation of the probe along the axis of the specimen. This technique makes it possible to extract the stress-strain curve from small deformation until fracture for monocrystalline and polycrystalline Si, as well as Ti and Ni films possible (Tsuchiya et al., 1998)

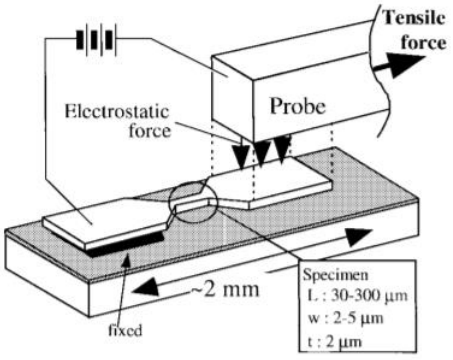

Fig. 2.18. *Schematic of tensile testing using electrostatic grips (taken from Tsuchiya., 1998).*

Sharpe et al, have developed a technique which used microfabrication to pattern the specimen in a dog bone shape. A silicon wafer is used as the substrate and etching the window underneath the specimen is done by bulk micromachining. The silicon frame with the specimen was placed on the testing stage and gripped at both ends. One grip is fixed and the other one is

glued to a load cell which is fixed on a piezoelectric actuator. After making the specimen free by cutting it with a rotary tool, tensile testing is performed. During testing, the load and strain are measured via the load cell laser-based interferometry (reflective gold strips are patterned on the surface of the specimen), respectively.

Later on, a technique was reported in which a specimen is created by microfabrication techniques connected to a plate containing a hole called a loading hole. The same thin-film deposit has been used to deposit the frame and the specimen on the Si substrate. The specimen is then released from the substrate except for one end, and a tungsten hook is engaged in the specimen through the hole. Then by using an external micromanipulator the load is applied to the hook and finally, the displacement and strain can be recorded (Cheng et al., 2005). In the mentioned techniques, the actuation source is external which cause difficulties in making the connection between the specimen and the actuator.

To solve this problem, the integration of specimen and actuator on the same wafer seems a good solution. A stage was fabricated by single-crystal silicon with one end fixed and the other attached to a piezoelectric actuator. The specimen is deposited on the stage, one end connected to the fixed beam (load sensor) and the other to support beam assembly. The whole chip is pulled and the displacement can be measured directly by the use of the cursors on the specimen (Haque & Saif, 2002). Then Espinosa reported a technique with test specimen on a stage with capacitive sensors and electrostatic or electrothermal actuators. In this technique, the actuators are used to load and captive sensors to measure the load (Espinosa et al., 2007). The schematic of the MEMS-based tensile testing is shown in Fig. 2.19.

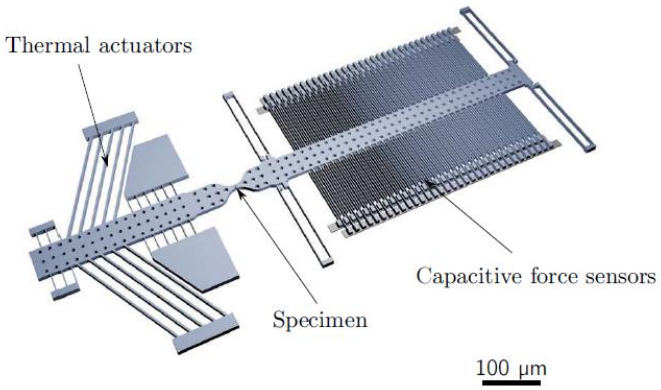

Fig. 2.19. *Schematic of MEMS-based tensile testing stage using electrothermal actuation developed by Espinosa et al. 2007 (taken from Coulombier thesis., 2012).*

The deformation and failure mechanisms in materials at the 2D limit are of fundamental importance but have been little studied by experiments.

A method has been developed for in-plane nanomechanical testing of $MoSe_2$ layers. An improved dry transfer approach has been used for fragile $MoSe_2$ membranes, and then the mentioned system has been used to investigate the mechanical behaviour of monolayer and bilayer $MoSe_2$. This system provides the in-plane tensile testing consisting of a thermally actuated shuttle and a load shuttle fixed to calibrate springs. Thermally actuated shuttle and the load shuttle are used to induce the tensile strain in materials and measure the pulling force, respectively. Thus the stress-strain curve can be directly measured (Y. Yang et al., 2017). The study of the mechanical response of patterned graphene nanoribbons (GNRs) with a width less than 100 nm has been done using in-situ quantitative tensile testing in a transmission electron microscope (TEM). The maximum local true strain of the nanoribbons was measured to be about 3% (Z. Liao et al., 2017). An in situ tensile testing has been performed on suspended graphene using a nanomechanical device in a scanning electron microscope (SEM). Performing tensile loading on pre-cracked graphene reveals a fracture in a brittle manner with sharp edges at fracture stress substantially lower than the intrinsic strength of graphene. The combination of experiments and modelling indicates that the classic Griffith theory of brittle fracture applies to graphene.

In the study performed by Zhang et al., they used a developed platform that integrates a micromechanical device and a nanoindenter. The graphene sample contains a pre-crack with a length of 10% of sample width. As the applied load increased to a critical value, brittle fracture occurred quickly from the pre-crack, resulting in two fractured pieces with flat edges. Figure 2.20 shows the in-situ SEM of nanomechanical tensile testing of fracture of graphene with a pre-crack. The fracture toughness of graphene is measured as the critical stress intensity factor of $4 \pm 0.6\ MPa\sqrt{m}$ and the equivalent critical strain energy release rate of $15.9\ Jm^{-2}$ (P. Zhang et al., 2014).

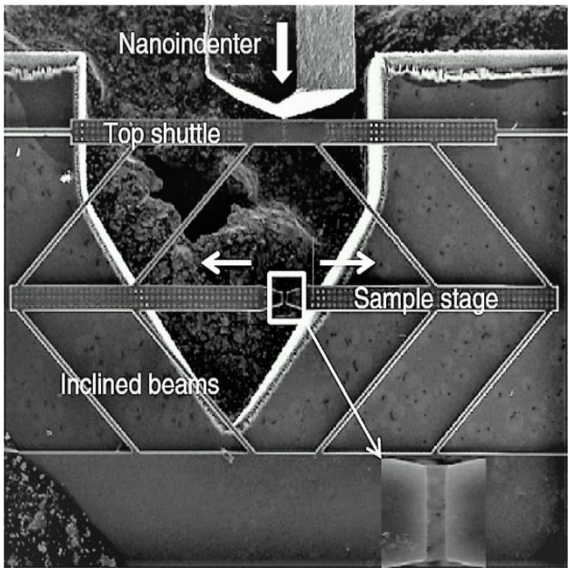

Fig. 2.20. *Nanomechanical testing of fracture of graphene with a pre-crack. The in-situ SEM tensile testing with a microdevice. Movement of the nanoindenter tip (shown by the white arrow) was converted to pure tension of the specimen on the sample stage by the inclined beams. Inset is the magnified image of the boxed region showing graphene across the gap of the sample stage (taken from Zhang et al., 2014).*

The key process of these methods contains the following two steps: (1) specific transfer of suspended 2D materials onto the testing stages; (2) patterning the transferred film into a rectangular shape with FIB for further tests. These devices can transfer the force exerted on the beam by the indenter to the tension of the stage by using the "push-to-pull" mechanism, thus the in-plane tensile test of 2D materials can be realized. Combining with SEM and TEM, manipulators provide us more flexibility to investigate various mechanical properties of 2D materials.

The technique used in this work has been developed at UCLouvain to apply uniaxial strain on thin films and 2D materials. In this technique, an effort has been done to avoid the issues in the mentioned techniques as well as providing a simple and versatile tool to make testing on a large range of materials at a micro-scale possible (André et al., 2007; Boé et al., 2009; Fabrègue et al., 2007; Gravier et al., 2009). Figures 2.21a and b show a schematic of the elementary tensile testing stage and a schematic of several tensile testing structures with different lengths of sample/actuator, respectively.

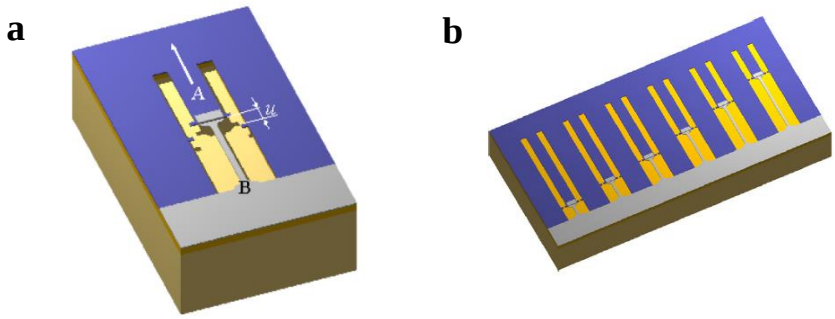

Fig. 2.21. *(a) Schematic of the elementary tensile testing stage; A is the actuator beam made of silicon nitride which loads sample beam B. After release, the displacement u can be measured using the cursors; (b) Several tensile testing structures with different lengths of sample/actuator to generate a full stress-strain curve up to fracture [taken from Boe et al., 2004].*

The main two advantages of this technique are:

1. The internal stress of the film deposited on the wafer is used to actuate the specimen.

2. There can be hundreds or thousands of devices on each wafer thanks to using the capability of microfabrication technology.

In this work, to investigate the effect of graphene on the creep and fracture behaviour of Cu thin film, this technique has been used. The process of sample preparation is very complicated which makes it challenging to extract statistical results. The steps of the process, material selections and the challenges regarding the procedure will be explained in chapter 6.

Chapter 3

Materials and test procedures

3.1 Introduction

This chapter outlines the main equipment and methods that have been employed to process and study the mechanical response of graphene systems.

The method section includes; first a description of the CVD equipment that has been used to process graphene. The transfer process is discussed in the second section which is divided into two subsections including the conventional PMMA-wet transfer method and the modified PMMA-wet transfer one. The etching process is explained in section 3.2.3. To deposit metallic thin films, electron beam evaporation has been used which is described in section 3.2.4. The positive and negative lithography procedure is mentioned in detail in section 3.2.5 followed by the description of scanning electron microscopy, Raman spectroscopy and transmission electron microscopy in sections 3.2.6, 3.2.7 and 3.2.8, respectively. Finite element (FE) simulations including Abaqus and Comsol are described in sections 3.3.1 and 3.3.2, respectively. The principle of discrete dislocation dynamics (DDD) simulation is explained in section 3.3.3.

3.2 Experimental Methods

3.2.1 CVD equipment

The CVD equipment consists of the CVD furnace, gas feedstock, mass flow controllers (MFCs), pumping system, throttle valve and pressure gage. The CVD furnace is composed of a CVD reactor with a horizontal hot-wall placed in a double layer steel casing. The tube with the heated zone is enfolded inside an alumina refractory sheath containing the heating elements. The CVD furnace is equipped with three gas bottles including, pure Ar and pure CH_4 with a research grade of 99.9999% and a mixture of Ar/H_2 (5%). The rate of gas flow is controlled using thermal mass controllers (Sevenstar, D07 series). These mass flow controllers assign various flow rate controlling ranges and are usually calibrated using nitrogen. The control of the gas pressure inside the CVD system is done by a throttle valve between the CVD furnace outlet and the pumping system. A cold cathode/Pirani hybrid gauge (PKR251, Pfeiffer vacuum) was used to measure the global pressure of the CVD which has been designed for vacuum measurement in the range of 5×10^{-9}-1000 mbar pressure. Figure 3.1 shows the schematic of CVD equipment containing different elements.

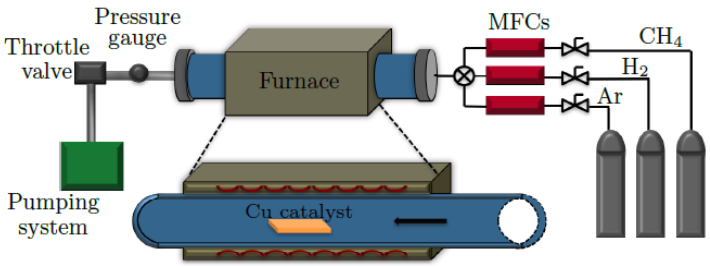

Fig. 3.1. *Schematic representation of the entire CVD system including different parts (taken from B. Huet, PhD thesis).*

In order to produce the graphene layers via CVD process, controlling different parameters such as gas pressure, temperature and the time duration of each step is of utmost importance. All details about the effect of these parameters have been mentioned in Dr. Benjamin Huet thesis. Figure 3.2 shows the schematic of CVD process that has been used by him to produce continuous single layer graphene including different steps such as furnace warming up, Cu annealing, graphene growth and furnace cooling down [Huet et al., 2018].

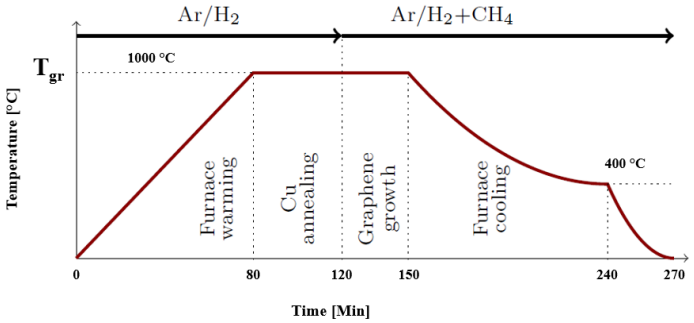

Fig. 3.2. *Schematic of graphene growth protocol via CVD experiments on Cu foils (taken from B. Huet, PhD thesis).*

3.2.2 Transfer procedure

A significant effort has been done to develop a transfer technique which is scalable, clean and can maintain the structural integrity of 2D materials. However, there are not enough procedures that can fulfil these criteria. In the framework of this thesis, CVD-grown graphene has been regularly transferred from the Cu foil onto a perforated SiO_2/Si substrate and wafers for Lab-on-

Chip process containing a thin layer of Cu. For these processes using the conventional PMMA-transfer method is not satisfying hence a modified PMMA-transfer method has been designed and used. Both techniques will be described in detail and the advantages of the modified version of transferring will be mentioned.

3.2.2.1 Classic PMMA-wet transfer method

CVD-graphene has been grown on Cu foil and after being removed from the furnace, it has been protected by a layer of PMMA (950 PMMA A9, MicroChem) diluted in anisole (99%, Sigma-Aldrich) which is directly spin-coated on the graphene for one minute. The concentration of PMMA is determined by the proportion between PMMA and anisole. The thickness of the PMMA layer was around 400 nm and can be controlled by the acceleration of the spin coater and the concentration of the PMMA. The stack of PMMA/Gr/Cu is placed on the $FeCl_3$ etchant in order to etch away the copper foil. Once the Cu substrate is etched, the etching solution is gradually replaced by de-ionized water to rinse graphene. The PMMA/Gr stack floating on the de-ionized water is scooped by the target substrate and vertically located in a clean place to be dried. The PMMA layer is then removed using a warm acetone bath (60°C) for at least 30 min. The bath is then naturally cooled down to room temperature before successively rinsing the sample with fresh clean acetone, isopropanol, and water. If necessary, PMMA residues can be removed using PG remover or diluted acetic acid. The schematic of the classic PMMA-wet transfer is presented in Fig. 3.3.

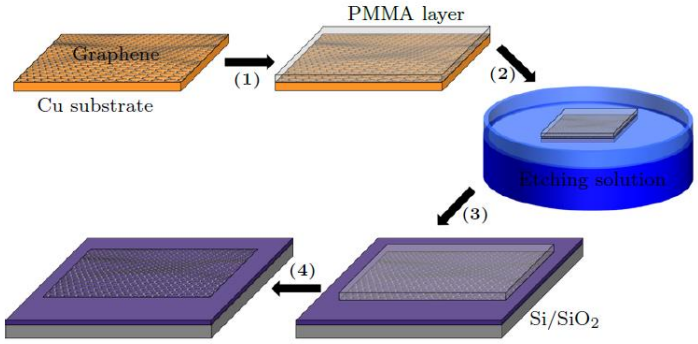

Fig. 3.3. *General process flow for the PMMA-wet transfer procedure; (1) PMMA spin-coating directly on the Gr/Cu substrate; (2) Cu removal in a Cu etching solution and graphene rinsing with de-ionized water; (3) PMMA/Gr scooping with the SiO_2/Si substrate and; (4) PMMA removal with acetone.*

3.2.2.2 Modified PMMA-wet transfer method

The modified version of the PMMA-wet transfer is almost the same as the conventional one including the modification in the step of scooping the stack of Gr/PMMA on the substrate. In this approach, in order to reduce the water accumulation between graphene and the substrate while fishing it from water, a piece of clean room paper has been used to catch the PMMA/Gr stack from the PMMA side. Then the stack of paper/PMMA/Gr is placed on a heating plate at 60°C to evaporate the water on the surface of graphene (this step should not take more than 2 to 5 mins, taking more than that cause the paper to be completely dry and graphene will be detached from the paper on the heating plate.) and finally, the stack is placed on the substrate from the graphene side. After completing the transfer, paper can get dried naturally or by using nitrogen and it gets separated from the PMMA. The last step, dissolving the PMMA in acetone, is the same as the conventional method. In this technique, the VdW forces between the paper and PMMA layer need to be less than the VdW forces between graphene and the target substrate, otherwise, graphene is torn while trying to place it on the target substrate. Considering that, the thickness of PMMA needs to not be less than 300 nm and all types of paper cannot be useful in this approach. Fig. 3.4 shows the schematic of the modified version of PMMA-wet transfer.

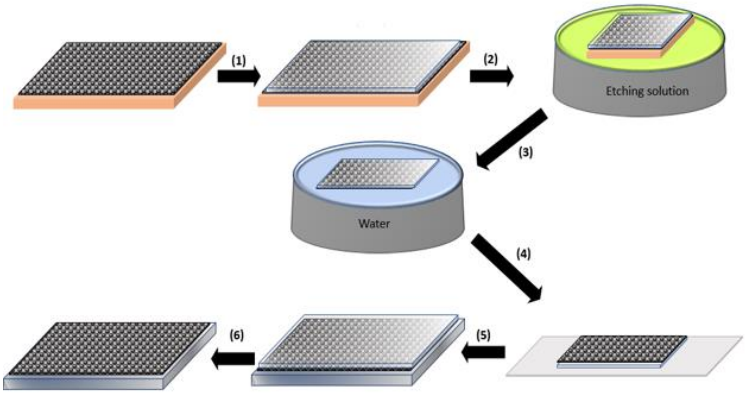

Fig. 3.4. *Modified process flow for the PMMA-wet transfer procedure; (1) PMMA spin-coating directly on the Gr/Cu substrate; (2) Cu removal in a Cu etching solution ($FeCl_3$) and graphene rinsing with de-ionized water; (3) PMMA/Gr catching with the piece of paper from PMMA side; (4) placing Gr/PMMA/paper on the target substrate and; (5) PMMA removal in acetone.*

When transferring graphene on the perforated substrates, less water accumulation between graphene and substrate means less water accumulation

inside the cavities/gaps which leads to less evaporation and less breakage in graphene. This method increases significantly the quality of transferring 2D materials on the patterned substrates as well as the suspension tendency of 2D layers. The improvement of the transfer on the perforated substrate is shown in Fig. 3.5.

On the other hand, while transferring 2D layers on metal substrates such as copper, using conventional PMMA-wet transfer accelerates the oxidation of the metal underneath of 2D layer resulting from the accumulation of water in between. In this case, using the modified transfer method is notably practical. The reduction in the oxidation of Cu underneath graphene after transferring can be seen in Fig. 3.6.

The possibility to control the position of graphene or any other 2D layer on the target substrate is another advantage of this method that cannot be achieved easily while scooping the layer from water with the target substrate.

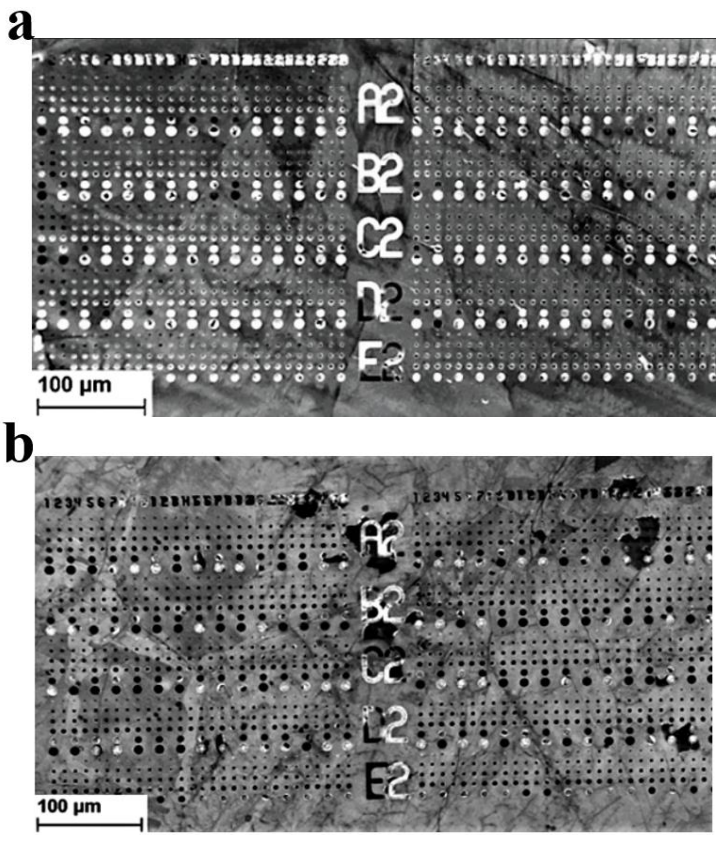

Fig. 3.5. *a) Transferring SLGr on Si/SiO_2 substrate containing the cavities with conventional PMMA-transfer method; b) transferring SLGr on Si/SiO_2 substrate containing the cavities with modified PMMA-transfer method.*

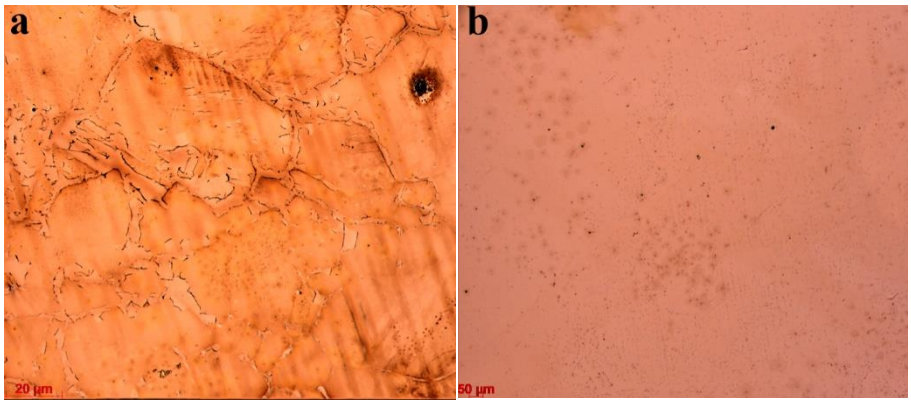

Fig. 3.6. *a) Severe oxidation of Cu underneath Gr transferred with conventional PMMA-transfer method; b) some small spots of oxidation of Cu underneath Gr transferred with modified PMMA-transfer method.*

3.2.3 Etching

One of the critical experimental steps during the fabrication process is etching. There are two different approaches in etching called wet and dry etching. Dry etching is usually a mixture of physical and chemical processes. Reactive ion (RIE) and XeF_2 etching are the most known dry etching procedures which have been used in this work. On the other hand, wet etching is a purely chemical process using a chemical solution depending on the material to be etched.

In RIE, a plasma is created by a flow of a mixture of etching gases into the chamber and an RF the powered magnetic field. The chemically reactive plasma bombards the target substrate with high-energy ions to remove materials deposited on wafers. O_2, CHF_3, SF_6, and Cl_2 are the main gases that are typically used for the RIE process regarding the materials to be etched. A highly anisotropic etch profile can be produced due to the vertical nature of the plasma ions bombardment. Consequently, the etching is directional, and it can produce patterns with high aspect ratios. However, the main drawback of RIE is the poor etching selectivity.

Etching selectivity is the etch rate ratio between the target material and the other materials present in the system.

The XeF_2 etch process is a purely chemical one and usually results in a rough etched surface. This isotropic process allows the etching of silicon with almost infinite selectivity from silicon to photoresist, silicon oxide, silicon nitride and aluminium. XeF_2 has a vapour pressure of 4 Torr (533Pa). The

equipment works in a pulsed mode and contains a chamber which is repeatedly filled with XeF_2 gas, then pumped out and replaced by N_2 gas. The etch time and pressure of XeF_2 gas inside the chamber can be controlled. By keeping the pressure and time small for each pulse, the etching process can be controlled in a better way.

On the other hand, a chemically active solution reacts with the target material in wet etching. Normally by selecting the right solution, high selectivity can be achieved in this type of etching. Despite better etching selectivity, the isotropic profile of wet etching leads to the etching of the target material in all directions. This makes the patterning of the structures with a high aspect ratio almost impossible in wet etching. Figure 3.7 illustrates three different profiles achieved by etching for the same structure.

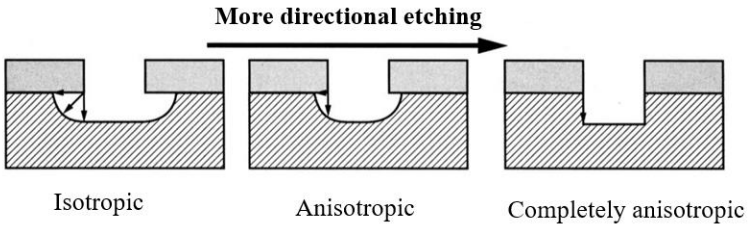

Fig. 3.7. *Three different patterns achieved by isotropic, anisotropic, and completely anisotropic etching.*

3.2.4 Electron beam evaporation

A wide range of vacuum deposition methods that enables the growth of thin films on a substrate, atom by atom is called physical vapour deposition (PVD). In vacuum deposition methods, the condensed material is vaporised in the vacuum environment in which a material starts from its condensed phase, is vaporised in the vacuum environment then re-condensed on the target substrate in order to form a thin film. One of well-known methods among different PVD methods is the electron beam evaporation used for the deposition of pure metal thin films such as copper and nickel. The schematic of the electron beam evaporation is shown in Fig. 3.8. In this physical process, the chosen metal is evaporated from the crucible (the source) by heating it at high vapour pressure with an electron beam under a vacuum of 10^{-2} Pa. A hot tungsten filament generates a high kinetic energy electron beam which is deviated by the electromagnetic field on the crucible. Electron beam causes the evaporation of the atoms from the source to deposit on the substrate in order to form the thin film.

Based on the position of the wafers inside the chamber, two types of depositions can be performed. When the wafers are placed perpendicular to the flow of evaporated atoms, and atoms are deposited on the wafer in a normal way, in a way snow falling vertically on a ledge, the mode of deposition is lift-off mode (Figure 3.9a). In order to have a more homogeneous deposition, the rotate mode can be chosen. The wafers rotate relative to the direction of flow during deposition and it makes it possible for atoms to be deposited on the target surface from all directions (Figure 3.9b) Based on the application and the necessities in the fabrication process, the mode of deposition can be chosen.

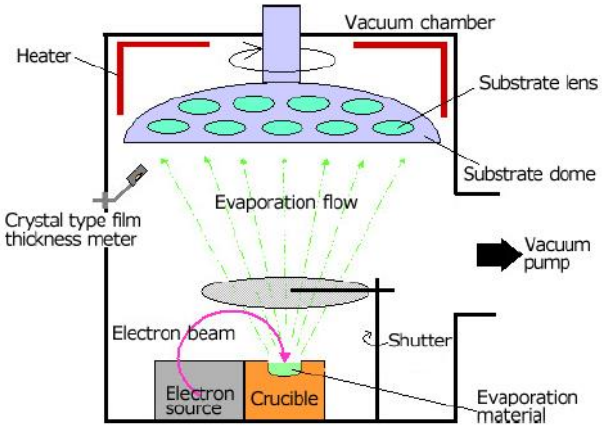

Fig. 3.8. *Schematic of the way that electron beam evaporation is functioning.*

Fig. 3.9 *Schematic of a) lift-off mode; b) rotate mode.*

3.2.5 Lithography

One of the most important techniques in any microfabrication process is lithography. Lithography is a method to transfer a pattern to a photosensitive material which is done by selective exposure to a radiation source such as light. The physical properties of a photosensitive material change after being exposed to the radiation source. The exposure can be performed by masking some of the radiation to design a desired pattern on the photosensitive material. The pattern is formed as the properties of the photosensitive material differ from the exposed and unexposed parts. The lithography process is categorised into two main types, first, photolithography, and second electron beam (e-beam) lithography. The main method that has been used in this work is photolithography. In photolithography, the exposure source is a UV light source. The light-sensitive material is a kind of resist which can be classified as a positive or negative resist. In a positive photoresist, the exposed portion to light becomes soluble to the photoresist developer and the unexposed part remains stable. On the other hand, a negative photoresist is a type of resist in which the portion of the photoresist that is exposed to light becomes insoluble to the photoresist developer and the unexposed portion is dissolved by the photoresist developer. The process starts by coating the substrate first with a thin layer of HMDS to promote the adhesion of the surface. It is followed by spin coating the photoresist. Then the exposure of the photoresist is performed by using a photomask with the desired pattern and finally, the photoresist is developed to dissolve the soluble parts of the resist. Mostly, this step is followed by etching exposed material and stripping the photoresist to achieve the final structure. Figure 3.10 shows a schematic illustrating the concept of lithography.

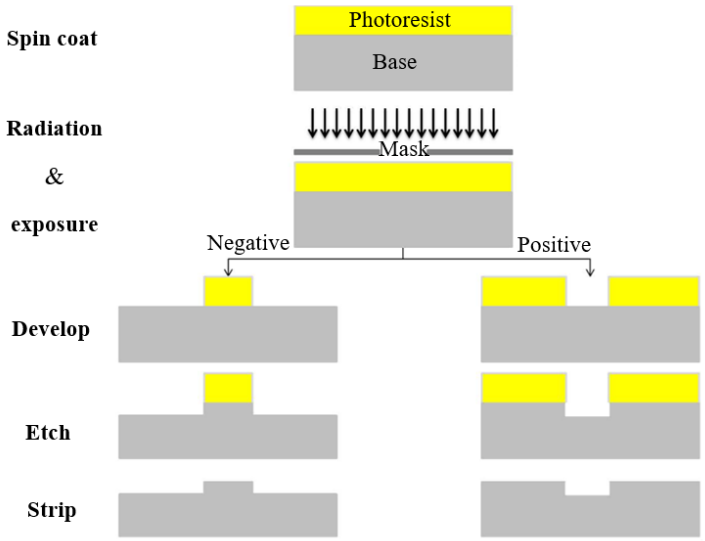

Fig. 3.10. *Schematic of photolithography steps for both positive and negative photoresists.*

3.2.6 Scanning electron microscopy (SEM)

Scanning electron microscopy (SEM) is an effective technique for imaging 2D layers in a rapid and non-invasive way on a wide variety of substrates. The SEM (Zeiss Gemini Ultra-55) is a versatile tool for detecting impurities, cracks, folds, wrinkles, voids and spatial variations of the number of layers at the micro and nano-scales. There are some challenges in properly imaging graphene or other 2D materials, including (i) probing the cross-section of the one-atom-thick material is beyond the SEM resolution limitations, (ii) the morphologies of the substrate supporting 2D sheets are mainly shown in the SEM images rather than the graphene itself due to the transparency of atomically thin film to high energy electron beams, and (iii) there is no strong contrast in SEM imaging of 2D layers resulted from their very smooth surface. Consequently, using suitable SEM settings is necessary to gain enough good contrast to probe the surface details including surface roughness, edges and additional layers.

3.2.6.1 Detector type

SEM is a type of electron microscope generating images of a sample by scanning through the surface with a focused beam of electrons. The working principle of SEM is based on the emission by using a very fine heated filament and acceleration of the kinetic energy of electrons to the desired limit when propagating down through the vertical column. To focus the electron beam down to the target substrate, there is a two-lens system installed in the Gemini column with the dedicated spot size. The incident electron beam interacts with atoms in the sample of interest, generates various types of signals which differ by their origin, energy and direction, and thus carries distinct information about the surface topography and composition of the sample.

In this thesis, two different detectors have been utilized to investigate the surface of graphene: a regular Everhart-Thorney (E-T) and an in-lens (also called in-column) detector. Both detectors collect the secondary electron (SE). Upon the radiation of the incident electron beam, these electrons are produced into the test sample at different depths. The in-lens detector efficiently collects the electrons generated close to the surface in the vicinity of the irradiated region which is called type I secondary electrons (SE1) and leaves the surface with a high angle (i.e. almost perpendicularly to the surface). On the other hand, the type II secondary electrons (SE2) are collected by the E-T detector and generated from a deeper and wider volume inside the substrate and leave the substrate surface at a lower angle.

As a result, the signal enriched in SE1 carries high-resolution surface-sensitive data of the sample which is transferred to the in-lens detector while lower-resolution topographical information can be delivered by the E-T detector. Although the in-lens detector is mainly utilized to observe the graphene film, the underlying substrate (Cu film/foil or SiO_2/Si substrates) is detected by using the E-T detector. Figs. 3.11a and b are representing the SEM imaging of graphene on different substrates in in-lens mode and Fig. 3.12 shows the SEM imaging of graphene on Cu substrate in E-T mode.

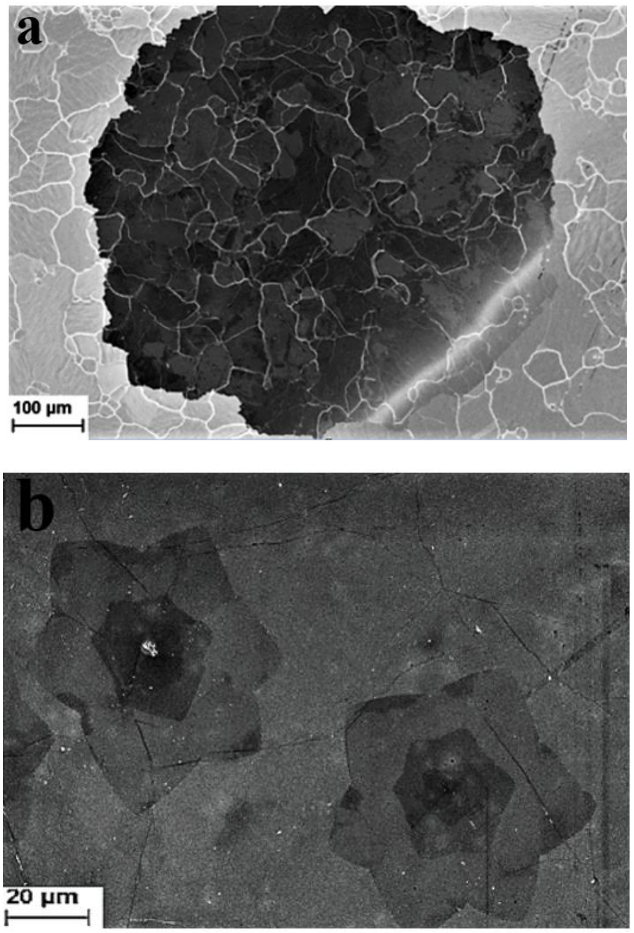

Fig. 3.11 *a) SEM in-lens imaging of as-grown Gr on Cu film substrate; b) SEM in-lens imaging of transferred Gr on Si/SiO_2 substrate.*

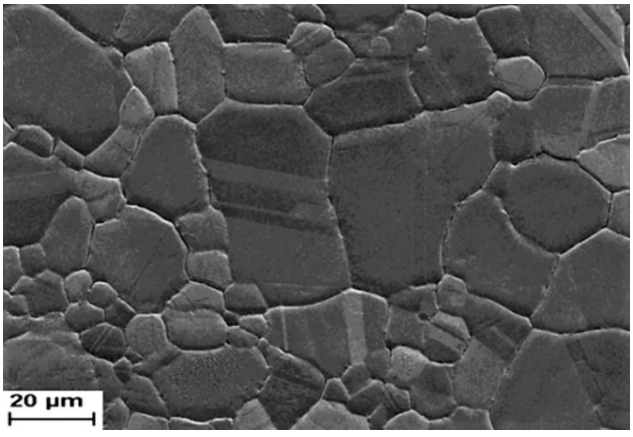

Fig. 3.12 *a) SEM imaging with E-H detector of Gr on Cu film substrate.*

3.2.7 Raman spectroscopy

Raman spectroscopy is a non-destructive technique and versatile characterisation tool. This technique is very useful in determining the number of layers of graphene, the stacking order of layers, the structural quality and types of edge as well as the origin of perturbations including mechanical strain, doping and disorder. Raman spectroscopy measurements are functioning based on monochromatic light which illuminates the sample and the analysis of scattered radiation. This radiation results from various interaction events between photons, electrons and phonons within the material. In this research, LabRAM HR equipment has been used to carry out Raman measurements by using a green laser (excitation energy of *2.41 eV* or *λ=514 nm*, power level below *1 mW*) on various graphene samples including as-grown on the Cu catalyst and transferred in the form of supported or suspended.

3.2.7.1 Basic principles of RAMAN

The scattered radiation coming from the re-emission of the incident radiation exposed on a sample can represent either a different wavelength (Stokes and Anti-Stokes Raman scattering) or an identical wavelength (Rayleigh scattering). Raman scattering is an inelastic scattering and it takes place when an incident photon excites an electron from a ground state and by transferring part of its energy to phonons, it returns to a different state. On the other hand, in Rayleigh scattering (also called elastic scattering) the pair returns to its initial state by emitting a photon with identical energy but a different propagation direction.

The Raman spectra in this work have been achieved with the Horiba equipment and the LabSpec software which represent the plot of the intensity of scattered light as a function of the Raman shift which is the difference between the incident and scattered photon energy. The Raman shift units are usually expressed in cm^{-1} which can easily be converted into energy units using the relation;

$$1meV = 8.0655447cm^{-1} \quad (3.1)$$

3.2.7.2 Raman spectroscopy on CVD-Gr

Raman spectroscopy can be carried out either directly on the grown graphene on donner substrate or after transferring graphene on another material substrate. In addition, it can be performed on supported or suspended graphene. However, it is important to consider proper acquisition parameters. Figure 3.13 represents the Raman spectra of graphene on different substrates.

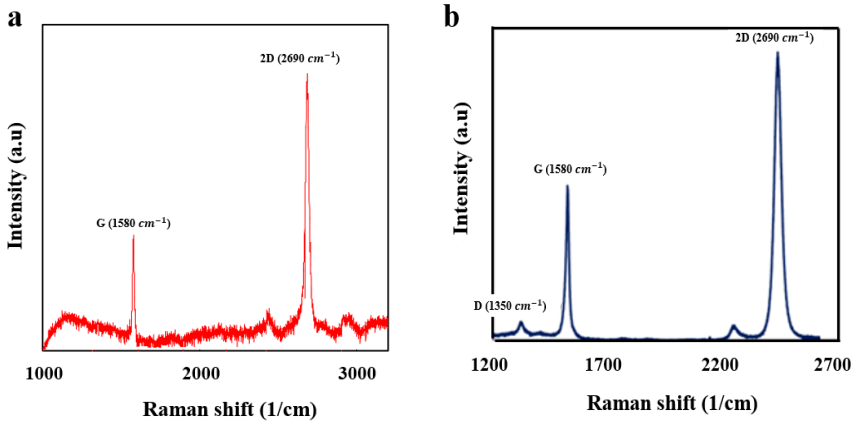

Fig. 3.13 *a) Raman spectrum of SLGr grown on Cu (the effect of background is removed); b) Raman spectrum of SLGr transferred on Si/SiO_2.*

3.2.8 Transmission electron microscopy (TEM)

The transmission electron microscope (TEM) is a versatile instrument engineered specifically for the investigation and visualization of samples with dimensions ranging from micron to nanometer. The revealing of highly complex levels of detail is a capability of TEM which is not an accessible feature in conventional light microscopes.

There is an electron source called gun or electron canon normally in a V-shaped filament made of LaB_6 (lanthanum hexaboride) or tungsten in the structure of TEM. A positive potential to the anode is applied to the gun and increases the temperature in the filament (cathode) to a limit. At this status, the filament can produce an electron current with a wavelength given by the De Broglie equation

$$\lambda = \frac{h}{\left[2m_0 eV\left(1 + \frac{eV}{2m_0 c^2}\right)\right]^{1/2}} \tag{3.2}$$

Where λ is the wavelength, h is the Planck constant, m_0 is the residual mass of the electron, e is the charge of the electron, V is the potential difference, and c is the speed of light.

In order to improve the light coherence, the electron beam is modified by the condenser and aperture lenses before reaching the sample (Escalante et al., 2019). When the electron beam hits the sample, there are two possibilities; either the electrons can affect the sample and disperse while avoiding the loss of energy (elastic) or the inelastic behaviour where electrons deliver part of their energy to the internal electrons of the sample. The objective lens focuses on the scattered beams to produce the first image. In this step, the diffraction process performed by the projection lens expands the electron beam and reflects it on the phosphor screen. The amplitude and phase alterations in the electron beam determine the image resolution. This alteration is determined by the contrast transfer function (*CTF*) and it is defined by:

$$CTF = A(q).\exp[iX(q)] \tag{3.3}$$

Where $A(q)$ is a function that describes the diffraction diagram truncation by the aperture of the objective lens, and $exp[iX(q)]$ defines the phase function that describes the distortion of the output wave by the objective lens.

Based on the value of CTF, the contrast can change. When CTF value is negative, the atoms are shown in black contrast with a white background, on the contrary, the atoms are represented in white contrast with a black background. Almost all kinds of materials can be characterised by using TEM. Today, many techniques based on imaging, spectroscopy and diffraction are used depending on the specific analysis required for each sample. In this work, the characterisation of graphene as grown on copper film and its effect on the movement of dislocations after nanoindentation have been performed by TEM. More details will be discussed in chapter 5.

Preparation of sample is a very significant factor in characterisation by TEM which makes it challenging while dealing with transferred graphene. As the residue of the supporting polymer is hard to remove completely as well as the quality of the graphene sheet can decrease when transferred on a grid or other substrates. It is not always straightforward to probe CVD-2D layers with TEM.

3.3 Simulation methods

3.3.1 Abaqus (FE simulation code)

Abaqus FEA (Finite element analysis) is a software suite for finite element analysis and computer-aided engineering, originally released in 1978. The Abaqus software consists of five core products: Abaqus/CAE, Abaqus/Standard, Abaqus/Explicit, Abaqus/CFD, Abaqus/Electromagnetic.

The package that has been used in this work is Abaqus/CAE (complete Abaqus environment), a software application used for both the modelling and analysis of mechanical components and assemblies (pre-processing) and visualizing the finite element analysis result. Every complete finite-element analysis consists of 3 separate stages: a) pre-processing or modelling (this stage involves creating an input file containing an engineer's design for a finite-element analyser/solver); b) processing or finite element analysis (this stage produces an output visual file); c) post-processing or generating a report, image, and animation from the output file (this stage is a visual rendering stage). 2D axisymmetric simulation of suspended graphene has been used in this work to verify the accuracy of the analytical equation that has been applied to analyse the extracted force-displacement curve from the deflection test by AFM. More details will be provided in chapter 4.

3.3.2 Comsol (FE simulation code)

Comsol multiphysics is a cross-platform finite element analysis, solver and multiphysics simulation software. It allows conventional physics-based user interfaces and coupled systems of partial differential equations (PDEs). It provides a unified workflow for electrical, mechanical, fluid, acoustics, and chemical applications. Besides the classical problems that can be addressed with application modules, the core multiphysics package can be used to solve PDEs in weak form. Several modules are available for Comsol, categorised according to the applications areas of electrical, mechanical, fluid, acoustic, chemical, multipurpose, and interfacing. After verifying the accuracy of the membrane-clamped equation with Abaqus, the analytical and simulation results have been compared with the one from Comsol. All the results were in good agreement with a small discrepancy that will be discussed more in chapter 4. In addition, the effect of the membrane shape and loading position has been evaluated by 3D simulation of suspended graphene in Comsol and the results were

in good agreement with the experimental results. The corresponded equations were extracted by using the data resulting from the simulations of the mispositioning of the tip and deviation in the membrane shape. These equations can help to calculate the correct value of the Young's modulus of 2D layers while facing the mentioned discrepancies. More details will be provided in chapter 4.

3.3.3 Discrete dislocation dynamics (DDD) simulations

Dislocation dynamics (DD) is a modelling approach that aims to simulate the motion and interaction of the dislocation lines to gain insights concerning the mechanical properties of the material. The DD approach is based on the fact that plastic deformation is dominated by the motion and interaction of dislocation lines, rather than the locations of all of the atoms. Consequently, to understand the plastic behaviour of a material in this approach, considering the dislocation lines is sufficient. DD requires the input of multiple physical models to describe the various behaviours of the dislocation lines. It means that some information needs to be provided either from experiments or more fundamental models. Unlike other mesoscale models of plasticity which consider the dislocation density in terms of a homogenised field, dislocation lines are treated explicitly in the DD approach. As a result individual dislocation-dislocation interactions can be properly captured. In order to simulate the motion and interaction of dislocation lines, a number of algorithms, rules, and procedures have been developed. The most basic ingredients necessary to conduct a DD simulation are:

- The application of driving forces on dislocations,
- The determination of dislocation velocities given by these forces,
- The discretisation and adaptive remeshing of the dislocation lines,
- The time integration of the equations of motion,
- The collision and reaction of dislocations,

Furthermore, the more advanced aspects of DD simulations are:

- Handling the dislocation junctions and intersections,
- The different types of boundary conditions,
- The change in glide planes of screw dislocations through cross-slip.

The concept of 3D discrete dislocation simulations was introduced by the code micromégas which is a simple model for dislocation lines of FCC single crystal. The mentioned dislocation lines are sub-divided into sets of edge and screw dislocation segments embedded in a continuum medium. Each dislocation segment generates a long-range elastic stress field within the entire simulated sample. When using linear elasticity properties, the effective stress applied on each dislocation is evaluated at the middle point of each segment. This induces a force given by the Peach-Koehler equation:

$$F = (\sigma_{int} + \sigma_{app})b * \xi \tag{3.4}$$

where σ_{int} and σ_{app} are internal and applied stress, respectively. b is the Burgers vector of the dislocation segment and ξ is the unit vector of the line direction. Once the force is known on each dislocation segment, the segments are displaced according to mobility functions which depend on the material properties. Typical outputs of DD simulations are the dislocation microstructures, however, more statistical data such as the dislocation densities, the cumulated shear strain, the stored energy, and the local stresses can be extracted from this approach. In this work, the effect of graphene on the propagation of dislocation inside Cu thin film after indentation was investigated by DDD simulations and the results were in good agreement with the experimental results. These simulations will be discussed more in chapter 4.

Chapter 4

Extraction of accurate elastic properties of graphene via membrane deflection

Abstract

In this chapter, the mechanical properties such as 2D stiffness, Young's modulus, and fracture strength of graphene (single and bilayer) have been investigated. To assure the accuracy of the extracted results, the error and uncertainties resulting from the instrumental calibration, experimental procedures like tip wear and loading position as well as sample preparation such as membrane shape have been investigated. The estimation of the error that can come from calibration parameters predicted 15% and it was compared to the experimental error that occurred on the extracted Young's modulus. All the mentioned uncertainties have been investigated precisely and their effects have been considered in the extracted mechanical response of single and bilayer graphene. FE simulations have been performed to determine the effect of membrane shape and loading position as well as to compare with experimental results. Finally, the Young's modulus and fracture strength of SLGr have been evaluated to be around 880 GPa and 45 N/m, respectively. In the case of BLGr, the average value of Young's modulus is approximately 700 GPa and its fracture strength is around 64 N/m. However, the angle between the layers has to be determined to evaluate the correct value of fracture strength for BLGr as it is strongly dependent on the orientation between the layers. In this work, the orientation between the layers has not been measured precisely, and these values are an average for the fracture strength and Young's modulus of BLGr without considering the orientation of the layers.

4.1 Introduction

The innovation of scanning tunnelling microscopy (STM) (Binning et al., 1982) was rapidly followed by the development of atomic force microscopy (AFM) which is a special type of microscope allowing to generate images at the nanoscale and measure surface properties on any type of materials (Binnig et al., 1986; Yue Zhang et al., 2012). In AFM, the interactions of the probe, a sharp tip mounted on a cantilever beam, in permanent contact, intermittent contact or close proximity with the surface are measured and used to reconstruct the sample surface topography or to characterise surface properties (Celano 2019; Pethica and Oliver 1987). Compared with optical microscopy and electron microscopies, atomic force microscopy has the advantage of 3D topography measurements in air with a spatial resolution down to the atomic or molecular scale (Xue et al., 2014).

Besides imaging, AFM is widely used to measure the mechanical and electromechanical properties of nanomaterials because of the convenient force and deflection measurements with an AFM probe (Cuenot et al., 2004; Z. Li et al., 2018). Among nanomaterials, 2D materials are well known for their unique physical properties (ultralow weight, high Young's modulus, and good strength) and outstanding electrical properties compared with their conventional bulk counterparts (Cai et al., 2018b; A. K. Singh et al., 2015). As these low-dimensional materials are promising candidates for new applications in flexible and stretchable electronics and photonics, investigating their mechanical properties is of vital importance (Z. Li et al., 2018; K. Liu et al., 2014b). Young's modulus, fracture strength, and friction coefficient of 2D materials can be directly measured with AFM methods (Cuenot et al., 2004; Z. Li et al., 2018). In the past few years, a range of studies has been done by AFM to extract the mechanical properties (Young's modulus and fracture strength) (C. Lee et al., 2008b; López-Polín et al., 2015; Ovid'ko, 2013), as well as the tribological properties (Filleter et al., 2009; C. Lee et al., 2009) of graphene (Gr), a pioneering discovery of 2D materials. The mechanical and tribological properties of other 2D materials such as hexagonal boron nitride (h-BN) (Cartamil-Bueno et al., 2017; Song et al., 2010b) and molybdenum disulfide, MoS_2, (K. Liu et al., 2014b) have been studied in a very limited number of researches. Although there are lots of studies based on molecular dynamic (MD) simulation, density functional theories (DFT), etc, that show the unique mechanical properties of pristine graphene such as Young's modulus of 1 TPa and the tensile strength of 130 GPa (Jing et al., 2012; F. Liu et al., 2007; H. Zhao et al., 2009; Zhou, Xue, et

al., 2013), however, experimental studies are not always in good agreement with the theoretical values (J. U. Lee et al., 2012; Yupeng Zhang & Pan, 2012b). Table 4.1 represents a comparison between experimental and simulation results. The most discussed reasons for this difference in the literature are rooted in the structural disorders of graphene, involving corrugations (ripples, wrinkles, crumples) (S. Deng & Berry, 2016; K. Xu et al., 2009), topological defects (disclinations, dislocations, grain boundaries) (Yazyev & Louie, 2010; J. Zhang et al., 2012) and, point defects (vacancies, adatoms) (Dewapriya & Rajapakse, 2014; López-Polín et al., 2015; Zandiatashbar et al., 2014b). In addition, the effect of edge orientation of graphene has been discussed widely (armchair or zigzag) (Dewapriya & Rajapakse, 2014; Reddy et al., 2009). Besides the structural parameters of 2D materials, the parameters related to testing, characterisation, and analysis methods can significantly affect the extracted mechanical properties of 2D materials (G. Cao, 2014a; G. Cao & Gao, 2019; Q. Y. Lin et al., 2013b; Zhou, Wang, et al., 2013).

Table. 4.1. Mechanical properties of monolayer graphene (comparison between experiments and simulations)(taken from Cao et al., 2018).

Methods	**Young's Modulus (TPa)**	**2D stiffness (N/m)**	**Poisson ratio**	**Strength (GPa)**
Experiment				
AFM testing	1.0	340	-	130
AFM testing	*0.910*	305	-	-
Simulation				
Density functional theory	1.029	345	0.149	110
Molcular dynamics	0.96	320	-	-
Finite element method	1.03	-	0.08	98

AFM membrane deflection is a commonly used tool to characterise the mechanical properties of 2D nanomaterials (Frank et al., 2007; C. Lee et al., 2008b; Song et al., 2010b). There are several factors affecting images and extracted mechanical values while using AFM, such as the amplitude setpoint (Thormann et al., 2010), the loading rate (Medalsy & Müller, 2013), the uncertainty on the tip geometry (Braga et al., 2004) which have been investigated in literature for different materials except for 2D materials. In membrane deflection, the effect of some other parameters such as the ratio of tip/membrane radius (G. Cao & Gao, 2019), uncertainty on the load, uncertainty on the membrane shape, and uncertainty on the displacement are important while extracting the mechanical behaviour of the material.

However, to the best of our knowledge, there is no systematic study on the effects of all the above-mentioned parameters on the imaging and mechanical

results extracted from deflection tests by AFM, especially in the case of 2D materials. In this work, we will discuss the impact of some of these parameters on imaging and the results of deflection tests on graphene membranes. By taking these effects into account, the mechanical properties of graphene (single and bilayer) can be extracted in a more accurate way and critically discussed concerning the membrane-clamped theory (G. Cao & Gao, 2019).

4.2 Materials and test procedures

4.2.1 Materials and sample preparation

In order to fabricate the suspended graphene membrane for the deflection tests, a mask has been designed by k-layout software including arrays of circular cavities with different diameters ranging from 1 µm to 8 µm. As the contrast of graphene on SiO_2 substrate with 300 nm thickness is very favourable, Si wafers have been thermally oxidized (SiO_2 thickness = 300 nm). Afterwards, Si\SiO_2 substrates have been patterned by positive photolithography using the mentioned mask. The exposed circular SiO_2 areas were etched using BHF solvent and deeper cavities were formed with XeF_2 gas etchant which etched the Si substrate, partially. The depth of the cavities was around 1 µm. The deeper the cavities, the better the contrast with SEM imaging and the easier the recognition between suspended and broken graphene. As there is not a big distance between the cavities on the designed mask, the cavities cannot be deeper than 1 µm as it merge the cavities to eachother.

Single-layer graphene (SLGr), as well as multilayer graphene (MLGr), have been grown on Cu foil by chemical vapour deposition (CVD). The CVD process is described elsewhere in detail (Huet & Raskin, 2018b, 2018c) and briefly in the chapter on materials and methods. The common method for graphene transfer is a wet transfer based on a poly(methyl methacrylate) (PMMA) layer spin-coated on the Gr-copper substrate, followed by etching of the copper and the transfer of the PMMA/Gr stack onto a target substrate (Yulaev et al., 2016).

The modified PMMA transfer has been used to increase the tendency of the suspension of graphene on the cavities. The schematic of the modified Gr transfer method is shown in Fig. 4.1. In this method, instead of fishing the graphene from water as in the traditional wet transfer method (Y. Chen et al.,

2016; Suk et al., 2011), the stack of graphene and PMMA was caught with a piece of cleanroom paper on the PMMA side. The stack of the paper/PMMA/Gr was placed on a heating plate for 1 to 2 min in order to let the water evaporate. Then the stack was laid from the graphene side on top of the cavities and after detaching the paper, PMMA was removed using acetone at 60°C for at least 30 mins. It should be noted that the thickness of the PMMA layer in this method needs to be larger than 200 nm to have good adhesion between the paper and the PMMA layer and to avoid delamination of the stack of graphene and PMMA on the paper.

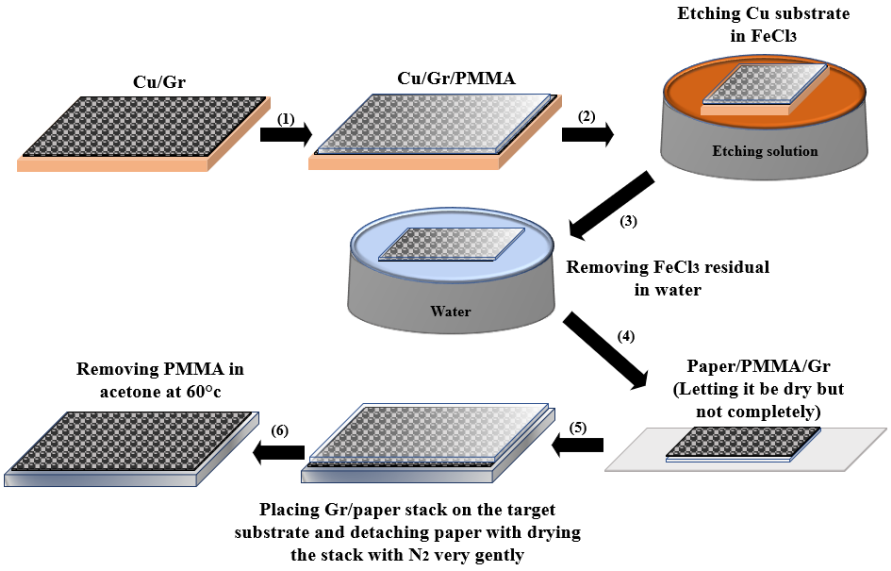

Fig. 4.1. *Scheme of the modified procedure for graphene transfer.*

4.2.2 Testing procedures

4.2.2.1 Structural and microstructural analysis

Raman spectroscopy (LabRAM HR by Horiba, excitation energy: 2.41 eV/514 nm, spot size: 1 μm) has been used to characterise the transferred graphene on the Si/SiO_2 substrate in the supported and suspended form.

To locate the graphene sheet on the target substrate, scanning electron microscopy (SEM) (Zeiss Gemini Ultra-55) was used. The graphene films

were mainly observed using the in-lens detector, which receives a signal enriched in type 1 secondary electrons (SE1) and provides high-resolution surface-sensitive information.

In order to check the quality of the suspension and the lack of contamination on the graphene membrane before the deflection test, AFM mapping (Dimension Icon by Bruker, standard tapping mode in air, linear scanning rate: 0.5 Hz) has been performed to collect images of the surface. Non-contact silicon probes (Nanosensors, PPP NCHR) with a nominal spring constant of 40 N/m, resonance frequency around 300 kHz, typical tip apex radius of 10 nm have been used.

4.2.2.2 Deflection test (AFM)

The mechanical properties (2D elastic stiffness (E^{2D}), Young's modulus, fracture strength) of the graphene membranes were measured by acquiring force-displacement curves at the centre of each membrane with an AFM (Dimension Icon by Bruker, ramp rate: 0.5 Hz), after mapping the target membrane. The curves were obtained by performing force spectroscopy measurements consisting in measuring the cantilever deflection, d, as a function of the imposed vertical displacement of the probe, z. The cantilever deflection in nanometers was obtained by converting the voltage measured on the photodetector, V_{PSPD}, into a vertical deflection using the sensitivity, S_{PSPD} in nm/V, previously calibrated on sapphire:

$$d = S_{PSPD} V_{PSPD} \,. \tag{4.1}$$

The load, F, was obtained using the Hooke's law with the calibrated spring constant, k_c of the cantilever (thermal noise method):

$$F = k_c d \,. \tag{4.2}$$

The membrane deflection, δ, is the difference between the imposed vertical displacement, z, and the cantilever deflection, d:

$$\delta = z - d \,. \tag{4.3}$$

The analytical relationship between the applied load and deflection of a clamped circular thin plate subjected to a point force at the centre of the plate (in this work called membrane-clamped equation) is given by (Cao and Gao 2019; Wan et al., 2003; Komaragiri, Begley, and Simmonds 2005):

$$F = \left[\frac{4\pi E^{2D} t^3}{3(1-\vartheta^2)a} + T\right]\frac{\delta}{a} + E^{2D} q^3 t a \left(\frac{\delta}{a}\right)^3, \tag{4.4}$$

$$\text{with} \quad T = \sigma_0^{2D}\pi a \quad \text{and,} \tag{4.5}$$

$$q = 1/(1.049 - 0.15\vartheta - 0.16\vartheta^2)\,. \tag{4.6}$$

where a is the plate radius, ϑ is the Poisson ratio of the material, t is the membrane thickness, T is the pretension that can be caused by the VdW interactions between the suspended 2D layer and the sidewall of the substrate. E^{2D} is the membrane 2D stiffness equal to $E^{2D} = E*t$, with Young's modulus (E) of the material.

The three terms in equation (4.4) corresponds to the bending, pre-tension, and stretching regimes, respectively. In the case of $\delta \gg t$, the first term $\frac{4\pi E^{2D} t^3}{3(1-\vartheta^2)}\left(\frac{\delta}{a}\right)$ in equation (4.4) is negligible. As a result, in the case of 2D materials where δ is always much larger than t, the load-displacement relationship extracted from the deflection test by AFM is fitted with the following equation:

$$F = \sigma_0^{2D}\pi\delta + \left(\frac{E^{2D} q^3}{a^2}\right)\delta^3. \tag{4.7}$$

When the load and the deflection are small, the elastic response is linear; under relatively large applied load, the relationship is cubic (Falin et al., 2017). In this work, a modified version of equation (4.7) has been used which includes a zero-deflection point, δ_0, as it needs to be considered before fitting. This modified equation was also considering the effect of tip-sample Van der Waals interactions, F_0 (Q. Y. Lin et al., 2013b; Suk et al., 2016). In this numerical approach, $\delta = \delta_{mes} - \delta_0$ and $F = F_{mes} - F_0$ with δ_{mes} and F_{mes} the as-measured membrane deflection and applied load, respectively. σ_0^{2D} is prestress in the membrane.

$$F_{mes} - F_0 = k_1(\delta_{mes} - \delta_0) + k_2(\delta_{mes} - \delta_0)^3, \tag{4.8}$$

$$F_{mes} = (F_0 - k_1\delta_0 - k_2\delta_0^3) + (k_1 + 3k_2\delta_0^2)\delta_{mes} - (3k_2\delta_0)\delta_{mes}^2 + k_2\delta_{mes}^3, \quad (4.9)$$

with $k_1 = \sigma_0^{2D}\pi$ and $k_2 = \frac{E^{2D}q^3}{a^2}$.

Considering F_0, k_1, k_2, and δ_0 as free parameters and fitting the load-deflection curve using equation (4.9), the precise values of F_0 and δ_0 can be obtained which leads to a more accurate determination of k_1 and k_2 and hence of the pretension and the 2D stiffness. For a clamped, linear elastic, circular membrane subject to deflection, an analytical relationship between the applied load and the maximum membrane stress σ_f in the contact region directly underneath the indenter can be approximately obtained (Bhatia and Nachbar, 1964) by:

$$\sigma_f^{2D} = \left(\frac{F_{max}E^{2D}}{4\pi R}\right)^{\frac{1}{2}}. \quad (4.10)$$

where F_{max} is the maximum load measured on the force-deflection curve before the membrane fracture and R is the apex radius of the AFM tip. The value of σ_f^{2D} corresponding to F_{max} is typically considered as the fracture strength of the membrane.

In order to measure the precise radius of the tip, TGX11 calibration grids have been used. This grid presents a re-entrant overhang with a sharp edge and there is a hole with an inclined wall with less than 90° angle below the overhang. The AFM image of the grid is shown in Figure 4.2.

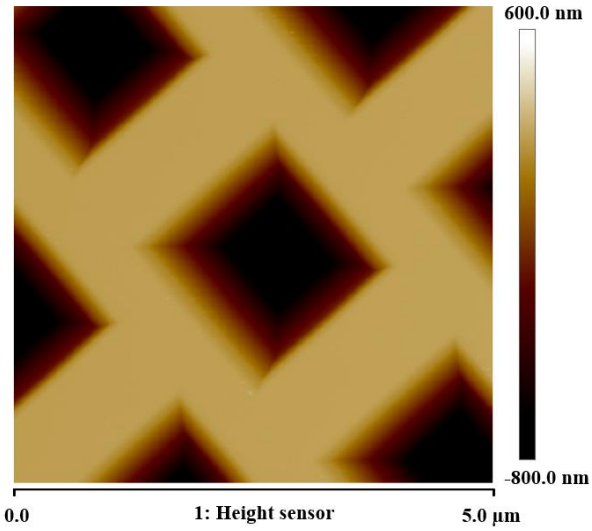

Fig. 4.2. *AFM imaging of TGX11 calibration grid.*

The tip radius of curvature, R, and its half-opening angle, α, can be estimated by analysing the AFM profile in the region where the tip is imaged by the overhang edge. The schematic of the cross-section of the TGX11 calibration grid and the expected profile of the tip is shown in Figure 4.3a. Fig. 4.3b shows the approach to determine the radius of curvature and half-opening angle from the AFM profile.

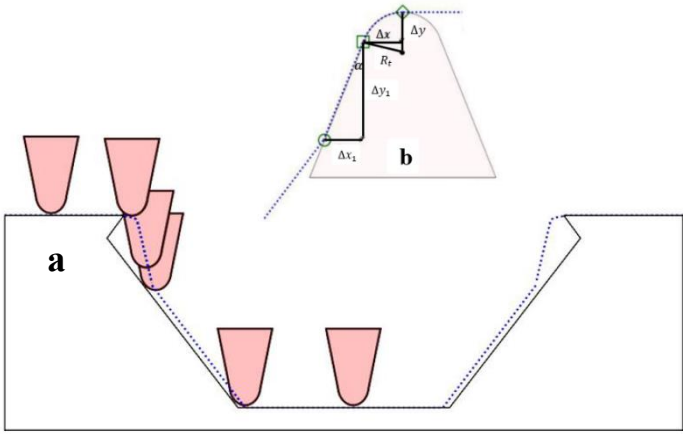

Fig. 4.3. *Schematic of (a) cross-section of the TGX11 calibration grid (black) and expected AFM profile (dashed blue) with a sphero-conical tip; (b) determination of the tip radius of curvature and half-opening angle from the AFM profile.*

As a result, R and α can be defined as:

$$R^2 = \Delta x^2 + R^2 - 2R + \Delta y^2 \,, \tag{4.11}$$

$$R = \frac{\Delta x^2 + \Delta y^2}{2\Delta y} \,, \tag{4.12}$$

$$\alpha = arctan\frac{\Delta x_1}{\Delta y_1} \,. \tag{4.13}$$

4.2.2.3 Simulation with Finite element (FE)-based software Comsol and Abaqus

The finite element-based software COMSOL Multiphysics has been used to investigate the effect of different parameters such as the uncertainty on loading position and the uncertainty on the shape of the membrane. In addition, a 2-dimensional simulation using shell elements have been performed with Abaqus with integration points of 4 and using elastic constitutive law to check the accuracy of the analytical solution and compare it with the result of the 3-dimensional simulation of COMSOL.

The COMSOL simulations have been performed in a 3D environment with shell elements (number of iterations = 4) by using linear elastic law for single-layer graphene with a thickness of 0.335 nm behaving as a clamped circular thin plate. The load has been considered as a point load because $a \gg R$. Here a is the radius of the circular thin plate and R is the apex radius of the AFM tip.

4.3. Results

4.3.1 Experimental results

4.3.1.1 Structural characterisation

Figure 4.4 shows the comparison of the Raman spectra obtained for the suspended Gr and the supported one on SiO_2. High *2D-to-G* peak intensity ratio and narrow *2D* band-width (equal to 2 and 25 cm^{-1}, respectively) prove the single atomic layer nature of the graphene sheets. In addition, the *D-to-G*

peak intensity ratio is smaller than 0.1, which indicates a low density of structural defects in transferred graphene. In the case of suspended graphene, the intensity ratio between the *2D* and the *G* peaks is larger than supported graphene. When graphene remains intact while it is suspended on the cavity, the intensity of the *D* peak is the same as the transferred graphene on a non-patterned substrate (supported graphene). Consequently, the intensity ratio between *D-to-G* peak remains smaller than 0.1.

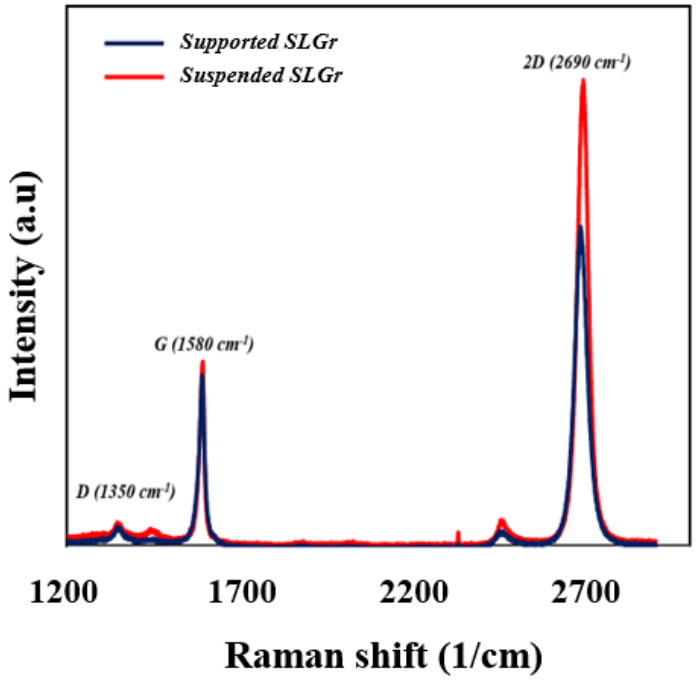

Fig. 4.4. *Raman spectra of supported SLGr (dark blue) and suspended SLGr (red).*

The domains of bilayer graphene have been investigated by Raman spectroscopy and as the orientation between layers can change for the different parts of the same domain, the related Raman spectra for each part can vary. The 10 different spectra of bilayer graphene are presented in Fig. 4.5.

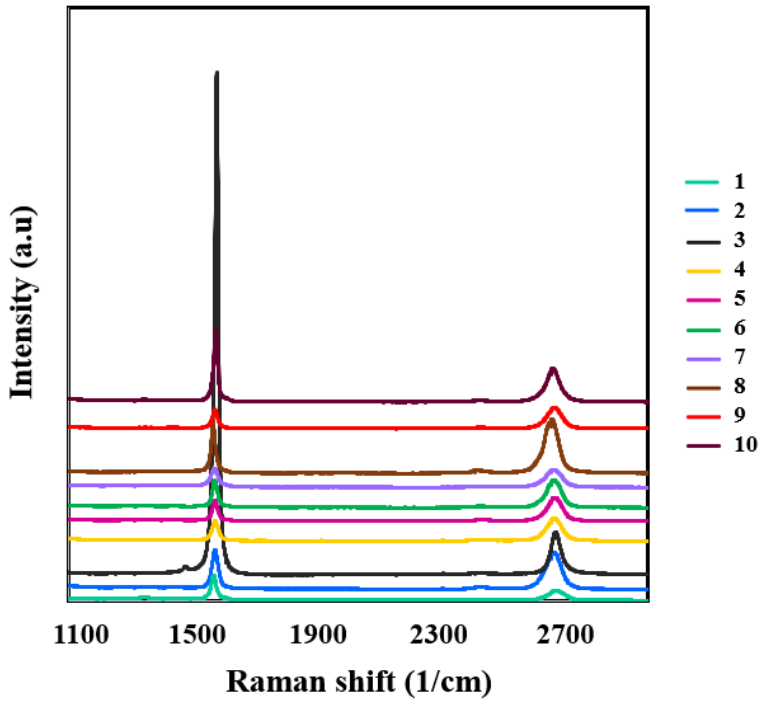

Fig. 4.5. *Raman spectra obtained on BLGr membranes transferred on the Si/SiO2 substrates. Different spectrum corresponds to different parts on a domain of BLGr.*

4.3.1.2 SEM characterisation of graphene membranes

The contrast difference between intact suspended graphene and broken one on the cavities can be recognised easily on the in-lens mode SEM images (Fig. 4.6). The darker holes as shown in the image correspond to suspended intact graphene. Where graphene is broken there is a brighter contrast.

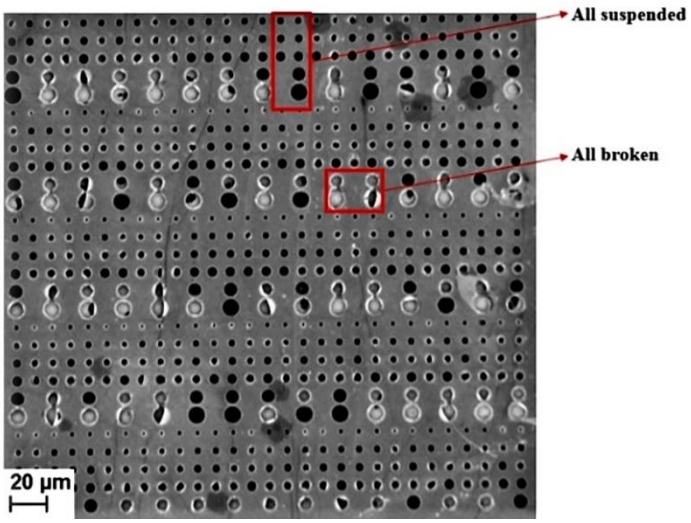

Fig. 4.6. *SEM image (in-lens mode) of broken (brighter) and intact (darker) suspended Gr sheets.*

The transferred multilayer graphene (MLGr) on perforated Si/SiO_2 and non-patterned Si/SiO_2 substrate are illustrated in Figs. 4.7a and b, respectively.

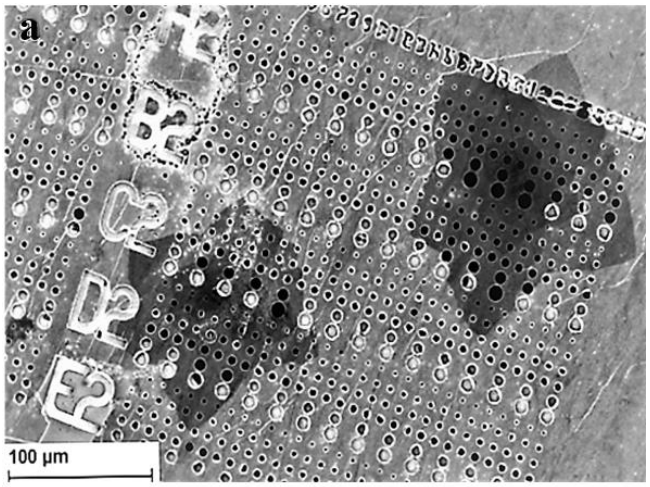

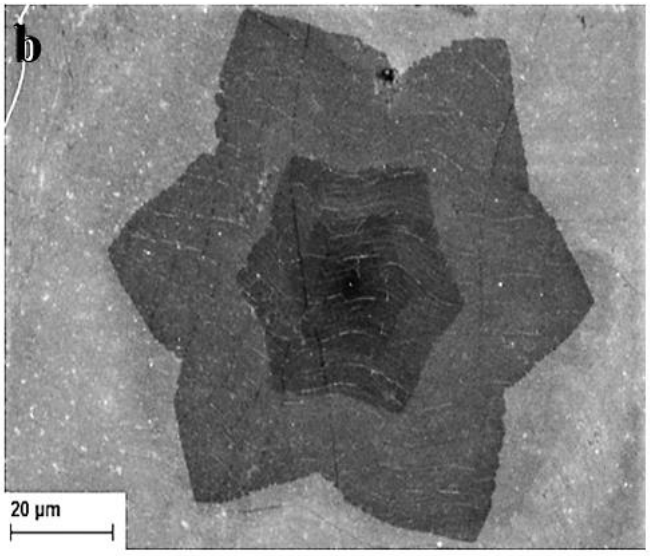

Fig. 4.7. *SEM image (in-lens mode); (a) MLGr on perforated Si/SiO2 substrate; (b) MLGr on supported on Si/SiO2 substrate.*

In order to show the improvement of the transfer with the modified version, the comparison of samples obtained with both methods, conventional and modified, is shown in Figs. 4.8a and 4.8b, respectively. The modified PMMA-transfer method reduces the possibility of water accumulation inside the cavities. As a result, less water evaporation occurs underneath the graphene sheet during drying, and the rupture of graphene on the cavities is less frequent. As it can be seen, the quality of the suspension with the modified method is much higher even in the case of cavities with a larger radius such as 3 µm and 4 µm.

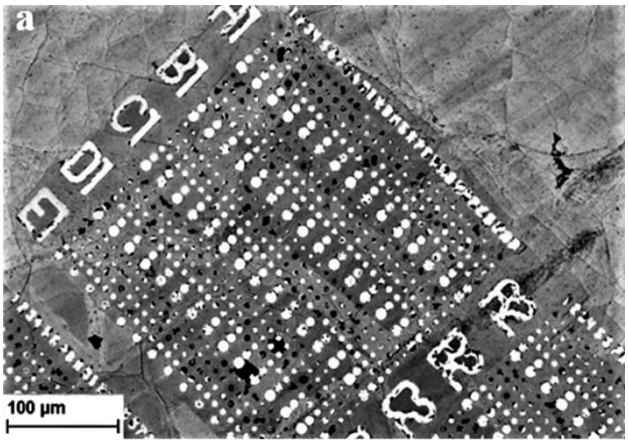

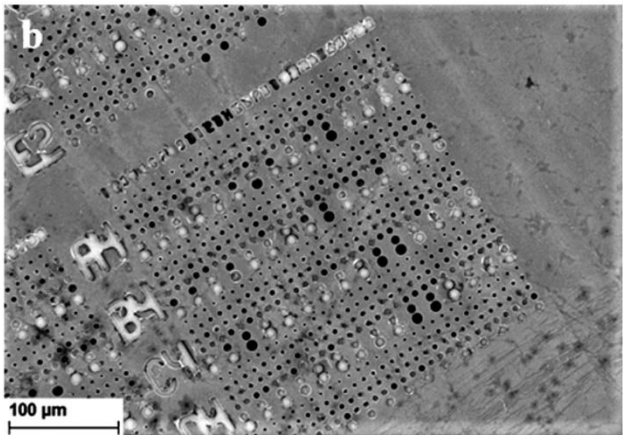

Fig. 4.8. *SEM image (in-lens mode) of samples obtained with; (a) the conventional PMMA-wet-transfer method; (b) the modified PMMA-wet-transfer method.*

4.3.1.3 Effect of amplitude setpoint on AFM membrane images

The effect of three different setpoint amplitudes, A_{sp} on the imaging of the membranes has been investigated while keeping the free amplitude, A_0 constant. As the value of setpoint amplitude gets closer to the value of free amplitude, the amount of A_{sp}/A_0 becomes larger and the tapping is softer. The type of tapping can be determined based on the ratio, R_{sp}, between amplitude setpoint, A_{sp}, and free amplitude, A_0:

$$R_{sp} = \frac{A_{sp}}{A_0} . \qquad (4.14)$$

Figure 4.9 represents images taken by using three different R_{sp} and the effect on the imaging in different modes (topography and phase) as well as on the cross-section profiles. By checking the cross-section profiles and images, it is clear that choosing an accurate ratio between setpoint and free amplitude is very important. In addition to imaging, it is significantly effective in the post-analytical process. In this work, the imaging and cross-sectional profile are in the best condition, when R_{sp} is around 0.9 which can be categorised in the soft tapping mode.

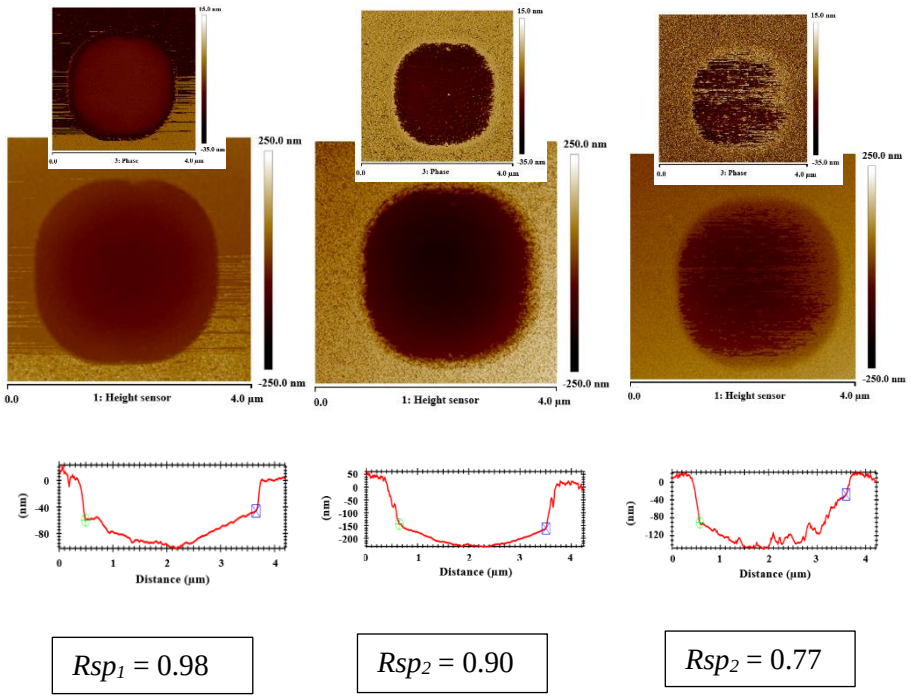

Fig. 4.9. *AFM phase (top) and topography (middle) images and corresponding topography cross-section profiles (bottom) of suspended SLGr obtained with three different setpoint ratios Rsp.*

4.3.1.4 Uncertainty due to the AFM calibration procedures and reproducibility of AFM measurements

The uncertainties on the applied load and on the membrane deflection influence the accuracy of the extracted 2D stiffness. They depend on different parameters including the calibration of the scanner in the z-direction, S_z, the calibration of the position-sensitive photodetector (PSPD) sensitivity, S_{PSPD}, and the calibration of the cantilever spring constant, k_c. Uncertainty on the value of the 2D stiffness extracted from the experimental procedure while keeping the calibration parameters including S_{PSPD} and k_c constant is around 1.7%. In order to calculate this uncertainty, the same tip with the same calibration was used to apply load successively on the same membrane. The process was performed in a way that after first imaging on the membrane, just by using the point and shoot function, the same load was applied to deflect the membrane and the force-deflection curve was extracted after each deflection. The resulting values for the same membrane in successive loading can be seen in Table 4.1.

Table. 4.1. *Values of 2D stiffness and Young's modulus ($E= E^{2D}/t$, t is graphene thickness equal to 0.355 nm for SLGr) obtained by fitting with Eq. 4.9. Load-deflection curves measured successively with the same probe and the same calibration on the same SLGr membrane with the radius of 2 µm.*

Test number	E^{2D} *(N/m)*	*Young's modulus (GPa)*	*Maximum load (nN)*
1	283.6	846.6	1000
2	288.5	861.2	1000
3	296.2	884.2	1000
4	295.7	882.7	1000
5	299.5	894.0	1000
6	296.1	883.9	1000
7	299.5	894.0	1000
8	300.2	896.1	1000
9	298.5	891.0	1000
10	295.1	880.9	1000

To make sure that these results are trustable, the same process has been repeated with different tips and on different membranes and the standard deviation remains always less than 2%. By calibrating the device for each measurement in order to consider the uncertainty on calibration in addition to other uncertainties while performing the deflection test such as changing the load position due to tip sliding, etc, the uncertainty reached 1.8% and the results are shown in Table 4.2.

Table. 4.2. *Values of 2D stiffness and Young's modulus obtained by fitting with Eq. 4.9. Load-deflection curves measured with 5 different probes and thus 5 different calibrations on the 5 different SLGr membrane on the same sample with the radius of 2 µm.*

Test number	E^{2D} *(N/m)*	*Young's modulus (GPa)*	*Maximum load (nN)*
1	305.3	911.3	1000
2	296.1	951.9	1000
3	297.0	853.7	1000
4	291.1	868.9	1000
5	290.7	867.7	1000

The average values, standard deviation values and relative errors were calculated using the following expressions:

$$\bar{x} = \frac{1}{N}\sum_{i=1}^{N} x_i \ , \qquad (4.15)$$

$$\Delta x = \sqrt{\frac{1}{N}\sum_{i=1}^{N}(x_i - \bar{x})^2}\,, \tag{4.16}$$

$$\varepsilon_x = \frac{\Delta x}{|\bar{x}|} \times 100\,. \tag{4.17}$$

where x_i is the measured quantities and N is the number of measurements. On the other hand, the calculated uncertainty on the 2D stiffness is approximately 5% while keeping the tip and calibration constant and performing the deflection test on different membranes on the same sample. In this case, the effect of tip ageing and uncertainty on the membrane radius is added to other uncertainties coming from the deflection test and the value for the uncertainty is representing a real experimental condition. The results of 5 different measurements are listed in Table 4.3.

Table. 4.3. *Values of 2D stiffness and Young's modulus obtained by fitting with Eq. 4.9. Load-deflection curves measured with the same probe and calibration on the 5 different SLGr membranes with a radius of 2 µm.*

Test number	*E^{2D} (N/m)*	*Young's modulus (GPa)*	*Maximum load (nN)*	*Radius (µm)*
1	330.9	987.7	1000	2.3
2	318.9	951.9	1000	2.3
3	297.0	866.6	1000	2.3
4	329.6	983.9	1000	2.3
5	291.1	868.9	1000	2.3

4.3.1.5 Uncertainty on tip geometry (wear)

Tip wear may constantly occur during scanning. It may not only affect the imaging but also influences the results extracted from the deflection test on the membrane. Therefore, it is important to check this effect. To our knowledge, it is the first time that the influence of tip wear on the mechanical response of the graphene membrane is investigated. Figures 4.10a and 4.10b show SEM images of the same tip before and after several scanning and deflection tests. Higher magnification of the fresh tip is highlighted inside Figure 4.10a.

AFM imaging with a fresh tip and the same tip after several scanning (an old one) shows the effect of the tip wear on topography and phase images of suspended graphene (Figs. 4.11a-d). Consequently, the effect of the tip ageing can be seen on the cross-section profiles (Figs. 4.11e-f). To see the effect of the tip wear on the elastic response of graphene, a deflection test has been performed on suspended graphene with a fresh tip and the same tip as it aged.

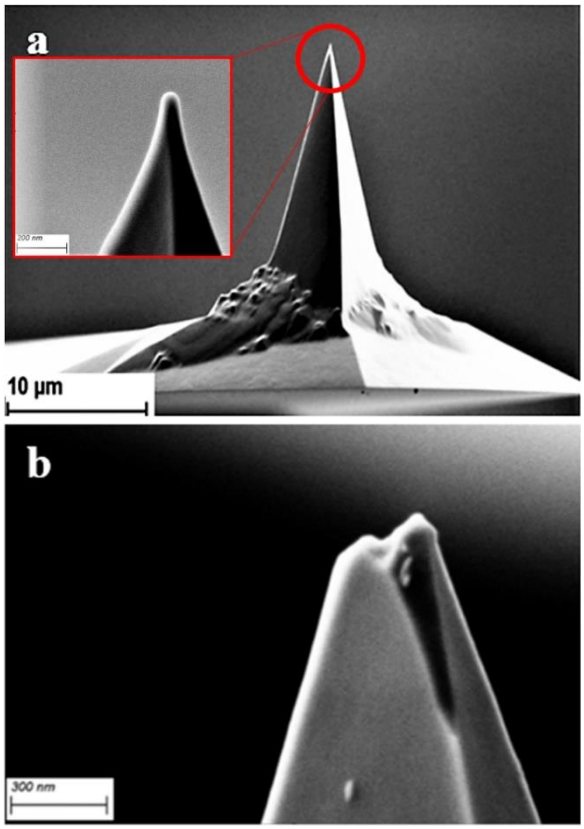

Fig. 4.10. *SEM image of (a) a fresh tip, (higher magnification of tip is highlighted) and (b) the same tip after scanning several AFM images.*

Fig. 4.12 presents the difference between load-displacement curves for the two mentioned tips. Table 4.4 listed the extracted 2D stiffness and Young's modulus from the graphs which have been shown in Fig 4.12. As it is possible that small damage occurs on the surface of graphene during the deflection test and to make sure there is no other effective parameters on the extracted Young's modulus of graphene, a new graphene membrane from the same sample has been tested each time.

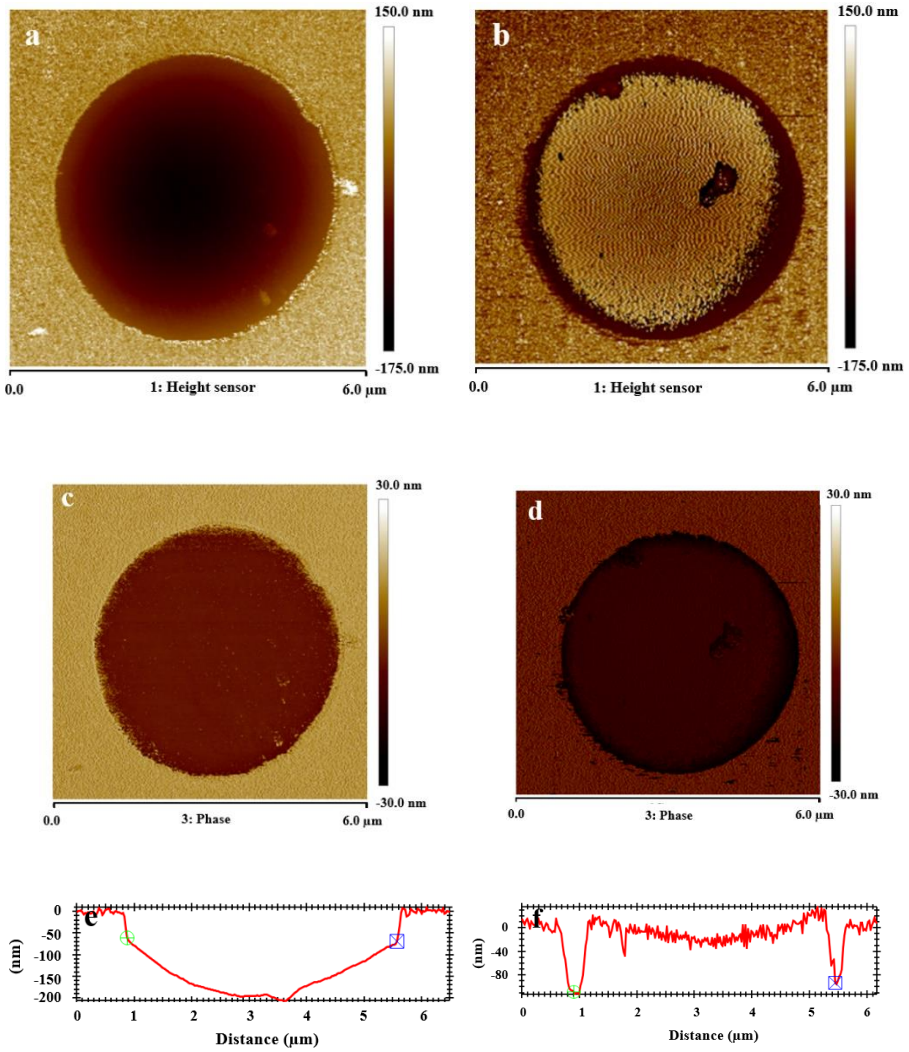

Fig. 4.11. *(a & b) AFM topography; (c & d) phase images; and (e & f) topography cross-section of suspended SLGr membrane imaged with a new tip (a, c & e); and with an old tip (b, d & f).*

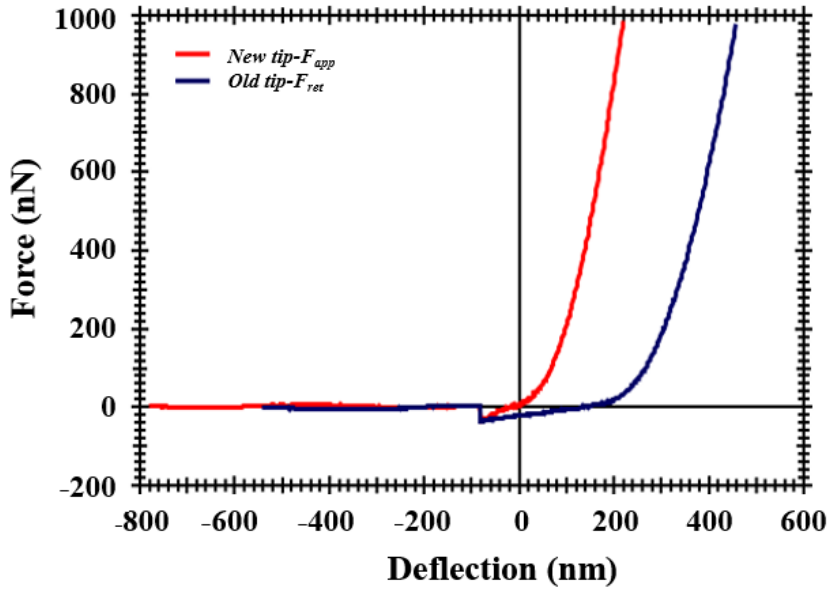

Fig. 4.12. *Load-deflection curves measured on the membrane presented in Fig. 4.11 with the new probe (red curve) and with the old probe (blue curve).*

To show the process of tip ageing and its effect on the extracted elastic results of suspended graphene, scanning and deflection tests have been performed on different membranes (from number 1 to number 10) on the same sample while keeping the tip constant. The extracted values of E^{2D} and Young's modulus for each suspended graphene membrane are presented in Table 4.5. The changes of 2D stiffness with tip wear is shown in Fig. 4.13. The values of the tested membranes from number 1 to number 7 are in good agreement with the expected value of Young's modulus of the graphene. The average value of E^{2D} and Young's modulus for SLGr in this work are 294.3 N/m and 875.6 GPa, respectively. In the case of membranes numbered 8 and 9, the values of these parameters are significantly smaller.

Table. 4.4. *Values of 2D stiffness and Young's modulus obtained by fitting the load-deflection curves presented in Fig. 4.11 with equation 4.9.*

Tip age	E^{2D} *(N/m)*	*Young's modulus (GPa)*	*Maximum load (nN)*	*Radius (μm)*
New tip	318.0	949.2	1000	2.3
Old tip	174.6	521.1	1000	2.3

Table. 4.5. *Values of 2D stiffness and Young's modulus obtained by fitting with Eq. 4.9. Load-deflection curves measured successively with the same probe on different SLGr membrane.*

Test number	*E^{2D} (N/m)*	*Young's modulus (GPa)*	*Maximum load (nN)*
1	330.9	987.7	1000
2	318.9	951.9	1000
3	297.0	886.6	1000
4	329.6	983.9	1000
5	291.1	868.6	1000
6	244.2	728.9	1000
7	241.7	721.5	1000
8	173.2	517.0	1000
9	133.8	399.4	1000

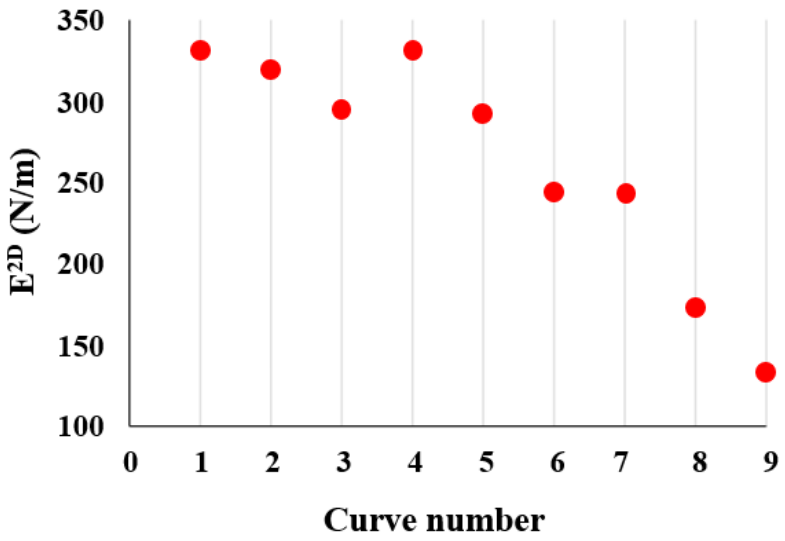

Fig. 4.13. *Evolution of the 2D stiffness obtained by fitting with Eq. 4.9. Load-deflection successively measured with the same probe on different SLGr membrane, (applied load = 1000 nN and membrane radius ~ 2µm).*

As these tests have been done successively with the same tip and on different membranes, one after another, the damage on the tip is more significant while testing on membrane numbered 8 and 9 which leads to an obvious reduction of 2D stiffness value. This trend is the clear effect of tip ageing on the elastic response of the graphene membrane. In addition, the same test has been done with different tips and on different samples to make sure that the data are reliable statistically.

The process continues till the load-deflection curve extracted from the deflection test by the same tip cannot be analysed. For instance, the load-displacement curve cannot be used to extract any results in the case of the membrane numbered 10, showing the tip is not functional anymore (Fig. 4.14).

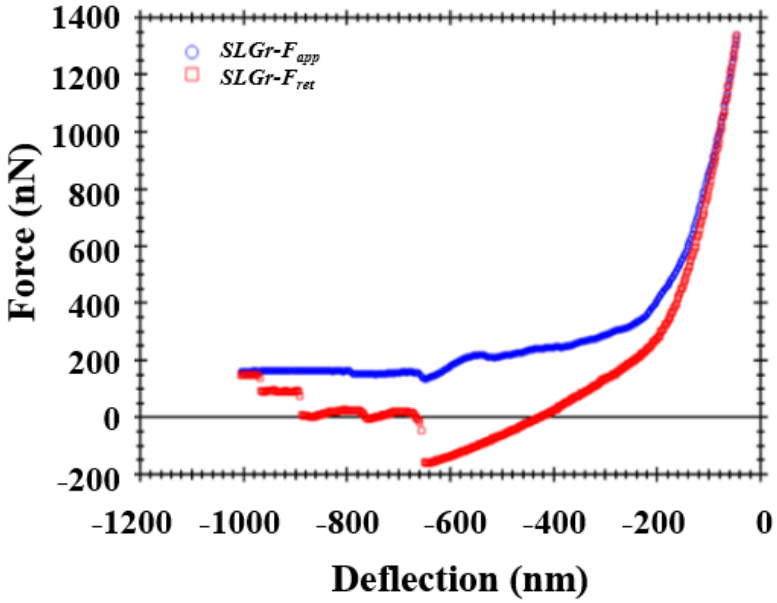

Fig. 4.14. *Example of the load-deflection curve measured with the worn tip, (Red curve is retraction and blue one is approach).*

4.3.1.6 Uncertainty of the loading position on the membrane

The position of the applied force (the distance from the centre toward edges) on the membrane can also have a significant effect on the extracted results. The point at which load is applied should be as precise as possible in the centre of the membrane. The comparison between load-deflection curves measured at different distances (five different positions) from the centre of SLGr membrane (0 to 1 µm) is presented in Fig. 4.15. Figure 4.16 shows the effect of the loading position on the extracted Young's modulus for about 100 different deflection tests presented as a function of the loading distance from the membrane centre.

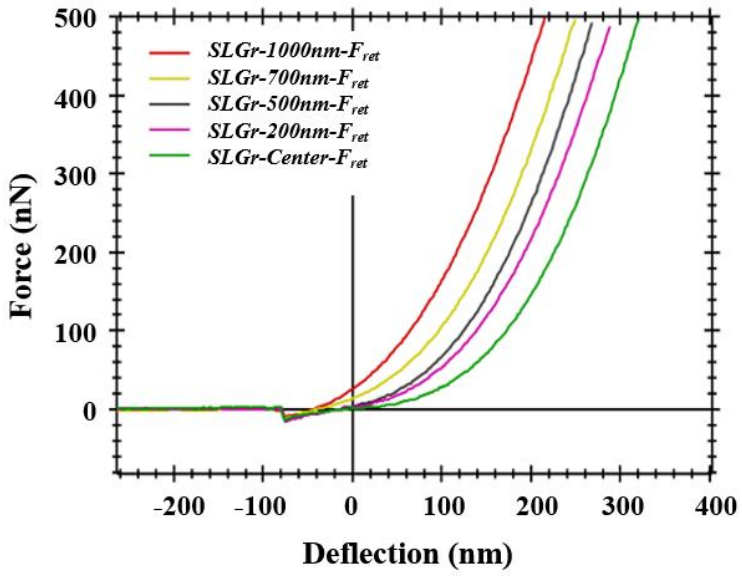

Fig. 4.15. *Comparison of force-deflection curves (F_{ret} = retraction curve) successively measured on a SLGr membrane (radius = 2 µm) at increasing distances from the centre; Center: 0.0 µm (green); 0.2 µm (pink); 0.5 µm (black); 0.7 µm (yellow); 1.0 µm (red).*

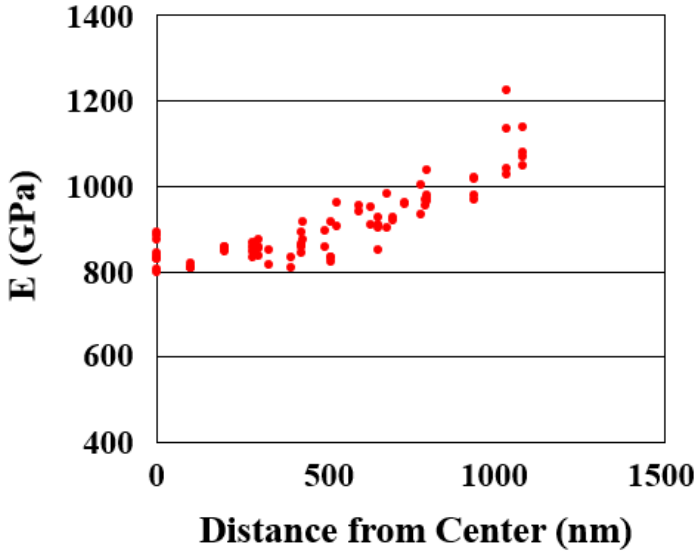

Fig. 4.16. *Evolution of Young's modulus extracted using Eq. 4.9 from load-deflection curves measured on SLGr membrane (radius = 2 µm) successively, with the distance from membrane centre.*

4.3.1.7 Uncertainty on the membrane shape

To extract precise Young's modulus based on Eq. 4.4, the shape of the cavities on which graphene has been suspended needs to be circular. Based on the design method and the lithography parameters, this shape can deviate from the circular shape. The deviation from circular shape to square can be seen in Figs. 4.17a and 4.17b in topography and phase mode. In our case, the design has been done with k-layout software. In this software, the sketching performed using the polygons and the number of the points used in the sketching is effective in determining the shape of the designed cavities. In this design, the cavities with a radius of 1 µm have not been designed with enough points which lead to the deviation from the circular shape.

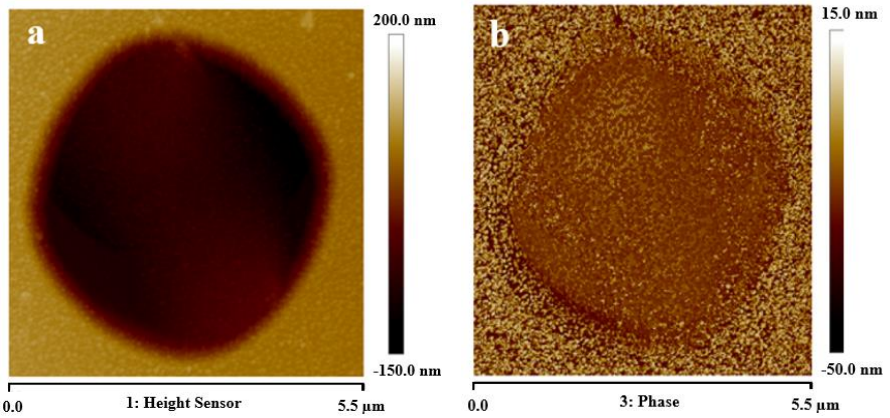

Fig. 4.17. *AFM imaging; (a) topography and; (b) phase mode of SLGr membrane suspended on a cavity (radius = 1 µm) revealing the non-circularity of the cavities.*

The measurements have been performed on 5 different membranes with the same deviation to prove the reproducibility of the results. Table 4.6 shows the values of E^{2D} and Young's modulus of these 5 different graphene membranes which have been suspended on cavities with a radius of 1 µm and have the same deviation from the circular shape. The average value of E^{2D} and Young's modulus are provided also in this table. Then a comparison between the average value of the mentioned membranes and the value of suspended graphene on cavities with a perfectly circular shape shows the effect of the shape on the apparent Young's modulus extracted by Eq. 4.9. The average value of E^{2D} for SLGr suspended on a cavity with a semi-circular shape equals 244.3 N/m while this value for the perfect circular cavity is 294.6 N/m.

Table. 4.6. *Values of 2D stiffness and Young's modulus obtained by fitting with Eq. 4.9. Load-deflection curves measured with the same probe and calibration on the 5 different SLGr membranes suspended on semi-circular cavities (radius = 1 μm).*

Test number	E^{2D} *(N/m)*	*Young's modulus (GPa)*	*Maximum load (nN)*
1	247.2	737.9	1000
2	258.9	772.8	1000
3	222.1	662.9	1000
4	238.2	711.0	1000
5	255.1	761.5	1000
Average	244.3	729.2	1000

4.3.1.8 Extracting mechanical response of single-layer and bilayer graphene by deflection test

The 2D stiffness, E^{2D}, Young's modulus, E, and fracture strength, σ_f^{2D} of SLGr suspended on cavities with different diameters (1 μm, 3 μm, and 4 μm) have been determined, considering the effects of the above-mentioned parameters. Typical load-deflection curves obtained on cavities with different diameters are presented in Figure 4.18.

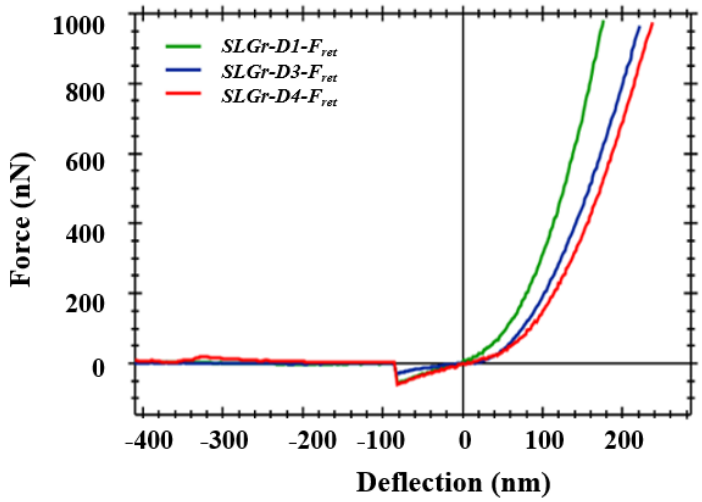

Fig. 4.18. *Typical load-deflection curves measured on SLGr membranes suspended over cavities of different radii with a maximum load of 1000 nN; a = 0.5 μm (green curve), a = 1.5 μm (blue curve), a = 2.0 μm (red curve).*

The average values of 2D stiffness, Young's modulus and fracture strength present in Table 4.7 are representatives of the elastic properties of SLGr produced by CVD in UCLouvain. Considering all the measurements performed with a maximum load of 1000 nN, an average value of 880 GPa was obtained for SLGr.

Table. 4.7. *Average values of the 2D stiffness and Young's modulus obtained by fitting with Eq. 4.9. Several load-deflection curves measured on SLGr membrane suspended on cavities with various values of radius. E^{2D} and Young's modulus extracted at applied load 1000 nN.*

Membrane Radius (μm)	*Number of tests*	*Average of E^{2D} (N/m)*	*Average of Young's modulus (GPa)*	*Average of fracture strength (N/m)*
0.5	10	291.34	869.67	47.32
1.5	10	300.18	896.06	43.81
2	10	292.44	872.95	43.81
Average	-	294.65	879.65	45.00

In most cases, the fracture of single-layer graphene occurs in the range of load between 3000 nN and 4000 nN, a force-deflection curve for broken graphene is presented in Fig. 4.19.

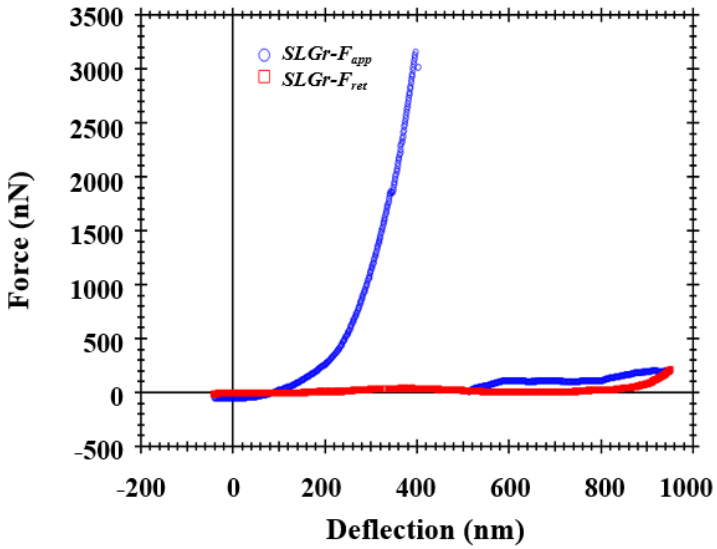

Fig. 4.19. *Example of the load-deflection curve with a load leading to graphene fracture, (Red curve is retraction and blue one is approach).*

Figs. 4.20a and 4.20b show an example of force-displacement curve and topography phase of AFM imaging on suspended BLGr, respectively.

The mechanical response of bilayer graphene (BLGr) has also been investigated by deflection test. Based on the Raman spectra (shown in Fig.

4.5), the orientation between the layers changed in some cases. In some spectra, the behaviour is more similar to single-layer graphene but in some cases, the proportion between *2D* and *G* peak intensities changed significantly which results from the change in the angle between two layers of graphene.

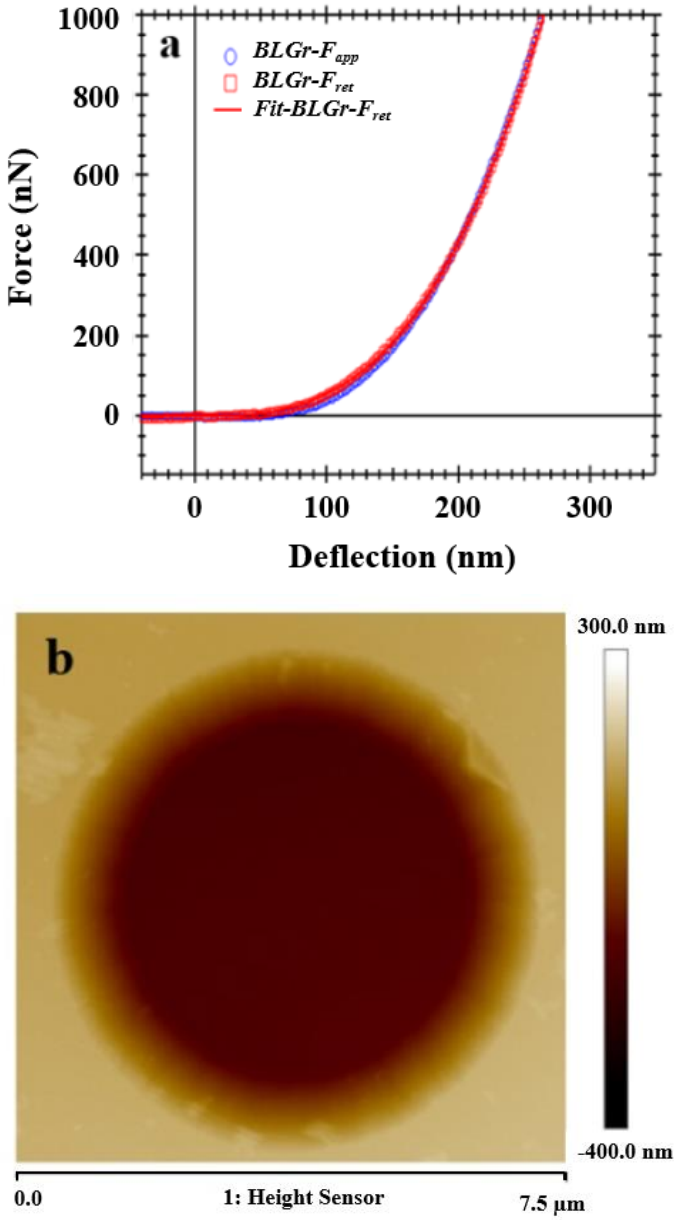

Fig. 4.20. *Typical AFM results obtained on BLGr membranes, (F_{app} and F_{ret}, are the approach and retraction curves, respectively); (a) load-deflection curve; (b) topographic image.*

The discrepancies between the values of 2D stiffness, Young's modulus and fracture strength in the case of BLGr is higher in comparison to SLGr in this work. The root cause of these discrepancies will be discussed more in the discussion section of this chapter. Table 4.8 shows the values of Young's modulus and 2D stiffness of BLGr with different orientations. The values of fracture strength for bilayer graphene as well as the maximum load can be seen in Table 4.9. The standard deviation on the extracted fracture strength for BLGr is around 6.5%.

Table. 4.8. *Values of 2D stiffness and Young's modulus obtained by fitting with Eq. 4.9. Ten load-deflection curves measured on BLGr membranes suspended over cavities (radius = 2 µm).*

Test number	E^{2D} *(N/m)*	*Young's modulus (GPa)*	*Maximum load (nN)*
1	473.0	705.9	1000
2	424.6	633.7	1000
3	533.3	795.9	1000
4	468.8	699.7	1000
5	466.8	696.7	1000
6	454.0	677.6	1000
7	456.9	681.9	1000
8	381.6	569.5	1000
9	574.8	857.9	1000
10	476.9	711.7	1000
Average	471.0	703.0	1000

Table. 4.9. *Values of fracture strength obtained by fitting with Eq. 4.10. Ten load-deflection curves measured on BLGr membranes suspended over cavities (radius = 2 µm). The average values of fracture strength and maximum load are 63.7 N/m and 6400 nN, respectively.*

Test number	*Fracture strength (N/m)*	*Maximum Load (nN)*
1	71.54	8000
2	61.95	6000
3	69.27	7500
4	61.95	6000
5	53.65	4500

4.3.2 Finite element (FE) simulation results

To show the good agreement between analytical (the extracted force for different deflection values based on using the theoretical values of graphene properties in Equation 4.4) and simulation results, the load-deflection curves have been shown for analytical data, and both FE simulations (COMSOL and ABAQUS). The values for Young's modulus, have been extracted and the

comparison between the graphs are shown in Fig. 4.21a and b. There is a small discrepancy in a part of the data which can be seen in the graph of Young's modulus versus displacement (Marked with a green circle).

While simulating the deflection tests, four different regimes are usually distinguished including (1) linear (F-δ relation is linear) where the small displacement plate theory is accurate (2) a transition regime where the small-displacement assumption for the plate theory is not valid anymore and the simulation is not completely in non-linear regime (3) a 'non-linear' regime (F-δ^3) where the membrane theory is valid, in this regime very small rotation can occur and (4) a regime with a large rotation where the small rotation assumption for the membrane theory becomes invalid (Komaragiri et al., 2005). The first three regimes can be seen in the log-log graph of load vs normalized deflection curve in Figure 4.21c. In the simulation that has been performed for this work, we are travelling through the first 3 regimes but as the rotation is large in regime (4), it makes the simulation in this regime less straightforward and in the case of this work, considering this regime is unnecessary. The small deviation that can be seen in the graphs related to Young's modulus for different simulations in comparison to analytical can result from the absence of the parameters related to the transition regime in Eq. 4.4. The error percentage that has occurred in the case of simulation compared to the analytical calculations in this regime can be seen in Fig. 4.21d.

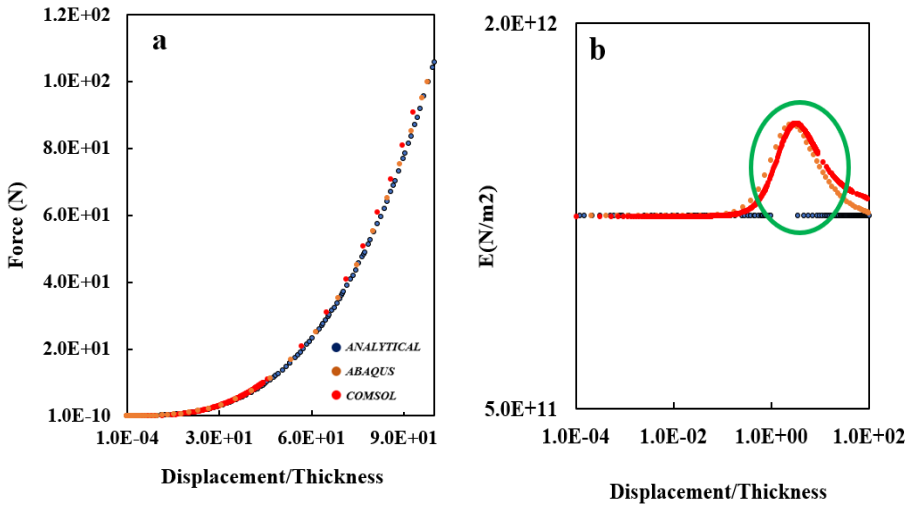

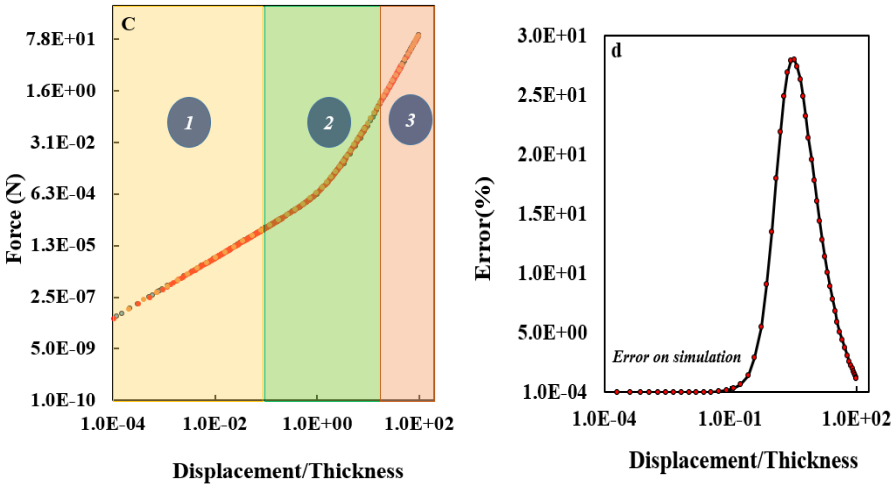

Fig. 4.21. *The comparison between the COMSOL and ABAQUS simulation and analytical calculations; (a) force vs normalized deflection; (b) Young's modulus vs normalized deflection (green circle highlights the deviation in transition regime); (c) three different regimes introduced in section 4.3.2 showing force vs normalized deflection (log-log) curve; (d) relative error on Young's modulus extracted by simulation compared to analytical calculations.*

4.3.2.1 Simulation of the error due to tip positioning

The error due to the off-centre positioning of the tip has been investigated by COMSOL simulation. More than 100 simulations have been performed for different loading positions and the simulated curves have been fitted with Eq. 4.4 to extract a value of Young's modulus, *E*. Figure 4.22 shows the change in the value of Young's modulus while the distance of the applied load from the centre of the membrane varies. E_N is normalized Young's modulus, the division of extracted Young's modulus based on the loading position by the value of Young's modulus when loading exactly in the centre of the membrane. In addition, the experimental results for a SLGr graphene membrane suspended on a cavity of radius a = 2 µm are shown in this figure which represents very good agreement with the simulation results. The simulated data were fitted with a 3rd degree polynomial expression:

$$E_N = P_0 + P_1 x + P_2 x^2 + P_3 x^3 \,, \qquad (4.18)$$

with x the distance between the membrane centre and the loading point. For the present simulation, values of $P_0 = 0.90$, $P_1 = 0.68$, $P_2 = -1.10$, and $P_3 = 0.74$ were obtained with a value of $R^2 = 0.994$

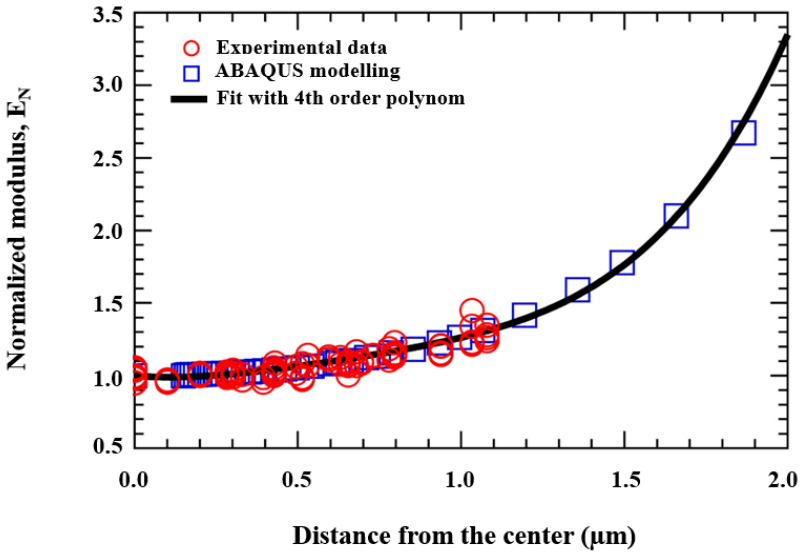

Fig. 4.22. *Variation of the value of the Young's modulus obtained by fitting simulated load-deflection curves with the distance of the loading point with respect to the membrane centre (radius = 2 μm), and the comparison with the experimental results.*

Furthermore, the error percentage regarding the loading position has been extracted to make the calculation of the error on the apparent Young's modulus based on the loading position easier. Figure 4.23 shows the error% vs load position and based on the fitting, equation 4.19 is extracted.

$$e\% = P_0 + P_1 x + P_2 x^2 + P_3 x^3 \,, \qquad (4.19)$$

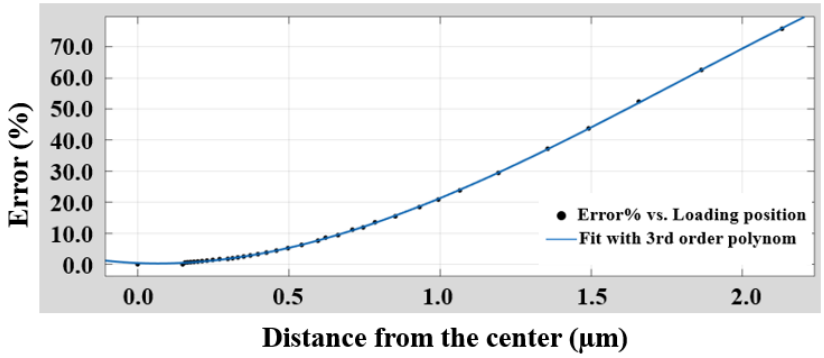

Fig. 4.23. *The percentage of error occurs on the value of the Young's modulus obtained by fitting simulated load-deflection curves with the distance of the loading point with respect to centre of the membrane (radius = 2 µm).*

Where *x* is the distance between the membrane centre and the loading point and the values of $P_0 = 0.40$, $P_1 = -5.65$, $P_2 = 30.58$, and $P_3 = -4.05$ were obtained with a value of $R^2 = 1$.

4.3.2.2 Simulation of the effect of the membrane shape

The shape of the membrane has also a significant effect on the extracted Young's modulus. This effect has been investigated by COMSOL simulation and the prediction of the correct value for a perfectly circular membrane is possible by using the analytical calculation obtained after fitting the extracted results for different shapes of a membrane (from the square shape, fillet = 0 to a circular shape, fillet = 1). The values for fillet obtained by dividing the normalized radius of the membrane (radius/thickness of graphene) by values between 0 to 20. The results are shown in Figure 4.24 which presents the variation of normalized Young's modulus extracted by fitting load-deflection curves simulated on membranes with varying shapes. The data were fitted with a polynomial expression of 4th degree:

$$E_N = G_0 + G_1 y + G_2 y^2 + G_3 y^3 + G_4 y^4 \qquad (4.20)$$

with *y* the filet value. The following values were obtained for different coefficients including: $G_0 = 0.99$, $G_1 = 1.04\times10^{-20}$, $G_2 = -1.60\times10^{-16}$, $G_3 = 2.62\times10^{-13}$, and $G_4 = 3.68\times10^{-9}$, with R^2 close to 1.

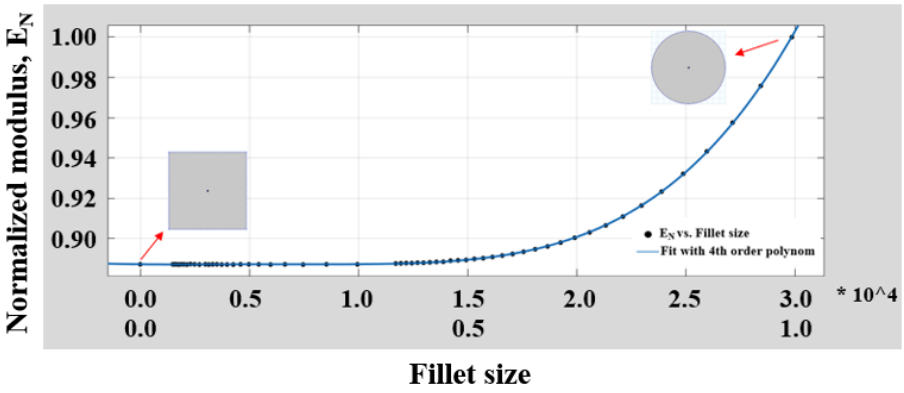

Fig. 4.24. *Simulation of the variation of the extracted Young's modulus as a function of the shape of the membrane (radius = 1 µm). Simulated values (black dots) and fit with 4th order polynom (blue line)*

In addition, the error percentage that occurs by changing the membrane shape from circular to square has been evaluated and Figure 4.25 shows the error% vs filet size. After fitting the extracted curve, equation 4.21 has been evaluated.

$$e\% = G_0 + G_1 y + G_2 y^2 + G_3 y^3 + G_4 y^4 \qquad (4.21)$$

Where y is the filet value and the values of $G_0 = 0.43$, $G_1 = -3.15\times10^{-7}$, $G_2 = -3.61\times10^{-11}$, $G_3 = 1.66\times10^{-14}$ and $G_4 = -1.05\times10^{-18}$ were obtained with a value of $R^2 = 1$.

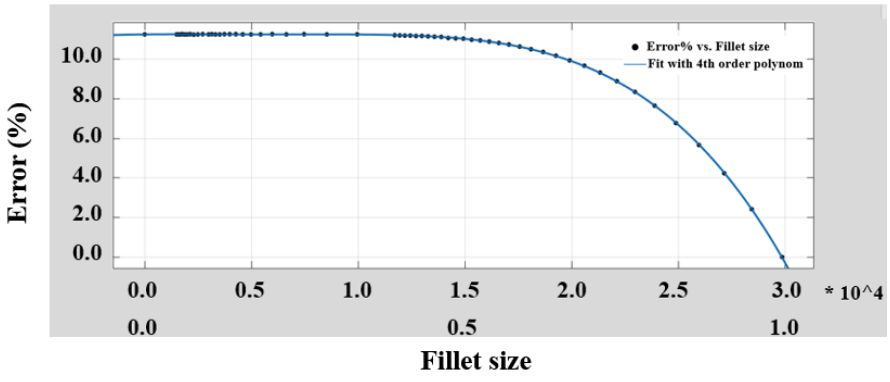

Fig. 4.25. *The percentage of error occurs on the value of the Young's modulus as a function of the shape of the membrane (radius = 1 µm). Simulated values (black dots) and fit with 4th order polynom (blue line).*

4.4. Discussion

Generally, the mechanical properties of nanostructures reported in the literature provide a standard deviation of experimental replicates without sufficiently considering the underlying uncertainties (G. Cao & Gao, 2019). It makes it difficult to compare the measurements between different groups, instruments and techniques. This can cast a shadow over the development of reliable nano-engineered materials and products following design rules established in the macro world and can be settled by considering the relevant uncertainties that arise from different sources (Wagner et al., 2011). The uncertainties which have been mentioned in section *3* can result from two different categories namely, the errors/uncertainties due to the various calibration procedures and the errors due to the experimental procedures that affect the reproducibility of the results even if the calibration is constant. In this work, the uncertainty on the load and the membrane deflection is categorised in instrumental errors as it is based on the calibration of different parameters in the AFM machine. On the other hand, the effect of tip ageing, the membrane shape and the loading position is categorised in the experimental procedure. FE simulations were performed in the case of the membrane shape and the loading position effect, to provide novel correction functions to improve the accuracy of the extracted Young's modulus based on Eq. 4.4.

4.4.1 The uncertainties on load and membrane deflection

The extraction of elastic properties from force-displacement curves by AFM is a well-known methodology (Butt et al., 2005). First, a series of calibration parameters have been used to convert the photodiode and Z-piezo voltages into forces and displacements. Next, the forces and distances need to be extracted from these forces and displacements. Finally, the fitting of force-deflection data to a material model containing a parameter related to the material property leads to the extraction of the properties of the test material. Because the calibration parameters play a central role in extracting the accurate values from these measurements (Wagner et al., 2011), it is necessary to investigate their effect.

The vertical sensitivity of the PSPD is calibrated by measuring approach-retraction curves on an infinitely stiff sample (sapphire).

The sensitivity is the inverse of the slope of the curve reporting the photodetector signal V_{PSPD} expressed in volt as a function of the scanner vertical displacement, *z*, expressed in nanometer:

$$\frac{1}{S_{PSPD}} = \frac{dv_{PSPD}}{dz} . \tag{4.22}$$

The uncertainty on the sensitivity depends on the uncertainty on the calibration of the scanner in *z* direction and the uncertainty on the measured voltage on the photodetector.

$$\varepsilon_{S_{PSPD}} = \sqrt{\varepsilon_z^2 + \varepsilon_{V_{PSPD}}^2} . \tag{4.23}$$

The uncertainties on the membrane deflection and on the load thus first depend on the accuracy of the scanner calibration in the *z*-direction. The relative error on the scanner vertical displacement, ε_z, is less than 2%. It is a systematic error that can be ignored in further calculations. Then equation 4.23 can be written as:

$$\varepsilon_{S_{PSPD}} = \varepsilon_{V_{PSPD}} . \tag{4.24}$$

In order to calculate the reproducibility of the photodetector signal ($\varepsilon_{V_{PSPD}}$), several calibrations have been done by keeping the tip constant and the deviation on the values of amplitude setpoint was calculated to be approximately 4%. Based on this value, the uncertainty on the photodetector sensitivity would be equal to 4%.

The other parameter which affects the uncertainty on the load and consequently on the modulus is the uncertainty on the calibrated cantilever spring constant. The cantilever spring constant is calibrated using the thermal noise method. To simplify the problem, consider that the spring constant, k_c, is given by

$$k_c \approx \frac{k_B T}{\langle d^2 \rangle} \tag{4.25}$$

with k_B the Boltzmann's constant, *T* the temperature and $\langle d^2 \rangle$ the quadratic average of the cantilever deflection due to the thermal noise. The uncertainty on the spring constant thus depends on the uncertainty of the temperature ($\varepsilon_T \approx \frac{1}{300} = 0.33\%$) and the uncertainty on the measured vertical deflection,

i.e. the uncertainty on the photodetector sensitivity, $\varepsilon_{S_{PSPD}}$. The relative error on the spring constant, ε_{k_c} , is thus given by

$$\varepsilon_{k_c} = \sqrt{\varepsilon_T^2 + 4\varepsilon_{S_{PSPD}}^2}\,. \tag{4.26}$$

By considering the relative uncertainty on the photodetector signal equal to 4%, the relative uncertainty on the spring constant is around 8%.

The normal load, *F*, applied by the cantilever is given by Hooke's law which is mentioned in equation 4.2. As a result, the relative error on the applied load, ε_F, is thus given by

$$\varepsilon_F = \sqrt{\varepsilon_{k_c}^2 + \varepsilon_{S_{PSPD}}^2}\,. \tag{4.27}$$

By using the values mentioned above, the relative error on the load is approximately 9%.

In order to calculate the relative uncertainty on 2D stiffness, the uncertainty on the sample deflection needs to be measured. Sample deflection, δ, is given by the difference between the scanner vertical displacement, *z*, and the cantilever vertical deflection, *d*, as mentioned in equation 4.3. Where, ε_z can be ignored then the relative error on sample deflection, ε_δ, is approximately equal to $\varepsilon_{S_{PSPD}}$. Based on equation 4.4, the relative uncertainty on the membrane 2D stiffness and hence on its modulus should be given by:

$$\varepsilon_E = \sqrt{\varepsilon_F^2 + 4\varepsilon_a^2 + 9\varepsilon_\delta^2}\,. \tag{4.28}$$

The relative error on the radius of the membrane is around 2%. By considering the error on *F*, *a* and δ, the relative error on 2D stiffness is 15.5%. By comparison of the error measured on the 2D stiffness extracted experimentally which is around 5% with the expected error predicted theoretically (15%), it can be seen the real error on the experimental results is much less than the expected maximum error resulting from the machine. These results show that the value of Young's modulus extracted experimentally is reliable and tip, calibration and all other parameters which can have an effect on the extracted results were in good condition.

4.4.2 The uncertainties on tip geometry

Tip ageing/wear occurs mostly while scanning across the sample. However, performing the deflection test with a load such as 1000 nN can accelerate the process. Tip geometry changes as a result of tip ageing and it needs to be considered as it is effective on imaging as well as on extracting the mechanical behaviour of the surface. Figures 4.10a and b present a new tip and the same tip after several scanning. The shape of the tip changed significantly and the changes cannot be predicted as they are generally not simple paraboloids or spheres. In addition, the tip's behaviour regarding tip/sample interactions and energy dissipation cannot be predicted easily. It is known that some sort of modifications occurs in the distribution of applied pressure in the contact region due to the change in the geometry of the tip. One effective parameter that can affect the shape of the tip is the force regime (low amplitude/attractive vs high amplitude/repulsive) (Vahdat et al., 2013). The wear of AFM probes depends significantly on the force regime as the tip/sample interaction forces and dissipated energy can change in different force regimes. Control and estimation of these changes are not straightforward (Garcí and San Paulo, 1999). However, it is possible to verify the tip wear effect by imaging and through the mechanical test data while keeping the other parameters such as the tip's material and properties (spring constant) and the test material constant. The effect of tip wear on imaging and topography profile can be observed in Figures 4.11a-f. After tip ageing, the artefact on images increases and the tip in this condition can damage the graphene.

From the mechanical point of view, Figure 4.12 and Table 4.1 present the effect of tip ageing on the force-deflection curve as well as extracted values of 2D stiffness and Young's modulus of the SLGr. It is shown that with a worn tip, the same force causes more deflection of the graphene membrane which leads to the underestimation of the stiffness and Young's modulus. To fit the extracted load-deflection curve properly with equation 4.9, the tip radius R needs to be much smaller than the membrane radius a (e.g., $a/R > 30$). The large a/R makes the indenter load-deflection relationship insensitive to the tip radius so that the indenter can be considered as a point load (Komaragiri et al., 2005). On the other hand, the smaller ratio of membrane radius to tip radius (e.g., $a/R < 30$), leads to a significant influence of the tip radius on the load-displacement relationship (Begley & Mackin, 2004). In the latter condition, the prediction of the accurate Young's modulus by fitting the force-deflection curve with equation 4.9 is not possible. It can be seen that in the presence of the blunted tip, the extracted load-deflection curve shows less stiff behaviour

than the one resulting from the sharp fresh tip. After fitting the curve with the mentioned equation, the underestimation of Young's modulus occurs. The gradual changes in the values of the stiffness and Young's modulus have been shown in Table 4.5 and Fig. 4.13 after applying force on ten different membranes with the same tip. The effect of gradual tip wear can be seen obviously on Young's modulus values and Fig. 4.13 shows a clear trend of it. At the final stage, retraction and approach curves extracted from the deflection test are not overlapped and any information cannot be achieved due to a non-functional tip. Fig. 4.14 shows the force-deflection curve on the tenth membrane which represents this condition.

4.4.3 The uncertainties on loading position

To extract the target mechanical properties of the material from force-deflection curves, a mathematical model needs to be introduced. Despite the determination of these mathematical models with the extension and completion of well-established models, they are facing some limitations (Marinello et al., 2010). The mathematical model that has been considered in this work to extract the E^{2D} is equation 4.4. As mentioned by Cao, this relationship is between the indentation load and deflection of a clamped circular thin plate subject to a point force at the centre of the plate (G. Cao & Gao, 2019). Based on this equation, the point force needs to be placed precisely in the centre of the circular plate but it is not always possible to perform it experimentally.

Thereby, it is possible to apply the load not exactly in the centre as the load position is determined manually by the operator. This leads to the misestimation of correct values of 2D stiffness and Young's modulus. Applying the force far from the centre of the plate and going toward the edges leads to the overestimation of apparent Young's modulus due to the stiffer response of the graphene membrane close to the clamped part.

To make it clearer, SLGr is placed on a substrate with open cavities and it adheres to the substrate by Van der Waals forces (Z. Lu & Dunn, 2010). The freestanding portion of the graphene over circular-cavity in the substrate is treated as a circumferentially clamped drum and the behaviour is the same as a drum (G. Cao & Gao, 2019; Pruessner et al., 2003). For the same load, it can be deflected more in the centre than near the edges. Therefore, to achieve the maximum deflection, the load needs to be applied exactly in the centre of the membrane. In this work, this effect has been investigated experimentally and

by simulation. The force-deflection curves regarding the effect of the loading position are shown in Figure 4.15. The trend of increasing the apparent Young's modulus by applying the load further from the centre of the membrane can be seen in Fig. 4.16. In addition, the simulation results show the same trend and the comparison between the simulation and experimental graphs shows a good agreement (Fig. 4.22). It can be seen that in both cases either experimental or simulation, the mechanical response gets stiffer by loading somewhere but not precisely in the centre. It is shown that by going toward the edges around 1000 nm, the response is stiffer around 100 N/m. To cope with this effect, equations 4.18 has been extracted from the data of simulation which can predict the value of the normalized Young's modulus. Equation 4.19 gives the possibility to calculate the error based on the loading position, and it makes it possible to correct the extracted Young's modulus values in the case of off-centre loading. The equations are functional even if the thickness or the radius of the membrane change.

4.4.4 The uncertainties on the membrane shape

As it is mentioned, the analytical relationship that is used to extract Young's modulus based on force-deflection data depends on the shape of the suspended thin film. In the case of freestanding 2D layers, the analytical solutions about the beam bending and membrane stretching can be used to predict the indentation response of 2D materials. The two later models are useful when extracting the elastic properties of 2D sheets placed on a substrate with trenches or circular holes called a doubly clamped beam or a circumferentially clamped drum, respectively (Wan et al., 2003; Nadler and Steigmann 2006; Jin et al. 2017).

In the case of freestanding graphene on circular holes, the analytical solution is the one that has been introduced as equation 4.4. It is important to note that this analytical solution is valid for clamped circular thin plates. However, in the experimental procedures can be some deviation from the circular shape resulting from the poor design or lithography. Almost all holes are perfectly circular in the designed mask of this work except the holes with a radius of 1 µm.

Fig. 4.17a and b show the real shape of the cavities with a radius of 1 µm in topography and phase modes, respectively. In designing the mask all polygons need to be sketched by connecting the points, however, the number of points was not sufficient in the case of the cavity with the radius of 1 µm.

This leads the array of holes of 1 μm to not be precisely a circle but a shape between a circle and a square which helps to see the effect of the shape of the cavity on the extracted E^{2D} values using the analytical solution. In addition to the experimental observation, simulations have been performed for different forms of cavities ranging from a complete square (fillet = 0) to a complete circle (fillet = 1).

In the experimental results, the average value of E^{2D} for a semi-circular cavity is equal to 244 N/m and the average value of a circular one is 294 N/m. The difference is about 50 N/m, the uncertainty that comes from this parameter is around 9% which is more than the expected error in the series of deflection tests performed in this work. Table 4.6 listed the values for five different membranes with the semi-circular shape and radius of 1 μm. These five different measurements have been performed to show the repeatability of the results and the average value was compared with the extracted value of SLGr on a completely circular cavity. The simulation results represent around 100 N/m difference from a complete circular shape to semi-circular and the value remains almost constant from the semi-circular to a complete square. This result can be seen in the graph which is represented in Fig. 4.24. To predict the value of Young's modulus in case of a deviation in the shape of the membrane, equation 4.20 has been extracted from the simulation data. By using this data, equation 4.21 can be extracted on the error percentage related to the apparent Young's modulus regarding the membrane shape. By knowing the size of the deviation, the error percentage can be calculated and the extracted Young's modulus can be corrected. These equations are useful in the case of different thickness or radius of the membrane.

4.4.5 Young's modulus and fracture strength of SLGr and BLGr

The unique mechanical properties of graphene are one of the reasons that make graphene a superior material both as an individual material and as a reinforcing element in composites (Ferralis, 2010; X. Zhao et al., 2010). The exceptional mechanical properties of graphene result from the stability of the sp^2 bonds that form the hexagonal lattice and oppose a variety of in-plane deformations (Papageorgiou et al., 2017). In this work, the 2D stiffness, Young's modulus and fracture strength of CVD graphene transferred on cavities of different sizes have been investigated. Figure 4.18 and Table 4.7 show the results obtained for cavities of different radii and the mean value is

the value that is considered the real Young's modulus for the CVD graphene in this work which is equal to 880 GPa. This value is around 12% less than the value reported in literature around 1 TPa (C. Lee et al., 2008b) but based on the discussed uncertainties and the possible defects and grain boundaries in the CVD graphene, 880 GPa is in a good range. Studies show that the presence of defects reduces the Young's modulus of graphene sheets and Young's modulus decreases with the increasing degree of defects (Jing et al., 2012). It is clear that the degree of defects increases inside of graphene after undergoing the transfer process and the Young's modulus decrease in comparison to pristine graphene. However, in most applications, the transferring of graphene is necessary so the value of this work is closer to the Young's modulus of graphene which is supposed to be used in real applications. The fracture strength of SLGr was measured and the mean value was approximately 45 N/m. The radius of the tip has been evaluated by using TGX11 calibration grids and based on Eq. 4.12 which gives the value of 40 nm. Fig. 4.19 shows the force-deflection curve of fractured SLGr at the load of 3000 nN.

Table 4.10. *The final extracted mechanical results of SLGr and BLGr by considering all the elements of uncertainties.*

Graphene	*Average of 2D stiffness (E^{2D}) (N/m)*	*Average Young's modulus (E) (GPa)*	*Average of fracture strength (N/m)*
SLGr	**296.0±3**	**880.0±7**	**45.0±1**
BLGr	**471.0±16**	**700.0±24**	**64.0±3**

In addition to single-layer graphene, the elastic behaviour of BLGr has been investigated. The extracted values of stiffness and Young's modulus are listed in Table 4.8. These results provide a smaller value of Young's modulus for bilayer graphene (~700 GPa) in comparison to SLGr which is in agreement with the literature (Neek-Amal & Peeters, 2010b). Figures 4.20a and b represent a load-deflection curve measured by AFM and the topography image on BLGr suspended on top of a cavity. BLGr is a layered material system where interlayer structure and coupling determine the key properties (Brown et al., 2012). It has been claimed that the elastic properties of twisted bilayer graphene (tBLGr) can be modified by changing the angle between layers and the defects or grain boundaries on each layer (A. Liu & Peng, 2018; J. Zhang & Zhao, 2013b). In addition, the layer with more defects has a dominant effect on the extracted results. In our work, the exact determination of the orientation type or the angle between the layers has not been straightforward. The first layer was a continuous layer which makes measuring the angle or analysing the orientation with AFM or SEM difficult.

Figures 4.7a and b show SEM images of multilayer graphene and it can be seen that the first layer is continuous. In Fig. 4.7a MLGr is placed on the substrate containing cavities and in Fig. 4.7b, it is transferred on a substrate with no holes. On the other hand, the presence of a small amount of polymer residue or other types of contaminations causes difficulties in TEM investigations. Based on our knowledge, a method that can clean graphene thoroughly after PMMA-transfer has not been discovered until this day. One of the reliable and available methods to characterise the relative orientation of the graphene sheets is Raman spectroscopy which can show qualitatively the effect of changing the angle between the layers on the spectrum. As can be seen in Fig. 4.5, the intensity ratio between *G* and *2D* peaks changed which is related to the changes in the angle between layers. However, an obvious trend in the modification of 2D stiffness, Young's modulus and fracture strength values with changing the intensity ratio between *2D* and *G* peaks has not been observed in this work. In fact, higher discrepancies was observed in the results regarding BLGr, which can be due to the different types of defects, grainboundaries, edges, interaction between layers, adhesion to the substrate as well as pretenstion existed in BLGr and can change significantely from one domain to another one. More precise investigations with having the good knowledge of the exact angle between the layers is necessary in order to systematically measure the elastic properties as well as fracture strength of BLGr.

On the other hand, it has been mentioned that for orientated bilayer graphene (oBLGr), the elastic properties have not been influenced by changing the angle between the layers (J. Zhang & Zhao, 2013b). However, all these assumptions are based on theoretical analysis and investigations with different approaches and there are contrary in some cases. Despite a decent amount of studies on BLGr which focused on the differences in the electronic properties and chemical properties (Y. Cao et al., 2018; Y. Ding et al., 2016; Yankowitz et al., 2018), the mechanical properties of tBLGr or oBLGr are not still clear. Based on our experimental procedure, the effect of the different angles between layers in BLGr on the elastic response is insignificant or it can be the fact that we are dealing with oBLGr which based on theoretical analysis is not sensitive to the angle between the layers (J. Zhang & Zhao, 2013a). Additionally, the presence of defects or grain boundaries can modify the elastic behaviour of BLGr. On the other hand, the fracture strength of BLGr is more sensitive to the angle between the layers. This can be due to the change in the fracture strength based on zigzag or armchair edges in graphene and the fact that changing the angle between layers shifts the edges from one type to

another (J. Zhang & Zhao, 2013a). This can cause significant differences between the load that can be resisted by BLGr placed in different parts of a graphene domain and the results can be seen in Table 4.9. A summary of the results related to the mechanical response of SLGr and BLGr is in Table 4.10.

4.5. Conclusion

Young's modulus and fracture strength of single and bilayer graphene have been detected by membrane deflection technique using atomic force microscopy. In addition, the effect of different uncertainties including the errors coming from calibration procedures and the experimental procedures on the reproducibility of the results has been investigated. The main findings of the work are the following: first, calibration uncertainties are effective on the extracted mechanical results. These uncertainties have been calculated theoretically at around 15% and have been compared to the extracted experimental values. The error on the experimental results is around 5% which shows the accurate calibration and good condition of tip and other parameters while deflection test. The uncertainties that arise from the experimental procedure are based on the tip worn, loading position and the shape of the membrane. The accurate Young's modulus can be calculated based on equation (4.9) when a sharp tip ($a/R > 30$) applies load at the centre of a circular membrane. As a result, a deviation from each of the mentioned parameters leads to a significant error on the elastic mechanical results which have been investigated experimentally. Tip wore and deviation in the membrane shape from circular to semi-circular lead to underestimation of the Young's modulus while the mispositioning of the applied load results in overestimation of this value. The effect of membrane shape and loading position has been evaluated by FE simulation and it is in good agreement with experimental results. By considering the effect of these uncertainties, Young's modulus and fracture strength of single-layer graphene produced at UCLouvain have been calculated to be around 880 GPa and 45 N/m, respectively. In the case of bilayer graphene, Young's modulus is measured at around 700 GPa which is in a good range when compared to other literature (Y. Y. Zhang et al., 2011). The fracture strength of bilayer graphene is dependent on the orientation between the layers and the calculated values in this work cannot be considered very reliable due to the lack of knowledge of the angle between the layers in BLGr.

Chapter 5

Single layer graphene controlled surface and bulk indentation plasticity in copper

Abstract

The impact of graphene reinforcement on the mechanical properties of metals has been a subject of intense investigation over the last decade in surface applications to mitigate the impact of tribological loadings or for strengthening purposes when dispersed into a bulk material. Here, the effect on the plastic indentation response of a single graphene layer grown on copper is analysed for two configurations: one with graphene at the surface, the other with graphene sandwiched under a 100 nm thick copper cap layer. Nanoindentation under both displacement and load control conditions show both earlier and shorter pop-in excursions compared to systems without graphene. Atomic force microscopy reveals much smoother pile-ups with no slip traces in the presence of a surface graphene layer. The configuration with the intercalated graphene layer appears as an ideal elementary system to address bulk hardening mechanisms by indentation testing. Transmission electron microscopy (TEM) cross-sections below indents show more diffuse and homogeneous dislocation activity in the presence of graphene. 3D dislocation dynamics simulations allow unraveling of the origin of these 3D complex phenomena and prove that the collective dislocation mechanisms are dominantly controlled by the strong back stress caused by the graphene barrier. These results provide a quantitative understanding of the impact of graphene on dislocation mechanisms for both surface and bulk applications, but with an impact that is not as large as anticipated from other studies or general literature claims.

5.1 Introduction

Graphene (Gr) possesses superior mechanical properties (Choi et al., 2010; Ovid'ko, 2013) which can improve the tribological performance of materials when used as surface coating and/or the bulk strength and stiffness when used as reinforcement in composites or as an interface in multilayers (Y. Kim et al., 2013; Z. Li et al., 2018; Park et al., 2017). These claimed beneficial impacts on mechanical behaviour in addition to the extra functionality resulting from the insertion of graphene in terms of electrical, thermal, or optical performances (Nieto et al., 2017; Porwal et al., 2013).

The composite effect has been demonstrated for polymer-based (Lahiri et al., 2011; Z. H. Ni et al., 2008b) and a few metal-based (Nieto et al., 2017; Tjong, 2013) nanocomposites, although at the expense often of ductility. In metals, the strengthening mainly originates from the impenetrability by dislocations of the metal-graphene interface similar to a strong grain boundary (Hwang et al., 2013; Y. Kim et al., 2013). The high strength of graphene allows building up very large stress without failure and dislocation penetration. These mechanisms have been studied both experimentally and numerically (Bartolucci et al., 2011; L. Y. Chen et al., 2012; Dorri Moghadam et al., 2015; Kuang et al., 2013; Tjong, 2013). For instance, an enhanced strength in Cu/Gr laminates has been attributed to dislocations piling up at the Cu and graphene interface (Y. Kim et al., 2013). A Cu/Gr nanolayered composite deformed by shear exhibits improved toughness and shear strength in comparison to pure metal (X. Y. Liu et al., 2016).

Regarding surface effects, one of the most convenient ways to determine the local resistance to a mechanical contact is by nanoindentation with the potential of quantifying the elastic stiffness and plastic strength (or hardness) for penetration depth at nanometer scale (Jian et al., 2010; W.C. Oliver, 1992). From the viewpoint of elasticity, the stiffer response of Gr-coated Cu has been demonstrated through experimental and theoretical studies (Hammad et al., 2017). This stiffening was found to result from the adhesionless contact between the nanoindenter and the graphene layer more than from a direct effect of graphene's high elastic modulus. The graphene layer acts thus as a shielding layer suppressing the adhesive forces and leading to an elastic response in almost perfect agreement with Hertz theory. The higher elastic modulus of Gr-coated Cu compared to Gr-free Cu was confirmed by Park et al. using also nanoindentation (Park et al., 2019). Klemenz et al. showed that Pt can resist higher loads in the presence of graphene coating for shallow indentation depth (Klemenz et al., 2014). From the viewpoint of plasticity du-

ring indentation, it is initiated by punching out dislocations when indenting almost defect-free regions of metallic crystals (Jian et al., 2010). When the maximum shear stress under the indenter reaches the theoretical shear stress, a discrete avalanche of dislocations is triggered causing the so-called "pop-in" excursions in the load-displacement curve (Gouldstone et al., 2000; Sato et al., 2019). The length of a pop-in is directly proportional to the number of dislocations involved in the avalanche (Suresh et al., 1999). A few studies recently addressed the plastic response of Gr-covered metallic materials. Molecular dynamics simulations of nanoindentation on Cu coated with single-layer graphene have shown an improved strength due to the modification of the dislocation activity near the Cu/Gr interface (X. Zhu et al., 2019). The plastic response of Cu/Gr under indentation has recently been investigated by Zhu et al. finding larger and later pop-in excursions when compared to bare Cu (X. Zhu et al., 2019). However, in the other recent investigation by Park et al. on the same system, pop-in excursions were found to be smaller and earlier in the presence of graphene (Park et al., 2019). Aside from the different trends observed in these two studies, open questions remain regarding the fundamental origin of the change of pop-in length in the presence of graphene, the statistical analysis of the phenomena, and the reasons explaining why graphene affects the onset of plasticity. Also, questions may be raised about possible artefacts coming from the use of a load control mode with respect to the unstable pop-in mechanism which cannot be properly resolved due to possible overshoot of the unstable pop-in penetration increment. Furthermore, no study has reported the interest of using indentation to study interface controlled plasticity effects with a small cap layer above the graphene layer.

The objective of this study is to investigate the effect of graphene on the contact plasticity when graphene is either coating a Cu substrate or buried under a thin cap layer made also of Cu (but with a much smaller grain size). More precisely, highly crystalline single-layer graphene is directly grown on Cu by chemical vapour deposition (Huet & Raskin, 2018a, 2018c). Using as-grown graphene circumvents the transfer process, which inevitably leads to graphene degradation and contamination. Moreover, the adhesion between CVD-grown graphene and the underlying Cu film is larger than for transferred Gr. The plastic response and underlying dislocation mechanisms are carefully studied by comparing four distinct systems: (i) annealed Cu film (as referred to as Cu_A) (ii) graphene as grown on Cu film (Cu_A/Gr), (iii) a 100 nm-thick Cu film directly evaporated on an annealed Cu film (Cu_A/Cu_N), (iv) a 100 nm-thick Cu film directly evaporated on as-grown graphene (Cu_A/Gr/Cu_N). In order to understand better the root causes of the observed effects on the plastic

flow, transmission electron microscopy (TEM) is used to compare samples after nanoindentation in terms of dislocation structures. Atomic force microscopy (AFM) provides additional pieces of evidence regarding the impact of graphene on the development and the localization of the plastic flow. Furthermore, 3D discrete dislocation dynamics (DDD) simulations are conducted to unravel more quantitatively how dislocations interact and multiply under the indent with and without the presence of graphene. This system offers a unique opportunity for direct comparisons of a 3D DDD framework on experimental results. The chapter starts with the presentation of the materials and test procedures in section 2 and is followed by section 3 including the results of nanoindentation in two different modes for the studied systems as well as all the other characterisation and modelling results. Finally, section 4 provides a discussion followed by the conclusions.

5.2 Materials and procedures

5.2.1 Materials

Cu substrates are produced by electron beam evaporation of 99.999% pure Cu pellets (Kurt J. Lesker) on 3 in. fused quartz wafers. The 1200 nm-thick Cu film is deposited at room temperature with a 4 Å/s under a base vacuum of about 2×10^{-7} mbar. The Cu film then serves as a catalyst for the synthesis of single-layer graphene, which takes place at about 1050°C under an atmosphere composed of methane, hydrogen, and argon. Additional Cu film substrates have been annealed under the same thermal protocol using only an Ar/ H_2 atmosphere in order to obtain a Cu sample with similar purity and microstructure but without any graphene. The CVD process is described somewhere else in detail (Huet & Raskin, 2018a, 2018b; Huet et al., 2019). For the final step of sample preparation, a Cu film with 100 nm thickness (Cu_N) has been deposited by evaporation on top of each type. Fig. 5.1 represents a schematic of the tests samples including (a) a bare annealed copper substrate (Cu_A), (b) a graphene-coated copper substrate (Cu_A/Gr), (c) an annealed copper substrate covered by a thin nanocrystalline copper layer (Cu_A/Cu_N), and (d) a graphene-coated copper substrate covered by nanocrystalline copper cap layer (Cu_A/Gr/Cu_N).

5.2.2. Test procedures

5.2.2.1. Structural and microstructural analyses

Raman spectroscopy (LabRAM HR by Horiba, excitation energy: 2.41 eV/514 nm, spot size:1 μm) has been used in order to characterise the as-grown graphene on the Cu substrate.

The grain characteristics of the Cu_A and Cu_N films have been characterised by scanning electron microscopy (SEM) (Zeiss Gemini Ultra-55) which also allowed positioning the indents with respect to the grain boundaries. Two types of detectors have been used, an in-lens and a regular Everhart-Thorney (E-T). EHT (electron high tension) and working distance were 2 kV and 4 mm, respectively. Electron backscatter diffraction (EBSD) relying on a MEB FEG ZEISS GeminiSEM500 with an EBSD camera CCD Hikari Super 1400 pts/ s EDAX) was used to determine the crystallographic texture.

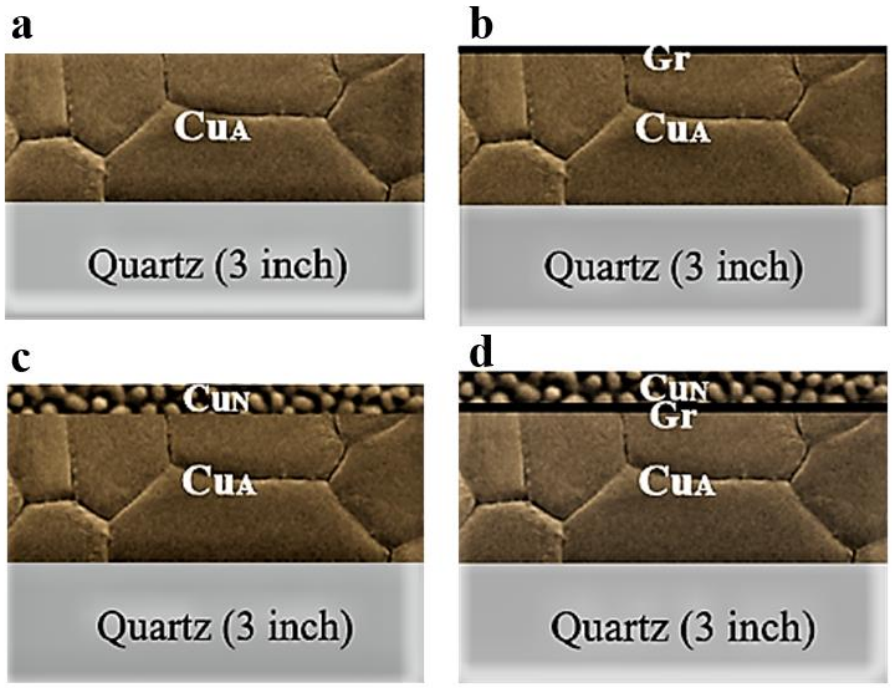

Fig. 5.1. *Schematics of the four different investigated systems; (a) annealed Cu film 1200 nm-thick (Cu_A); (b) graphene as grown on a 1200 nm-thick Cu film (Cu_A/Gr); (c) 100 nm-thick nanocrystalline Cu film evaporated on a 1200 nm-thick annealed Cu film (Cu_A/Cu_N); (d) 100 nm-thick nanocrystalline Cu film evaporated on as-grown graphene (Cu_A/Gr/Cu_N).*

AFM mapping (Dimension Icon Instrument by Bruker, standard tapping mode in air, linear scanning rate: 0.5 Hz) has been performed to collect images of the surface before indentation as well as of the indents in order to compare the topography and to determine the height of the pile-ups. Non-contact silicon probes (Nanosensors, PPP NCHR) have been used with a nominal spring constant of 40 N/m and tip radius <10 nm.

Cross-sectional TEM thin films have been prepared under the indents using a dual-beam focused ion beam (FIB) instrument (FEI Helios Nanolab 650). Electron beam followed by ion beam deposition of Pt layers was used in order to protect the surface of the film during FIB thinning. Bright-field images have been taken with a FEI Tecnai G2 F20 transmission electron microscope operated at 200 kV in order to analyse the dislocation structures and decohesion/failure events at interfaces.

5.2.2.2 Nanoindentation

Two different nanoindentation devices were used in order to determine the load-penetration responses and cross-validate the delicate measurements of pop-in lengths taking place at very small penetration depth. A pop-in involves an avalanche of dislocations, which is a dynamic phenomenon. Hence, during a pop-in under load control conditions, the indenter is abruptly losing contact with the surface and the indenter tip is suddenly accelerated. When the tip gets again in contact with the surface, equilibrium is not reached instantaneously and, due to inertia, an extra penetration is thus possible. The unstable nature of the pop-in under load control mode may thus lead to an overestimation of the pop-in length. Hence, displacement control experiments, which are less commonly used, have also been performed with other equipment. Under displacement control, a decrease of the force is allowed, stabilizing the response during a pop-in event. Independently of the application of two different loading modes, the use of two devices also provides a more robust basis of results for the analysis.

The load-controlled test campaigns were performed with the Agilent nanoindenter relying on the continuous stiffness measurement (CSM) mode at a representative strain rate of 0.05 s^{-1} and on the use of a diamond Berkovich tip. The radius of the tip has been measured as equal to ~40 nm by scanning electron microscopy (Ultra-55 from Zeiss) and the tip was calibrated on a standard silica sample with a known Young's modulus equal to 72 GPa. More than 300 indents have been performed with the Agilent system in order to

generate statistically valid data. The displacement-controlled tests have been performed with a UNHT^3 Anton Paar system including a feedback loop on the applied force signal. In this case, the displacement is calculated from the relative altitude measured between the indenter and a reference sphere in contact with the surface. This gives a theoretically infinite stiffness to the system avoiding any stiffness correction to cancel thermal drift. A diamond Berkovich tip was used, with a radius of curvature equal to ~100 nm.

5.2.2.3. Discrete dislocation dynamics (DDD) simulations

The 3D DDD setup has been described in several references (Marc C. Fivel, 2008; Verdier et al., 1998). It combines a DDD code (TRIDIS) which solves the dislocation kinetics and equilibrium, and a Finite Element (FE) code (CAST3M, FE Software available at www-cast3m. cea) in order to treat full boundary value problems. Such a combination is required in the case of nanoindentation simulations in order to consider the heterogeneous stress induced by the indenter correctly and to account for the image forces associated with the indented free surface. Only the Cu_A and Cu_A/Gr systems have been modelled.

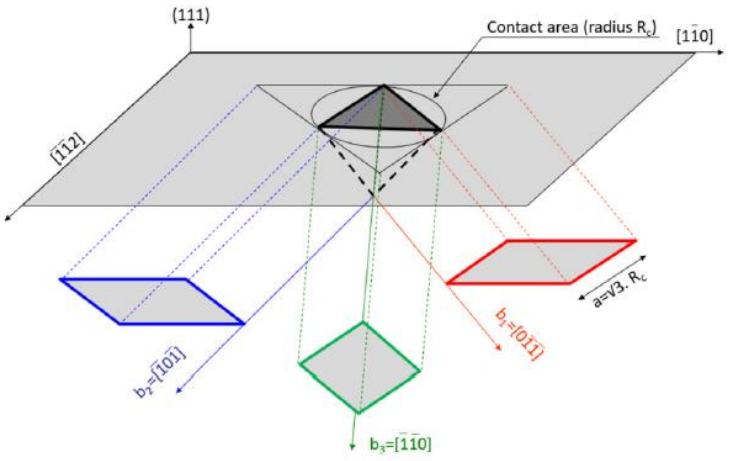

Fig. 5.2. *The geometry of the dislocation nucleation process under the indent within the 3D DDD framework, consisting of 3 interstitial prismatic loops as determined from MD simulations in the case of (111) spherical indentation.*

The nanoindentation test has been simulated by applying force with a rigid spherical punch to penetrate through small displacement increments inside the solid. After each displacement increment, several iterations are necessary to reach a state of equilibrium for the dislocations in the box. The Cu substrate is described through its elastic constants assuming elastic isotropy (E = 112 GPa, ν = 0.324). For the graphene layer, a purely elastic (E = 1000 GPa, ν = 0.19) row of elements is introduced sharing common nodes with the Cu solid assuming perfect adhesion. The validity of this assumption of good adhesion for the case of graphene grown on Cu has been indirectly verified in previous work based on molecular dynamics simulations (Hammad et al., 2017). In the DDD framework, a strong planar interface is introduced to reproduce the presence of the Gr layer. In the simulations reported in this paper, a perfect interface is considered, but a stress-based decohesion criterion can also be taken into account.

The DDD framework also requires the introduction of dislocation sources in order to initiate the dislocation multiplication process. Thus, empirical choices had to be guided by the physics of the problem. The simulations are conducted in a quasi-static loading mode; the indenter position is changed after the dislocation microstructure is fully relaxed. The relaxation condition is based on the rate of changes of the indentation force: equilibrium position is assumed when the force did not change by more than 0.1% between 10 consecutive dislocation dynamic computation steps. A convergence analysis has been carefully performed to ensure that the response is independent of the way the loading is applied, and of the number of introduced prismatic loops. This led to the number of prismatic loops introduced to be equal to 8 sets of three interstitial loops and their corresponding 24 vacancy loops. Molecular dynamic (MD) simulations of nanoindentation in (111) oriented Cu crystal have shown (Chang et al., 2010; Fivel, 2011) that nucleation occurs through the inoculation of a first defect below the surface, just beneath the indenter, which quickly degenerates into three prismatic loops. These prismatic loops correspond to three interstitial loops built on the three <110> directions, which are not included in the surface plane (see Fig. 5.2). The size of the loops is defined by the radius of the contact area, *Rc*, at a given penetration depth. Note that the presence of prismatic loops for low penetration indentation has been confirmed experimentally for FCC metals by TEM observations in 316L stainless steel (M. C. Fivel et al., 1998). In previous studies (H. J. Chang et al., 2010), this nucleation process has been successfully introduced in the DDD code, and spherical indentation on a (111) Cu single crystal (in agreement with the experimental texture (Huet & Raskin, 2018c) was

performed. It is shown that the dislocation microstructure evolution followed two regimes. The artificially inserted interstitial dislocation loops are initially gliding along with their cylinder similar to what is predicted by the MD simulations. Since the loop size is proportional to the contact radius, the loops get larger with increasing penetration depth and, at some point; their size gets large enough for the Frank-Read mechanism to operate on each arm of the loop, leading to a dislocation avalanche and a large increase of the dislocation density. After this stage, the induced dislocation density is capable of perfectly accommodating the spherical shape of the indenter without any need for additional dislocation nucleation events. Hence, in the present study, the same procedure has been used to initiate the plasticity mechanisms with a specific focus on the strain bursts induced by the dislocation nucleation process. The main differences with the previous study are: (i) the radius of the indenter tip is equal to 40 nm in order to match with the experiments; (ii) the nucleation process is triggered at a pre-defined penetration depth equal to 5, 10, 15 or 20 nm in order to check the effect of the penetration depth on the size of the strain bursts; (iii) the nucleation mechanism consists of a sufficiently large number of prismatic loops, typically 8 per activated Burgers vector, such that the dislocation dynamics process is already in the avalanche regime; (iv) in the case of the Cu_A/Gr system, an impenetrable surface (facet) is introduced at the interface between the Cu substrate and the graphene layer; (v) for each inserted interstitial prismatic loop, there exists an equivalent vacancy loop located on the same cylinder but closer to the graphene layer in the case of Cu_A/Gr and outside the simulated volume in the case of Cu_A. This has been imposed in order to trigger a mechanism with no mass loss and to ensure the consistency of the calculation of the surface steps as demonstrated in (M. Fivel & Depres, 2014). The calibration of the DDD simulation and the principles regarding that have been detailed in other works(H. J. Chang et al., 2010).

5.3. Results

5.3.1. Experimental results

5.3.1.1. Characterisation of structure and microstructure

Fig. 5.3 shows the Raman spectrum obtained for the graphene on Cu_A/Gr sample. A high *2D-to-G* peak intensity ratio and narrow *2D* bandwidth (larger than 2 and 20 cm^{-1}, respectively) prove the single atomic layer nature of the

graphene. In addition, the *D-to-G* peak intensity ratio is smaller than 0.1, which indicates a low density of structural defects in as-grown graphene.

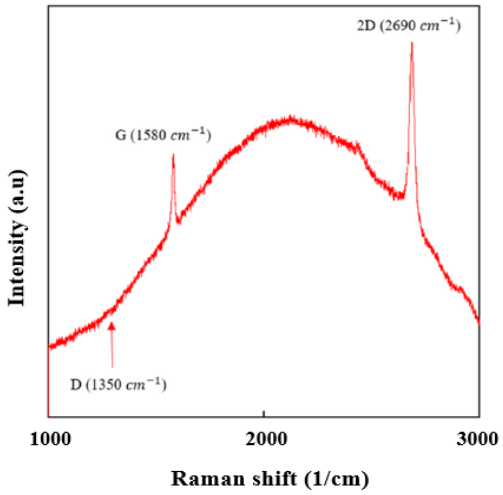

Fig. 5.3. *Typical Raman spectrum directly acquired on as-grown graphene. D, G, and 2D band, respectively located at 1350, 1580 and 2690 cm^{-1} are the main Raman peaks expected for graphene.*

Fig. 5.4a and b compare SEM of the surface of the Cu_A and Cu_N films. The Cu_A exhibits relatively large grains in micrographs the 10–100 μm range, as a result of the high-temperature annealing associated with the graphene growth process. This large grain size will avoid possible artefacts from the interaction between the plastic size below the indent with the constraint associated with the grain boundaries (see further). The Cu_N film has a grain size in the 50 to 100 nm range (which cannot be clearly seen on a SEM image but confirmed by TEM analysis, see further), commensurate with the thickness as commonly observed with thin metallic films. Fig. 5.4c and d provide EBSD maps and pole figures, respectively, of a Cu_A film revealing the expected sharp (111) texture.

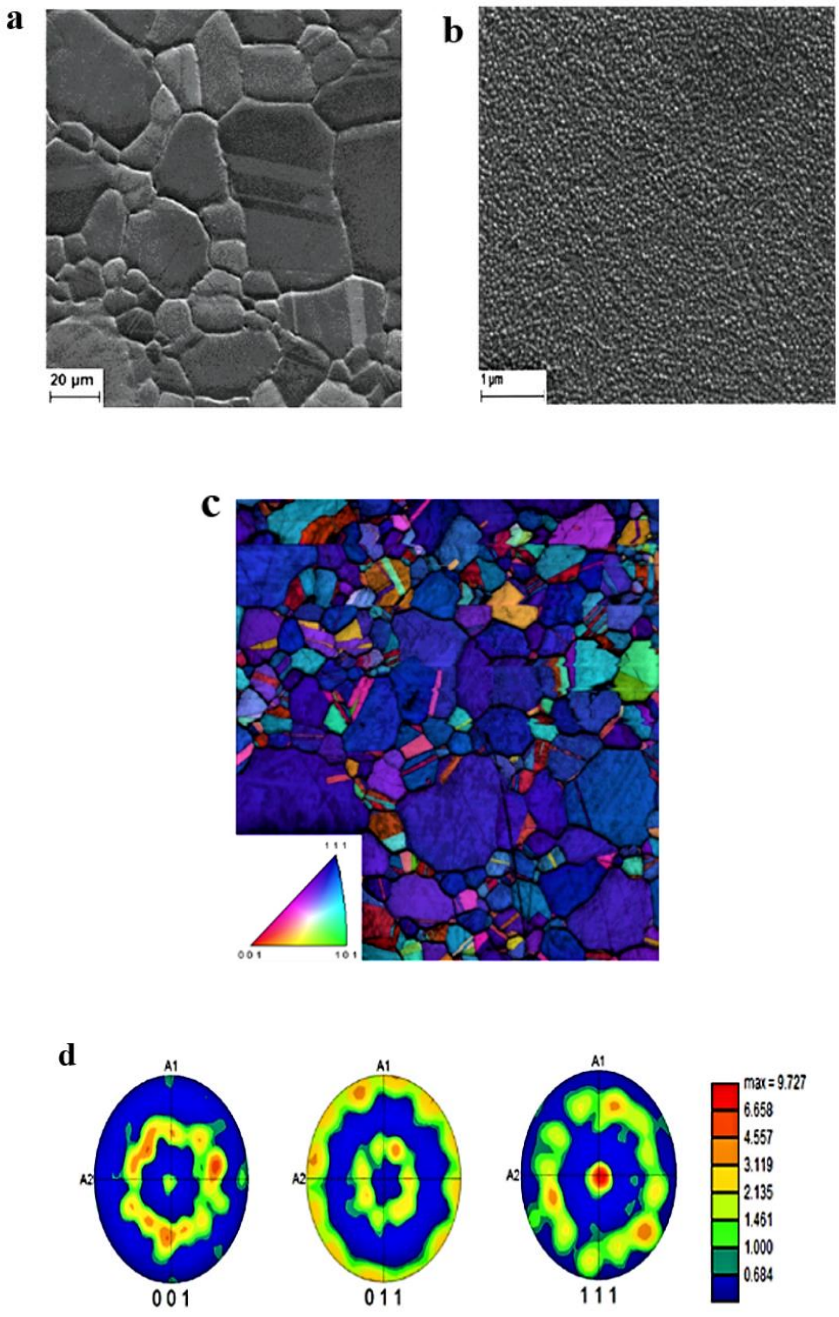

Fig. 5.4. *Grain characteristics of the Cu films; SEM micrographs of (a) the 1200 nm thick Cu_A film; (b) 100 nm thick Cu_N film; (c) EBSD map; (d) pole figures.*

5.3.1.2. Indentation of Cu_A and Cu_A/Gr

Fig. 5.5 is a SEM micrograph showing a set of indents inside a Cu_A grain. Only indents produced sufficiently far from the grain boundaries were kept for further analysis in order to avoid specific interaction effects between dislocations and grain boundaries, which may convolute with the interactions with the graphene layer. Furthermore, the indents were all made in (111) grains, avoiding the effect of crystallographic orientation on the plastic indentation response [Britton et al., 2010; Selvarajou et al., 2014].

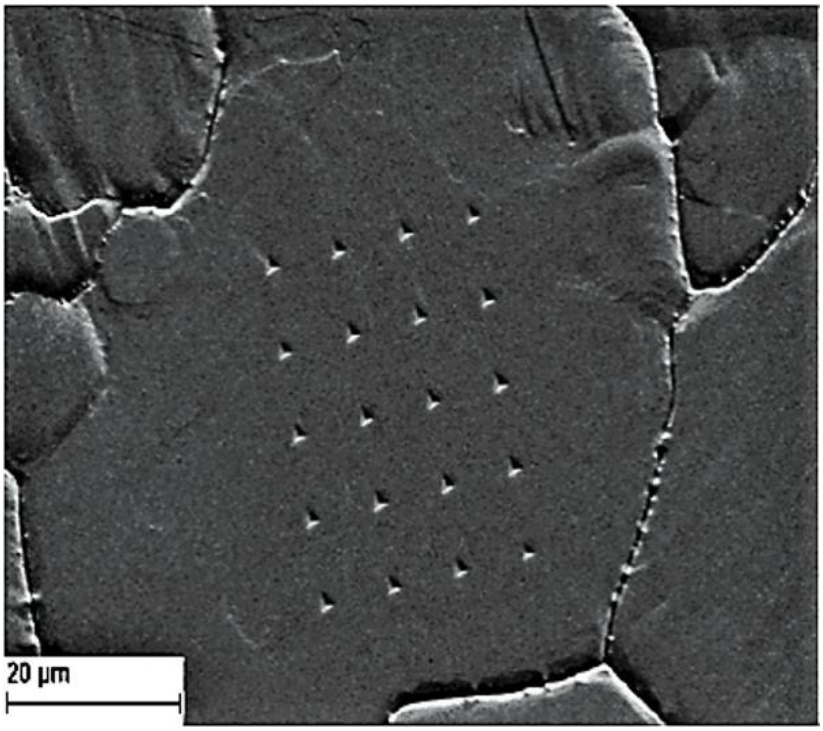

Fig. 5.5. *SEM micrograph showing a series of indent inside a Cu_A grain, sufficiently remote from grain boundaries to avoid plastic interactions.*

Fig. 5.6a and b show representative load-penetration curves for the Cu_A and Cu_A/Gr systems as measured under load-controlled and displacement-controlled conditions, respectively. The pop-in produced under load-control leads to a plateau associated with a sudden finite penetration (Fig. 5.6a with a zoom on the pop-ins) while it leads to a force drop which involves some extra displacement due to the non-instantaneous feedback loop operation under

displacement-control mode. In the last case, the pop-in length is determined to be equal to the displacement difference from the load drop point to the point at which the load increases back to the same value as before the drop shown in Fig. 5.6b. The differences in the elastic response between bare Cu and Cu/Gr as well as on result of a Hertzian analysis of the elastic regime have already been investigated in depth by Hammad et al. (2017), see the introduction. The focus of this work is on the initiation of plasticity and pop-in events detected in each load-penetration curve which have been systematically analysed to determine the quantitative effect of graphene on the elastoplastic indentation response of the Cu layer.

More than one pop-in is observed in most load-displacement curves. In the case of Cu_A, second pop-ins rarely occur and third pop-ins are never observed as shown in Fig. 5.6c. However, in Cu_A/Gr system, besides the first and second pop-ins, third pop-ins frequently occur as can be observed in Fig. 5.6d. Fig. 5.6e shows variations of the pop-in length as a function of the load at the onset of the pop-in in Cu_A and Cu_A/Gr systems under load control mode. The comparison of the collections of first and second pop-ins in Cu_A with first, second and third pop-ins in Cu_A/Gr shows that, in the case of Cu_A, the pop-in length increases with the load whereas it remains relatively constant in Cu_A/Gr system. Fig. 5.6f and g provide the variations of the first pop-in length as a function of the critical load at the onset of the plastic burst of more than 300 indents, for the Cu_A and Cu_A/Gr systems in load-control and displacement-control modes, respectively. The results are similar under both conditions with less dispersion in displacement-control mode. The load at the onset of plasticity is on average smaller in the case of the Cu_A/Gr system compared to the bare Cu_A. Finally, Fig. 5.6h and 5.6i plot the probability function of pop-in lengths in different ranges as a function of load for the load-control and displacement-control conditions, respectively.

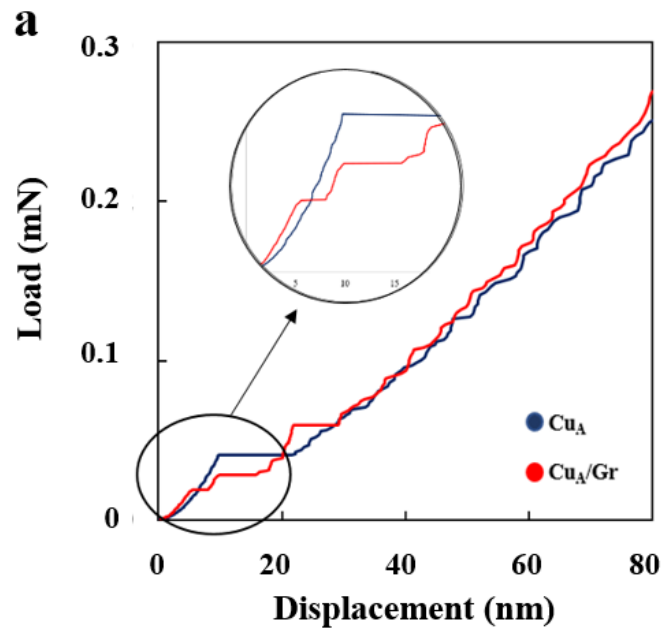
a
0.3
0.2
0.1
0
Load (mN)
0
20
40
60
80
Displacement (nm)
Cu_A
Cu_A/Gr

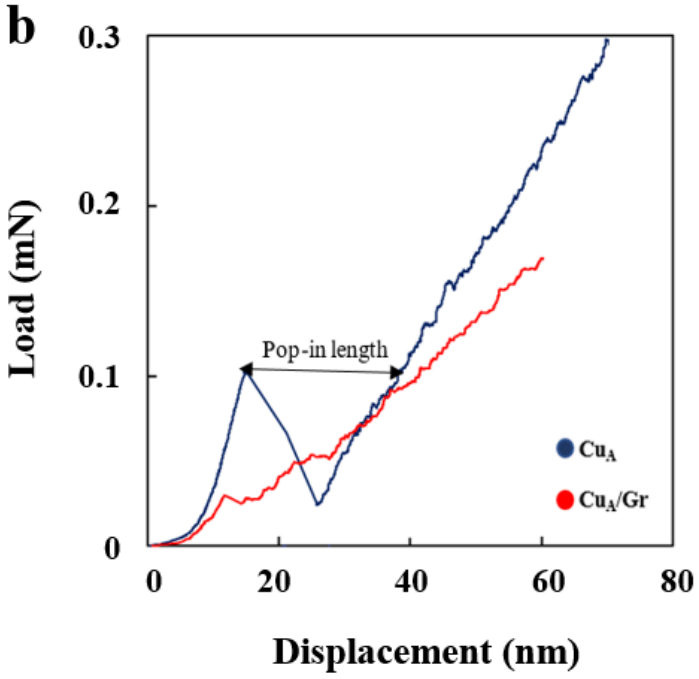
b
0.3
0.2
0.1
0
Load (mN)
Pop-in length
0
20
40
60
80
Displacement (nm)
Cu_A
Cu_A/Gr

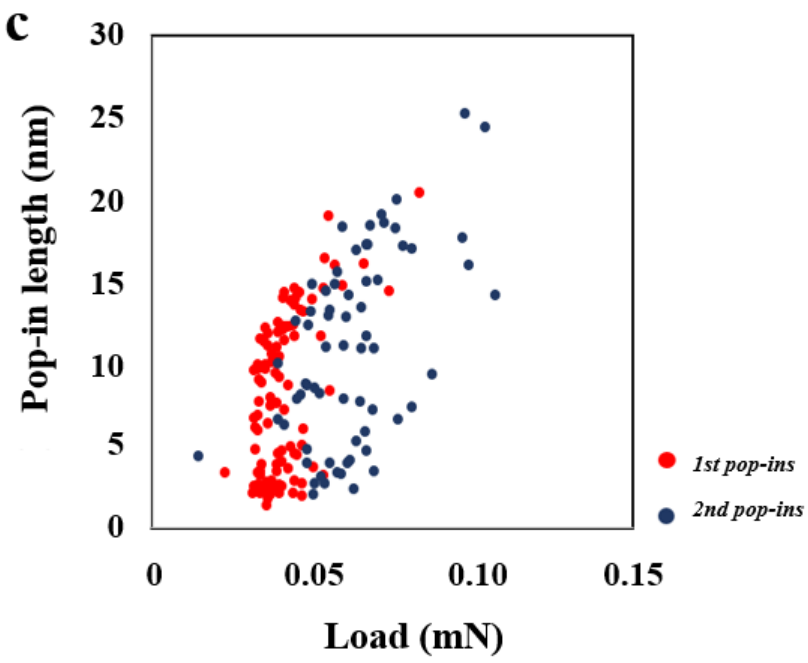
c
Pop-in length (nm)
30
25
20
15
10
5
0
0
0.05
0.10
0.15
Load (mN)
1st pop-ins
2nd pop-ins

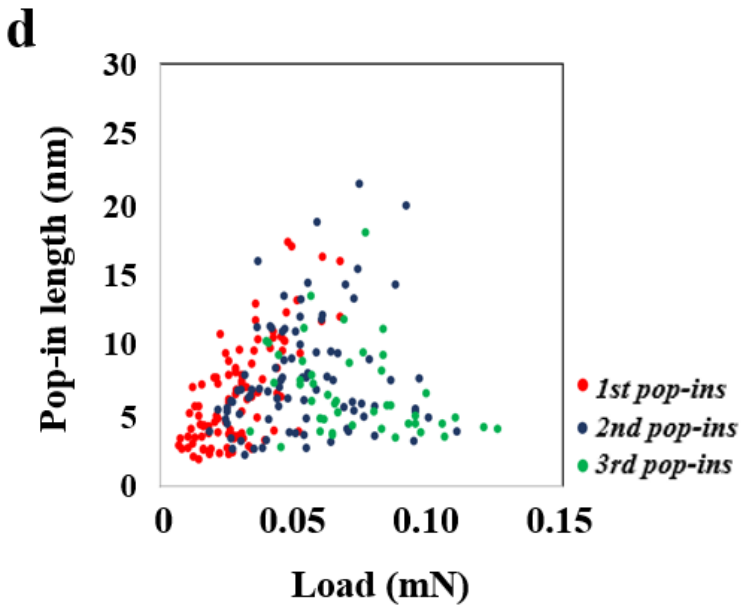
d
Pop-in length (nm)
30
25
20
15
10
5
0
0
0.05
0.10
0.15
Load (mN)
1st pop-ins
2nd pop-ins
3rd pop-ins

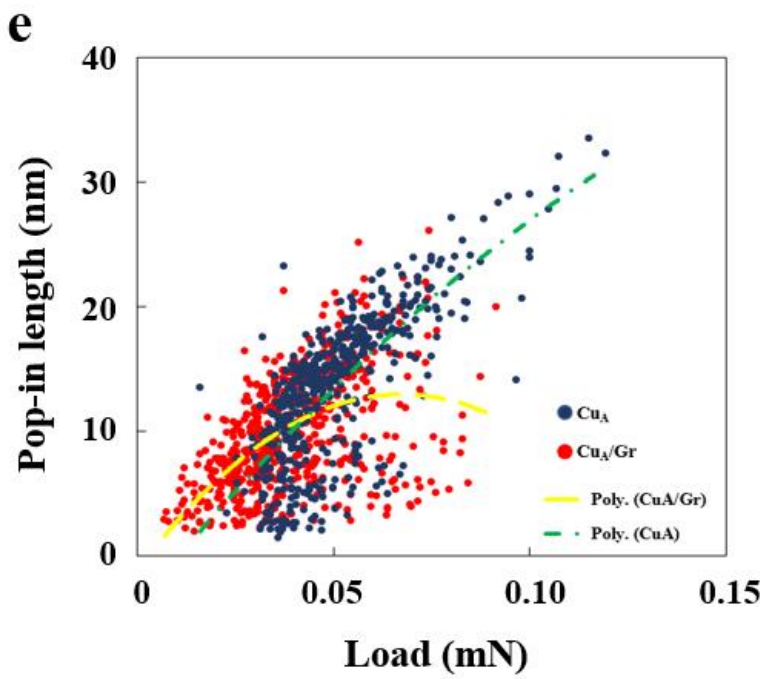
e
Pop-in length (nm)
Load (mN)
0
10
20
30
40
0
0.05
0.10
0.15
Cu_A
Cu_A/Gr
Poly. (CuA/Gr)
Poly. (CuA)

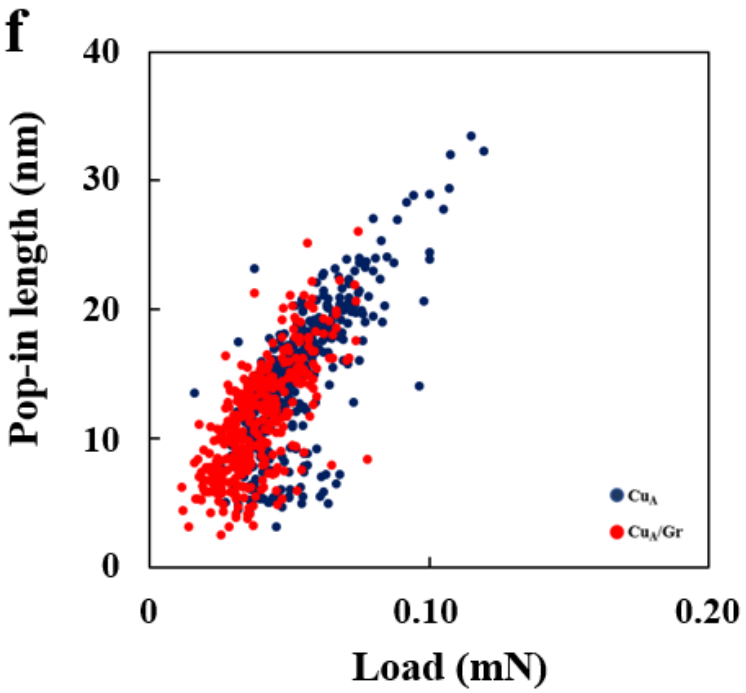
f
Pop-in length (nm)
Load (mN)
0
10
20
30
40
0
0.10
0.20
Cu_A
Cu_A/Gr

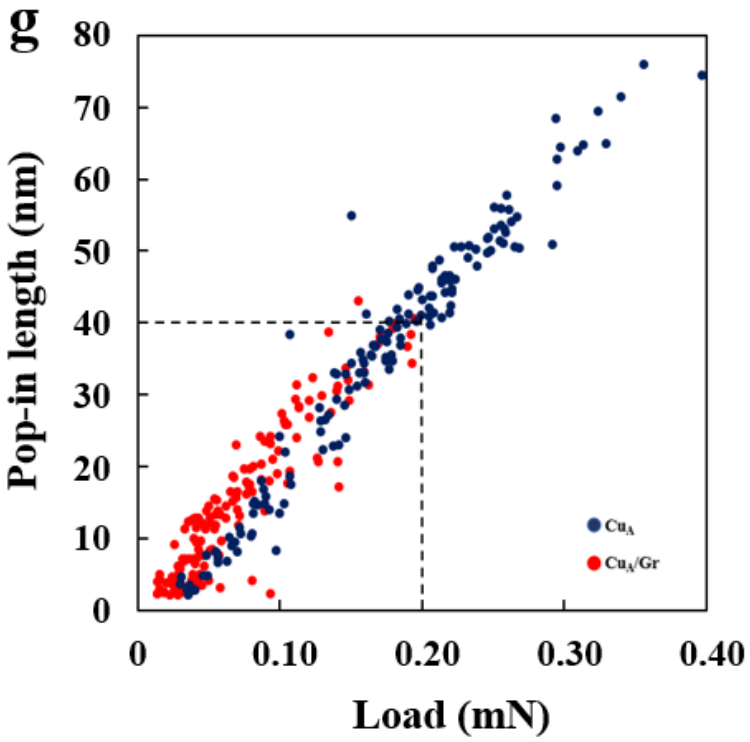
g
Pop-in length (nm)
80
70
60
50
40
30
20
10
0
0
0.10
0.20
0.30
0.40
Load (mN)
Cu_A
Cu_A/Gr

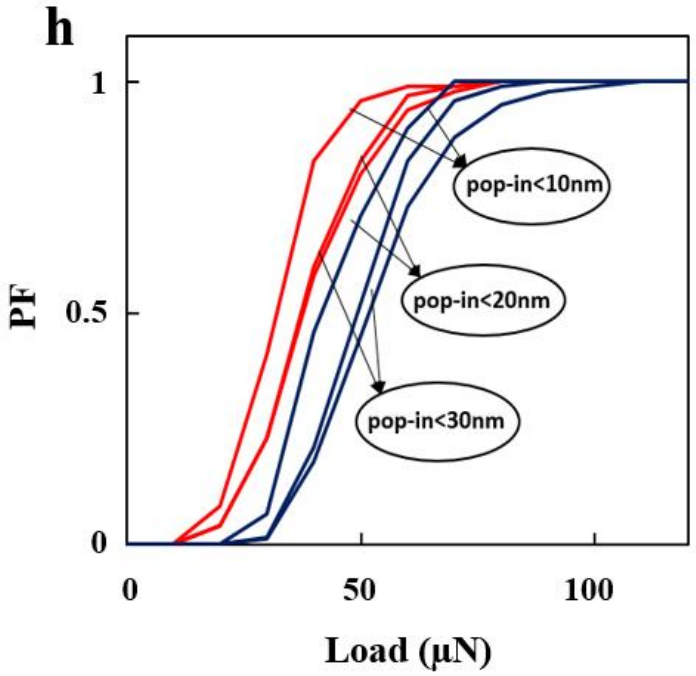
h
PF
1
0.5
0
0
50
100
Load (μN)
pop-in<10nm
pop-in<20nm
pop-in<30nm

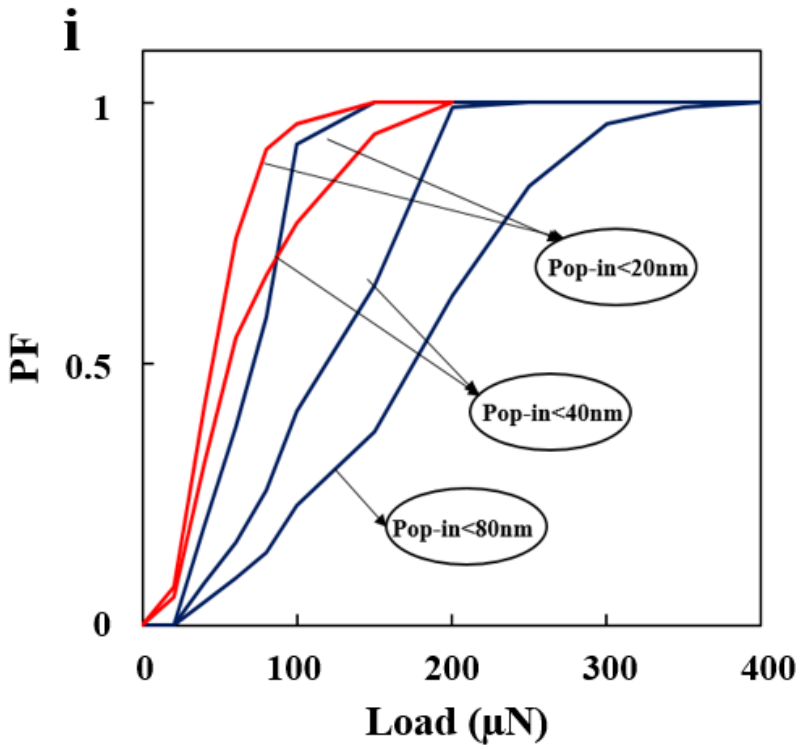

Fig. 5.6. *(a) Comparison of load-penetration curves for Cu_A and Cu_A/Gr in load-control mode; (b) comparison of load-penetration curves for Cu_A and Cu_A/Gr in displacement-control mode; (c) first and second pop-ins in Cu_A system; (d) first, second, and third pop-ins in Cu_A/Gr system; (e) comparison the length of first and second pop-ins of Cu_A with first, second and third pop-ins of Cu_A/Gr in load-control mode; (f) comparison the first pop-in length vs load of Cu_A and Cu_A/Gr in load-control mode; (g) comparison the first pop-in length vs load of Cu_A and Cu_A/Gr in displacement-control mode; (h) comparison of probability function vs load of Cu_A and Cu_A/Gr in load-control mode; (i) comparison of probability function vs load of Cu_A and Cu_A/Gr in displacement-control mode.*

5.3.1.3. Indentation of Cu_A/Cu_N and $Cu_A/Gr/Cu_N$

All tests made on the sandwich configurations were performed under load-controlled mode using the Agilent nanoindenter, based on the earlier validation that both loading modes provide similar pop-in behaviour. The indents have been characterised first by SEM to verify the absence of cracks in the Cu_N films. Due to the nanocrystalline nature and the expected high strength/low ductility behaviour, there was indeed a possibility of indentation-induced damage and cracks that we had to discard. Fig. 5.7a shows the

comparison of two representative load-displacement curves for the Cu_A/Cu_N and $Cu_A/Gr/Cu_N$ systems. The comparison of pop-in length in Fig. 5.7b indicates the clear influence of the graphene interlayer on the pop-in length. The pop-in length is significantly reduced in the presence of a graphene layer. The difference is clearly stronger than for the Cu_A/Gr versus Cu_A systems.

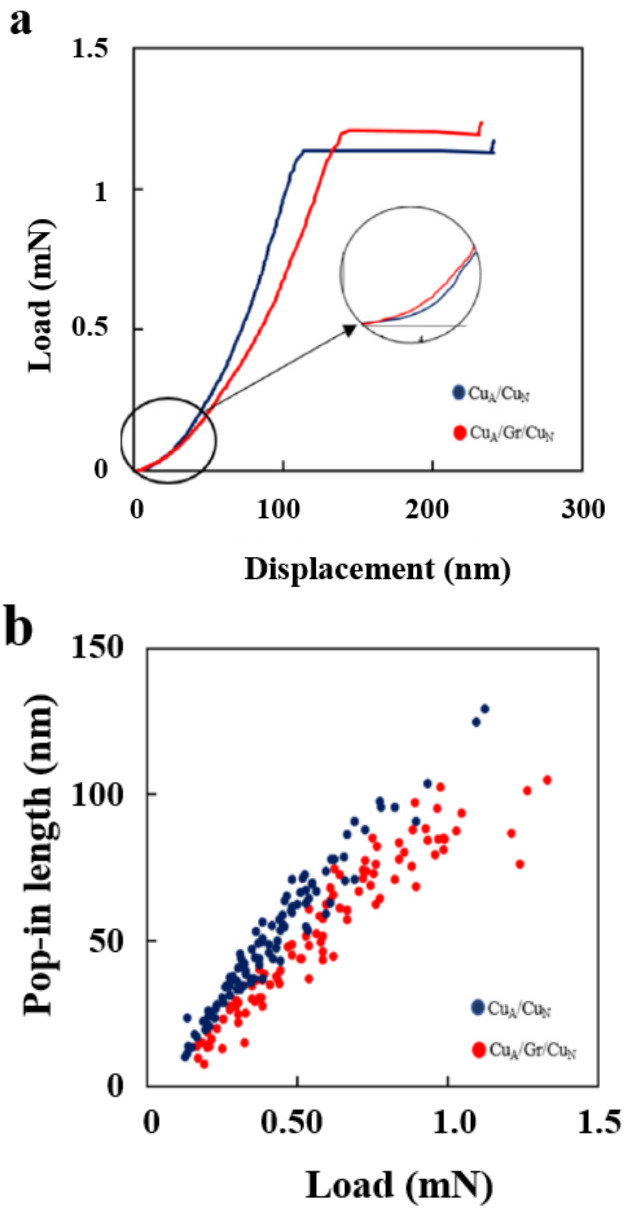

Fig. 5.7. *(a) Comparison of the load-penetration curves for Cu_A/Cu_N and $Cu_A/Gr/Cu_N$ in load-control mode; (b) comparison of the first pop-in length of Cu_A/Cu_N and $Cu_A/Gr/Cu_N$ in load-control mode.*

5.3.1.4. Indentation of Cu_A and Cu_A/Cu_N

Fig. 5.8 provides a comparison of 5 randomly chosen load-penetration curves for the Cu_A and Cu_A/Cu_N systems. It reveals a significant difference in the length of the first pop-in when comparing these two systems. The pop-in occurs at a much larger depth in the Cu_A/Cu_N system, which is an indication that the pop-in is induced by a plastic burst taking place inside the Cu_A substrate. Furthermore, the zoom on the Cu_A/Cu_N system shows many small pop-ins before the first large one. As a useful information for further interpreting the indentation data on the systems with the Cu_N cap layer, Fig. 5.9 shows the variation of the hardness extracted using the Oliver and Pharr method as a function of penetration depth (Oliver & Pharr, 1992). After a regime dominated by the elastic and elastoplastic transition, the hardness of the Cu_N is found to be ~2.5 GPa. Deeper indentation leads to a response dominated by plasticity inside the Cu_A substrate with a hardness converging towards the Cu_A hardness, near 1.4 GPa.

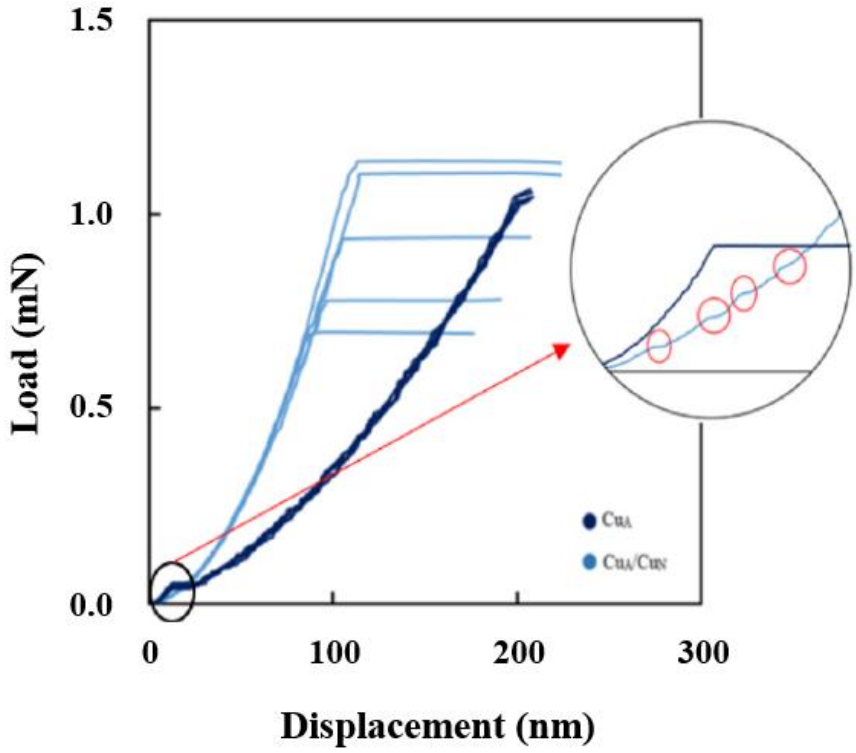

Fig. 5.8. *Comparison of pop-in length for Cu_A and Cu_A/Cu_N. The inset shows the small pop-ins in one of the curves which occur before the first large pop-in in Cu_A/Cu_N.*

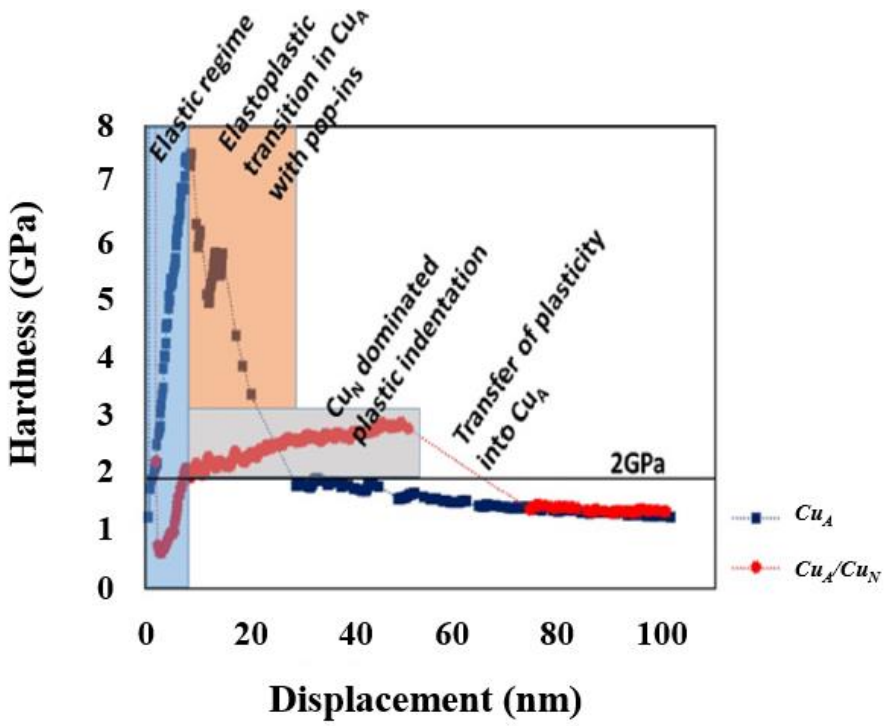

Fig. 5.9. *Variation of hardness as a function of penetration depth for Cu_A and Cu_A/Cu_N, showing the significantly larger hardness of Cu_N before the plasticity is transferred into the underlying Cu_A layer with the hardness following then the trend obtained for a single Cu_A film.*

5.3.1.5. AFM investigation

Fig. 5.10a and b compare the initial surface topography of Cu_A and Cu_A/Gr systems before indentation. The surface in the presence of graphene exhibits a finer topography. This is in agreement with other observations in the literature, which indicate the existence of Cu steps/terraces bunching under graphene. It is explained in (Kang et al., 2016; Yi et al., 2018) that Cu atoms re-arrange underneath graphene during the high-temperature CVD process in order to minimize the compressive strain or the local bending energy in graphene. The deep black lines marked in the figures correspond to the grain boundaries.

Fig. 5.10c–f provide AFM images of the indented regions in order to characterise the differences between systems with and without graphene. Some indents show higher penetration depth, which could result from the

existence of some defects in the Cu_A surface below the indenter. However, these indents have been discarded from the analysis.

Small patterns (particle-like) are observed especially around the indents on the Cu_A samples while they are not observed on the Cu_A/Gr one. Analysis of the height profiles across the indents (Fig. 10g–j) shows that the presence of graphene induces significantly smaller pile-ups. The use of AFM to characterise pile-ups has been validated in the literature (Kese & Li, 2006). On the other hand, the comparison of the AFM profiles for the Cu_A/Gr/Cu_N versus Cu_A/Cu_N systems does not reveal significant variations.

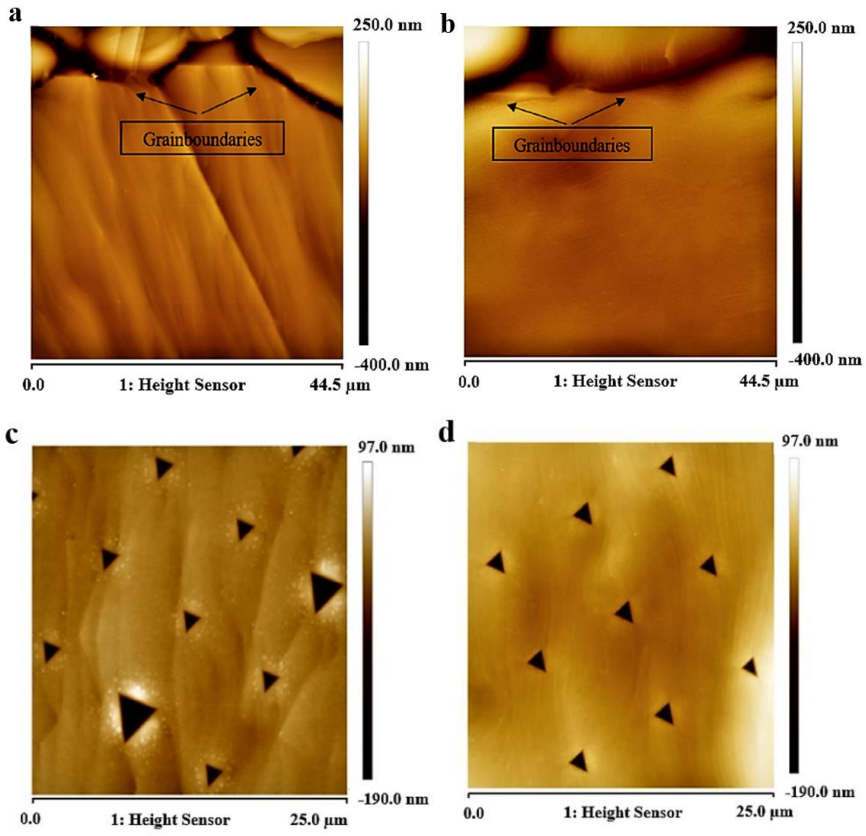

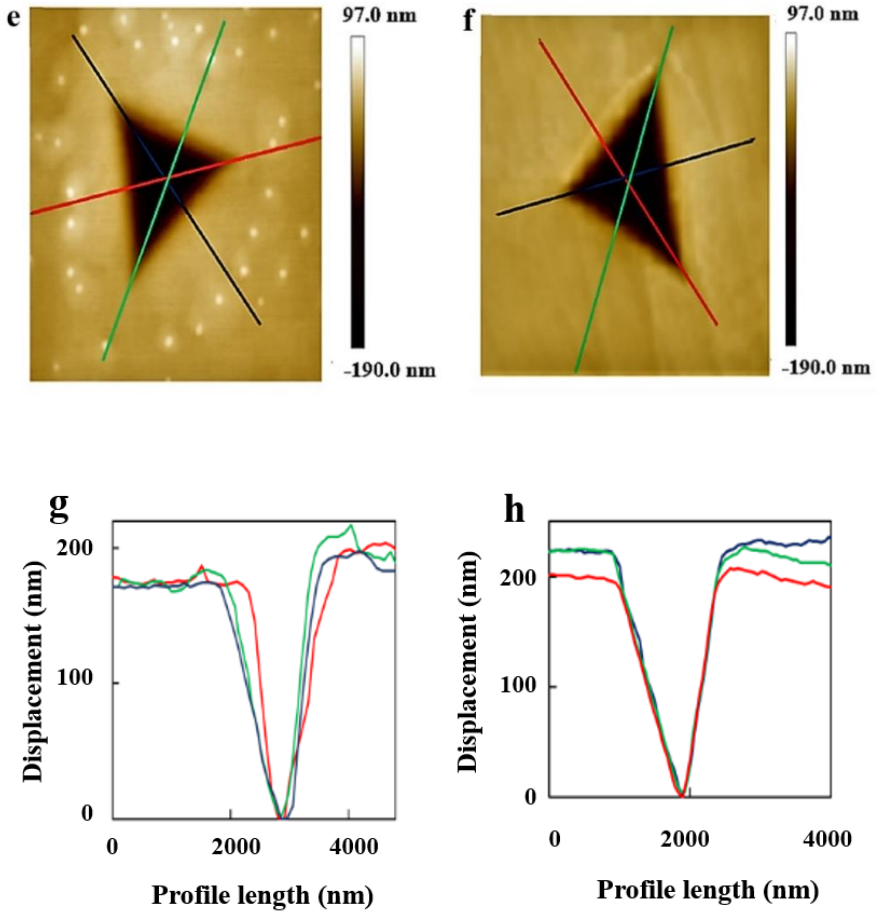
e
97.0 nm
-190.0 nm
f
97.0 nm
-190.0 nm
g
Displacement (nm)
200
100
0
0
2000
4000
Profile length (nm)
h
Displacement (nm)
200
100
0
0
2000
4000
Profile length (nm)

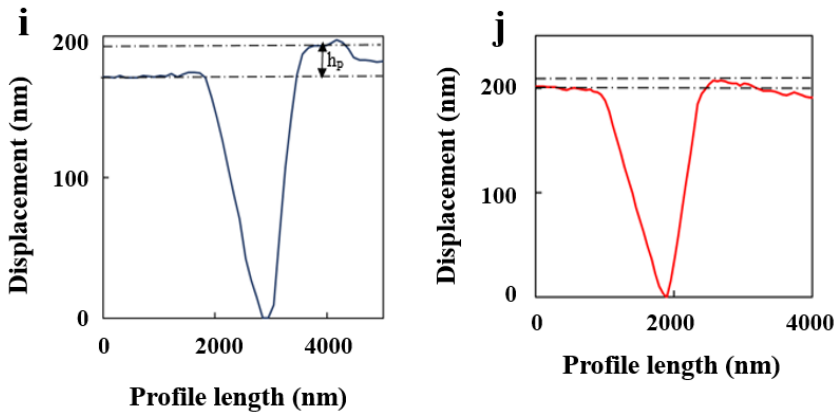

Fig. 5.10. *(a) AFM image before indentation on Cu_A (size of the square box is 44.5 × 44.5 μm2); (b) AFM image before indentation on Cu_A/Gr (size of the square box is 44.5 × 44.5 μm2); (c) AFM image after indentation on Cu_A (size of the square box is 25 × 25 μm2); (d) AFM image after indentation on Cu_A/Gr (size of the square box is 25 × 25 μm2); (e) Higher magnification of one indent on Cu_A; (f) higher magnification on one indent on Cu_A/Gr; Cu_A; (g) three height profiles across the indent shown in (e); (h) three height profiles across the indent shown in (f); (i) height profile (dark blue) across the indent shown in (e); (j) height profile (red) across the indent shown in (f). (For interpretation of the references to color in this figure legend, the reader is referred to the Web version of this article).*

5.3.1.6. TEM characterisation

TEM micrographs after indentation down to 200 nm depth reveal the difference between dislocation arrangements in Cu_A and Cu_A/Gr systems under indents (Fig. 5.11a–b). The formation of dislocations walls in the Cu_A system and the much more spread and homogenous distribution of dislocations in the Cu_A/Gr system is a signature of the influence of the graphene barrier on dislocation activity. Fig. 5.12a–b show TEM micrographs of the dislocation microstructure in the Cu_A/Cu_N and Cu_A/Gr/Cu_N systems for 100 nm indentation depth where the main pop-in has already occurred.

Performing a TEM characterisation on a section corresponding to 100 nm indentation depth, i.e. just after the first pop-in, was chosen to limit the distortion of the interface with the graphene layer and to make easier the characterisation. The system with graphene requires a higher force for inducing almost the same pop-in length (see Fig. 5.12c). A high density of dislocations is stored against the graphene barrier. The root cause of this phenomenon will be discussed in the next section

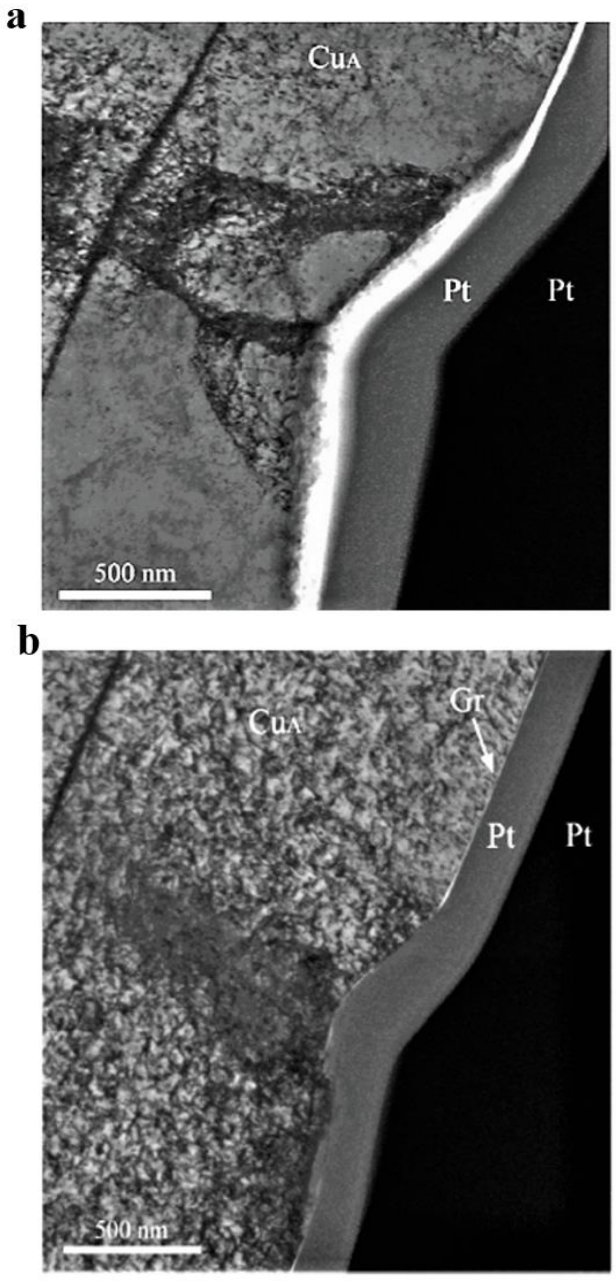

Fig. 5.11. *(a) TEM micrograph showing the dislocation arrangements in Cu_A; (b) TEM micrograph showing the dislocations structures in the Cu_A/Gr system. The two top layers consist of successively deposited electron beam Pt layer and ion beam Pt layer from the left to the right side, respectively.*

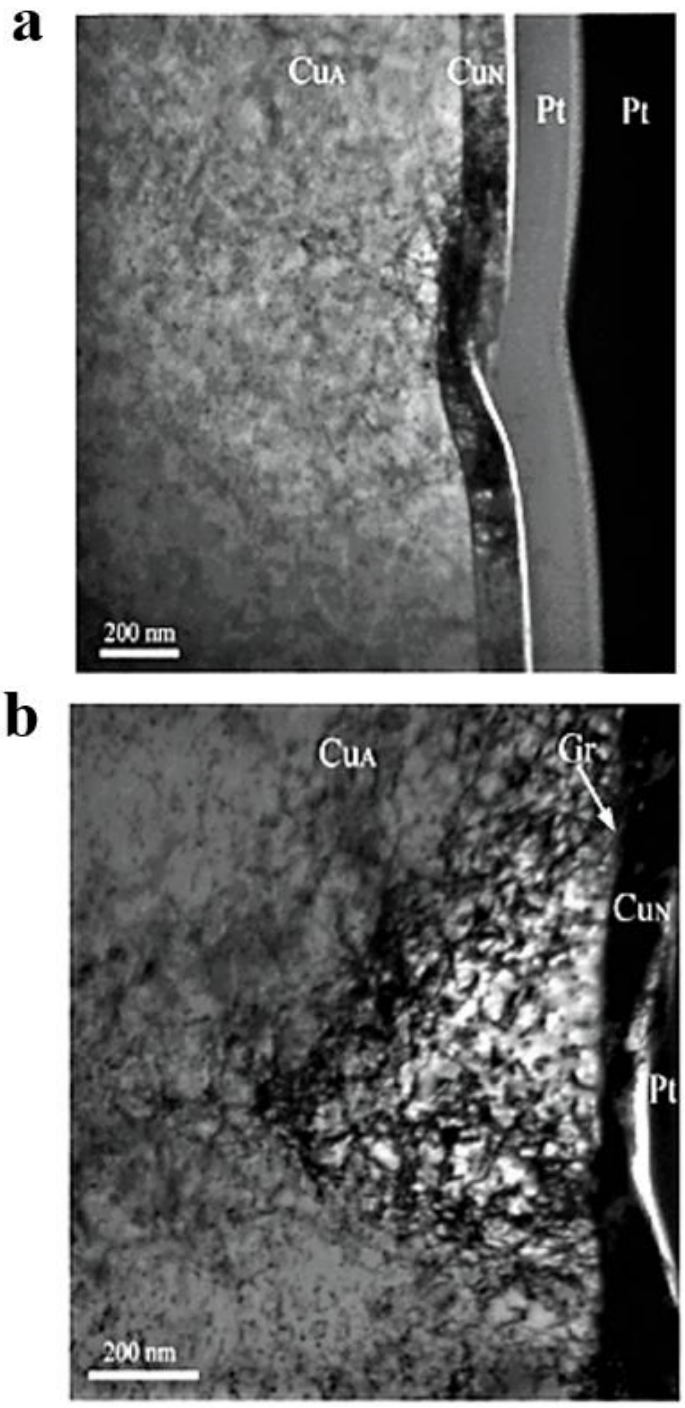
a
CuA
CuN
Pt
Pt
200 nm
b
CuA
Gr
CuN
Pt
200 nm

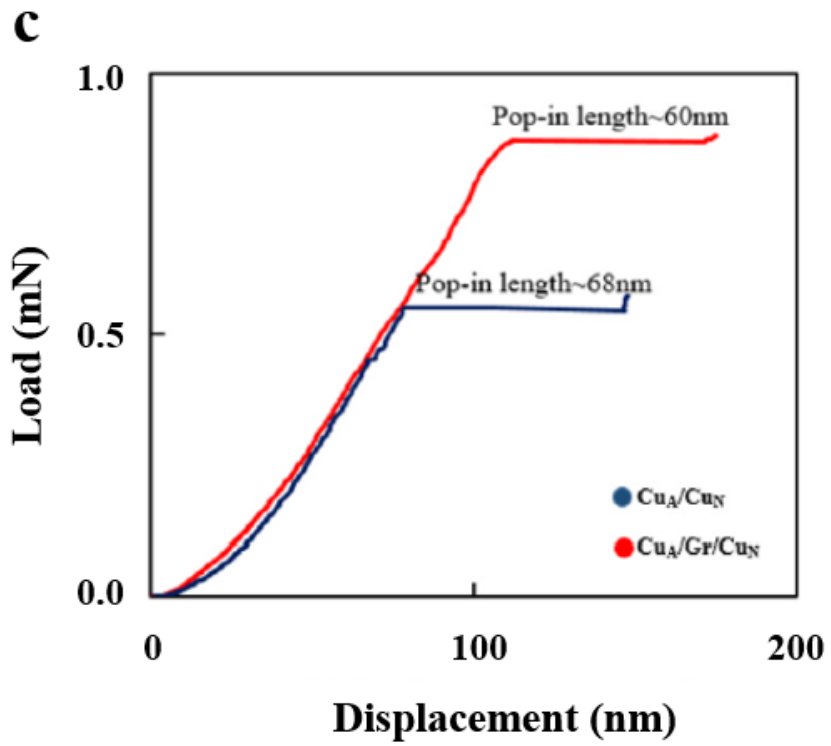

Fig. 5.12. *(a) TEM micrograph showing the dislocation structure under a 100 nm-deep indent in the Cu_A/Cu_N film; (b) TEM micrograph showing the dislocation structure under a 100 nm-deep indent in the $Cu_A/Gr/Cu_N$ film; (c) comparison of the load-penetration curves for Cu_A/Cu_N and $Cu_A/Gr/Cu_N$ under load-control mode.*

Many TEM observations show local failure events at the level of the graphene layer after indentation. This can be due to graphene fracture and/or decohesion. Some evidence can be seen in Fig. 5.11b in the form of a white band at the level of the graphene boundary in the system Cu_A/Gr. The size of this white band is much larger due to the presence of some fragments of the Cu films under the indent, which hinders a good cohesion between the electron beam deposited Pt layer and the Cu film. It can thus be concluded that the white band in Fig. 5.11b is due to the presence of fragments of graphene under the indent. Fig. 5.13 shows a more obvious example of decohesion for the $Cu_A/Gr/Cu_N$ system in a micrograph taken under the high-angle annular dark field scanning TEM (HAADF-TEM) imaging mode. Still, care should be taken in the interpretation of the micrograph of Fig. 5.13 as there is no full guarantee that decohesion is between the Cu_A layer and graphene, and not between the Cu_N layer and graphene.

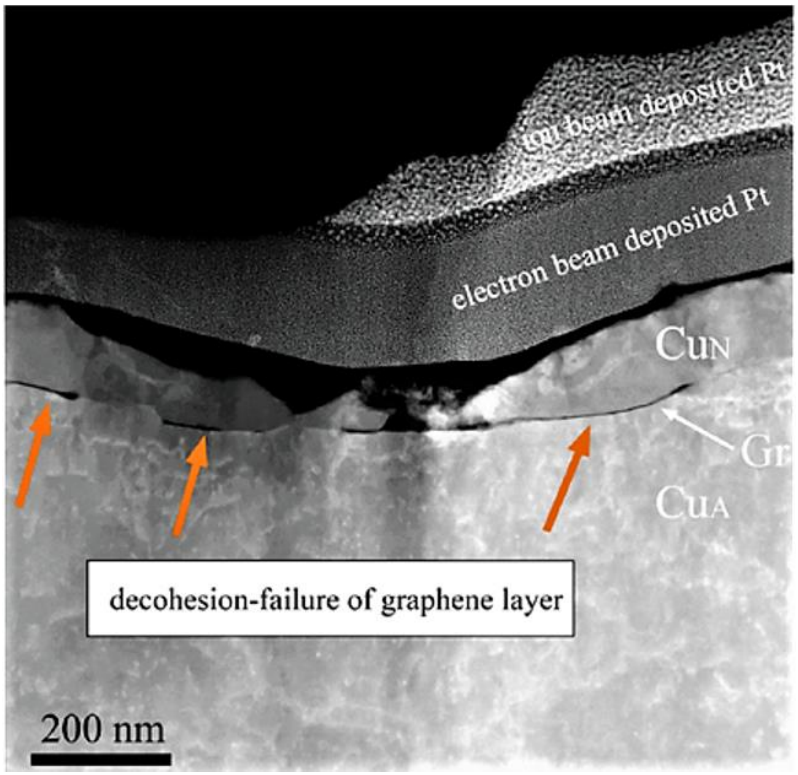

Fig. 5.13. *HAADF STEM micrograph of the region below an indent performed in a CuA/Gr/CuN system exhibiting decohesion/failure at the graphene layer level.*

5.3.2. DDD results

Fig. 5.14 shows the force-penetration curves computed by DDD in the case of Cu_A and Cu_A/Gr for different values of the critical depth to trigger the nucleation process. The case of Cu_A is plotted in Fig. 5.14a. The mechanical response starts with an elastic response, which follows the Hertz model. After dislocation nucleation, the elastic loading curve shifts to a plastic master curve which nicely matches the experiments. A higher critical load at nucleation leads to a higher pop-in length as measured experimentally. This is a direct signature of the transition from the Hertz regime to the plastic regime.

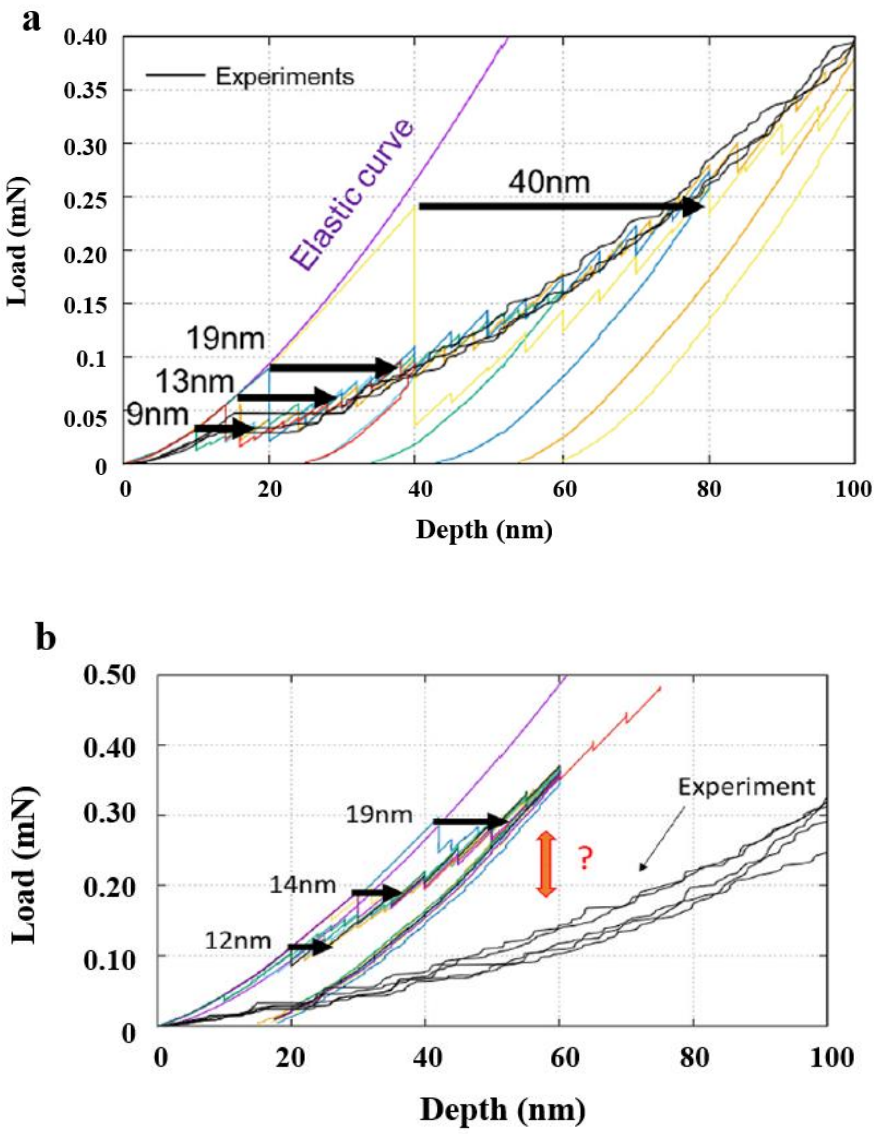

Fig. 5.14. *(a) DDD predicted load-penetration curve for Cu_A for the different onset of the nucleation algorithm; (b) DDD load-penetration curve for Cu_A/Gr, which shows a stiffer mechanical response.*

Fig. 5.14b shows that in the case of Cu_A/Gr, the spreading of the pop-in length is significantly reduced in agreement with the experiments. However, the plastic curve after nucleation does not match well with the experiments as a stiffer response is predicted by the DDD simulations. This discrepancy will be discussed in the next section.

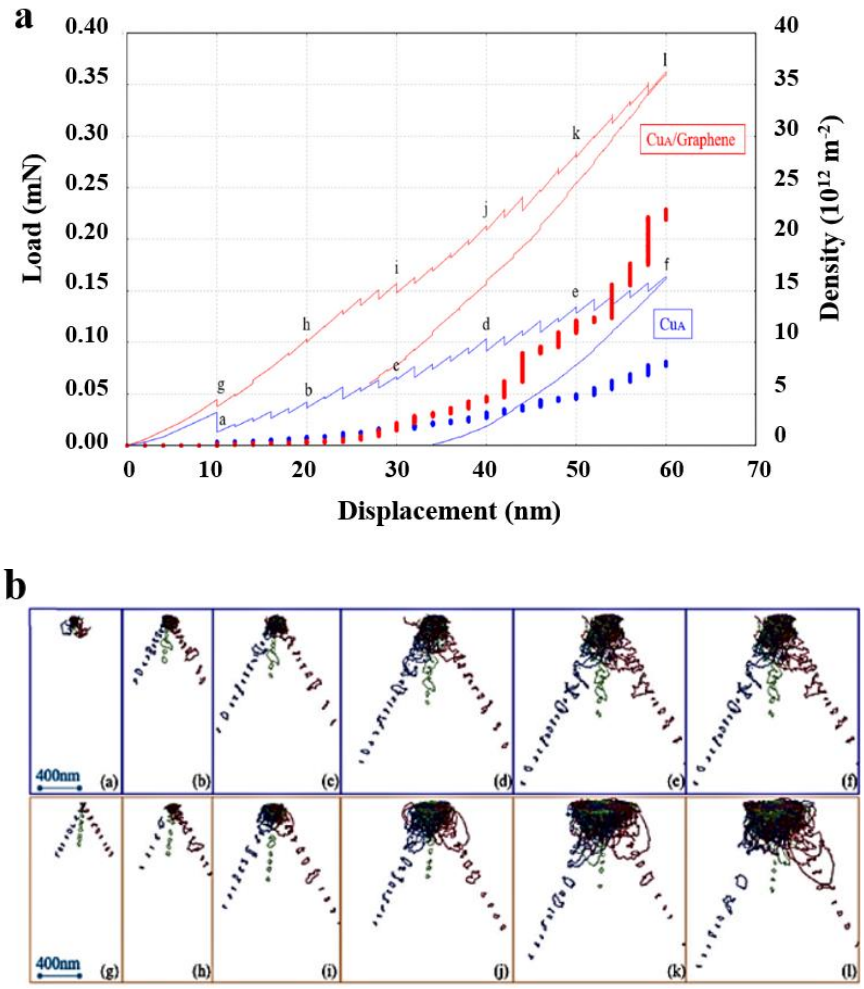

Fig. 5.15. *(a) DDD load-penetration curve and evolution of dislocation density (filled circles) for CuA and CuA/Gr when plasticity is triggered at 10 nm depth; (b) dislocation arrangements for CuA and CuA/Gr at different instants of indentation as indicated on the load-penetration curve.*

Fig. 5.15 shows the dislocation arrangements as well as the density of the dislocations computed in a cubic box of size 5 × 5 × 5 μm^3 for both systems at different instants of the indentation process in the case of a nucleation process triggered at 10 nm depth. The full movies are available at (http://www.numodis.fr/tridis/cugraphene.html). The dislocation densities are similar until a penetration depth of 30 nm and then the density increases a lot more in the case of Cu_A/Gr. For a penetration depth of 60 nm, the Cu_A/Gr system contains four times more dislocations than the Cu_A. There is a marked difference between the arrangement of the dislocations. The plastic zone,

corresponding to the zone with the highest dislocation density is contained in a sphere in the case of Cu_A whereas it expands as a half-sphere in the case of Cu_A/Gr with a larger volume and more delocalized plastic flow. This difference in the dislocation arrangement is correlated to the indentation force, which is found to be higher in the presence of graphene. In order to illustrate the back force induced by the dislocations on the indenter, we have plotted in Fig. 5.16 the normal component of the internal stress field generated by the dislocations as if they were in an infinite medium. This highlights the much stronger long-range field development in the case of the Cu_A/Gr system compared to Cu_A.

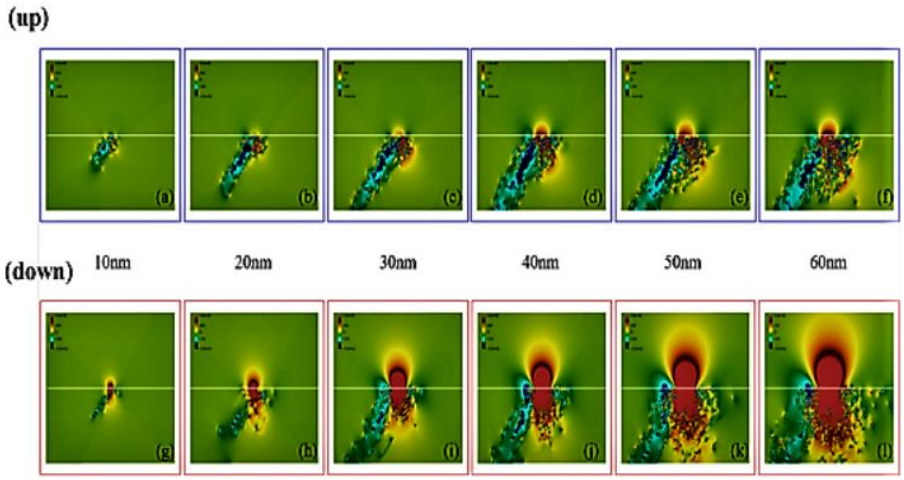

Fig. 5.16. *Evolution of the normal stress nT.σ.n with n=(111) for different indentation depths inside (up) CuA, (down) CuA/Gr; the color range is within [-500 MPa:500 MPa]. Note a higher long-range normal stress zone in CuA/Gr.*

5.4. Discussion

5.4.1. Cu_A versus Cu_A/Gr systems

The results presented in section 5.3 confirm the earlier finding described in the literature (Y. Kim et al., 2013; X. Y. Liu et al., 2016; Park et al., 2019; X. Zhu et al., 2019) that the presence of single-layer graphene affects the development of the plastic flow. The effect of the presence of graphene requires a sufficient adhesion between the graphene and the substrate and results from the very large strength of graphene, which can support extreme stresses and distortions without fracture. However, the present study brings

about both new elements of discussion, some more nuanced interpretations as well as some mitigated claims regarding the true potential of graphene to increase the strength of surfaces.

When comparing the elastic response of Cu_A and Cu_A/Gr after indentation in Fig. 5.6a, we confirm the enhancement of the load to be imposed to reach the same indentation depth for the Cu_A/Gr system, as shown in the zoom of Fig. 5.6a for penetration depths below 10 nm, before first pop-ins, and reported by other researchers (Hammad et al., 2017; Park et al., 2019). The underlying reason is, as explained in the introduction, the adhesionless contact between the tip of the indenter and the surface in the presence of graphene, and not a stiffening effect related to the high elastic modulus of graphene. The adhesion force between the tip and the surface in the case of bare Cu modifies the contact area and the load transfer. The absence of adhesion between the indenter tip and the surface in the Cu_A/Gr system makes the tip exert the entire load required to achieve the same indentation depth, leading to higher applied forces (Hammad et al., 2017).

Nevertheless, the core of this study is on the plastic response under mechanical contact. When indenting a material with a sufficiently low density of defects, the first plastic event is caused by the nucleation, glide, and an avalanche of dislocations (Corcoran et al., 1997; Gouldstone et al., 2000; Sato et al., 2019; Suresh et al., 1999). This avalanche leads to a displacement burst under load-control. A proportional relationship between the pop-in length and the critical load is expected for metals, as elaborated by Shibutani (Shibutani et al., 2007). These authors worked out a relationship showing that the pop-in length increases linearly with load because a proportional number of dislocations is required to release the increasing stored elastic energy. The linear relationship between the pop-in length and the load is not well respected in the presence of graphene (Fig. 5.6e). As shown in Fig. 5.6a and b, the presence of graphene affects the length of the pop-in as well as the onset of the first pop-in, revealing the influence of graphene on the nucleation and propagation of dislocations. The smaller pop-in length is the first evidence of the limitation of the number of dislocations participating in an avalanche in the presence of graphene. This effect of graphene has been revealed in recent literature (S. W. Chang et al., 2013; Lu Wang et al., 2018; C. Zhang et al., 2019). Furthermore, the Cu_A/Gr system never shows very large pop-ins when compared to the Cu_A system, see Fig. 5.6f–i. The effect of graphene is the same in both nanoindentation modes while the less scattered distribution of pop-in lengths under displacement-control probably results from the lack of partly uncontrolled overshoot in this later mode.

AFM mappings of Cu_A and Cu_A/Gr systems after indentation confirm the effect of graphene by showing clear differences in the topography. In the Cu_A system, the presence of a particle-like pattern (Gaillard et al., 2003) indicates the sustained activity of dislocations along the same slip planes leading to larger and sharper pile-ups around the indent, see Fig. 5.10c. In the presence of graphene, see Fig. 5.10d, there are no marked patterns around the indents, which would otherwise indicate that dislocations could escape by piercing through the surface. This leads to smoother pile-ups around the indent. The heights of the pile-ups have been measured for both Cu_A and Cu_A/Gr systems based on sections across several indents. Figs. 5.10g–h show height profiles corresponding to three sections on the indents shown in Fig. 5.10e–f which quantitatively prove the effect of graphene on the height of the pile-ups. To make it clearer, one of the profiles is shown separately in Fig. 5.10i–j for both systems. The average values of the pile-up height were measured for five different indents on both systems and are equal to 26 nm for Cu_A and 3 nm for Cu_A/Gr, respectively.

The TEM observations confirm, from another angle, the interpretation above. The micrograph in Fig. 5.11a reveals a relatively localized mode of plastic deformation under the indent for Cu_A along specific slip planes, as predicted by the DDD simulations as well. The high density of dislocations walls near the edges of the indented region is proof of the formation of pile-ups around the indents.

Even though the AFM and TEM data are obtained from indents significantly deeper than the penetration corresponding to the first pop-ins, they represent the aggregated effect associated with the accumulation of several pop-ins and plastic activity. They concur to the same message: the dislocations mobilized to accommodate the penetration of the indent are more homogeneously distributed under the indented region showing that other slip systems must be activated in the presence of a graphene barrier (Fig. 5.11b).

The DDD simulations provide quantitative explanations for these observations. The simulations show that the dislocation arrangement is completely different when comparing Cu_A with and without graphene coating (see Fig. 5.15). For the Cu_A system, the plastic zone exhibits a spherical shape while for Cu_A/Gr, the plastic volume resembles a large half-sphere. The load very much increases in Cu_A/Gr after the first plastic burst, which shows that an alternative mechanism of deformation starts at this point. Generally speaking, dislocations accumulated at an interface could lead to both directional back stress hardening and non-directional accumulation of obstacles which alleviate further dislocation motion that results in isotropic

hardening (Fribourg et al., 2011; L. Zhao et al., 2019). A detailed analysis of the internal stress field induced by the dislocations indicates that the stress component normal to the free surface has a much longer range in the Cu_A/Gr system compared to Cu_A. This can be appreciated when comparing the evolution of the internal stress at different indentation depths in Fig. 5.16 (up) Cu_A and (down) Cu_A/Gr. Therefore, large back stress builds up in the system with graphene, which forces the dislocations to glide on other slip planes, hence delocalizing the plastic activity and leading to larger plastic volume, which can be clearly seen at the indentation depth of 60 nm in Fig. 5.16 (down). In the sample with no graphene, dislocations are not stopped and can move freely towards the surface. There is only a very small back stress generation at 60 nm penetration depth, see Fig. 5.16 (up). All these results from indentation, TEM, AFM and DDD simulations confirm the ability of graphene to block the transmission of dislocations between layers but also to delocalize the dislocation activity.

Nevertheless, the DDD simulations overestimate the load increase after the pop-in has occurred. This suggests that an additional mechanism takes place in Cu_A/Gr, limiting the force increase. The discrepancy most probably comes from the partial debonding, fracture, and/or slipping observed at the Cu/Gr interface, which is not taken into account in the DDD simulations. Preliminary simulations with a stress-based adhesion criterion show indeed that debonding reduces the load after the pop-in compared to perfect adhesion. Upon debonding, dislocations are free to move out of the material and relax the load compared to an impenetrable boundary. Further works aim at addressing this question of the impact of a limited adhesion of graphene on the plasticity mechanisms.

Another observation induced by the presence of graphene is its influence on the onset of plasticity. This is probably the most unexpected result in this study. The presence of graphene causes the plasticity to start sooner when compared to the Cu_A system. Elementary linear elastic finite element simulations of a system made of a stiff coating such as graphene lying on a more compliant substrate (with a factor 10 stiffness mismatch) have been performed with the software Abaqus. We only found an extremely small increase of the maximum shear stress or of the equivalent von Mises below the indent at penetration deeper than a few nanometers, hardly explaining why plasticity could start much sooner in the presence of graphene. The second explanation for the earlier onset of plasticity could find its origin in the small roughness generated at the Cu surface in the presence of graphene (Fig. 5.10b). These perturbations could create stress concentrations that would

trigger earlier pop-ins. Nevertheless, the length scale associated with this roughness is on the order of a micrometre. The first pop-in usually occurs at indentation depth typically below 20 nm. The contact region is thus smaller than 100 nm, which is one order of magnitude smaller. Hence, the argument is not convincing either. Finally, the best explanation comes from the indirect stiffening effect induced by the adhesionless contact in the presence of graphene, as evidenced by MD simulations, and explained at the beginning of the discussion. This means that, in the Cu_A/Gr system, a higher load is required for the same indentation depth, as seen in Fig. 5.6a, for a very small indentation depth (<10 nm). A higher load leads to larger stress levels under the indent, which causes an earlier onset of plasticity in the presence of graphene.

5.4.2. Other systems

The purpose of the investigation performed on the Cu_A/Cu_N and $Cu_A/Gr/Cu_N$ systems was to shed light upon the application of graphene for reinforcing metallic systems through a composite effect associated with the insertion of hard interfaces. In this system, the graphene layer is sandwiched between two copper films having two very different grain sizes. The nanoindentation response is obviously sensitive to the specific properties of the two layers, independently of the presence or not of graphene. But, while the cap layer is the same in both Cu_A/Cu_N and $Cu_A/Gr/Cu_N$ systems, any differences in the behaviour between these two systems can be attributed to the presence of the graphene layer.

The smaller pop-in length in the case of $Cu_A/Gr/Cu_N$ compared to Cu_A/Cu_N shown in Fig. 5.7a and b reveals again the effect of graphene on dislocation glide. The comparison of the TEM micrographs for the two systems demonstrates that graphene blocks the movement of the mobile dislocations in the Cu_A substrate towards the surface, which results in large back stress (Fig. 5.12a–b). Furthermore, a higher load is required to produce the same pop-in length (hence, the same number of dislocations involved in the avalanche) in $Cu_A/Gr/Cu_N$ as graphene makes the glide of dislocations more difficult (Fig. 5.12c). From a methodological viewpoint, this sandwich structure is the most elementary stack that can be imagined to test the bulk strengthening effect of graphene. Deconvoluting the effect of graphene from the indentation curve in order to predict an expected change of yield stress for instance is not straightforward and left for future works. But, the present

results show that the approach is very sensitive to the presence of graphene and can be used to easily compare different configurations, graphene qualities, number of stacks without producing a bulk system.

There are two more findings not related to the presence of graphene but worth discussing further. The focus on the load-displacement curve of Cu_A/Cu_N in Fig. 5.8 shows several very small pop-ins before the main large pop-in in the Cu_A/Cu_N system which is connected with the high density of grain boundaries in the nanocrystalline copper. The high density of grain boundaries hinders the activity of dislocations and causes only small burst of dislocations instead of a true avalanche. The limited burst leads to the formation of only very small pop-ins during indentation (Y. Kim et al., 2013; Rupert et al., 2012) which explains also the different behaviour in terms of hardness evolution at small indentation depth in Fig. 5.9. After the elastic regime below 10 nm indentation depth, the hardness of the Cu_N is found to be ~2.5 GPa. The hardness of Cu_N moderately increases, probably due to the interaction of the plastic flow with the constrained interface with Cu_A. Further increase of the penetration leads to the burst of plasticity inside the Cu_A underneath layer, associated with a large pop-in. The hardness then converges towards the hardness Cu_A, near 1.4 GPa, with a slight, but continuous decrease with penetration associated with the indentation size effect. Assuming a ratio of 3 between the yield stress and hardness, the yield stress of Cu_N would be ~800 MPa. This value is in the expected range for 50–100 nm grain size using the Hall-Petch law parameters as established for instance in the literature (Cheng et al., 2005; N. Lu et al., 2010). The yield stress of the Cu_A film is more difficult to determine (Gertsman et al., 1994) as the response corresponds to a single crystal (for which the parameter "3" does not apply due to strain hardening and strain gradient plasticity effects) with no interaction with the grain boundaries nor with the quartz substrate for the investigated range of indentation depth which remains smaller than 1/10 of the film thickness. The important conclusion is that the strength of Cu_N is much larger than for Cu_A at least by a factor of two. Furthermore, once the plasticity has started in Cu_A, the presence of the Cu_N cap layer does not play a major role anymore in dictating the overall hardness of the system, which is similar to a bare Cu_A layer.

The other finding when comparing the Cu_A and Cu_A/Cu_N systems is the length of the first pop-in which is much larger in the Cu_A/Cu_N system. The first large pop-in occurs at higher load and higher penetration in the Cu_A/Cu_N system leading to the activation of more dislocation sources during the indentation process (Fig. 5.8). There can be three different sources of

dislocations including; pre-existing dislocations, punched-out dislocations during deformation, and threading dislocations (Dehm et al., 2018; Jian et al., 2010). In the case of annealed copper, the first displacement burst results from the full avalanche of the pre-existing dislocations and punched-out dislocations during nanoindentation when the local energy underneath and around the indenter reaches a critical value. In the case of the Cu_A/Cu_N systems, the small grain size in the nanocrystalline Cu_N cap layer prevents the development of a significant avalanche of dislocations immediately blocked by the high density of grain boundaries, confirmed also by the smooth evolution of hardness in Fig. 5.9. Very large elastic energy builds up under the indent inside the cap layer until the threshold for initiating plasticity in the Cu_A is attained. This large amount of elastic energy is released through very large pop-ins. In other words, the presence of the cap layer can be simply seen as a way to avoid any pop-in in the Cu_A substrate before a large load is reached.

5.5. Conclusion

The plastic deformation behaviour of copper upon nanoindentation has been studied for two different configurations involving a single graphene layer. The main findings of the work are the following: The pop-in length is, on average, shorter in the presence of a graphene layer, as confirmed under both force- and displacement-controlled indentation modes. As a side conclusion, we prove that the results obtained by both modes agree with one another regarding pop-in behaviour. TEM analysis of cross-sections taken below the indents shows that the dislocation activity occurs in a much larger volume and is more homogenous in the presence of graphene. This is associated with a much smoother pile-up and the absence of slip steps on the surface, as measured by AFM. 3D DDD simulations reveal that the origin of these effects is the large back stress induced by the presence of the impenetrable graphene barrier, leading to the spreading and delocalization of the plasticity process. Plasticity starts earlier in the presence of graphene compared to bare Cu, presumably due to higher stress levels associated with adhesionless contact, compared to bare Cu. Another side result of this study is the interest to look at an elementary stack made of a graphene layer intercalated under a cap layer to quantify its potential impact on the strength when inserted in the bulk of materials. In conclusion, the presence of a single layer of graphene as a coating or interlayer below a Cu cap layer modifies the plastic flow under the contact

for indentation depth much larger than the graphene layer thickness, by spreading the plasticity over a much larger volume. The impact is mainly on the pop-in behaviour and smoothing of the pile-ups. This delocalization of the plasticity can be useful for applications involving repeated contacts to mitigate the induced roughness such as in electrical switches or under mild erosion conditions where the amplitude of the induced roughness under impact is often responsible for the wear mechanism. Nevertheless, the magnitude of the effects discussed in the work is not large enough to provide significant wear or erosion mitigation with a single graphene layer in the case of severe loading conditions.

Chapter 6

Lab-on-chip application on Cu/Gr and Cu systems with Ni beam actuator

Abstract

Despite the fact that the uniaxial tensile test provides straightforward interpretable data to extract the mechanical behaviour of a material, the adaptation from bulk testing to small-sized specimen testing is not trivial. Indeed, new concerns arise such as specimen preparation, handling and mounting. In this chapter, tensile-on-chip has been performed by using lab-on-chip technique developed in UCLouvain to investigate the effect of graphene on fracture and relaxation response of Cu thin film. Ni is used as an actuator which is a rare choice for this process. The key part of the process is the sample preparation which includes: Gr growth and transfer, deposition of Cu and Ni thin film, photolithography of actuator and specimen beams as well as the release of these beams. All these steps need to be compatible and adapted to the material used as specimen and actuator. To achieve reproducible and reliable data, some sort of modifications have been performed in this work and some results have been extracted. However, Gr did not lead to a positive effect on the extracted results due to the poor adhesion of the graphene to Cu substrate as well as the negative effect of lift-off resist and XeF_2 etching on the quality of graphene. The displacement is even higher for the same load in the presence of graphene which can also result from the localized oxidation of copper underneath the transferred Gr.

6.1 Introduction

A large range of thin films systems including polysilicon, silicon nitride, different oxides and some metals are used to fabricate microelectromechanical systems and microdevices (Sharpe et al., 1997). Besides thin films, 2D layers show attractive features which make them interesting to be used in these systems (Hu et al., 2020). First, the discovery of 2D materials with weak interlayer interaction can provide more opportunities in the fabrication of ultrathin coatings and solid lubricants (Mai et al., 2019; Rosenkranz et al., 2019) that can be functional and efficient. Additionally, their ability to integrate and adhere to various substrates makes them promising materials for microelectronics (Huyghebaert et al., 2018). 2D materials are very good candidates for flexible, stretchable and foldable electronic devices due to their atomic thickness and ultrahigh flexibility (K. S. Kim et al., 2009; Rogers et al., 2010; W. Zhang et al., 2013), therefore having knowledge of their deformation and fracture behaviour is very important. The fabrication of 2D materials-based electronic devices has been investigated in a huge range of studies (Lanza et al., 2020). Excellent performance has been reported such as field-effect transistors (FETs) with on/off current ratios $>10^9$ (J. Xu et al., 2017), photodetectors with a high form factor and modulation bandwidths for communication beyond 180 Gb/s (Schall et al., 2018), and memristors with excellent flexibility, transparency, and thermal stability (M. Wang et al., 2018). In addition to the strain that can be generated naturally, it can also be intentionally induced and controlled in graphene by different techniques (Si et al., 2016). Furthermore, from theoretical and experimental points of view (Conley et al., 2013; Nayak et al., 2015), it has been observed that the electronic, magnetic and optoelectronic properties of 2D materials can be modified with strain engineering (P. Lu et al., 2012; Y. Ma et al., 2012; H. Zhu et al., 2015).

One of the important modifications that can be applied to single-layer graphene is the engineering of the bandgap under large enough strain (Choi et al., 2010; Pereira et al., 2009). As it has been investigated SLGr could be theoretically deformed up to 25% without fracture besides its high thermal conductivity (3000-5000 W m^{-1} K^{-1}), its excellent optical transparency of 98%, and an extremely high Young's modulus of 1 TPa, (Li Wang et al., 2019). During the experimental procedure, strains are expected to arise naturally in graphene. For instance, transferring graphene on a substrate

usually leads to a moderate strain due to the surface corrugations of the substrate (Teague et al., 2009) or the lattice mismatch between graphene and the substrate (Z. H. Ni et al., 2008b). To ensure the safety and functioning of these materials, a precise investigation of the mechanical properties and the underlying mechanisms is necessary for the development of new applications (Xing Li et al., 2018). To measure accurately the mechanical properties of thin films or 2D layers with very small thickness, new techniques and advanced procedures are required for sample preparation, handling, and loading (Sharpe et al., 1997).

Quantitative mechanical testing of 2D materials is extremely challenging. Nowadays, nanoindentation and atomic force microscopy are methods to extract the mechanical properties such as Young's modulus and fracture strength of 2D layers (Y. Yang et al., 2017) as has been mentioned in previous chapters. However, there are some limitations regarding the application of these methods for 2D layers. For example, films typically thinner than one hundred nanometers should not be tested by nanoindentation as the maximum indentation depth should be limited to a small fraction of the specimen thickness in order to avoid substrate effects. This fraction depends on the stiffness mismatch between the film and the substrate and can vary from less than 1% to more than 20%. Too small indented volumes are not representative of the test material and too large volumes will be affected by the mechanical response of the substrate. In addition, in the AFM technique, the loading transverse is local which can cause more uncertainties and make complexity in the extraction of the mechanical behaviour. These complexities resulted from the non-uniformity of the deformed volume as well as the distribution of non-uniform pressure on the layer which results in non-uniform tension. Generally, the easiest way to extract the mechanical properties of a material is to perform a uniaxial tensile test. In this method the deformation conditions are well known which allows us to measure the total deformation of the specimen and the data reduction is more direct.

By using the adapted tensile testing for thin films and 2D layers, the data related to both elastic and plastic properties can be extracted in a straightforward approach. Tensile tests on individual InAs nanowires were performed *in-situ* in a SEM, and their fracture strength and strain were obtained in addition to Young's modulus. They have tested the two types of nanowires and both types exhibited brittle fracture with a large elastic strain of up to ~10% and had similar fracture strength of ~2–5 GPa (X. Li et al., 2014). In other scientific report, Cao et al. directly performed in situ tensile tests in a scanning electron microscope on CVD-graphene with measured

Young's modulus around 1 TPa. They have presented the engineering tensile strength of ~50-60 GPa and the elastic strain up to ~6% (K. Cao et al., 2020). Even though, the deformation and failure mechanisms in materials at the 2D limit are of fundamental importance but have been little studied experimentally.

In this work, a recent mechanical characterisation technique developed by Gravier, Coulombier et al., in 2009 at UCLouvain (Gravier et al., 2009) has been used to apply the tensile test on samples of Cu thin films covered or not by graphene. The method for data reduction is provided in Section 6.2. The fabrication process is composed of several steps and lithographies which will be described more in detail in Section 6.3. The predicted and experimental results are presented in Section 6.4. The challenges and issues that we faced while performing the fabrication process will be discussed in Section 6.5 as well as solutions will be provided in some cases. In the last section, the conclusions are drawn.

6.2 Data analysis

6.2.1 Data reduction scheme

The principle of the tensile-on-chip (TOC) is to provide actuation through an auxiliary material under high tensile internal stress. This auxiliary material, called the actuator, is attached to the specimen thanks to adhesion. After releasing the structures based on the method that will be explained in Section 6.3.8, the only measurable quantity resulting from this release is the displacement of the actuator-specimen interface. The distance *'u'* between the cursors indicates the displacement that the specimen undergoes as a result of the release. The specimen can be extended (positive displacement) or retracted (in the rare case of a specimen pulling more than the actuator beams due to very large internal stress), however, the negative displacements are not considered. The measurement of this displacement and having knowledge of specific properties of specimen and actuator lead us to probe the fracture behaviour of the target material.

To determine the mechanical properties of the specimen obtaining its Young's modulus and its stress-strain curve is necessary. Knowing the strain and the force within the lab-on-chip structures is needed. The tensile internal stress in the actuator needs to be large enough and this stress is considered as

the initial force F_0 in the actuator beam. Different configurations of actuator beam are shown in Fig. 6.1

When the actuator is not connected to any specimen (free actuator), it contracts by an amount of u_{free} . On the other hand, the actuator is not free and it is connected to a specimen beam which prevents the actuator from being fully relaxed. Consequently, the actuator is subjected to a force F and it contracts by an amount u smaller than u_{free} as can be seen in Figure 6.1c. The measured displacements of u and u_{free} can be directly linked to force *(F)*, the actuator geometry and the material properties of the system (Eq. 6.3).

Based on the knowledge of the mechanical properties of the actuator, the force can be calculated from the displacement of the cursors, as a result, the actuator is acting as a force sensor in the lab-on-chip. The total strain in the actuator is the sum of the mechanical strain and mismatch strain which can be written as:

$$\varepsilon_a^t = \varepsilon_a^{mech} + \varepsilon_a^{mis} = \ln\left(\frac{L_{a0} - u}{L_{a0}}\right) \tag{6.1}$$

where L_{a0} is the actuator length before the release at test temperature, u is the displacement (of a constrained structure) between the position of the cursors before and after the release. ε_a^t is the total strain and ε_a^{mech} is the mechanical strain in the actuator beam after release. ε_a^{mis} is the mismatch strain of a constrained actuator beam resulting from the deposition and fabrication process.

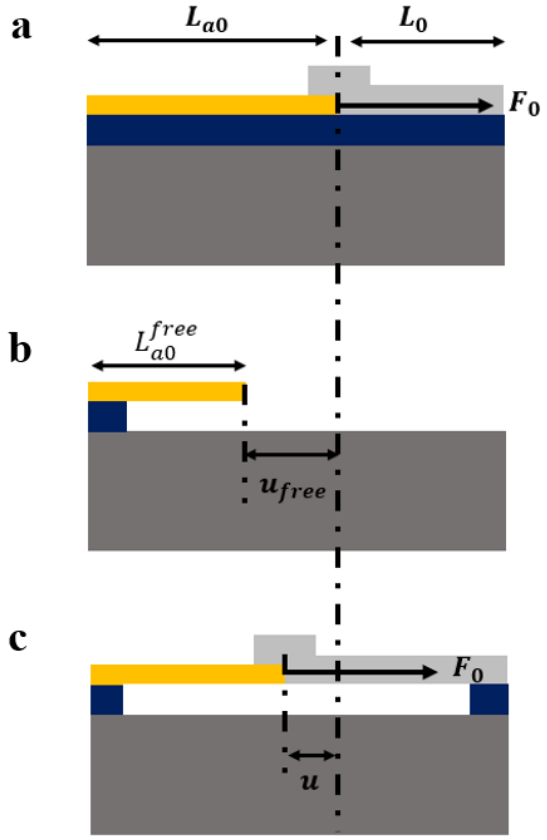

Fig. 6.1. *Different configurations of the actuator beam: (a) actuator beam is not yet released, (b) actuator beam is free to contract after the release, (c) actuator beam is constrained by a force F smaller than F0, the initial force (e.g., by being attached to the specimen beam).*

In addition, the linear elastic behaviour of the actuator is defined by:

$$\sigma_a = E_a \varepsilon_a^{mech} \tag{6.2}$$

where E_a is Young's modulus of the actuated material and σ_a is the true stress of the actuator beam after release.

In the case of the free actuator, the stress is equal to zero and $\varepsilon_a^{mech} = 0$, thus the release of the free actuator provides the value of mismatch strain. For the constrained actuator shown in Figure 6.1c, the load can be defined as:

$$F = S_a E_a \varepsilon_a^{mech} = S_a E_a \left(\frac{-u}{L_{a0}} - \frac{-u_{free}}{L_{a0}} \right) = \frac{S_a E_a}{L_{a0}} \left(u - u_{free} \right) \quad (6.3)$$

where the last equality shows that the force (F) can be estimated only through the measurement of u and u_{free}. In this equation, S_a is the cross-sectional area of the actuator beam after release.

The behaviour of the actuator in a force-displacement curve is a straight line which can be seen in Fig. 6.2. When the linear curve intersects with the horizontal axis, it provides the behaviour of a free actuator and reveals the maximum displacement. The intersection with the vertical axis represents the maximum force in the constrained actuator beam before release. As increasing the length of the actuator while keeping the width constant, the intersection of the linear graph with the Y-axis remains the same resulting from the fact that internal stress is equal for all actuators on the same chip. The linear graph moves toward larger displacements on the horizontal axis. The strain in the actuator beam is very small, the variation of the cross-sectional area can be neglected and $S_a \sim S_{a0}$.

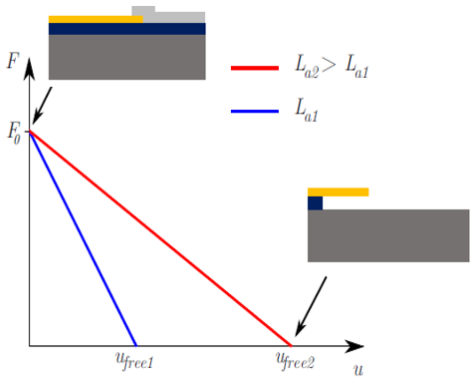

Fig. 6.2. *Force-displacement curves of actuators with L_{a1} (blue) and L_{a2} (red).*

The load F is induced by the specimen beam attached to an actuator beam in every lab-on-chip sample. The total strain inside of the specimen can be written as:

$$\varepsilon = \varepsilon^{mech} + \varepsilon^{mis} = \ln\left(\frac{L_0 + u}{L_0} \right) \quad (6.4)$$

where ε and ε^{mech} are total and mechanical strains in the specimen beam after release, respectively. ε^{mis} is the mismatch strain in the specimen beam due to the deposition and fabrication process. u is the imposed displacement after release. In the latter equation, the small strain assumption is not made as the specimen can undergo large strains in the case of testing a ductile material. This results in the calculation of the mechanical strain inside the specimen beam by measuring the values of u and ε^{mis}.

The stress in the specimen beam is calculated simply from face equilibrium as:

$$\sigma = \frac{F}{S} = E_a \frac{S_a}{S}\left(\frac{-u}{L_{a0}} - \varepsilon_a^{mis}\right) \tag{6.5}$$

To analyse the mechanical behaviour of the specimen material, Eq. 6.4 and Eq. 6.5 are the most important ones as they provide the stress-strain response of the specimen beam. The same as in the case of the actuator beam, the behaviour of the specimen beam can be extracted from the force-displacement curve as can be seen in Fig. 6.3.

Figure 6.3 represents the force-displacement curve of a ductile material. At zero displacement, the force-displacement graph begins. The force at zero displacement cannot be zero resulting from an internal force in the specimen beam due to the deposition and fabrication process. By increasing the displacement, the force increases linearly due to the elastic behaviour of the material. When plastic deformation starts the slope of the curve starts to decrease as a result of dislocation and defects propagation. The plastic localisation occurs when the force reaches the maximum value. Afterwards, the force decreases till the fracture of the specimen beam. As it is mentioned, the displacement u is zero before release. In this condition, there is the maximum force inside the actuator and the minimum inside the specimen beam. While performing the release process, the displacement of the specimen increases till it reaches the intersection point between the two characteristic curves. This point is the equilibrium point where the force inside the specimen beam is equal to the force in the actuator beam.

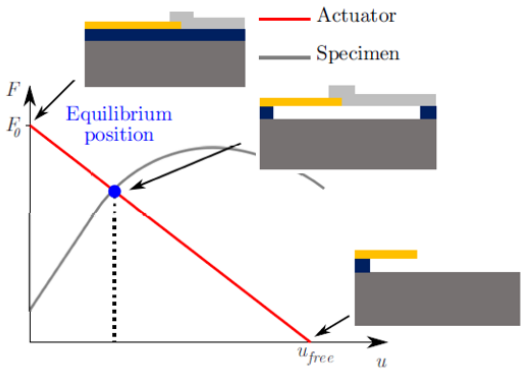

Fig. 6.3 *Force-displacement curves of the actuator (red) and specimen (grey) beams.*

6.3 Fabrication process

Several technical and processing issues have to be addressed to investigate the effect of graphene on the stress-strain curve and fracture behaviour of Cu film. The schematic of the process steps is shown in Figure 6.4 and the process flow of these devices can be described as follows:

1. Silicon wafer selection
2. Deposition of the specimen material on the Si substrate
3. Gr-transfer with modified wet-PMMA transfer approach
4. Patterning the specimen thin film (includes Cu and Gr) into beams using photolithography and etching (oxygen plasma and wet etching)
    a. Spin coating of the positive resist and prebake
    b. Patterning of the specimen beams
    c. Post-exposure baking and using the developer to remove the exposed parts of the resist
    d. Etching graphene with oxygen plasma
    e. Etching Cu in APS (Ammonium per sulfate-wet etching)
5. Patterning the Ni thin film into beams using photolithography and lift-off
    a. Spin coating of the negative resist and prebake
    b. Patterning of the actuator beams
    c. Post-exposure baking and using the developer to remove the unexposed parts of the resist
6. Deposition of the actuator material (nickel) thin film
7. Lift-off of Ni (in acetone)

8. Release of the structure with XeF_2 (gas phase etchant)

Every step and material must be selected in a way to avoid damaging the graphene during processing.

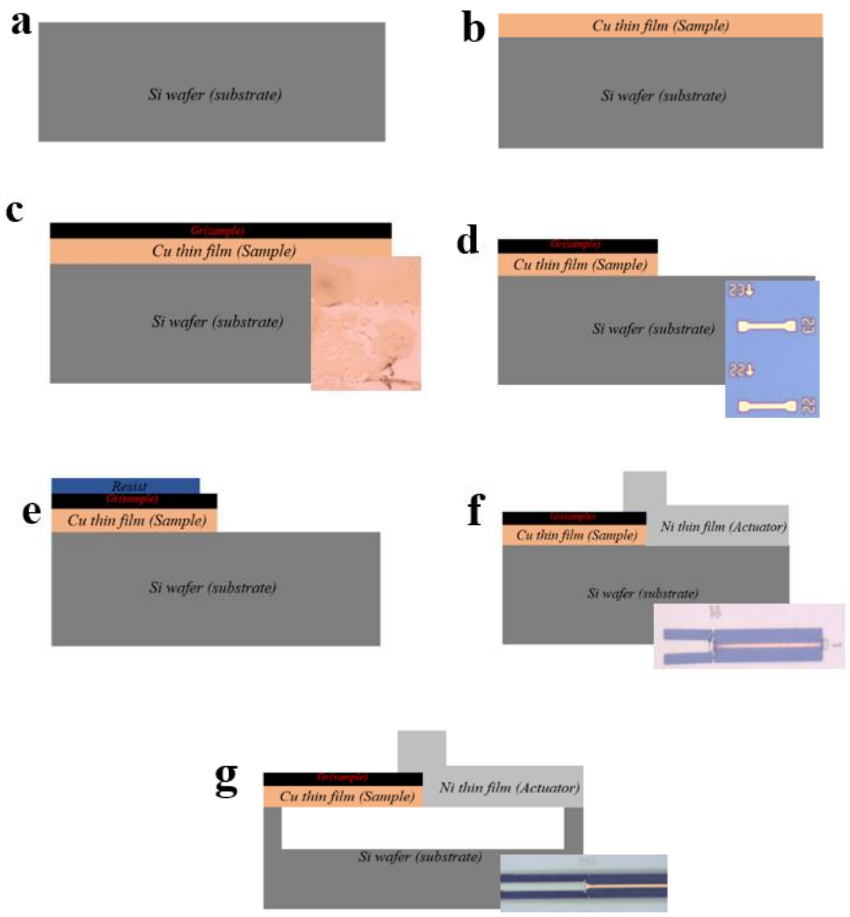

Fig. 6.4. *Schematic of the fabrication process steps of Cu/Gr tensile lab-on-chip (TOC): (a) selection of the Si wafer; (b) deposition of the Cu thin film; (c) Gr transfer; (d) patterning of Cu/Gr in the form of the specimen beams with positive photolithography; (e) patterning the actuator beams with negative photolithography; (f) deposition of Ni thin film and lift-off of Ni; (g) release of the TOC with XeF_2 etching.*

6.3.1 Wafer selection

Silicon wafers of 3 inches in diameter polished on the front face have been used as a substrate for the fabrication of the TOC in WINFAB. The wafers are monocrystalline silicon, and the thickness is around 380 µm. To calculate the internal stress in the deposited layers on the wafers, it is important to select wafers with monotonic curvature (Boé et al., 2009). The schematic of the preferred monotonic curvature of silicon wafers is shown in Figure 6.5. To determine the curvature of the wafer, the profilometer tip is running along the axis of the wafer. In order to calculate the internal stress in the deposited film, a curvature measurement is performed before and after each film deposition. The change in curvature before and after film deposition is linked to the internal stress arising in the film which can be calculated through the well-known Stoney equation:

$$\sigma = \frac{1}{6}\frac{E_S}{1-\vartheta_S}\frac{t_s^2}{t_f}\left(\frac{1}{R_{post}} - \frac{1}{R_{pre}}\right) \tag{6.6}$$

where σ is stress in the film, $\frac{E_S}{1-\vartheta_S}$ is biaxial modulus of substrate material, t_s and t_f are thicknesses of the substrate and the film, respectively. $\frac{1}{R_{pre}}$ and $\frac{1}{R_{post}}$ are initial and final curvatures of the substrate.

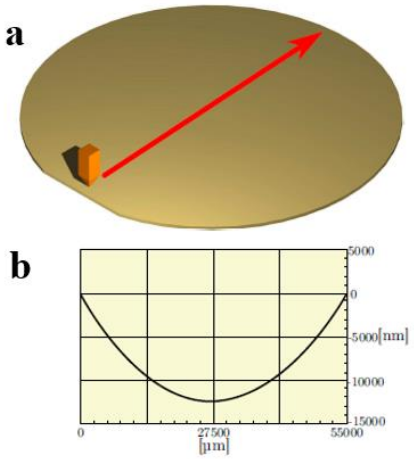

Fig. 6.5. *Schematic of (a) curvature measurement performed with a profilometer; (b) monotonic profile.*

6.3.2 Standard cleaning

The so-called standard cleaning is used to remove any contamination or oxidation on the Si wafer that could influence the process. This process is almost the same for all fabrications on chips and follows the standard procedure defined within WINFAB (UCLouvain cleanroom). The process contains two baths of Piranha solution which is a mixture of sulfuric acid (H_2SO_4) and hydrogen peroxide (H_2O_2) and a bath of 2% hydrofluoric acid (HF). Piranha acts as a strong oxidizing agent which can dissolve most organic matters. After rinsing the wafers in DI water, 2% HF solution is used for 15 s to remove the oxide layer on the silicon (SiO_2) and then the wafer is rinsed in different baths of water and dried in the centrifuge.

6.3.3 Deposition of Cu

The Cu film is deposited by electron beam evaporation of 99.999% pure Cu pellets (Kurt J. Lesker) on Si wafers of 3-inch. The process has been explained in Section 3.4. The 80 nm-thick Cu film is deposited at room temperature with 2 Å/s under a base vacuum of about 2×10^{-7} mbar. In order to get a homogeneous thin film of copper with almost the same thickness all over the Si wafer, the "rotate" mode of the electron beam evaporation method has been chosen for this step. The value of internal stress of the deposited Cu film is very important for the data reduction of the tensile lab-on-chip structures. An extra wafer is added to the chamber for the same deposition process as the target wafer in order to measure the internal stress in the deposited Cu film.

6.3.4 Gr transfer

The modified version of the PMMA-wet-transfer method mentioned in Chapter 3 is used to transfer the graphene sheet on Cu film. As has been previously mentioned, the modified PMMA-transfer not only is more functional in the case of transferring graphene on cavities, it is also more reliable in this case as it reduces the oxidation of the Cu surface underneath graphene. While using the classic PMMA-wet transfer and fishing graphene from water with the target substrate, water accumulation between graphene and Cu surface causes fast oxidation of the Cu surface. However, using the modified version of transfer reduces oxidation significantly.

6.3.5 Specimen beam patterning

The patterning of the specimen layer is processed by positive lithography. The principle of this approach is explained in Section 3.5. This process follows four different steps as shown in Figure 6.6.

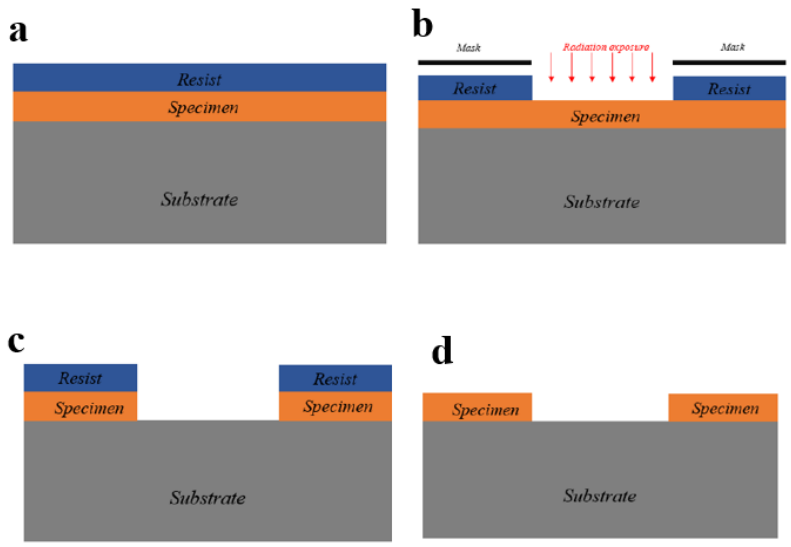

Fig. 6.6. *Schematic of positive photolithography steps: a) spin-coating of the positive resist on the Cu film; b) Patterning of the photoresist by exposing it to UV light; c) removal of the parts of the sample which are not protected; d) removal of the remaining parts of the photoresist.*

A positive photoresist (Az Mir 701, Micro Chemicals) is spin-coated on the Cu film-covered wafer for the patterning of the specimen beams. Before spin-coating the resist on the wafer, it is placed in an LPIII oven for surface treatment with HDMS (hexamethyldisilazane) process at the temperature of 120°C for around 30 min. This step improves the adhesion of the photoresist on Cu film as it modifies the surface of the thin film. After spin-coating the photoresist, it is baked for 90 s at 110°C, this also improves the adhesion of the photoresist to the Cu film. After prebaking, the photoresist is exposed to a pattern of UV light using the "specimen2020 mask". This mask is transparent where the light must modify the photoresist, and opaque where the resist needs to be intact. In order to have a good resolution of the patterned structures, vacuum contact has been used and suitable exposure doses are required to be chosen. These parameters can change based on the resist, the type of material on the wafer, and the mask.

After post-exposure bake, the exposed parts of the positive photoresist are dissolved in a TMAH (Tetra Methyl Ammonium Hydroxide)-based solution called developer. In the next step, the removal of unprotected parts of graphene and copper is done by oxygen plasma and APS etchant, respectively.

The thickness of copper was around 80 nm and it took around 30 s to be etched completely by wet etching in APS etchant. In the last step, the dissolution of the remaining photoresist on the wafer is performed by immersing the wafer in acetone at 60°C for 30 min to make it ready for the next step.

6.3.6 Actuator beam patterning

For patterning the actuator beams of the on-chip test specimens negative lithography is used. For this part, a negative photoresist (nLOF 5510, Micro Chemicals) is deposited on the patterned part of the wafer. The photoresist is patterned in a way that after exposure and using the developer, the lift-off resist stays on the parts of wafers that no actuator is supposed to stand. This lithography is almost similar to the positive one and follows four steps which are represented by a schematic in Fig. 6.7. The same surface treatment process in LPIII has been performed before spin-coating the negative resist to improve the adhesion of the resist to the wafer.

After LPIII process, the first step is the spin-coating of the negative photoresist on the wafer followed by a prebake at 110°C for 90 s. Then the photoresist is exposed to UV light at a defined dose. The mask that is called "actuator2020 mask" is used for this step. After the exposure, the post-bake is performed and the developer will remove the soft and unexposed parts of the photoresist. In negative photolithography, the exposed portions underneath the transparent parts are resistant to the TMAH developer and the unexposed portion can be dissolved by the developer. Afterwards, the wafer is ready for the deposition of a thin film of Ni which is performed by electron beam evaporation and is explained in more detail in the next section. The final step is the lift-off of Ni in acetone at 60°C for several hours. The parts of Ni film which are placed on the photoresist are removed as a result of the dissolution of the photoresist underneath and the actuator beams remain intact.

6.3.7 Deposition of Ni

The Ni film which acts as the actuator part is deposited by electron beam evaporation (the same approach which has been used for Cu deposition) of 99.999% pure Ni pellets on 3-inch wafer which is already patterned with specimen beams. In this case, lift-off mode of the deposition is chosen based on the explanation given in Section 3.4. The 100 nm-thick Ni film is deposited at room temperature with 2 Å/s under a base vacuum of about 2×10^{-7} mbar. After covering the wafer with Ni thin film (the vertical edges of the photoresist are not covered as it is lift-off mode), the lift-off process is then performed to remove the parts of Ni which are placed on the negative resist and the remaining parts of the Ni film shape the actuator beams.

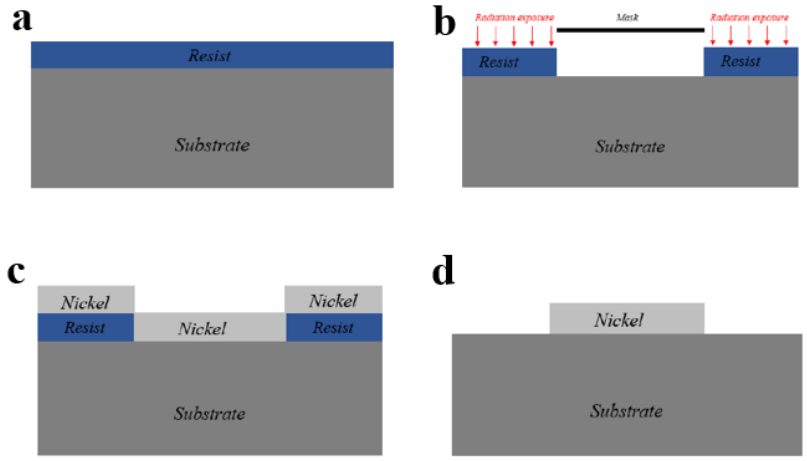

Fig. 6.7. *Schematic of negative photolithography steps: a) spin-coating of the negative resist; b) patterning of the photoresist by exposing it to UV light and removal of the protected parts of the resist with the developer; c) deposition of Ni; d) lift off of Ni.*

After completing the fabrication process, the wafer contains all the necessary structures to extract the strain-stress curve of the specimens. Figure 6.8 represents the layout of the wafer when it is fully fabricated as well as different parts of the test structure.

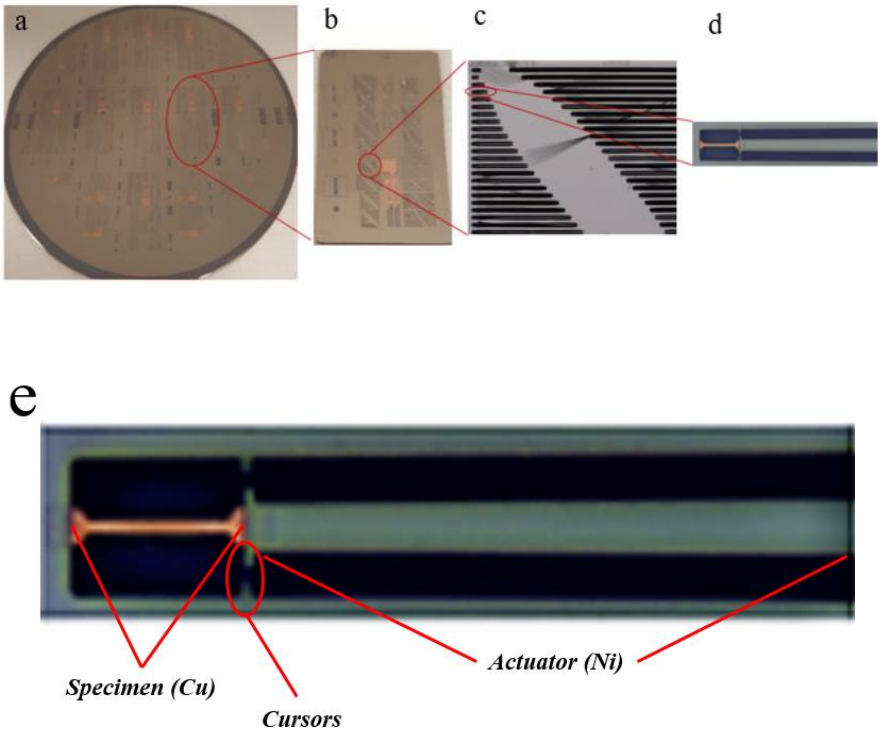

Fig. 6.8. *Layout of the wafer (mask 2020); a) wafer level; b) die level; c) instance level; d) test structure; e) different parts of test structure including Ni actuator, Cu specimen and cursors.*

6.3.8 Release process (XeF_2 dry etching)

The last step of the fabrication process is the release of the structures when the silicon substrate underneath the samples is etched by XeF_2 in the gas phase. The reaction that takes place is as follows:

$$2XeF_{2(g)} + Si_{(s)} \rightarrow SiF_{4(g)} + 2Xe_{(g)} \qquad (6.7)$$

The etching rate of monocrystalline silicon by XeF_2 is 460-700 nm/min. The apparatus used for dry etching contains three chambers: a chamber that contains XeF_2 crystals at atmospheric pressure, the expansion chamber and the etching chamber. The sample is placed in the etching chamber which can be evacuated to P = 10 Pa. To deliver a pulse of gas to the sample, the expansion chamber is evacuated and brought into contact with the chamber

containing the XeF_2 crystals, at atmospheric pressure. The pressure in both chambers drops below the vapour pressure of the XeF_2, allowing some of the crystals to sublime. The gaseous XeF_2 flows into the expansion chamber. The time and the pressure of the XeF_2 gas inside the chamber can be programmed. After making sure that all TOC are released, the evacuation of the system is done by purging N_2 gas inside the chamber. As the etching power of XeF_2 is high, the use of several small pulses of XeF_2 around 100 Pa for 10 s is recommended

In the lab-on-chip process, the gas diffuses underneath the structures from both sides as a result the etched distance needs to be half-width of the actuator to release the samples completely. The maximum width of the structures is 15 µm. After release, the silicon underneath the structures turns black due to the change in its morphology (rough and porous morphology) which reflects the light in all directions. The morphology of Si underneath lab-on-chip structures can be seen in Fig. 6.9 representing the self-actuated Cu structure.

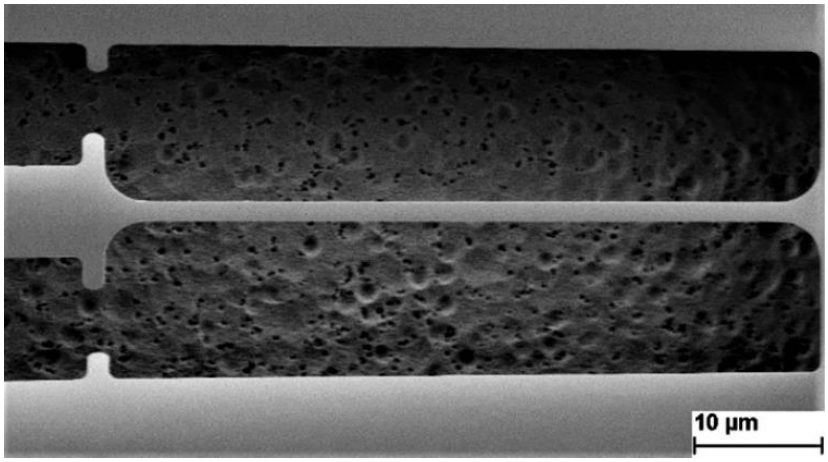

Fig. 6.9. *SEM image of self-actuated Cu lab-on-chip, it shows the roughness of the Si substrate underneath the structure after XeF_2 release.*

It is important to note that for the structures containing Cu, it is necessary to pump the device for 4 to 5 hours before starting the etching process to make sure there is no water in the system. When there is water in the system, the following reaction can take place and the produced HF can damage the Cu structures. In this work, the structures are more sensitive to the produced HF, as Ni has been used as an actuator and HF can damage Ni beams as well.

$$2H_2O + 2XeF_2 \rightarrow O_2 + 2Xe + 4HF \qquad (6.8)$$

6.4 Results

6.4.1 Expected results of Cu/Gr tensile-on-chip (TOC)

Two approaches can be considered to predict the expected results of tensile on chip on Cu/Gr specimen. The first simple approach is to consider a specimen fabricated by the superposition of two materials with different mechanical properties. The second approach is to consider not only the simple superposition but also the possible interactions between the layers.

Based on the first approach, with the actuation of Cu/Gr specimens, both materials are subjected to the same strain and both represent their internal stress. As the theoretical Young's modulus of pristine graphene is 1 TPa, and as it is much higher in comparison to Cu, it is expected that Cu is reinforced in the presence of graphene coating. As a result, it is expected that a Cu/Gr specimen will deform less than a beam of pure Cu. It has been calculated theoretically, by considering the balanced force established of released test structures with and without the graphene layer, as well as by measuring the displacement *u* at equilibrium. The left part of the equation is the force of the actuator, which should be equal to the sum of the force in the copper layer and the graphene sheet.

$$S_a E_a \left(ln\left(\frac{L_{a0}-u}{L_{a0}}\right) - \varepsilon_a^{miss} \right) = S_{s,Cu} E_{s,Cu} \left(ln\left(\frac{L_{s0}+u}{L_{s0}}\right) - \varepsilon_s^{miss} \right) + S_{s,Gr} E_{s,Gr} \left(ln\left(\frac{L_{s0}+u}{L_{s0}}\right) \right) \quad (6.9)$$

where S_a, $S_{s,Cu}$ and $S_{s,Gr}$ are the cross-sectional areas of the nickel actuator, of copper and graphene, respectively. $\varepsilon_a^{miss} = 0.0035$ is the mismatch strain of Ni actuator and $\varepsilon_s^{miss} = 0.0009$ is one of Cu specimens. There is no mismatch in the graphene sheet resulting from the lack of internal stress. $E_a = 214\ GPa$, $E_{s,cu} = 130\ GPa$ and $E_{s,gr} = 1000\ GPa$ are the Young's moduli of nickel, copper and graphene, respectively.

For example, a nickel actuator of 105 nm-thick and 14 µm-wide and the Cu specimen beam of 70 nm-thick and 4 µm-wide, with no graphene or in the presence of graphene with the same dimensions and about 0.3 nm thickness can be chosen. By considering a TOC structure, with the actuator and specimen length equal to $L_{a0} = 1000\ \mu m$ and $L_{s0} = 100\ \mu m$, respectively. The displacement (u) can be determined by solving equation 6.9 while the forces

are in equilibrium in the test structure. Numerically solving the equation resulted in a displacement of 1580 nm and a force of 0.603 mN for the specimen with no graphene. For the Cu coated Gr, the values for displacement and force are equal to 1553 nm and 0.612 mN, respectively. As expected, the presence of graphene decreases the computed displacement by 27 nm. This result has been obtained for an actuator of 1000 µm-long. For shorter actuators, the difference will be less.

The second approach is considering the interactions between two materials and the effect on plastic deformation. Based on the results that have been achieved in this work from nanoindentation on Cu/Gr samples, Gr can have a reinforcing effect when it is used as a coating on Cu thin film. As it is mentioned, Gr can act as a barrier to the movement of the dislocations and it can limit their propagation. In the presence of Gr, dislocations cannot escape through the surface of the copper layer, as a result, their concentration inside the Cu film increases. Accumulation of dislocations inside the film reduces the possibility of the dislocations moving freely which makes it necessary to apply a higher load in order to deform the specimen. In addition, the prevention of dislocation movements causes strain hardening inside Cu thin film. This means that graphene could significantly impact the creep and relaxation rate of copper thin films. Consequently, less displacement in the specimen for the same level of force and less relaxation during the time is expected in the presence of graphene.

6.4.2 Results of Cu and Cu/Gr TOC

By using the fabrication process that has been described in the previous section, the wafers containing TOC of Cu and Cu/Gr specimen beams have been fabricated. To extract the results, the beams with more promising characteristics regarding the presence of high-quality graphene, the better quality of lift-off process and the absence of photoresist residue have been analysed. Both Cu beams and Cu/Gr ones are on the same wafer, as a result, they have experienced the same process. Therefore, all parameters such as mismatch of copper, mismatch of nickel, as well as thicknesses and widths are the same. Several free beams structures of the copper/graphene specimen beams were measured and the mismatch strain of 0.0043 for the nickel actuator and 0.0009 for the copper specimen were computed. Figure 6.10 shows the force-displacement curves of Cu and Cu/Gr specimens actuated by Ni beams on the same wafer. As it can be seen, the results are not in agreement

with what was expected in the presence of graphene. For the same load, the Cu/Gr specimen shows higher displacement and the specimen beams were broken at a smaller imposed load. In addition, the maximum strain is lower in the case of the Cu/Gr specimen (~1.3%) in comparison to Cu specimen (~5%), as can be seen in the stress-strain curves of Cu/Gr and Cu shown in Fig 6.11a and b. These results indicate that graphene does not play a significant role regarding the strengthening effect or acting as a barrier against the movement of dislocation in this system. This can result from poor adhesion of graphene on Cu substrate as a result of transferring as well as the deterioration of graphene quality after contacting with negative resist or/ and XeF_2 gas. Not only the maximum strain has not improved in the presence of graphene also it decreases. This can be the result of the Cu oxidation underneath graphene after transfer. In the presence of graphene, the quality of the TOC structures can be affected by different parameters such as negative resist, the fluorination of graphene, poor adhesion between graphene and Cu and the localised oxidation of Cu underneath graphene even with using the modified version of PMMA-transfer. All these factors will be discussed in more detail in the next section.

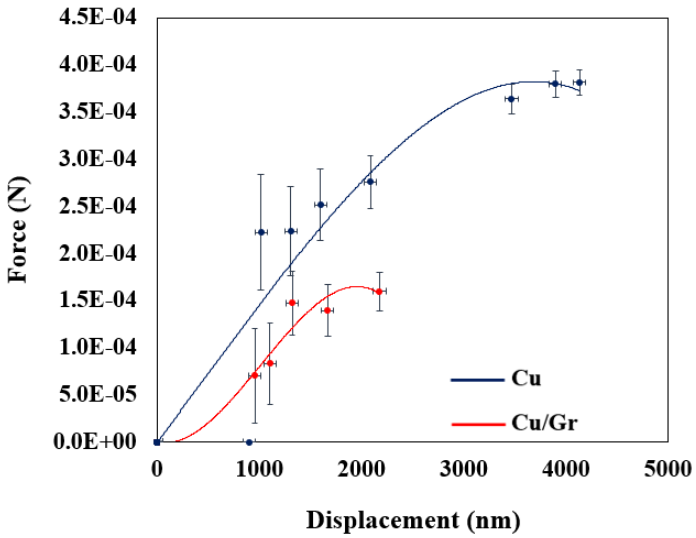

Fig. 6.10. *Comparison of force-displacement curves of Cu and Cu/Gr specimen on the same wafer with a width of 2.5 µm with Cu thickness of 70 nm.*

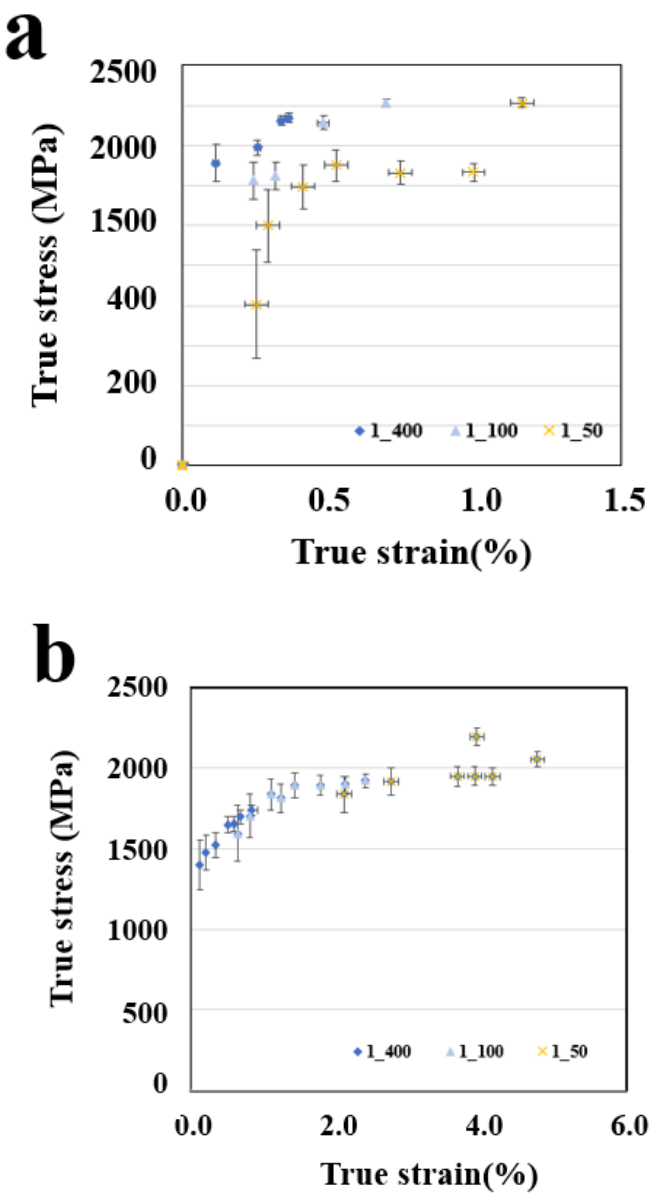

Fig. 6.11. *Comparison of force-displacement curves of Cu and Cu/Gr specimen on the same wafer with a width of 2.5 µm. In the legend, 1 means the first measurments that have been done on these samples and 50, 100 and 400 are the length of the specimen in micrometer.*

6.5 Challenges and perspectives in testing Cu/Gr specimens

6.5.1 Material selection for actuator beams

In this section, we explain why the unusual choice of Ni actuators was made.

Till today, the most optimum choice for the actuator material by the UCLouvain team was the low-pressure chemical vapour deposited (LPCVD) Si_3N_4. Different characteristics of Si_3N_4 that lead it to be the most proper candidate for actuator beams are; first, the biaxial internal stress is about 1 GPa regardless of its thickness which provides enough mismatch strain to relax and pull on the specimen beams. In addition, the deposited film possesses very good uniformity regarding the thickness as it varies around 1 nm over a 3-inch wafer. After deposition, curvature measurement does not change during the time which shows its stable microstructure and the absence of any form of stress relaxation. The mechanical properties of LPCVD Si_3N_4 can be described completely by its Young's modulus and its fracture strength as it is an elastic isotropic brittle material. Its Young's modulus has been measured at around 270 GPa by nanoindentation.

In this work, the test material is Cu coated graphene, the initial interest was to use LPCVD Si_3N_4 as the material for the actuator beam. In the case of using LPCVD Si_3N_4 as actuator beams, the fabrication process can be performed as follow:

1. Silicon wafer selection;
2. Deposition of the Si_3N_4 on a Si substrate;
3. Patterning the Si_3N_4 film into the actuator beam by means of photolithography and etching;
4. Cu deposition by electron beam evaporation;
5. Gr-transfer with modified wet-PMMA transfer approach;
6. Patterning the specimen thin film (includes Cu and Gr) into beams employing photolithography and etching (oxygen plasma and wet etching);
7. Release of the structure with XeF_2 (dry etching).

As it has been mentioned, the Si_3N_4 actuator material is the most optimum choice as a result of its well-known mechanical behaviour and the constant value of its internal stress and no relaxation. Despite these advantages, there are some limitations which lead us to use Ni thin film as an actuator material.

By using Si_3N_4 as the actuator, the most important issue that can be faced is the position of graphene in the structure. It has been mentioned that

graphene needs to be transferred on Cu substrate in the lab-on-chip fabrication and based on the fabrication steps when using Si_3N_4 as an actuator, graphene is the most top layer. The adhesion between the transferred graphene and Cu substrate is not adequate due to the nanocrystalline Cu surface which causes graphene to not conform well on the surface. Poor adhesion between graphene and Cu leads to sliding and delamination of graphene.

There are three options for dealing with this problem such as (i) transferring graphene underneath of copper instead on top of it, (ii) using overlap marks on the interface between actuator and specimen, or (iii) changing the material of the actuator to some material which can be deposited after specimen.

It needs to be considered that performing any characterisations with RAMAN or SEM on graphene is impossible when transferring graphene underneath copper. This results in the absence of information about the quality of graphene which acts as the specimen, for instance, graphene can be delaminated because of poor adhesion to copper and it cannot be detected.

Using overlap marks which can act as glue to keep graphene attached to the surface on the interface of actuator and specimen, requires the design of a new mask and makes the process more complicated as it leads to the third lithography. As a result, the last option, changing the material of the actuator has been selected.

The Cu coated Gr specimen can be easily oxidized or burnt if subjected to high temperatures. As a result, a material should be chosen that can be deposited at room temperature which also helps to change the order of the fabrication and deposit the actuator at the end of the fabrication process. In this way, the actuator is placed on the specimen which can protect graphene from sliding. Several tests have been carried out in WINFAB by other researchers (Dr. Romain Tuyaerts), with platinum, palladium and nickel as actuators. In addition, it has been mentioned that the adhesion between the specimen and the actuator can be improved when using metallic actuators instead of Si_3N_4. As an example, in the case of graphene, nickel actuators seem to have a higher adherence than silicon nitride.

Nickel thin film deposited by electron beam evaporation was eventually selected as actuators. The internal stress in nickel thin film deposited in the mentioned conditions in Section 6.3.7 is around 500 MPa which is high enough for performing lab-on-chip and it is not too high to cause delamination and cracking. In addition, nickel thin films are compatible with the XeF_2 process. The major disadvantage of metallic actuators is their mechanical properties. It has been observed that for Ni actuator stress relaxation can occur

after a few days. Although the relaxation is not very significant, it can be effective on the extracted results from TOC. In addition, when the mechanical properties of the actuators are not well known, the evaluation of the stress inside the samples is not possible. However, the main purpose of this work is the comparison of fracture behaviour of Cu thin film with and without graphene, these disadvantages can be neglected to some extent. Considering that both Cu and Cu/Gr specimens are subjected to the same conditions.

6.5.2 Poor adhesion of transferred graphene on Cu thin film

In order to avoid transferring the graphene on Cu film and preventing the poor adhesion between Gr and Cu, as-grown CVD graphene on Cu thin film could be considered. However, the growth of graphene on Cu film which has been used to fabricate the TOC was not possible due to two main reasons.

The first challenge resulted from the difficulties in maintaining the Cu film's physical integrity at the high temperature (Huet & Raskin, 2017). Therefore, a copper thin film with a thickness of less than 1 μm cannot be utilized to grow graphene in CVD-furnace. During the CVD process at high temperatures, the degradation of Cu occurs resulting from evaporation losses (A. L. Lee et al., 2015) and dewetting (Ismach et al., 2010). Consequently, when the thickness of Cu thin film is very small, Cu grains detach from each other and form Cu droplets. Another problem regarding Cu is interdiffusion with the underlying substrate at high temperatures (Howsare et al., 2012). In this work, the substrate that is used for Cu thin film is Si. At high temperatures, Si acts as a sponge and it causes the formation of copper silicide and it cannot act as a catalytic substrate for graphene production anymore. In addition, Si substrate causes contamination inside the CVD furnace.

As a result, Gr needs to be transferred on Cu thin-film with the optimum thickness for the TOC. The transfer of graphene on Cu film leads to poor adhesion between graphene and Cu substrate which causes difficulties in the TOC process and causes large uncertainties in the extracted results from force-deflection curves after release. The significant delamination of the graphene layer occurs after removing the PMMA in acetone which is shown in Fig. 6.12a. In addition, in some cases after release, the structure has been detached at the interface between the actuator and the specimen (see Figure 6.12b). While this issue has not been observed on the samples which contain Cu as the specimen with no graphene and it has proven that Ni has good adhesion regarding the graphene specimen (Sahar Jaddi has performed TOC of

graphene with Ni actuators), this issue can result from the good adhesion of graphene to Ni and its poor adhesion to copper. Graphene can attach to the Ni actuator and delaminate from the copper surface when the stress increases and high strains achieve.

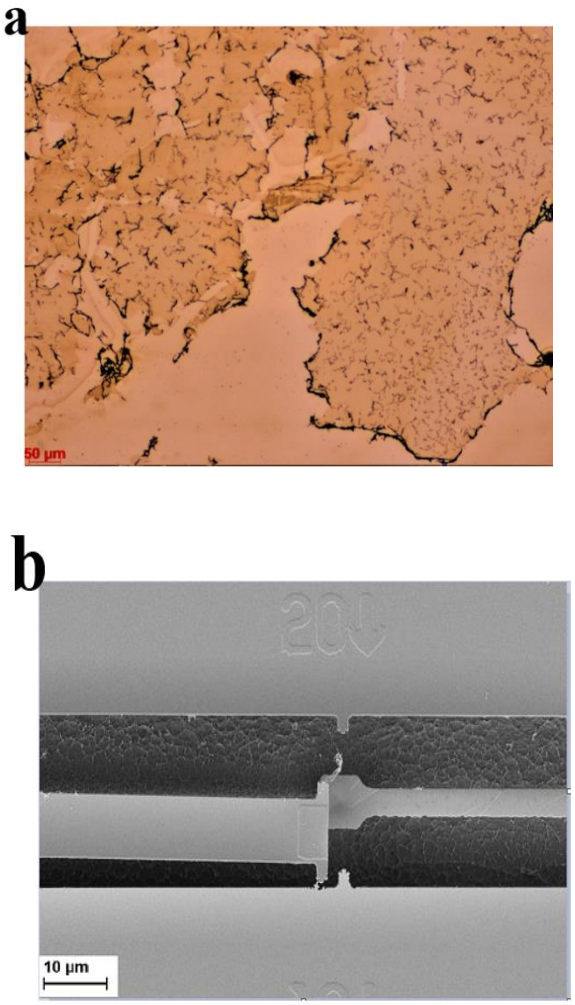

Fig. 6.12. *a) Delamination of transferred graphene on copper after removing PMMA. Black lines are rolled graphene; b) adhesion issue between nickel actuator (on the left) and Cu/Gr specimen (on the right).*

One of the approaches to decrease the risk of delamination is by modifying the PMMA-removal process. To improve the adhesion, the wafer has been heated at 60°C before removing the PMMA (as PMMA act as a protective layer) for some minutes. The higher temperature cannot be used for two main

reasons; a thin film of Cu can be oxidized very fast and PMMA gets stiffer and its removal is more difficult. After short heat treatment of the sample, fresh PMMA has been added and dried on the heater. Finally, the sample was placed in the hot acetone at 60°C to remove the PMMA. The delamination decreased after performing this treatment and it can be seen in Fig. 6.13.

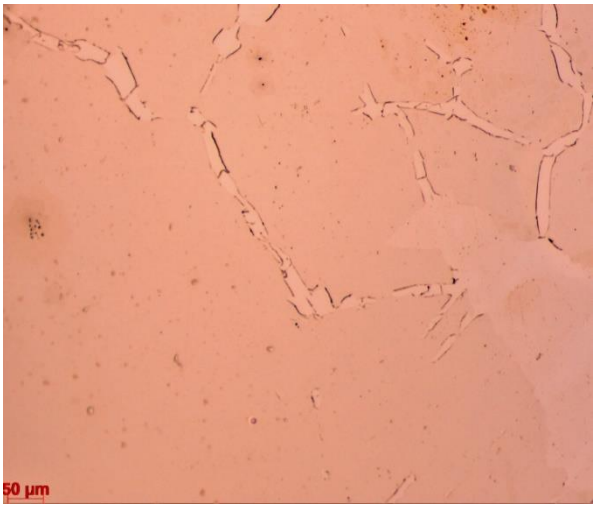

Fig. 6.13. *Less delamination has been observed after modifying the PMMA-removal step.*

There are other suggestions to improve the adhesion. For example, by reducing the roughness of the host substrate used for graphene production during CVD process. As graphene follows all the traces on the host surface, so less roughness and grain boundaries lead to more flat graphene which results in better adhesion behaviour to the target substrate (Huet et al., 2020). In addition, paraffine pastilles can be used instead of PMMA. Recent studies proved that the adhesion of graphene on nanostructured substrates can be improved by using paraffine (Leong et al., 2019). There are two reasons that paraffin can improve the quality of graphene transfer and adhesion: first, its simple unreactive chemical structure makes it easy to be removed and second its thermal expansion coefficient is quite high. For instance, by heating the graphene sample protected by paraffine at 40°C, the paraffin layer experiences thermal expansion which results in the stretching of the graphene film and the effective reduction of graphene nonuniformity such as ripples and wrinkles (Leong et al., 2019).

6.5.3 Negative effect of lift-off resist on graphene

The other problem that is faced during the fabrication process of TOC of Cu/Gr beams is the degradation of graphene after negative photolithography. It seems that the adhesion between graphene and the negative resist is so strong that most of the graphene is delaminated or broken after the lift-off process. As graphene is transparent, there is no contrast when transferred on Cu substrate. Therefore, probing graphene on Cu with microscopy techniques is difficult. However, RAMAN spectroscopy makes it possible to investigate the presence of Gr and its characteristics. In this case, before negative lithography and after the lift-off, the structures have been investigated by RAMAN spectroscopy. Before negative lithography, the graphene can be detected easily with RAMAN spectroscopy but after the process, the detection of graphene was difficult on the beams except on some spots.

There is an approach that can help to diminish the destructive effect of the negative resist on graphene and it is using an interlayer between graphene and negative resist which is compatible with both graphene and the resist. In this regard, two kinds of interlayers have been used including a very thin layer of PMMA and the positive resist (Az Mir 701, Micro Chemicals) both resists show compatible behaviour regarding graphene. However, the problem has not been solved with either of the mentioned resists as interlayers. When PMMA is applied as an interlayer, a severe interaction occurs between the negative resist and PMMA. Fig. 6.14 represents the side products of this interaction which are star-shape on the surface.

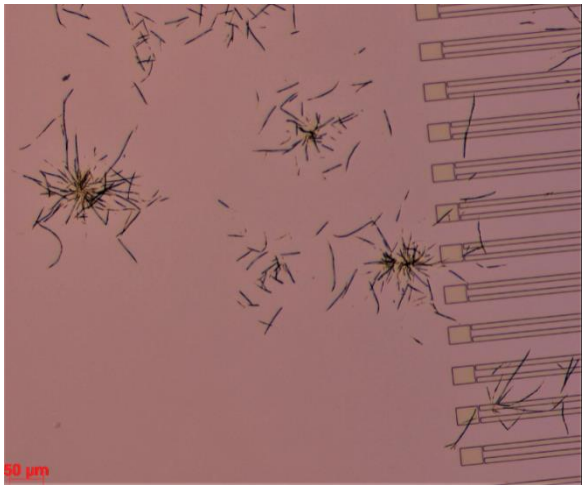

Fig. 6.14. *Side products on the wafer after using a thin layer of PMMA as an interlayer between graphene and negative resist.*

On the other hand, the deposition of the positive resist as an interlayer causes the intermixture of positive and negative resists and based on the observation, the properties of the negative resist are dominant. There is another category of resist that can be used to diminish the effect of the negative resist on graphene but has not been tried in this work. Here is a short explanation about the resists and the approach to apply them in different procedures. LOR and PMGI resists which are based on polydimethylglutarimide. The LOR and PMGI resists can be used either as a sacrificial layer or as an interlayer in bi-layer lift-off processing and as a result of the unique properties of polydimethylglutarimide, they perform exceptionally well in these applications. Araujo et al. used LOR5A resist to make the lift-off process cleaner and easier and they could achieve good results (de Araujo et al., 2019). The schematic of the process is shown in Fig. 6.15.

Not only the strong adhesion between graphene and negative resist leads to the degradation of graphene quality also the negative resist causes limitations during lift-off process. When using the negative resist for TOC fabrication, lift-off process takes several hours to be almost completed in acetone at 60°C. However, a big amount of residue remains on the edges of the structures at the end of the process which makes around 30% of the beams nonfunctional. Figure 6.16 shows this issue clearly.

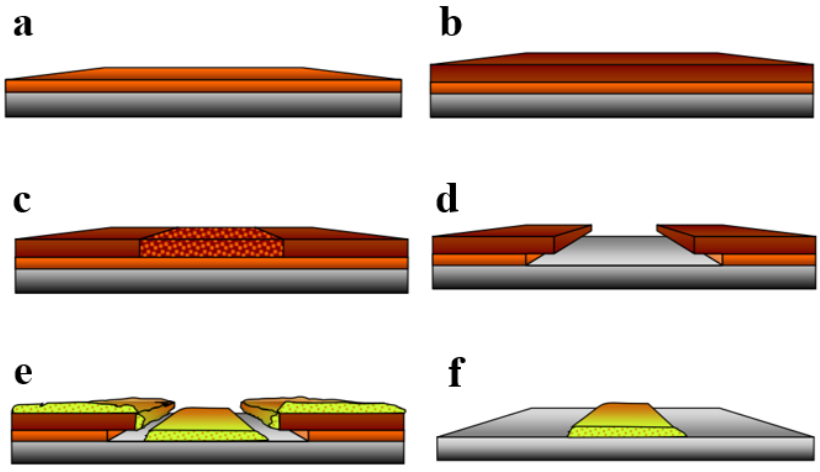

Fig. 6.15. *Schematic of the steps of negative photolithography in the presence of LOR; a) deposition and soft bake of the LOR; b) deposition and soft bake of the negative resist; c) patterning of the negative resist with exposing the UV light; d) developing the negative resist and LOR; e) Deposition of the thin film; f) lift-off of the bilayer stack and residual deposition.*

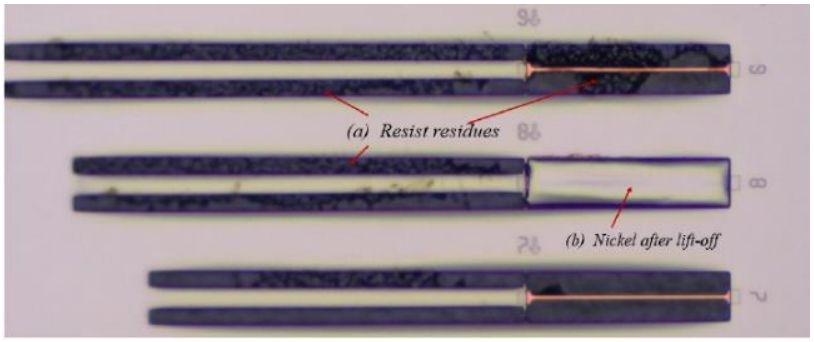

Fig. 6.16. *Schematic of the steps of negative photolithography in the presence of LOR; a) deposition and soft bake of the LOR; b) deposition and soft bake of the negative resist; c) patterning of the negative resist with exposing the UV light; d) developing the negative resist and LOR; e) Deposition of the thin film; f) lift-off of the bilayer stack and residual deposition*

6.5.4 Graphene fluorination in the presence of XeF_2

As mentioned the last step of the fabrication process is the release of the TOC with XeF_2 etching. It has been investigated in different published articles that exposing graphene in the chamber containing XeF_2 gas can lead to the fluorination of graphene (Stine et al., 2013). It is claimed that *2D* and *G* peaks did not change significantly but the intensity of *D* peak varied. Nair et al, have reported an obvious increase in the *D* peak intensity after fluorination of graphene. In addition, it has been noted that fully fluorinated graphene is quite stable (Nair et al., 2010) and it is observed that graphene can be defluorinated in the presence of humidity as well (Nair et al., 2010; Okotrub et al., 2009). The substrate, the etching and the storage conditions can affect the fluorination of graphene (Stine et al., 2013).

In our case, RAMAN spectroscopy has been performed after releasing the structures by XeF_2 etching and the appearance of the *D* peak was so significant which shows the change in the structure of the graphene. The spectra of RAMAN spectroscopy before and after release are shown in Fig 6.17. Although based on recent researches, the chemical and electrical properties of graphene can be modified when it is fluorinated (Robinson et al., 2010). There are some reports on the modification of its mechanical properties at high doses of XeF_2 (from 50 to 500 pulses). It has been shown that a reduced modulus increases approximately 8 times by the addition of 3% of fluorine. In another work, the fluorinated graphene showed a Young's modulus around 100±30

N/m which is 3 times less stiff than pristine graphene(Nair et al., 2010). During the release process in this work, there are around 10 pulses of XeF_2 with low pressure at a very short length (around 10 seconds), the fluorination will remain low and the precited effects will not be strong. However, the effect of fluorine needs to be considered in the lab-on-chip fabrication while graphene is involved.

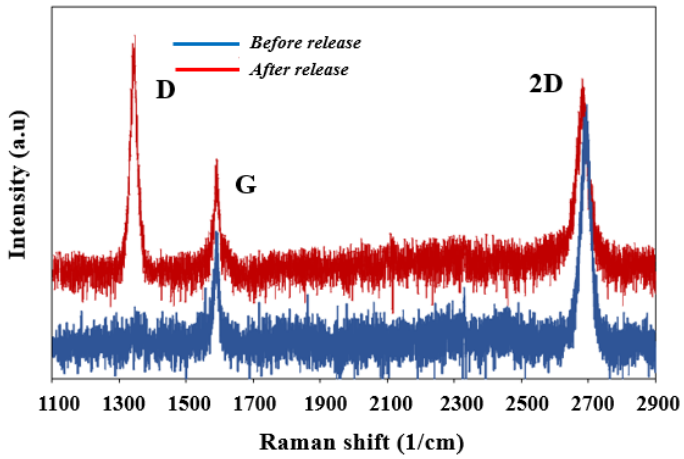

Fig. 6.17. *Comparison of RAMAN spectra of Gr on Cu beams; before release (blue) and after release (red).*

6.6 Conclusion

In this chapter, lab-on-chip technique developed in UCLouvain has been used to investigate the effect of graphene on fracture, relaxation and creep behaviour of Cu thin film. The rare choice of Ni as an actuator has been done in order to make the process more compatible with specimen materials (Cu and Gr). This process includes several steps such as deposition of thin films, Gr transfer, photolithography of specimen and actuators as well as an etching process. All these steps need to be compatible with graphene to make the integration of graphene in the system possible. A lot of challenges have been faced regarding the preparation of the lab on chip structures and it was observed that some steps cause real deterioration effects on graphene which need to be modified or replaced. Among these steps, the usage of lift-off resist and XeF_2 etching has the most negative effect on the quality of graphene. As it is mentioned, the lift-off resist could be replaced or a protective interlayer

which is compatible with the process, as well as graphene and negative resist, can be used to deal with this problem. One of the other important issues that were faced during the process is the poor adhesion of graphene on Cu substrate as a result of the transfer process. Some of the mentioned solutions for this problem are the modification of CVD process or using paraffine instead of PMMA. The experimental results have been extracted from the part of the structures that were in the best conditions. However, these results are not in agreement with the expected results when graphene is present as a very thin coating on Cu substrate. In fact, these results show that Cu/Gr samples displace more while applying the same load in comparison to pure Cu. These results clarify that this fabrication process is not completely compatible with graphene and graphene can not play an effective role in the fracture behaviour of Cu thin film. This can result from the poor adhesion between graphene and copper or/and the reduction of the quality of graphene when going through the different steps of the process. More modifications in CVD process of graphene, Gr transfer, photolithography process, and the release step are required in order to get reliable and reproducible results for these structures.

Chapter 7

Conclusion and perspectives

Conclusion and perspectives

This thesis focused on the study of the elastic and plastic properties of graphene in the form of mono- and bi-layer with three different nanomechanical test methods. 2D materials are promising candidates for many applications involving structural resistance, e.g. flexoelectricity, as a result knowing their mechanical properties is of utmost importance. Graphene is not only the first discovery of 2D materials but is also one of the important components in making the 2D heterostructure. The conclusion and perspectives of the thesis are provided by following the structure of the document.

Chapter 4 addresses the response of single and bilayer graphene when deflected with an AFM under the form of a suspended membrane. The goal is the extraction of the elastic properties of the mentioned layers such as 2D stiffness, Young's modulus and fracture strength. In addition, the discrepancies of extracted elastic properties that have been determined in the literature lead us to investigate the root cause of these effects. In many studies, the intrinsic defects of 2D layers have been investigated as the main reason for these discrepancies; however, several instrumental and processing factors are very effective on the extracted properties. **This study clarifies the effect of different parameters on the extraction of the elastic properties of graphene**. These parameters are:

- **AFM calibration:** the uncertainties in the value of the applied load and membrane deflection, which arise from the calibration parameters, can cause relative errors in the extracted elastic stiffness and fracture strength. It has been calculated theoretically that the standard deviation on the 2D stiffness while working with AFM is around 15%. On the other hand, the experimental results after precise calibration in each step, reveal around a 5% deviation which confirms all the tests have been performed in reliable calibration conditions.
- **The tip shape:** during the process of imaging or mechanical testing, tip wear can occur which has a significant effect on the elastic mechanical results as well as fracture strength. The resulted tip shape after wear is not known, but the radius is obviously increased which change the ratio between membrane radius and tip radius (a/R). When this ratio is less than 30, the tip radius needs to be considered in the calculation of the Young's modulus, which is not the case in the

clamped circular membrane theory. In addition, the tip radius has significant effect on the extracted fracture strength as can be seen in Eq. (4.10). This effect has been investigated and an obvious reduction in the value of apparent 2D stiffness as well as the quality of imaging has been observed in the presence of damaged tip. Furthermore, when tip degradation is significant, the extraction of any information from force-deflection curve is impossible as a result of a non-functional tip.

- **The shape of the membrane:** the theory (Eq. 4.4) that is used in this work to extract the elastic response of the membrane is required a complete circular membrane. The deviation from the circular shape due to the design or experimental procedure results in error in the extracted results. This deviation has been evaluated in this work experimentally and by simulation. The experimental investigation reveals a reduction of 50 N/m in the value of extracted 2D stiffness while deviation occurs from circular to semi-circular. From simulation point of view, the reduction is about 100 N/m and it remains almost constant from semi-circular to a complete square.
- **The loading position:** based on the theory, the applied load should be exactly placed in the center of the circular membrane. The mis-positioning of the load causes the overestimation of the apparent Young's modulus. This parameter has been investigated experimentally and by simulation. Experiments shows that 1000 nm distance from the center toward the edges leads to 100 N/m overestimation in the extracted 2D stiffness.

By considering the effect of these parameters and repeating the process on different membranes on different graphene samples, **the Young's modulus of SLGr have been extracted to be 880 GPa**. The measurements of the tip radius and the maximum applied load that cause the fracture of graphene, give the possibility to calculate **the fracture strength of SLGr equal to 45 N/m**. For BLGr, the orientation between the layers plays a significant role in the value of fracture strength and might influence on the extracted Young's modulus. There are not enough evidences to prove it and there are contrary results in the literature regarding this effect. In this work, the available graphene samples contain continuous graphene with multilayer domains which make it difficult to measure the angle between the layers with available techniques such as AFM or SEM. Raman spectroscopy is a method that can show the change in the orientation qualitatively by changing the ratio between the different

peaks, but it needs more precise and time-consuming measurements in order to quantify the angle between layers by this method. However, more than 10 different deflection tests have been performed on BLGr disregarding the angle between the layers. **The values for Young's modulus and fracture strength of BLGr have been determined to be around 700 GPa and 64 N/m, respectively.**

For the perspectives, Raman spectroscopy can be used to determine the angle between the layers quantitatively. To measure the angle between the layers with this method, low energy Raman modes (below 100 cm^{-1}) are required to be considered. In order to obtain these modes, using a higher acquisition time and a larger range of the spectrum is necessary. The process of extracting the Raman spectrum might take longer than usual. On the other hand, polarized RAMAN spectroscopy can be used to measure the orientation of graphene layers on different substrates. In addition, by producing separated domains of bilayer graphene and transferring them on the substrates which show good contrast while microscopy, there is a possibility to determine the angle between the layers by SEM, AFM, PFM (piezoresponse force microscopy) and TEM techniques. Another 2D layer which has high potential to be used in flexoelectric devices is hBN. In this study, hBN (which has been produced in UClouvain) has been transferred and investigated by atomic force microscopy. However, the thickness of the produced hBN was around 4 to 6 nm in the best condition as can be seen in Fig. 7.1a and b, and the surface was very rough (Fig. 7.1c) and inhomogeneous (Fig. 7.1d and e) which makes it difficult to perform the mechanical evaluations. As the thickness of hBN is effective on its mechanical response, controlling the thickness of hBN while produced by CVD is necessary. By improving the CVD-production of BLGr and hBN and considering the uncertainties involved in the membrane deflection process, the elastic properties and fracture strength of BLGr and hBN can accurately be measured. In addition, by transferring these layers in the form of heterostructure by modified PMMA-transfer introduced in this work, heterostructure can be built on different types of substrates with preferred orders of layers. Afterwards, the membrane deflection method can be used to predict the elastic response of the heterostructures by considering all sources of uncertainties investigated in this work.

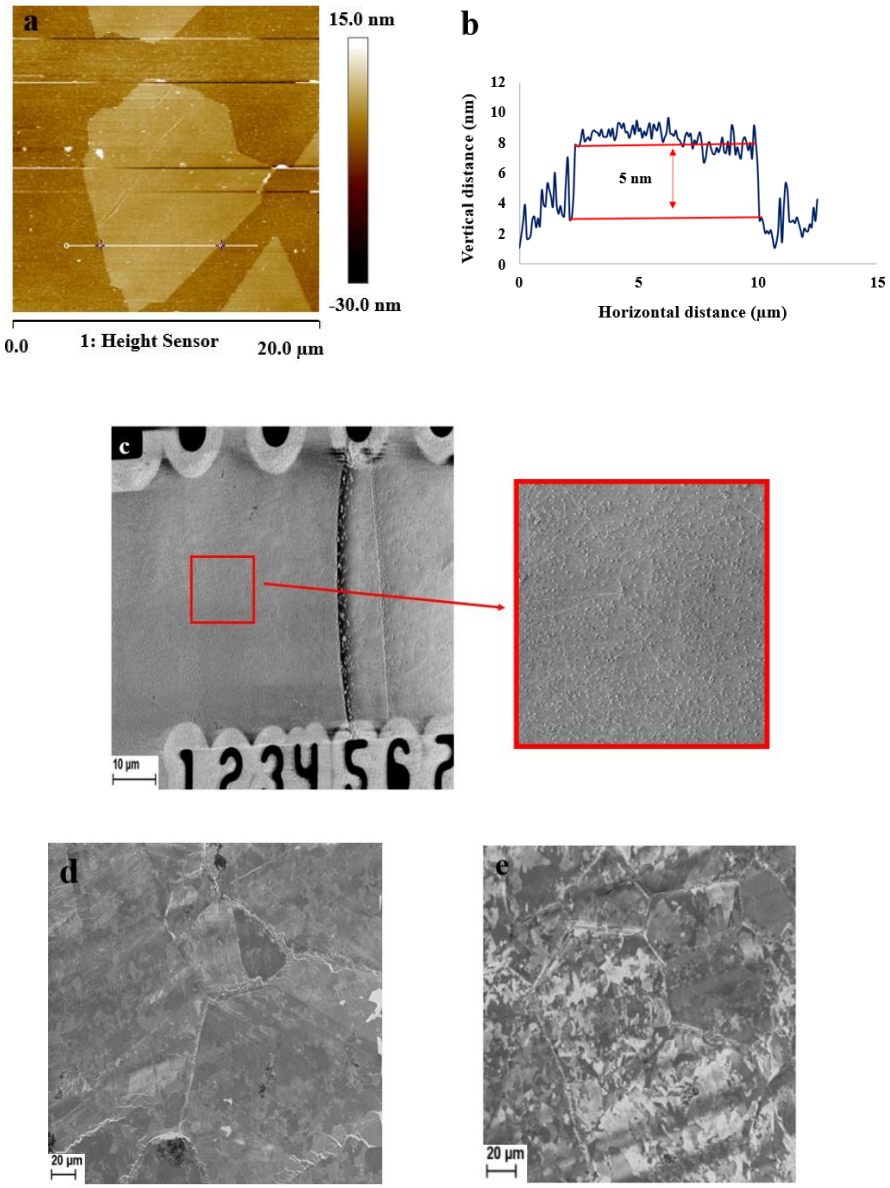

Fig. 7.1. *(a) AFM mapping of hBN flakes on Si/SiO2 substrate (height sensor mode); (b) Cross-sectional profile of the flake which represents the thickness of hBN flake; (c) SEM image of hBN sample which shows the roughness of the surface of the hBN samples; (e &d) SEM images of hBN (almost continueous) show the inhomogeneous morphology of the h-BN layer.*

Chapter 5 deals with the effect of a SLGr cap surface layer on the plastic deformation of Cu film as revealed under nanoindentation loading. The role of graphene on the plasticity of copper has been evaluated in two forms 1) graphene as a coating on the Cu substrate, 2) graphene as an interlayer between two films of Cu. Graphene has been grown on Cu substrate by CVD process as a result no transfer process was required. In this condition, the adhesion of Gr to the substrate is better and the quality of graphene is higher. The significant effect of graphene on the movement and propagation of dislocations when it acts as a coating or as an interlayer has been evaluated and compared with samples without graphene.

- This effect has been observed in **force-displacement curves extracted from nanoindentation** method in two different modes (load-control and displacement-control) by monitoring the length of the pop-ins. The length of pop-ins is almost constant in Cu_A/Gr system but it increases with load in Cu_A system. An unexpected discovery shows the sooner start of plasticity in the presence of graphene which results from the stiffening effect induced by the adhesionless contact due to the presence of graphene. In Cu_A/Gr/Cu_N system, the length of the pop-ins is shorter in comparison to Cu_A/Cu_N one which reveals the blockage of the dislocations propagations by graphene. In addition, the first pop-in occurs at a higher load and higher displacement in the presence of graphene.
- In addition, **AFM mapping** reveals the smaller pile-ups around the indents in the Cu_A/Gr sample in comparison to Cu_A, which is also proof of the blockage of dislocations movements towards the surface in the presence of graphene. For the system that which graphene acts as an interlayer, the morphology of the indented surface for the sample with and without graphene is the same. As the 100 nm-thick Cu film on the surface is controlling the morphology.
- **TEM observation and DDD simulations** show the larger back stress builds up in the system with graphene which causes delocalisation of the plastic activity and gliding of dislocations on other slip planes. On the other hand, dislocations move freely towards the surface when there is no graphene and no blockage of the dislocation movement.

The effect of graphene on dislocation movements and propagation is much larger than its thickness and it is related to the homogenous distribution of dislocation in the presence of graphene. Another interesting result that has

been represented in this work is the more significant effect of graphene when it is buried under a cap layer of an extra Cu thin film.

Some simulations related to the later configuration need to be performed to see what is the root cause of this phenomenon.

Chapter 6 focuses on the investigation of the effect of graphene on the fracture and relaxation behaviour of freestanding copper film under tension. In this part, pure Cu and Cu/Gr have been processed as the specimen in the tensile-on-chip structure that has been developed in UCLouvain. To make the process more compatible with graphene, Ni thin film has been used as actuator. In order to extract reliable and reproducible results, each step of the process needs to be compatible with the materials that have been used as the specimen and actuator, especially graphene. The good integration of Gr in the process and on the structures is the key point in proceeding with the lab-on-chip of Cu/Gr. There are some key issues in the process which have been investigated and dealt with, including:

- **Poor adhesion of graphene on Cu thin film:** as the thickness of copper is very thin which makes it impossible to grow graphene directly on Cu substrate by CVD, Gr transfer is necessary. Gr transfer leads to poor adhesion between graphene and Cu which causes delamination and fracture on Gr layer during the next steps of the process. In order to deal with this problem, the modified PMMA-wet transfer method has been used besides the modification in the PMMA removal step. This modification includes the warming up of the wafer containing Gr/PMMA layer to 60°C for around 10 mins, PMMA can be softened on graphene and help the better adhesion of graphene to the Cu substrate. However, the issue has not been solved by using both modifications and it remains one of the key issues of the process.
- **Negative effect of the lift-off resist on graphene:** negative resist reduces the quality of graphene, significantly. It was supposed that the use of an interlayer between graphene and resist which is compatible with the process and both materials can diminish this issue. In this work, PMMA and positive resist have been applied as the interlayer but could not improve the process due to the production of side-products and intermixture of the resists in the presence of PMMA and positive resists, respectively.
- **Negative effect of XeF_2 during release step:** XeF_2 can lead to fluorination of graphene which leads to an increase in the *D* peak in

Raman characteristic peaks. This can reveal the presence of more defects on graphene after being in contact with XeF_2 which causes the deterioration of the graphene quality.

- **Ni as an actuator:** the choice of Ni as an actuator can cause more complexity in the process, first as a result of the unknown mechanical behaviour of Ni and then due to the relaxation of Ni actuators during the time. The relaxation of Ni actuators causes the change in the curvature measurements and internal stress.

Some results have been extracted with the produced samples which show a higher displacement for Cu/Gr sample in the presence of the same load. These results show that graphene does not positively impact the mechanical response of the Cu thin film which can result from the poor adhesion and/or the achieved low quality of the graphene during the process. In addition, Cu could be oxidized as a result of the wet transfer which leads to the deterioration of the mechanical response of copper.

For future work, it is necessary to modify the process regarding the adhesion of graphene, lift-off resist as well as XeF_2 etching. It has been mentioned that by using polished Cu foil in the CVD process for Gr production, Gr texture is flatter which causes better adhesion to the substrate. Using paraffine instead of the PMMA can result in higher adhesion of graphene to the target substrate, as well. In addition, using an interlayer of LOR and PMGI resists can eliminate the negative effect of the lift-off resists on the quality of graphene.

In general, this thesis addressed the uncertainties and challenges that can be faced in different nanomechanical testing techniques for 2D layers in suspended and supported forms. In addition, the true Young's modulus of SLGr and BLGr have been evaluated by considering most of the uncertainties arising in the deflection test by AFM. The limitations of two modes of nanoindentation have been investigated and by combining them in addition to simulations, the precise effect of graphene on the plastic deformation of copper has been studied. Last but not least, all the challenges and uncertainties that exist in the TOC of Cu/Gr have been investigated and some solutions have been provided which make the procedure more straightforward and performable in future.

List of Conferences

1. On the extraction of accurate stiffness and strength properties of 2D materials using atomic force microscopy induced membrane deflection, F. Bahrami, M. W. Malik, C. D'Haese, J.P. Raskin, B. Nysten, T. Pardoen. Advanced small-scale mechanical characterization: strength, plasticity, fracture and fatigue (Symposium K), E-MRS spring meeting, virtual conference, May 31-June 3, 2021, (Poster presentation).

2. Summer school on Sustainable ICT (SICT 2021), UCLouvain, Louvain La Neuve (Belgium), September 7-11, 2020.

3. Graphene effect on mechanical response of metal substrate, F. Bahrami, M. Hammad, M. Fivel, B. Huet, C. D'Haese, L. Ding, B. Nysten, H. Idrissi, J.P. Raskin, T. Pardoen. Micro- and nano-mechanics – characterization and modelling (symposium D5), EUROMAT, Stockholm, Sweden, September 1-5, 2019, (Oral presentation).

4. Graphene effect on mechanical response of copper film, F. Bahrami, M. Hammad, M. Fivel, B. Huet, C. D'Haese, L. Ding, B. Nysten, H. Idrissi, J.P. Raskin, T. Pardoen. Nanomechanical Testing in Materials Research and Development VII, ECI, Malaga, Spain, September 30 to October 4, 2019, (Poster).

5. Graphene effect on mechanical response of metal substrate, F. Bahrami, M. Hammad, M. Fivel, B. Huet, C. D'Haese, L. Ding, B. Nysten, H. Idrissi, J.P. Raskin, T. Pardoen. Microscopy, RBSM, Louvain-La-Neuve, Belgium, September 9, 2019, (Poster), Abstract booklet, P.13

6. GDRi Mecano International School on the mechanics of nano-objects in IESC, Cargèse (Corsica, France) from October 28 to November 2, 2018.

7. International Cargèse school entitled "Frontier research in 2D materials", Cargèse, (Corsica, France), from April 2-14, 2018.

List of publications

- F. Bahrami, M. Hammad, M. Fivel, B. Huet, C. D'Haese, L. Ding, B. Nysten, H. Idrissi, J.P. Raskin, T. Pardoen, "Single layer graphene controlled surface and bulk indentation plasticity in copper", International Journal of Plasticity 138 (2021) 102936.

References

References

Abbas, G., Li, Y., Wang, H., Zhang, W. X., Wang, C., & Zhang, H. (2020). Recent Advances in Twisted Structures of Flatland Materials and Crafting Moiré Superlattices. *Advanced Functional Materials*, *30*(36), 1–23. https://doi.org/10.1002/adfm.202000878

Abergel, D. S. L., Apalkov, V., Berashevich, J., Ziegler, K., & Chakraborty, T. (2010). Properties of graphene: A theoretical perspective. *Advances in Physics*, *59*(4), 261–482. https://doi.org/10.1080/00018732.2010.487978

AbuShanab, W. S., Moustafa, E. B., Ghandourah, E., & Taha, M. A. (2020). Effect of graphene nanoparticles on the physical and mechanical properties of the Al2024-graphene nanocomposites fabricated by powder metallurgy. *Results in Physics*, *19*(June), 103343. https://doi.org/10.1016/j.rinp.2020.103343

Ahmad, Y. H., & Mohamed, A. M. A. (2014). Electrodeposition of nanostructured Nickel-Ceramic composite coatings: A review. *International Journal of Electrochemical Science*, *9*(4), 1942–1963.

AK, G. (2009). Graphene: status and prospects. *Science*, *324*(5934), 1530–1534.

Akinwande, D., Brennan, C. J., Bunch, J. S., Egberts, P., Felts, J. R., Gao, H., Huang, R., Kim, J. S., Li, T., Li, Y., Liechti, K. M., Lu, N., Park, H. S., Reed, E. J., Wang, P., Yakobson, B. I., Zhang, T., Zhang, Y. W., Zhou, Y., & Zhu, Y. (2017a). A review on mechanics and mechanical properties of 2D materials—Graphene and beyond. *Extreme Mechanics Letters*, *13*, 42–77. https://doi.org/10.1016/j.eml.2017.01.008

Akinwande, D., Brennan, C. J., Bunch, J. S., Egberts, P., Felts, J. R., Gao, H., Huang, R., Kim, J. S., Li, T., Li, Y., Liechti, K. M., Lu, N., Park, H. S., Reed, E. J., Wang, P., Yakobson, B. I., Zhang, T., Zhang, Y. W., Zhou, Y., & Zhu, Y. (2017b). A review on mechanics and mechanical properties of 2D materials—Graphene and beyond. In *Extreme Mechanics Letters* (Vol. 13, pp. 42–77). Elsevier Ltd. https://doi.org/10.1016/j.eml.2017.01.008

Al-Quraishi, K. K., He, Q., Kauppila, W., Wang, M., & Yang, Y. (2020). Mechanical testing of two-dimensional materials: a brief review. *International Journal of Smart and Nano Materials*, *00*(00), 207–246. https://doi.org/10.1080/19475411.2020.1791276

Albrecht, T. R., Grütter, P., Horne, D., & Rugar, D. (1991). Frequency modulation detection using high-Q cantilevers for enhanced force microscope sensitivity. *Journal of Applied Physics*, *69*(2), 668–673. https://doi.org/10.1063/1.347347

Allen, M. J., Tung, V. C., Gomez, L., Xu, Z., Chen, L. M., Nelson, K. S., Zhou, C., Kaner, R. B., & Yang, Y. (2009). Soft transfer printing of chemically converted graphene. *Advanced Materials*, *21*(20), 2098–2102. https://doi.org/10.1002/adma.200803000

André, N., Coulombier, M., De Longueville, V., Fabrègue, D., Gets, T., Gravier, S., Pardoen, T., & Raskin, J. P. (2007). Microfabrication-based nanomechanical laboratory for testing the ductility of submicron aluminium films. *Microelectronic Engineering*, *84*(11), 2714–2718. https://doi.org/10.1016/j.mee.2007.05.039

Andrew, R. C., Mapasha, R. E., Ukpong, A. M., & Chetty, N. (2012). Mechanical properties of graphene and boronitrene. *Physical Review B - Condensed Matter and Materials Physics*, *85*(12), 1–9. https://doi.org/10.1103/PhysRevB.85.125428

Androulidakis, C., Zhang, K., Robertson, M., & Tawfick, S. (2018). Tailoring the mechanical properties of 2D materials and heterostructures. *2D Materials*, *5*(3). https://doi.org/10.1088/2053-1583/aac764

Annamalai, M., Mathew, S., Jamali, M., Zhan, D., & Palaniapan, M. (2012). Elastic and nonlinear response of nanomechanical graphene devices. *Journal of Micromechanics and Microengineering*, *22*(10). https://doi.org/10.1088/0960-1317/22/10/105024

Bahr, D. F., Kramer, D. E., & Gerberich, W. W. (1998). Non-linear deformation mechanisms during nanoindentation. *Acta Materialia*, *46*(10), 3605–3617. https://doi.org/10.1016/S1359-6454(98)00024-X

Barrios-Vargas, J. E., Mortazavi, B., Cummings, A. W., Martinez-Gordillo, R., Pruneda, M., Colombo, L., Rabczuk, T., & Roche, S. (2017). Electrical and Thermal Transport in Coplanar Polycrystalline Graphene-hBN Heterostructures. *Nano Letters*, *17*(3), 1660–1664. https://doi.org/10.1021/acs.nanolett.6b04936

Bartolucci, S. F., Paras, J., Rafiee, M. A., Rafiee, J., Lee, S., Kapoor, D., & Koratkar, N. (2011). Graphene-aluminum nanocomposites. *Materials Science and Engineering A*, *528*(27), 7933–7937. https://doi.org/10.1016/j.msea.2011.07.043

Begley, M. R., & Mackin, T. J. (2004). Spherical indentation of freestanding circular thin films in the membrane regime. *Journal of the Mechanics and Physics of Solids*, *52*(9), 2005–2023. https://doi.org/10.1016/j.jmps.2004.03.002

Bertolazzi, S., Brivio, J., & Kis, A. (2011). Stretching and breaking of ultrathin MoS 2. *ACS Nano*, *5*(12), 9703–9709. https://doi.org/10.1021/nn203879f

Bhatia, N. M., & Nachbar, W. (n.d.). *FINITE INDENTATION OF AN ELASTIC MEMBRANE BY A SPHERICAL INDENTER*.

Bhimanapati, G. R., Lin, Z., Meunier, V., Jung, Y., Cha, J., Das, S., Xiao, D., Son, Y., Strano, M. S., Cooper, V. R., Liang, L., Louie, S. G., Ringe, E., Zhou, W., Kim, S. S., Naik, R. R., Sumpter, B. G., Terrones, H., Xia, F., … Robinson, J. A. (2015). Recent Advances in Two-Dimensional Materials beyond Graphene. *ACS Nano*, *9*(12), 11509–11539. https://doi.org/10.1021/acsnano.5b05556

Binnig, G., Quate, C. F., & Gerber, C. (1986). Atomic force microscope. *Physical Review Letters*, *56*(9), 930–933. https://doi.org/10.1103/PhysRevLett.56.930

Boé, A., Safi, A., Coulombier, M., Fabrègue, D., Pardoen, T., & Raskin, J. P. (2009). MEMS-based microstructures for nanomechanical characterization of thin films. *Smart Materials and Structures*, *18*(11). https://doi.org/10.1088/0964-1726/18/11/115018

Boldrin, L., Scarpa, F., Chowdhury, R., & Adhikari, S. (2011). Effective mechanical properties of hexagonal boron nitride nanosheets. *Nanotechnology*, *22*(50). https://doi.org/10.1088/0957-4484/22/50/505702

Bonaccorso, F., Lombardo, A., Hasan, T., Sun, Z., Colombo, L., & Ferrari, A. C. (2012). Production and processing of graphene and 2d crystals. *Materials Today*, *15*(12), 564–589. https://doi.org/10.1016/S1369-7021(13)70014-2

Borkar, T., & Harimkar, S. P. (2011). Effect of electrodeposition conditions and reinforcement content on microstructure and tribological properties of nickel composite coatings. *Surface and Coatings Technology*, *205*(17–18), 4124–4134. https://doi.org/10.1016/j.surfcoat.2011.02.057

Brown, L., Hovden, R., Huang, P., Wojcik, M., Muller, D. A., & Park, J. (2012). Twinning and twisting of tri- and bilayer graphene. *Nano*

Letters, *12*(3), 1609–1615. https://doi.org/10.1021/nl204547v

Butt, H. J., Cappella, B., & Kappl, M. (2005). Force measurements with the atomic force microscope: Technique, interpretation and applications. In *Surface Science Reports* (Vol. 59, Issues 1–6, pp. 1–152). Elsevier. https://doi.org/10.1016/j.surfrep.2005.08.003

Cai, Z., Liu, B., Zou, X., & Cheng, H. M. (2018a). Chemical Vapor Deposition Growth and Applications of Two-Dimensional Materials and Their Heterostructures. *Chemical Reviews*, *118*(13), 6091–6133. https://doi.org/10.1021/acs.chemrev.7b00536

Cai, Z., Liu, B., Zou, X., & Cheng, H. M. (2018b). Chemical Vapor Deposition Growth and Applications of Two-Dimensional Materials and Their Heterostructures. In *Chemical Reviews* (Vol. 118, Issue 13, pp. 6091–6133). American Chemical Society. https://doi.org/10.1021/acs.chemrev.7b00536

Cao, G. (2014a). Atomistic studies of mechanical properties of graphene. In *Polymers* (Vol. 6, Issue 9, pp. 2404–2432). MDPI AG. https://doi.org/10.3390/polym6092404

Cao, G. (2014b). Atomistic studies of mechanical properties of graphene. *Polymers*, *6*(9), 2404–2432. https://doi.org/10.3390/polym6092404

Cao, G., & Gao, H. (2019). Mechanical properties characterization of two-dimensional materials via nanoindentation experiments. In *Progress in Materials Science* (Vol. 103, pp. 558–595). Elsevier Ltd. https://doi.org/10.1016/j.pmatsci.2019.03.002

Cao, K., Feng, S., Han, Y., Gao, L., Hue Ly, T., Xu, Z., & Lu, Y. (2020). Elastic straining of free-standing monolayer graphene. *Nature Communications*, *11*(1), 1–7. https://doi.org/10.1038/s41467-019-14130-0

Cao, Y., Fatemi, V., Fang, S., Watanabe, K., Taniguchi, T., Kaxiras, E., & Jarillo-Herrero, P. (2018). Unconventional superconductivity in magic-angle graphene superlattices. *Nature*, *556*(7699), 43–50. https://doi.org/10.1038/nature26160

Cartamil-Bueno, S. J., Cavalieri, M., Wang, R., Houri, S., Hofmann, S., & van der Zant, H. S. J. (2017). Mechanical characterization and cleaning of CVD single-layer h-BN resonators. *Npj 2D Materials and Applications*, *1*(1). https://doi.org/10.1038/s41699-017-0020-8

Castellanos-Gomez, A., Poot, M., Steele, G. A., Van Der Zant, H. S. J., Agraït, N., & Rubio-Bollinger, G. (2012). Elastic properties of freely suspended MoS2 nanosheets. *Advanced Materials*, *24*(6), 772–775. https://doi.org/10.1002/adma.201103965

Castro Neto, A. H., Guinea, F., Peres, N. M. R., Novoselov, K. S., & Geim, A. K. (2009). The electronic properties of graphene. *Reviews of Modern Physics*, *81*(1), 109–162. https://doi.org/10.1103/RevModPhys.81.109

Celano Editor, U. (n.d.). *NanoScience and Technology Electrical Atomic Force Microscopy for Nanoelectronics*. http://www.springer.com/series/3705

Chang, H. J., Fivel, M., Rodney, D., & Verdier, M. (2010). Simulations multi-échelles de l'indentation de métaux CFC: De l'atome au milieu continu. *Comptes Rendus Physique*, *11*(3–4), 285–292. https://doi.org/10.1016/j.crhy.2010.07.007

Chang, S. W., Nair, A. K., & Buehler, M. J. (2013). Nanoindentation study of size effects in nickel-graphene nanocomposites. *Philosophical Magazine Letters*, *93*(4), 196–203. https://doi.org/10.1080/09500839.2012.759293

Chen, J., Guo, X., Tang, Q., Zhuang, C., Liu, J., Wu, S., & Beake, B. D. (2013). Nanomechanical properties of graphene on poly(ethylene terephthalate) substrate. *Carbon*, *55*, 144–150. https://doi.org/10.1016/j.carbon.2012.12.020

Chen, L. Y., Konishi, H., Fehrenbacher, A., Ma, C., Xu, J. Q., Choi, H., Xu, H. F., Pfefferkorn, F. E., & Li, X. C. (2012). Novel nanoprocessing route for bulk graphene nanoplatelets reinforced metal matrix nanocomposites. *Scripta Materialia*, *67*(1), 29–32. https://doi.org/10.1016/j.scriptamat.2012.03.013

Chen, M., Stekovic, D., Li, W., Arkook, B., Haddon, R. C., & Bekyarova, E. (2017). Sublimation-assisted graphene transfer technique based on small polyaromatic hydrocarbons. *Nanotechnology*, *28*(25). https://doi.org/10.1088/1361-6528/aa72d5

Chen, Y., Gong, X. L., & Gai, J. G. (2016). Progress and Challenges in Transfer of Large-Area Graphene Films. In *Advanced Science* (Vol. 3, Issue 8). Wiley-VCH Verlag. https://doi.org/10.1002/advs.201500343

Chen, Z., Qi, Y., Chen, X., Zhang, Y., & Liu, Z. (2019). Direct CVD Growth

of Graphene on Traditional Glass: Methods and Mechanisms. *Advanced Materials*, *31*(9), 1–18. https://doi.org/10.1002/adma.201803639

Cheng, S., Ma, E., Wang, Y. M., Kecskes, L. J., Youssef, K. M., Koch, C. C., Trociewitz, U. P., & Han, K. (2005). Tensile properties of in situ consolidated nanocrystalline Cu. *Acta Materialia*, *53*(5), 1521–1533. https://doi.org/10.1016/j.actamat.2004.12.005

Chiou, Y. C., Olukan, T. A., Almahri, M. A., Apostoleris, H., Chiu, C. H., Lai, C. Y., Lu, J. Y., Santos, S., Almansouri, I., & Chiesa, M. (2018). Direct Measurement of the Magnitude of the van der Waals Interaction of Single and Multilayer Graphene. *Langmuir*, *34*(41), 12335–12343. https://doi.org/10.1021/acs.langmuir.8b02802

Choi, W., Lahiri, I., Seelaboyina, R., & Kang, Y. S. (2010). Synthesis of graphene and its applications: A review. *Critical Reviews in Solid State and Materials Sciences*, *35*(1), 52–71. https://doi.org/10.1080/10408430903505036

Conley, H. J., Wang, B., Ziegler, J. I., Haglund, R. F., Pantelides, S. T., & Bolotin, K. I. (2013). Bandgap engineering of strained monolayer and bilayer MoS2. *Nano Letters*, *13*(8), 3626–3630. https://doi.org/10.1021/nl4014748

Corcoran, S., Colton, R., Lilleodden, E., & Gerberich, W. (1997). Anomalous plastic deformation at surfaces: Nanoindentation of gold single crystals. *Physical Review B - Condensed Matter and Materials Physics*, *55*(24), R16057–R16060. https://doi.org/10.1103/PhysRevB.55.R16057

Cuenot, S., Frétigny, C., Demoustier-Champagne, S., & Nysten, B. (2004). Surface tension effect on the mechanical properties of nanomaterials measured by atomic force microscopy. *Physical Review B - Condensed Matter and Materials Physics*, *69*(16). https://doi.org/10.1103/PhysRevB.69.165410

Das, A., Pisana, S., Chakraborty, B., Piscanec, S., Saha, S. K., Waghmare, U. V., Novoselov, K. S., Krishnamurthy, H. R., Geim, A. K., Ferrari, A. C., & Sood, A. K. (2008). Monitoring dopants by Raman scattering in an electrochemically top-gated graphene transistor. *Nature Nanotechnology*, *3*(4), 210–215. https://doi.org/10.1038/nnano.2008.67

de Araujo, E. N. D., Stephan Lacerda de Sousa, T. A., Guimarães, L. de M., & Plentz, F. (2019). Effects of post-lithography cleaning on the yield

and performance of CVD graphene-based devices. *Beilstein Journal of Nanotechnology*, *9*(1), 349–355. https://doi.org/10.3762/bjnano.10.34

Dean, C. R., Young, A. F., Meric, I., Lee, C., Wang, L., & Sorgenfrei, S. (n.d.). <10054917.Pdf>. *Nature.Com*. https://www.nature.com/nnano/journal/v5/n10/abs/nnano.2010.172.html

Dean, C., Young, A. F., Wang, L., Meric, I., Lee, G. H., Watanabe, K., Taniguchi, T., Shepard, K., Kim, P., & Hone, J. (2012). Graphene based heterostructures. *Solid State Communications*, *152*(15), 1275–1282. https://doi.org/10.1016/j.ssc.2012.04.021

Dehm, G., Jaya, B. N., Raghavan, R., & Kirchlechner, C. (2018). Overview on micro- and nanomechanical testing: New insights in interface plasticity and fracture at small length scales. *Acta Materialia*, *142*, 248–282. https://doi.org/10.1016/j.actamat.2017.06.019

Deng, S., & Berry, V. (2016). Wrinkled, rippled and crumpled graphene: An overview of formation mechanism, electronic properties, and applications. In *Materials Today* (Vol. 19, Issue 4, pp. 197–212). Elsevier B.V. https://doi.org/10.1016/j.mattod.2015.10.002

Deng, Z., Smolyanitsky, A., Li, Q., Feng, X. Q., & Cannara, R. J. (2012). Adhesion-dependent negative friction coefficient on chemically modified graphite at the nanoscale. *Nature Materials*, *11*(12), 1032–1037. https://doi.org/10.1038/nmat3452

Deokar, G., Avila, J., Razado-Colambo, I., Codron, J. L., Boyaval, C., Galopin, E., Asensio, M. C., & Vignaud, D. (2015). Towards high quality CVD graphene growth and transfer. *Carbon*, *89*, 82–92. https://doi.org/10.1016/j.carbon.2015.03.017

Dewapriya, M. A. N., & Rajapakse, R. K. N. D. (2014). Effects of free edges and vacancy defects on the mechanical properties of graphene. *Proceedings of the IEEE Conference on Nanotechnology*, 908–912. https://doi.org/10.1109/NANO.2014.6968087

Ding, X., Ko, W. H., & Mansour, J. M. (1990). Residual stress and mechanical properties of boron-doped p+-silicon films. *Sensors and Actuators: A. Physical*, *23*(1–3), 866–871. https://doi.org/10.1016/0924-4247(90)87048-N

Ding, Y., Peng, Q., Gan, L., Wu, R., Ou, X., Zhang, Q., & Luo, Z. (2016). Stacking-Mode-Induced Reactivity Enhancement for Twisted Bilayer

Graphene. *Chemistry of Materials*, *28*(4), 1034–1039. https://doi.org/10.1021/acs.chemmater.5b04002

Doerner, M. F. (1986). Doerner, Nix - 1986 - Journal of Materials Research.pdf. In *Journal of Materials Research* (Vol. 1, Issue 4, pp. 601–609).

Dorri Moghadam, A., Omrani, E., Menezes, P. L., & Rohatgi, P. K. (2015). Mechanical and tribological properties of self-lubricating metal matrix nanocomposites reinforced by carbon nanotubes (CNTs) and graphene - A review. *Composites Part B: Engineering*, *77*, 402–420. https://doi.org/10.1016/j.compositesb.2015.03.014

Du, Y. (2021). *Strain Range Dependence of Young ' s Modulus and Size Effects of Mechanical Properties for Chiral Graphene by Molecular Dynamics Simulations*. 0–13.

Elder, R. M., Neupane, M. R., & Chantawansri, T. L. (2015). Stacking order dependent mechanical properties of graphene/MoS2 bilayer and trilayer heterostructures. *Applied Physics Letters*, *107*(7). https://doi.org/10.1063/1.4928752

Espinosa, H. D., Zhu, Y., & Moldovan, N. (2007). Design and operation of a MEMS-based material testing system for nanomechanical characterization. *Journal of Microelectromechanical Systems*, *16*(5), 1219–1231. https://doi.org/10.1109/JMEMS.2007.905739

Fabrègue, D., André, N., Coulombier, M., Raskin, J. P., & Pardoen, T. (2007). Multipurpose nanomechanical testing machines revealing the size-dependent strength and high ductility of pure aluminium submicron films. *Micro and Nano Letters*, *2*(1), 13–16. https://doi.org/10.1049/mnl:20065068

Falin, A., Cai, Q., Santos, E. J. G., Scullion, D., Qian, D., Zhang, R., Yang, Z., Huang, S., Watanabe, K., Taniguchi, T., Barnett, M. R., Chen, Y., Ruoff, R. S., & Li, L. H. (2017). Mechanical properties of atomically thin boron nitride and the role of interlayer interactions. *Nature Communications*, *8*. https://doi.org/10.1038/ncomms15815

Fang, W., Hsu, A. L., Song, Y., & Kong, J. (2015). A review of large-area bilayer graphene synthesis by chemical vapor deposition. *Nanoscale*, *7*(48), 20335–20351. https://doi.org/10.1039/c5nr04756k

Ferralis, N. (2010). Probing mechanical properties of graphene with Raman spectroscopy. In *Journal of Materials Science* (Vol. 45, Issue 19, pp.

5135–5149). Kluwer Academic Publishers. https://doi.org/10.1007/s10853-010-4673-3

Filleter, T., McChesney, J. L., Bostwick, A., Rotenberg, E., Emtsev, K. V., Seyller, T., Horn, K., & Bennewitz, R. (2009). Friction and dissipation in epitaxial graphene films. *Physical Review Letters*, *102*(8). https://doi.org/10.1103/PhysRevLett.102.086102

Fivel, M. C., Robertson, C. F., Canova, G. R., & Boulanger, L. (1998). Three-dimensional modeling of indent-induced plastic zone at a mesoscale. *Acta Materialia*, *46*(17), 6183–6194. https://doi.org/10.1016/S1359-6454(98)00278-X

Fivel, M., & Depres, C. (2014). An easy implementation of displacement calculations in 3D discrete dislocation dynamics codes. *Philosophical Magazine*, *94*(28), 3206–3214. https://doi.org/10.1080/14786435.2014.949326

Fivel, Marc C. (2008). Discrete dislocation dynamics: an important recent break-through in the modelling of dislocation collective behaviour. *Comptes Rendus Physique*, *9*(3–4), 427–436. https://doi.org/10.1016/j.crhy.2007.11.005

Frank, I. W., Tanenbaum, D. M., van der Zande, A. M., & McEuen, P. L. (2007). Mechanical properties of suspended graphene sheets. *Journal of Vacuum Science & Technology B: Microelectronics and Nanometer Structures*, *25*(6), 2558. https://doi.org/10.1116/1.2789446

Fribourg, G., Bréchet, Y., Deschamps, A., & Simar, A. (2011). Microstructure-based modelling of isotropic and kinematic strain hardening in a precipitation-hardened aluminium alloy. *Acta Materialia*, *59*(9), 3621–3635. https://doi.org/10.1016/j.actamat.2011.02.035

Gaillard, Y., Tromas, C., & Woirgard, J. (2003). Pop-in phenomenon in MgO and LiF: Observation of dislocation structures. *Philosophical Magazine Letters*, *83*(9), 553–561. https://doi.org/10.1080/09500830310001594273

Gao, Y., Kim, S., Zhou, S., Chiu, H. C., Nélias, D., Berger, C., De Heer, W., Polloni, L., Sordan, R., Bongiorno, A., & Riedo, E. (2015). Elastic coupling between layers in two-dimensional materials. *Nature Materials*, *14*(7), 714–720. https://doi.org/10.1038/nmat4322

Garcí, R., & San Paulo, A. (n.d.). *Attractive and repulsive tip-sample*

interaction regimes in tapping-mode atomic force microscopy.

García, R., & Pérez, R. (2002). Dynamic atomic force microscopy methods. In *Surface Science Reports* (Vol. 47, Issues 6–8). https://doi.org/10.1016/s0167-5729(02)00077-8

Geim, A. K., & Grigorieva, I. V. (2013). Van der Waals heterostructures. *Nature*, *499*(7459), 419–425. https://doi.org/10.1038/nature12385

Gertsman, V. Y., Hoffmann, M., Gleiter, H., & Birringer, R. (1994). The study of grain size dependence of yield stress of copper for a wide grain size range. *Acta Metallurgica Et Materialia*, *42*(10), 3539–3544. https://doi.org/10.1016/0956-7151(94)90486-3

Giannitsis, A. T. (2011). Biomeditsiiniliste kiiplaborite valmistamine. *Estonian Journal of Engineering*, *17*(2), 109–139. https://doi.org/10.3176/eng.2011.2.03

Gómez-Navarro, C., Burghard, M., & Kern, K. (2008). Elastic properties of chemically derived single graphene sheets. *Nano Letters*, *8*(7), 2045–2049. https://doi.org/10.1021/nl801384y

Gouldstone, A., Koh, H. J., Zeng, K. Y., Giannakopoulos, A. E., & Suresh, S. (2000). Discrete and continuous deformation during nanoindentation of thin films. *Acta Materialia*, *48*(9), 2277–2295. https://doi.org/10.1016/S1359-6454(00)00009-4

Gravier, S., Coulombier, M., Safi, A., André, N., Boé, A., Raskin, J. P., & Pardoen, T. (2009). New on-chip nanomechanical testing laboratory - Applications to aluminum and polysilicon thin films. *Journal of Microelectromechanical Systems*, *18*(3), 555–569. https://doi.org/10.1109/JMEMS.2009.2020380

Gupta, S., Ramesh, K., Ahmed, S., & Kakkar, V. (2016). Lab-on-chip technology: A review on design trends and future scope in biomedical applications. *International Journal of Bio-Science and Bio-Technology*, *8*(5), 311–322. https://doi.org/10.14257/ijbsbt.2016.8.5.28

Gutkin, M., Ovid'ko, I., & Pande, C. (2001). Theoretical models of plastic deformation processes in nanocrystalline materials. *Reviews on Advanced Materials Science(Russia)*, *2*(1), 80–102.

Hamaker, H. C. (1937). The London-van der Waals attraction between spherical particles. *Physica*, *4*(10), 1058–1072. https://doi.org/10.1016/S0031-8914(37)80203-7

Hammad, M., Adjizian, J. J., Sacré, C. H., Huet, B., Charlier, J. C., Raskin, J. P., & Pardoen, T. (2017). Adhesionless and near-ideal contact behavior of graphene on Cu thin film. *Carbon*, *122*, 446–450. https://doi.org/10.1016/j.carbon.2017.06.037

Haque, M. A., & Saif, M. T. A. (2002). In-situ tensile testing of nano-scale specimens in SEM and TEM. *Experimental Mechanics*, *42*(1), 123–128. https://doi.org/10.1177/0018512002042001797

Howsare, C. A., Weng, X., Bojan, V., Snyder, D., & Robinson, J. A. (2012). Substrate considerations for graphene synthesis on thin copper films. *Nanotechnology*, *23*(13). https://doi.org/10.1088/0957-4484/23/13/135601

Hu, K. M., Bo, P., Li, X. Y., Xin, Y. H., Bai, X. R., Li, L., & Zhang, W. M. (2020). Resonant nano-electromechanical systems from 2D materials. *Epl*, *131*(5). https://doi.org/10.1209/0295-5075/131/58001

Huet, B., & Raskin, J. P. (2017). Pressure-Controlled Chemical Vapor Deposition of Single-Layer Graphene with Millimeter-Size Domains on Thin Copper Film. *Chemistry of Materials*, *29*(8), 3431–3440. https://doi.org/10.1021/acs.chemmater.6b04928

Huet, B., & Raskin, J. P. (2018a). Role of Cu foil in-situ annealing in controlling the size and thickness of CVD graphene domains. *Carbon*, *129*, 270–280. https://doi.org/10.1016/j.carbon.2017.12.043

Huet, B., & Raskin, J. P. (2018b). Role of Cu foil in-situ annealing in controlling the size and thickness of CVD graphene domains. *Carbon*, *129*, 270–280. https://doi.org/10.1016/j.carbon.2017.12.043

Huet, B., & Raskin, J. P. (2018c). Role of the Cu substrate in the growth of ultra-flat crack-free highly-crystalline single-layer graphene. *Nanoscale*, *10*(46), 21898–21909. https://doi.org/10.1039/c8nr06817h

Huet, B., Raskin, J. P., Snyder, D. W., & Redwing, J. M. (2020). Fundamental limitations in transferred CVD graphene caused by Cu catalyst surface morphology. *Carbon*, *163*, 95–104. https://doi.org/10.1016/j.carbon.2020.02.074

Huyghebaert, C., Schram, T., Smets, Q., Agarwal, T. K., Verreck, D., & Brems, S. (2018). *2D materials : roadmap to CMOS integration*. *1*, 512–515.

Hwang, J., Yoon, T., Jin, S. H., Lee, J., Kim, T. S., Hong, S. H., & Jeon, S.

(2013). Enhanced mechanical properties of graphene/copper nanocomposites using a molecular-level mixing process. *Advanced Materials*, *25*(46), 6724–6729. https://doi.org/10.1002/adma.201302495

Ismach, A., Druzgalski, C., Penwell, S., Schwartzberg, A., Zheng, M., Javey, A., Bokor, J., & Zhang, Y. (2010). Direct chemical vapor deposition of graphene on dielectric surfaces. *Nano Letters*, *10*(5), 1542–1548. https://doi.org/10.1021/nl9037714

Jian, S. R., Juang, J. Y., Chen, N. C., Jang, J. S. C., Huang, J. C., & Lai, Y. S. (2010). Nanoindentation-induced structural deformation in GaN/AlN multilayers. *Nanoscience and Nanotechnology Letters*, *2*(4), 315–321. https://doi.org/10.1166/nnl.2010.1100

Jiang, H., Zheng, L., Liu, Z., & Wang, X. (2020). Two-dimensional materials: From mechanical properties to flexible mechanical sensors. *InfoMat*, *2*(6), 1077–1094. https://doi.org/10.1002/inf2.12072

Jin, C., Davoodabadi, A., Li, J., Wang, Y., & Singler, T. (2017). Spherical indentation of a freestanding circular membrane revisited: Analytical solutions and experiments. *Journal of the Mechanics and Physics of Solids*, *100*, 85–102. https://doi.org/10.1016/j.jmps.2017.01.005

Jing, N., Xue, Q., Ling, C., Shan, M., Zhang, T., Zhou, X., & Jiao, Z. (2012). Effect of defects on Young's modulus of graphene sheets: A molecular dynamics simulation. *RSC Advances*, *2*(24), 9124–9129. https://doi.org/10.1039/c2ra21228e

Kang, J. H., Moon, J., Kim, D. J., Kim, Y., Jo, I., Jeon, C., Lee, J., & Hong, B. H. (2016). Strain Relaxation of Graphene Layers by Cu Surface Roughening. *Nano Letters*, *16*(10), 5993–5998. https://doi.org/10.1021/acs.nanolett.6b01578

Kese, K., & Li, Z. C. (2006). Semi-ellipse method for accounting for the pile-up contact area during nanoindentation with the Berkovich indenter. *Scripta Materialia*, *55*(8), 699–702. https://doi.org/10.1016/j.scriptamat.2006.06.030

Kim, C., Yoon, M.-A., Jang, B., Kim, J.-H., & Kim, K.-S. (2020). *Tribology and Lubricants A Review on Transfer Process of Two-dimensional Materials*. *36*(1), 1–10. https://doi.org/10.9725/kts.2020.36.1.1

Kim, K. S., Zhao, Y., Jang, H., Lee, S. Y., Kim, J. M., Kim, K. S., Ahn, J. H., Kim, P., Choi, J. Y., & Hong, B. H. (2009). Large-scale pattern

growth of graphene films for stretchable transparent electrodes. *Nature*, *457*(7230), 706–710. https://doi.org/10.1038/nature07719

Kim, S. M., Hsu, A., Park, M. H., Chae, S. H., Yun, S. J., Lee, J. S., Cho, D. H., Fang, W., Lee, C., Palacios, T., Dresselhaus, M., Kim, K. K., Lee, Y. H., & Kong, J. (2015). Synthesis of large-area multilayer hexagonal boron nitride for high material performance. *Nature Communications*, *6*. https://doi.org/10.1038/ncomms9662

Kim, W., Oh, H. S., & Shon, I. J. (2015). The effect of graphene reinforcement on the mechanical properties of Al2O3 ceramics rapidly sintered by high-frequency induction heating. *International Journal of Refractory Metals and Hard Materials*, *48*, 376–381. https://doi.org/10.1016/j.ijrmhm.2014.10.011

Kim, Y., Lee, J., Yeom, M. S., Shin, J. W., Kim, H., Cui, Y., Kysar, J. W., Hone, J., Jung, Y., Jeon, S., & Han, S. M. (2013). Strengthening effect of single-atomic-layer graphene in metal-graphene nanolayered composites. *Nature Communications*, *4*, 1–7. https://doi.org/10.1038/ncomms3114

Klemenz, A., Pastewka, L., Balakrishna, S. G., Caron, A., Bennewitz, R., & Moseler, M. (2014). Atomic scale mechanisms of friction reduction and wear protection by graphene. *Nano Letters*, *14*(12), 7145–7152. https://doi.org/10.1021/nl5037403

Koenig, S. P., Boddeti, N. G., Dunn, M. L., & Bunch, J. S. (2011). Ultrastrong adhesion of graphene membranes. *Nature Nanotechnology*, *6*(9), 543–546. https://doi.org/10.1038/nnano.2011.123

Komaragiri, U., Begley, M. R., & Simmonds, J. G. (2005). The mechanical response of freestanding circular elastic films under point and pressure loads. *Journal of Applied Mechanics, Transactions ASME*, *72*(2), 203–212. https://doi.org/10.1115/1.1827246

Koren, E., Rawlings, C., Knoll, A. W., & Duerig, U. (2015). Graphite Contacts. *Science*, *348*(6235), 679–684.

Koskinen, J., Steinwall, J. E., Soave, R., & Johnson, H. H. (1993). Microtensile testing of free-standing polysilicon fibers of various grain sizes. *Journal of Micromechanics and Microengineering*, *3*(1), 13–17. https://doi.org/10.1088/0960-1317/3/1/004

Kovalčíková, A., Balko, J., Balázsi, C., Hvizdoš, P., & Dusza, J. (2014). Influence of hBN content on mechanical and tribological properties of

Si3N4/BN ceramic composites. *Journal of the European Ceramic Society*, *34*(14), 3319–3328. https://doi.org/10.1016/j.jeurceramsoc.2014.02.021

Kuang, D., Xu, L., Liu, L., Hu, W., & Wu, Y. (2013). Graphene-nickel composites. *Applied Surface Science*, *273*, 484–490. https://doi.org/10.1016/j.apsusc.2013.02.066

Kudin, K. N., Scuseria, G. E., & Yakobson, B. I. (2001). (formula presented) BN, and C nanoshell elasticity from ab initio computations. *Physical Review B - Condensed Matter and Materials Physics*, *64*(23), 1–10. https://doi.org/10.1103/PhysRevB.64.235406

Kurland, N. E., Drira, Z., & Yadavalli, V. K. (2012). Measurement of nanomechanical properties of biomolecules using atomic force microscopy. *Micron*, *43*(2–3), 116–128. https://doi.org/10.1016/j.micron.2011.07.017

Lahiri, I., Verma, V. P., & Choi, W. (2011). An all-graphene based transparent and flexible field emission device. *Carbon*, *49*(5), 1614–1619. https://doi.org/10.1016/j.carbon.2010.12.044

Lanza, M., Smets, Q., Huyghebaert, C., & Li, L. J. (2020). Yield, variability, reliability, and stability of two-dimensional materials based solid-state electronic devices. *Nature Communications*, *11*(1), 1–5. https://doi.org/10.1038/s41467-020-19053-9

Lee, A. L., Tao, L., & Akinwande, D. (2015). Suppression of copper thin film loss during graphene synthesis. *ACS Applied Materials and Interfaces*, *7*(3), 1527–1532. https://doi.org/10.1021/am506601v

Lee, C., Wei, X., Kysar, J. W., & Hone, J. (2008a). Measurement of the elastic properties and intrinsic strength of monolayer graphene. *Science*, *321*(5887), 385–388. https://doi.org/10.1126/science.1157996

Lee, C., Wei, X., Kysar, J. W., & Hone, J. (2008b). *of Monolayer Graphene*. *321*(July), 385–388.

Lee, C., Wei, X., Li, Q., Carpick, R., Kysar, J. W., & Hone, J. (2009). Elastic and frictional properties of graphene. *Physica Status Solidi (B) Basic Research*, *246*(11–12), 2562–2567. https://doi.org/10.1002/pssb.200982329

Lee, G. H., Yu, Y. J., Cui, X., Petrone, N., Lee, C. H., Choi, M. S., Lee, D. Y., Lee, C., Yoo, W. J., Watanabe, K., Taniguchi, T., Nuckolls, C.,

Kim, P., & Hone, J. (2013). Flexible and transparent MoS2 field-effect transistors on hexagonal boron nitride-graphene heterostructures. *ACS Nano*, *7*(9), 7931–7936. https://doi.org/10.1021/nn402954e

Lee, J. S., Choi, S. H., Yun, S. J., Kim, Y. I., Boandoh, S., Park, J. H., Shin, B. G., Ko, H., Lee, S. H., Kim, Y. M., Lee, Y. H., Kim, K. K., & Kim, S. M. (2018). Wafer-scale single-crystal hexagonal boron nitride film via self-collimated grain formation. *Science*, *362*(6416), 817–821. https://doi.org/10.1126/science.aau2132

Lee, J. U., Yoon, D., & Cheong, H. (2012). Estimation of young's modulus of graphene by Raman spectroscopy. *Nano Letters*, *12*(9), 4444–4448. https://doi.org/10.1021/nl301073q

Lee, K., & Ye, J. (2016). Significantly improved thickness uniformity of graphene monolayers grown by chemical vapor deposition by texture and morphology control of the copper foil substrate. *Carbon*, *100*, 441–449. https://doi.org/10.1016/j.carbon.2016.01.032

Lee, Y., Bae, S., Jang, H., Jang, S., Zhu, S. E., Sim, S. H., Song, Y. Il, Hong, B. H., & Ahn, J. H. (2010). Wafer-scale synthesis and transfer of graphene films. *Nano Letters*, *10*(2), 490–493. https://doi.org/10.1021/nl903272n

Legleiter, J. (2009). The effect of drive frequency and set point amplitude on tapping forces in atomic force microscopy: Simulation and experiment. *Nanotechnology*, *20*(24). https://doi.org/10.1088/0957-4484/20/24/245703

Leong, W. S., Wang, H., Yeo, J., Martin-Martinez, F. J., Zubair, A., Shen, P. C., Mao, Y., Palacios, T., Buehler, M. J., Hong, J. Y., & Kong, J. (2019). Paraffin-enabled graphene transfer. *Nature Communications*, *10*(1), 1–8. https://doi.org/10.1038/s41467-019-08813-x

Li, C., Bando, Y., Zhi, C., Huang, Y., & Golberg, D. (2009). Thickness-dependent bending modulus of hexagonal boron nitride nanosheets. *Nanotechnology*, *20*(38). https://doi.org/10.1088/0957-4484/20/38/385707

Li, X., Wei, X. L., Xu, T. T., Ning, Z. Y., Shu, J. P., Wang, X. Y., Pan, D., Zhao, J. H., Yang, T., & Chen, Q. (2014). Mechanical properties of individual InAs nanowires studied by tensile tests. *Applied Physics Letters*, *104*(10). https://doi.org/10.1063/1.4868133

Li, Xiaodong, & Bhushan, B. (2002). A review of nanoindentation

continuous stiffness measurement technique and its applications. *Materials Characterization*, *48*(1), 11–36. https://doi.org/10.1016/S1044-5803(02)00192-4

Li, Xing, Sun, M., Shan, C., Chen, Q., & Wei, X. (2018). Mechanical Properties of 2D Materials Studied by In Situ Microscopy Techniques. In *Advanced Materials Interfaces* (Vol. 5, Issue 5). Wiley-VCH Verlag. https://doi.org/10.1002/admi.201701246

Li, Z., Fu, X., Guo, Q., Zhao, L., Fan, G., Li, Z., Xiong, D. B., Su, Y., & Zhang, D. (2018). Graphene quality dominated interface deformation behavior of graphene-metal composite: The defective is better. *International Journal of Plasticity*, *111*(March), 253–265. https://doi.org/10.1016/j.ijplas.2018.07.020

Liao, L., Wang, H., Peng, H., Yin, J., Koh, A. L., Chen, Y., Xie, Q., Peng, H., & Liu, Z. (2015). Van Hove Singularity Enhanced Photochemical Reactivity of Twisted Bilayer Graphene. *Nano Letters*, *15*(8), 5585–5589. https://doi.org/10.1021/acs.nanolett.5b02240

Liao, Z., Sandonas, L. M., Zhang, T., Gall, M., Dianat, A., Gutierrez, R., Mühle, U., Gluch, J., Jordan, R., Cuniberti, G., & Zschech, E. (2017). In-situ stretching patterned graphene nanoribbons in the transmission electron microscope. *Scientific Reports*, *7*(1), 1–7. https://doi.org/10.1038/s41598-017-00227-3

Lin, C. Y., Wu, J. Y., Chiu, Y. H., Chang, C. P., & Lin, M. F. (2014). Stacking-dependent magnetoelectronic properties in multilayer graphene. *Physical Review B - Condensed Matter and Materials Physics*, *90*(20), 1–10. https://doi.org/10.1103/PhysRevB.90.205434

Lin, L. Y., Kim, D. E., Kim, W. K., & Jun, S. C. (2011). Friction and wear characteristics of multi-layer graphene films investigated by atomic force microscopy. *Surface and Coatings Technology*, *205*(20), 4864–4869. https://doi.org/10.1016/j.surfcoat.2011.04.092

Lin, Q. Y., Jing, G., Zhou, Y. B., Wang, Y. F., Meng, J., Bie, Y. Q., Yu, D. P., & Liao, Z. M. (2013a). Stretch-induced stiffness enhancement of graphene grown by chemical vapor deposition. *ACS Nano*, *7*(2), 1171–1177. https://doi.org/10.1021/nn3053999

Lin, Q. Y., Jing, G., Zhou, Y. B., Wang, Y. F., Meng, J., Bie, Y. Q., Yu, D. P., & Liao, Z. M. (2013b). Stretch-induced stiffness enhancement of graphene grown by chemical vapor deposition. *ACS Nano*, *7*(2), 1171–1177. https://doi.org/10.1021/nn3053999

Liu, A., & Peng, Q. (2018). A molecular dynamics study of the mechanical properties of twisted bilayer graphene. *Micromachines*, *9*(9). https://doi.org/10.3390/mi9090440

Liu, F., Ming, P., & Li, J. (2007). Ab initio calculation of ideal strength and phonon instability of graphene under tension. *Physical Review B - Condensed Matter and Materials Physics*, *76*(6). https://doi.org/10.1103/PhysRevB.76.064120

Liu, K., Yan, Q., Chen, M., Fan, W., Sun, Y., Suh, J., Fu, D., Lee, S., Zhou, J., Tongay, S., Ji, J., Neaton, J. B., & Wu, J. (2014a). Elastic properties of chemical-vapor-deposited monolayer MoS2, WS2, and their bilayer heterostructures. *Nano Letters*, *14*(9), 5097–5103. https://doi.org/10.1021/nl501793a

Liu, K., Yan, Q., Chen, M., Fan, W., Sun, Y., Suh, J., Fu, D., Lee, S., Zhou, J., Tongay, S., Ji, J., Neaton, J. B., & Wu, J. (2014b). Elastic properties of chemical-vapor-deposited monolayer MoS2, WS2, and their bilayer heterostructures. *Nano Letters*, *14*(9), 5097–5103. https://doi.org/10.1021/nl501793a

Liu, X. Y., Wang, F. C., Wang, W. Q., & Wu, H. A. (2016). Interfacial strengthening and self-healing effect in graphene-copper nanolayered composites under shear deformation. *Carbon*, *107*, 680–688. https://doi.org/10.1016/j.carbon.2016.06.071

Liu, Yanping, Zhang, S., He, J., Wang, Z. M., & Liu, Z. (2019). Recent Progress in the Fabrication, Properties, and Devices of Heterostructures Based on 2D Materials. *Nano-Micro Letters*, *11*(1), 1–24. https://doi.org/10.1007/s40820-019-0245-5

Liu, Yuan, Weiss, N. O., Duan, X., Cheng, H. C., Huang, Y., & Duan, X. (2016). Van der Waals heterostructures and devices. *Nature Reviews Materials*, *1*(9). https://doi.org/10.1038/natrevmats.2016.42

López-Polín, G., Gómez-Navarro, C., Parente, V., Guinea, F., Katsnelson, M. I., Pérez-Murano, F., & Gómez-Herrero, J. (2015). Increasing the elastic modulus of graphene by controlled defect creation. *Nature Physics*, *11*(1), 26–31. https://doi.org/10.1038/nphys3183

Lu, N., Suo, Z., & Vlassak, J. J. (2010). The effect of film thickness on the failure strain of polymer-supported metal films. *Acta Materialia*, *58*(5), 1679–1687. https://doi.org/10.1016/j.actamat.2009.11.010

Lu, P., Wu, X., Guo, W., & Zeng, X. C. (2012). Strain-dependent electronic

and magnetic properties of MoS 2 monolayer, bilayer, nanoribbons and nanotubes. *Physical Chemistry Chemical Physics*, *14*(37), 13035–13040. https://doi.org/10.1039/c2cp42181j

Lu, Z., & Dunn, M. L. (2010). Van der Waals adhesion of graphene membranes. *Journal of Applied Physics*, *107*(4). https://doi.org/10.1063/1.3270425

Ma, L. P., Ren, W., & Cheng, H. M. (2019). Transfer Methods of Graphene from Metal Substrates: A Review. *Small Methods*, *3*(7), 1–13. https://doi.org/10.1002/smtd.201900049

Ma, Y., Dai, Y., Guo, M., Niu, C., Zhu, Y., & Huang, B. (2012). Evidence of the existence of magnetism in pristine VX 2 monolayers (X = S, Se) and their strain-induced tunable magnetic properties. *ACS Nano*, *6*(2), 1695–1701. https://doi.org/10.1021/nn204667z

Mahmoud, K. A., Mansoor, B., Mansour, A., & Khraisheh, M. (2015). Functional graphene nanosheets: The next generation membranes for water desalination. *Desalination*, *356*, 208–225. https://doi.org/10.1016/j.desal.2014.10.022

Mai, Y. J., Li, Y. G., Li, S. L., Zhang, L. Y., Liu, C. S., & Jie, X. H. (2019). Self-lubricating Ti3C2 nanosheets/copper composite coatings. *Journal of Alloys and Compounds*, *770*, 1–5. https://doi.org/10.1016/j.jallcom.2018.08.100

Marinello, F., Carmignato, S., Voltan, A., Savio, E., & De Chiffre, L. (2010). Error sources in atomic force microscopy for dimensional measurements: Taxonomy and modeling. *Journal of Manufacturing Science and Engineering, Transactions of the ASME*, *132*(3), 0309031–0309038. https://doi.org/10.1115/1.4001242

Martin, Y., Williams, C. C., & Wickramasinghe, H. K. (1987). Atomic force microscope-force mapping and profiling on a sub 100-Å scale. *Journal of Applied Physics*, *61*(10), 4723–4729. https://doi.org/10.1063/1.338807

Mas-Ballesté, R., Gómez-Navarro, C., Gómez-Herrero, J., & Zamora, F. (2011). 2D materials: To graphene and beyond. *Nanoscale*, *3*(1), 20–30. https://doi.org/10.1039/c0nr00323a

Medalsy, I. D., & Müller, D. J. (2013). Nanomechanical properties of proteins and membranes depend on loading rate and electrostatic interactions. *ACS Nano*, *7*(3), 2642–2650.

https://doi.org/10.1021/nn400015z

Mohiuddin, T. M. G., Lombardo, A., Nair, R. R., Bonetti, A., Savini, G., Jalil, R., Bonini, N., Basko, D. M., Galiotis, C., Marzari, N., Novoselov, K. S., Geim, A. K., & Ferrari, A. C. (2009). Uniaxial strain in graphene by Raman spectroscopy: G peak splitting, Grüneisen parameters, and sample orientation. *Physical Review B - Condensed Matter and Materials Physics*, *79*(20), 1–8. https://doi.org/10.1103/PhysRevB.79.205433

Moustafa, E. B., & Taha, M. A. (2020). Preparation of high strength graphene reinforced Cu-based nanocomposites via mechanical alloying method: microstructural, mechanical and electrical properties. *Applied Physics A: Materials Science and Processing*, *126*(3), 1–16. https://doi.org/10.1007/s00339-020-3412-0

Mukhopadhyay, T., Mahata, A., Adhikari, S., & Zaeem, M. A. (2017). Effective mechanical properties of multilayer nano-heterostructures. *Scientific Reports*, *7*(1), 1–13. https://doi.org/10.1038/s41598-017-15664-3

Muñoz, R., & Gómez-Aleixandre, C. (2013). Review of CVD synthesis of graphene. *Chemical Vapor Deposition*, *19*(10–12), 297–322. https://doi.org/10.1002/cvde.201300051

Nadler, B., & Steigmann, D. J. (2006). Modeling the indentation, penetration and cavitation of elastic membranes. *Journal of the Mechanics and Physics of Solids*, *54*(10), 2005–2029. https://doi.org/10.1016/j.jmps.2006.04.007

Nair, R. R., Ren, W. C., Jalil, R., Riaz, I., Kravets, V. G., Britnell, L., Blake, P., Schedin, F., Mayorov, A. S., Yuan, S., Katsnelson, M. I., Cheng, H. M., Strupinski, W., Bulusheva, L. G., Okotrub, A. V., Grigorieva, I. V., Grigorenko, A. N., Novoselov, K. S., & Geim, A. K. (2010). arXiv1006.3016. *Spectroscopy*, 1–20. http://arxiv.org/ftp/arxiv/papers/1006/1006.3016.pdf

Nayak, A. P., Pandey, T., Voiry, D., Liu, J., Moran, S. T., Sharma, A., Tan, C., Chen, C. H., Li, L. J., Chhowalla, M., Lin, J. F., Singh, A. K., & Akinwande, D. (2015). Pressure-dependent optical and vibrational properties of monolayer molybdenum disulfide. *Nano Letters*, *15*(1), 346–353. https://doi.org/10.1021/nl5036397

Neek-Amal, M., & Peeters, F. M. (2010a). Nanoindentation of a circular sheet of bilayer graphene. *Physical Review B - Condensed Matter and*

Materials Physics, *81*(23), 1–6. https://doi.org/10.1103/PhysRevB.81.235421

Ni, G. X., Zheng, Y., Bae, S., Kim, H. R., Pachoud, A., Kim, Y. S., Tan, C. L., Im, D., Ahn, J. H., Hong, B. H., & Özyilmaz, B. (2012). Quasi-periodic nanoripples in graphene grown by chemical vapor deposition and its impact on charge transport. *ACS Nano*, *6*(2), 1158–1164. https://doi.org/10.1021/nn203775x

Ni, Z. H., Yu, T., Lu, Y. H., Wang, Y. Y., Feng, Y. P., & Shen, Z. X. (2008a). Uniaxial strain on graphene: Raman spectroscopy study and band-gap opening. *ACS Nano*, *2*(11), 2301–2305. https://doi.org/10.1021/nn800459e

Ni, Z. H., Yu, T., Lu, Y. H., Wang, Y. Y., Feng, Y. P., & Shen, Z. X. (2008b). Uniaxial strain on graphene: Raman spectroscopy study and band-gap opening. *ACS Nano*, *2*(11), 2301–2305. https://doi.org/10.1021/nn800459e

Nieto, A., Bisht, A., Lahiri, D., Zhang, C., & Agarwal, A. (2017). Graphene reinforced metal and ceramic matrix composites: a review. *International Materials Reviews*, *62*(5), 241–302. https://doi.org/10.1080/09506608.2016.1219481

Nimbalkar, A., & Kim, H. (2020). Opportunities and Challenges in Twisted Bilayer Graphene: A Review. *Nano-Micro Letters*, *12*(1). https://doi.org/10.1007/s40820-020-00464-8

Niu, T., Cao, G., & Xiong, C. (2016). Fracture behavior of graphene mounted on stretchable substrate. *Carbon*, *109*, 852–859. https://doi.org/10.1016/j.carbon.2016.08.087

Novoselov, K. S., Geim, A. K., Morozov, S. V., Jiang, D., Katsnelson, M. I., Grigorieva, I. V., Dubonos, S. V., & Firsov, A. A. (2005). Two-dimensional gas of massless Dirac fermions in graphene. *Nature*, *438*(7065), 197–200. https://doi.org/10.1038/nature04233

Novoselov, K. S., Jiang, D., Schedin, F., Booth, T. J., Khotkevich, V. V., Morozov, S. V., & Geim, A. K. (2005). Two-dimensional atomic crystals. *Proceedings of the National Academy of Sciences of the United States of America*, *102*(30), 10451–10453. https://doi.org/10.1073/pnas.0502848102

Novoselov, K. S., Mishchenko, A., Carvalho, A., & Castro Neto, A. H. (2016). 2D materials and van der Waals heterostructures. *Science*,

353(6298). https://doi.org/10.1126/science.aac9439

Novoselov, Kostya S., Andreeva, D. V., Ren, W., & Shan, G. (2019). Graphene and other two-dimensional materials. *Frontiers of Physics, 14*(1). https://doi.org/10.1007/s11467-018-0835-6

Okotrub, A. V., Asanov, I. P., Yudanov, N. F., Babin, K. S., Gusel'nikov, A. V., Nedoseikina, T. I., Gevko, P. N., Bulusheva, L. G., Osváth, Z., & Biró, L. P. (2009). Development of graphene layers by reduction of graphite fluoride C2F surface. *Physica Status Solidi (B) Basic Research*, *246*(11–12), 2545–2548. https://doi.org/10.1002/pssb.200982296

Oliver, W. C., & Pharr, G. M. (1992). An improved technique for determining hardness and elastic madulus using load and displacement. *J Mater Res*, *7*(1), 1564–1583.

Oliver, W. C., & Pharr, G. M. (2004). Measurement of hardness and elastic modulus by instrumented indentation: Advances in understanding and refinements to methodology. *Journal of Materials Research*, *19*(1), 3–20. https://doi.org/10.1557/jmr.2004.19.1.3

Ovid'ko, I. A. (2013). Mechanical properties of graphene. *Reviews on Advanced Materials Science*. https://doi.org/10.1039/c2nr31164j

Papageorgiou, D. G., Kinloch, I. A., & Young, R. J. (2017). Mechanical properties of graphene and graphene-based nanocomposites. In *Progress in Materials Science* (Vol. 90, pp. 75–127). Elsevier Ltd. https://doi.org/10.1016/j.pmatsci.2017.07.004

Park, S. Y., Gwak, E. J., Huang, M., Ruoff, R. S., & Kim, J. Y. (2017). Nanolaminate of metallic glass and graphene with enhanced elastic modulus, strength, and ductility in tension. *Scripta Materialia*, *139*, 63–66. https://doi.org/10.1016/j.scriptamat.2017.06.031

Park, S. Y., Kim, Y. C., Ruoff, R. S., & Kim, J. Y. (2019). Incipient plasticity and fully plastic contact behavior of copper coated with a graphene layer. *APL Materials*, *7*(3). https://doi.org/10.1063/1.5086333

Pereira, V. M., Castro Neto, A. H., & Peres, N. M. R. (2009). Tight-binding approach to uniaxial strain in graphene. *Physical Review B - Condensed Matter and Materials Physics*, *80*(4), 1–8. https://doi.org/10.1103/PhysRevB.80.045401

Pethica, J. B., & Oliver, W. C. (1987). Tip Surface Interactions in STM and

AFM Tip Surface Interactions in STM and A F M. In *Physica Scripta* (Vol. 19). http://iopscience.iop.org/1402-4896/1987/T19A/010

Pharr, G. M., & Oliver, W. C. (1992). Measurement of Thin Film Mechanical Properties Using Nanoindentation. *MRS Bulletin*, *17*(7), 28–33. https://doi.org/10.1557/S0883769400041634

Pirkle, A., Chan, J., Venugopal, A., Hinojos, D., Magnuson, C. W., McDonnell, S., Colombo, L., Vogel, E. M., Ruoff, R. S., & Wallace, R. M. (2011). The effect of chemical residues on the physical and electrical properties of chemical vapor deposited graphene transferred to SiO2. *Applied Physics Letters*, *99*(12), 3–5. https://doi.org/10.1063/1.3643444

Porwal, H., Grasso, S., & Reece, M. J. (2013). Review of graphene-ceramic matrix composites. *Advances in Applied Ceramics*, *112*(8), 443–454. https://doi.org/10.1179/174367613X13764308970581

Pruessner, M. W., King, T. T., Kelly, D. P., Grover, R., Calhoun, L. C., & Ghodssi, R. (2003). Mechanical property measurement of InP-based MEMS for optical communications. *Sensors and Actuators, A: Physical*, *105*(2), 190–200. https://doi.org/10.1016/S0924-4247(03)00102-X

Qu, J., Li, B. W., Shen, Y., Huo, S., Xu, Y., Liu, S., Song, B., Wang, H., Hu, C., & Feng, W. (2019). Evaporable Glass-State Molecule-Assisted Transfer of Clean and Intact Graphene onto Arbitrary Substrates. *ACS Applied Materials and Interfaces*, *11*(18), 16272–16279. https://doi.org/10.1021/acsami.8b21946

Rasool, H. I., Ophus, C., Klug, W. S., Zettl, A., & Gimzewski, J. K. (2013). Measurement of the intrinsic strength of crystalline and polycrystalline graphene. *Nature Communications*, *4*, 1–7. https://doi.org/10.1038/ncomms3811

Reddy, C. D., Ramasubramaniam, A., Shenoy, V. B., & Zhang, Y. W. (2009). Edge elastic properties of defect-free single-layer graphene sheets. *Applied Physics Letters*, *94*(10). https://doi.org/10.1063/1.3094878

Robinson, J. T., Burgess, J. S., Junkermeier, C. E., Badescu, S. C., Reinecke, T. L., Perkins, F. K., Zalalutdniov, M. K., Baldwin, J. W., Culbertson, J. C., Sheehan, P. E., & Snow, E. S. (2010). Properties of fluorinated graphene films. *Nano Letters*, *10*(8), 3001–3005. https://doi.org/10.1021/nl101437p

Rogers, J. A., Someya, T., & Huang, Y. (2010). Materials and mechanics for stretchable electronics. *Science*, *327*(5973), 1603–1607. https://doi.org/10.1126/science.1182383

Rosenkranz, A., Grützmacher, P. G., Espinoza, R., Fuenzalida, V. M., Blanco, E., Escalona, N., Gracia, F. J., Villarroel, R., Guo, L., Kang, R., Mücklich, F., Suarez, S., & Zhang, Z. (2019). Multi-layer Ti3C2Tx-nanoparticles (MXenes) as solid lubricants – Role of surface terminations and intercalated water. *Applied Surface Science*, *494*(July), 13–21. https://doi.org/10.1016/j.apsusc.2019.07.171

Ruiz-Vargas, C. S., Zhuang, H. L., Huang, P. Y., Van Der Zande, A. M., Garg, S., McEuen, P. L., Muller, D. A., Hennig, R. G., & Park, J. (2011). Softened elastic response and unzipping in chemical vapor deposition graphene membranes. *Nano Letters*, *11*(6), 2259–2263. https://doi.org/10.1021/nl200429f

Rupert, T. J., Trelewicz, J. R., & Schuh, C. A. (2012). Grain boundary relaxation strengthening of nanocrystalline Ni-W alloys. *Journal of Materials Research*, *27*(9), 1285–1294. https://doi.org/10.1557/jmr.2012.55

Sato, Y., Shinzato, S., Ohmura, T., & Ogata, S. (2019). Atomistic prediction of the temperature- And loading-rate-dependent first pop-in load in nanoindentation. *International Journal of Plasticity*, *121*(April), 280–292. https://doi.org/10.1016/j.ijplas.2019.06.012

Schall, D., Pallecchi, E., Ducournau, G., Avramovic, V., Otto, M., & Neumaier, D. (2018). Record high bandwidth integrated graphene photodetectors for communication beyond 180 Gb/s. *2018 Optical Fiber Communications Conference and Exposition, OFC 2018 - Proceedings*, 1–3.

Schiøtz, J., Di Tolla, F. D., & Jacobsen, K. W. (1998). Softening of nanocrystalline metals at very small grain sizes. *Nature*, *391*(6667), 561–563. https://doi.org/10.1038/35328

Sharpe, W. N., Yuan, B., & Edwards, R. L. (1997). A new technique for measuring the mechanical properties of thin films. *Journal of Microelectromechanical Systems*, *6*(3), 193–198. https://doi.org/10.1109/84.623107

Shibutani, Y., Tsuru, T., & Koyama, A. (2007). Nanoplastic deformation of nanoindentation: Crystallographic dependence of displacement bursts. *Acta Materialia*, *55*(5), 1813–1822.

https://doi.org/10.1016/j.actamat.2006.10.055

Shinde, S. M., Das, T., Hoang, A. T., Sharma, B. K., Chen, X., & Ahn, J. H. (2018). Surface-Functionalization-Mediated Direct Transfer of Molybdenum Disulfide for Large-Area Flexible Devices. *Advanced Functional Materials*, *28*(13), 1–11. https://doi.org/10.1002/adfm.201706231

Si, C., Sun, Z., & Liu, F. (2016). Strain engineering of graphene: A review. *Nanoscale*, *8*(6), 3207–3217. https://doi.org/10.1039/c5nr07755a

Singh, A. K., Mathew, K., Zhuang, H. L., & Hennig, R. G. (2015). Computational screening of 2D materials for photocatalysis. In *Journal of Physical Chemistry Letters* (Vol. 6, Issue 6, pp. 1087–1098). American Chemical Society. https://doi.org/10.1021/jz502646d

Singh, D., Shukla, V., Khossossi, N., Ainane, A., & Ahuja, R. (2021). Harnessing the unique properties of MXenes for advanced rechargeable batteries. *JPhys Energy*, *3*(1). https://doi.org/10.1088/2515-7655/abceac

Soldano, C., Mahmood, A., & Dujardin, E. (2010). Production, properties and potential of graphene. *Carbon*, *48*(8), 2127–2150. https://doi.org/10.1016/j.carbon.2010.01.058

Solís-Fernández, P., Bissett, M., & Ago, H. (2017). Synthesis, structure and applications of graphene-based 2D heterostructures. *Chemical Society Reviews*, *46*(15), 4572–4613. https://doi.org/10.1039/c7cs00160f

Song, L., Ci, L., Lu, H., Sorokin, P. B., Jin, C., Ni, J., Kvashnin, A. G., Kvashnin, D. G., Lou, J., Yakobson, B. I., & Ajayan, P. M. (2010a). Large scale growth and characterization of atomic hexagonal boron nitride layers. *Nano Letters*, *10*(8), 3209–3215. https://doi.org/10.1021/nl1022139

Song, L., Ci, L., Lu, H., Sorokin, P. B., Jin, C., Ni, J., Kvashnin, A. G., Kvashnin, D. G., Lou, J., Yakobson, B. I., & Ajayan, P. M. (2010b). Large scale growth and characterization of atomic hexagonal boron nitride layers. *Nano Letters*, *10*(8), 3209–3215. https://doi.org/10.1021/nl1022139

Sreeprasad, T. S., & Berry, V. (2013). How do the electrical properties of graphene change with its functionalization? *Small*, *9*(3), 341–350. https://doi.org/10.1002/smll.201202196

Stine, R., Lee, W., Whitener, K. E., Robinson, J. T., & Sheehan, P. E. (2013). *Nl4021039.Pdf*.

Stone, D. S., Wu, T. W., Alexopoulos, P.-S., & Lafontaine, W. R. (1988). Indentation Technique to Investigate Elastic Moduli of Thin Films on Substrates. *MRS Proceedings*, *130*, 105–110. https://doi.org/10.1557/proc-130-105

Su, Q., Li, Y., Hu, R., Song, F., Liu, S., Guo, C., Zhu, S., Liu, W., & Pan, J. (2020). Heterojunction Photocatalysts Based on 2D Materials: The Role of Configuration. *Advanced Sustainable Systems*, *4*(9), 1–19. https://doi.org/10.1002/adsu.202000130

Suk, J. W., Kitt, A., Magnuson, C. W., Hao, Y., Ahmed, S., An, J., Swan, A. K., Goldberg, B. B., & Ruoff, R. S. (2011). Transfer of CVD-grown monolayer graphene onto arbitrary substrates. *ACS Nano*, *5*(9), 6916–6924. https://doi.org/10.1021/nn201207c

Suk, J. W., Na, S. R., Stromberg, R. J., Stauffer, D., Lee, J., Ruoff, R. S., & Liechti, K. M. (2016). Probing the adhesion interactions of graphene on silicon oxide by nanoindentation. *Carbon*, *103*, 63–72. https://doi.org/10.1016/j.carbon.2016.02.079

Suresh, S., Nieh, T. G., & Choi, B. W. (1999). Nano-indentation of copper thin films on silicon substrates. *Scripta Materialia*, *41*(9), 951–957. https://doi.org/10.1016/S1359-6462(99)00245-6

Tang, L. C., Wan, Y. J., Yan, D., Pei, Y. B., Zhao, L., Li, Y. B., Wu, L. Bin, Jiang, J. X., & Lai, G. Q. (2013). The effect of graphene dispersion on the mechanical properties of graphene/epoxy composites. *Carbon*, *60*, 16–27. https://doi.org/10.1016/j.carbon.2013.03.050

Teague, M. L., Lai, A. P., Velasco, J., Hughes, C. R., Beyer, A. D., Bockrath, M. W., Lau, C. N., & Yeh, N. C. (2009). Evidence for strain-induced local conductance modulations in single-layer graphene on SiO 2. *Nano Letters*, *9*(7), 2542–2546. https://doi.org/10.1021/nl9005657

Thormann, E., Pettersson, T., Kettle, J., & Claesson, P. M. (2010). Probing material properties of polymeric surface layers with tapping mode AFM: Which cantilever spring constant, tapping amplitude and amplitude set point gives good image contrast and minimal surface damage? *Ultramicroscopy*, *110*(4), 313–319. https://doi.org/10.1016/j.ultramic.2010.01.002

Tjong, S. C. (2013). Recent progress in the development and properties of novel metal matrix nanocomposites reinforced with carbon nanotubes and graphene nanosheets. *Materials Science and Engineering R: Reports*, *74*(10), 281–350. https://doi.org/10.1016/j.mser.2013.08.001

Tozar, A., & Karahan, İ. H. (2019). Investigation of the mechanical properties of Ni-B/hBN composite coatings electrodeposited in presence of CTAB as the surfactant. *Materials Research Express*, *6*(12). https://doi.org/10.1088/2053-1591/ab5c5a

Tsuchiya, T., Tabata, O., Sakata, J., & Taga, Y. (1996). Tensile Testing of Polycrystalline Silicon Thin Films Using Electrostatic Force Grip. *IEEJ Transactions on Sensors and Micromachines*, *116*(10), 441–446. https://doi.org/10.1541/ieejsmas.116.441

Tsuchiya, T., Tabata, O., Sakata, J., & Taga, Y. (1998). Specimen size effect on tensile strength of surface-micromachined polycrystalline silicon thin films. *Journal of Microelectromechanical Systems*, *7*(1), 106–113. https://doi.org/10.1109/84.661392

Tyagi, R., Xiong, D. S., Li, J., & Dai, J. (2010). Elevated temperature tribological behavior of Ni based composites containing nano-silver and hBN. *Wear*, *269*(11–12), 884–890. https://doi.org/10.1016/j.wear.2010.08.022

Vahdat, V., Grierson, D. S., Turner, K. T., & Carpick, R. W. (2013). Mechanics of interaction and atomic-scale wear of amplitude modulation atomic force microscopy probes. *ACS Nano*, *7*(4), 3221–3235. https://doi.org/10.1021/nn305901n

Van Vliet, K. J., Yip, S., Suresh, S., Li, J., Zhu, T., Yip, S., Van Vliet, K. J., & Li, J. (2003). Quantifying the early stages of plasticity through nanoscale experiments and simulations. *Physical Review B - Condensed Matter and Materials Physics*, *67*(10), 1–15. https://doi.org/10.1103/PhysRevB.67.104105

Verdier, M., Fivel, M., & Groma, I. (1998). Mesoscopic scale simulation of dislocation dynamics in fcc metals: Principles and applications. *Modelling and Simulation in Materials Science and Engineering*, *6*(6), 755–770. https://doi.org/10.1088/0965-0393/6/6/007

Vlassak, J. J., & Nix, W. D. (1992). A new bulge test technique for the determination of Young's modulus and Poisson's ratio of thin films. *Journal of Materials Research*, *7*(12), 3242–3249. https://doi.org/10.1557/JMR.1992.3242

W.C. Oliver, G. M. P. (1992). An improvved techniques for determining Hardness and elastic modulus using .pdf. In *J. Mater.* (Vol. 7, pp. 1564–1583).

Wagner, R., Moon, R., Pratt, J., Shaw, G., & Raman, A. (2011). Uncertainty quantification in nanomechanical measurements using the atomic force microscope. *Nanotechnology*, *22*(45). https://doi.org/10.1088/0957-4484/22/45/455703

Wang, Hong, Liu, F., Fu, W., Fang, Z., Zhou, W., & Liu, Z. (2014). Two-dimensional heterostructures: Fabrication, characterization, and application. *Nanoscale*, *6*(21), 12250–12272. https://doi.org/10.1039/c4nr03435j

Wang, Huaping, & Yu, G. (2016). Direct CVD Graphene Growth on Semiconductors and Dielectrics for Transfer-Free Device Fabrication. *Advanced Materials*, *28*(25), 4956–4975. https://doi.org/10.1002/adma.201505123

Wang, L., & Zhang, Q. (2012). Elastic behavior of bilayer graphene under in-plane loadings. *Current Applied Physics*, *12*(4), 1173–1177. https://doi.org/10.1016/j.cap.2012.02.043

Wang, Li, Xu, X., Zhang, L., Qiao, R., Wu, M., Wang, Z., Zhang, S., Liang, J., Zhang, Z., Zhang, Z., Chen, W., Xie, X., Zong, J., Shan, Y., Guo, Y., Willinger, M., Wu, H., Li, Q., Wang, W., … Liu, K. (2019). Epitaxial growth of a 100-square-centimetre single-crystal hexagonal boron nitride monolayer on copper. *Nature*, *570*(7759), 91–95. https://doi.org/10.1038/s41586-019-1226-z

Wang, Lu, Jin, J., Cao, J., Yang, P., & Peng, Q. (2018). Interaction of edge dislocations with graphene nanosheets in graphene/Fe composites. *Crystals*, *8*(4), 1–10. https://doi.org/10.3390/cryst8040160

Wang, M., Cai, S., Pan, C., Wang, C., Lian, X., Zhuo, Y., Xu, K., Cao, T., Pan, X., Wang, B., Liang, S. J., Yang, J. J., Wang, P., & Miao, F. (2018). Robust memristors based on layered two-dimensional materials. *Nature Electronics*, *1*(2), 130–136. https://doi.org/10.1038/s41928-018-0021-4

Wang, Y., Zheng, Y., Xu, X., Dubuisson, E., Bao, Q., Lu, J., & Loh, K. P. (2011). Electrochemical delamination of CVD-grown graphene film: Toward the recyclable use of copper catalyst. *ACS Nano*, *5*(12), 9927–9933. https://doi.org/10.1021/nn203700w

Wei, X., Fragneaud, B., Marianetti, C. A., & Kysar, J. W. (2009). Nonlinear elastic behavior of graphene: Ab initio calculations to continuum description. *Physical Review B - Condensed Matter and Materials Physics*, *80*(20), 1–8. https://doi.org/10.1103/PhysRevB.80.205407

Weihs, T. P., Hong, ,S, Bravman, J. C., & Nix, W. D. (1988). Mechanical deflection of cantilever microbeams: A new technique for testing the mechanical properties of thin films. *Journal of Materials Research*, *3*(5), 931–942. https://doi.org/10.1557/JMR.1988.0931

Xing, S., Wu, W., Wang, Y., Bao, J., & Pei, S. S. (2013). Kinetic study of graphene growth: Temperature perspective on growth rate and film thickness by chemical vapor deposition. *Chemical Physics Letters*, *580*, 62–66. https://doi.org/10.1016/j.cplett.2013.06.047

Xu, J., Chen, L., Dai, Y. W., Cao, Q., Sun, Q. Q., Ding, S. J., Zhu, H., & Zhang, D. W. (2017). A two-dimensional semiconductor transistor with boosted gate control and sensing ability. *Science Advances*, *3*(5), 1–8. https://doi.org/10.1126/sciadv.1602246

Xu, K., Cao, P., & Heath, J. R. (2009). Scanning tunneling microscopy characterization of the electrical properties of wrinkles in exfoliated graphene monolayers. *Nano Letters*, *9*(12), 4446–4451. https://doi.org/10.1021/nl902729p

Xu, M., Liang, T., Shi, M., & Chen, H. (2013). *Graphene-Like Two-Dimensional Materials*.

Xue, B., Yan, Y., Hu, Z., & Zhao, X. (2014). Study on effects of scan parameters on the image quality and tip wear in AFM tapping mode. *Scanning*, *36*(2), 263–269. https://doi.org/10.1002/sca.21099

Yang, G., Li, L., Lee, W. B., & Ng, M. C. (2018). Structure of graphene and its disorders: a review. *Science and Technology of Advanced Materials*, *19*(1), 613–648. https://doi.org/10.1080/14686996.2018.1494493

Yang, X., & Yan, M. (2020). Removing contaminants from transferred CVD graphene. *Nano Research*, *13*(3), 599–610. https://doi.org/10.1007/s12274-020-2671-6

Yang, Y., Li, X., Wen, M., Hacopian, E., Chen, W., Gong, Y., Zhang, J., Li, B., Zhou, W., Ajayan, P. M., Chen, Q., Zhu, T., & Lou, J. (2017). Brittle Fracture of 2D MoSe2. *Advanced Materials*, *29*(2), 1–7. https://doi.org/10.1002/adma.201604201

Yankowitz, M., Jung, J., Laksono, E., Leconte, N., Chittari, B. L., Watanabe, K., Taniguchi, T., Adam, S., Graf, D., & Dean, C. R. (2018). Dynamic band-structure tuning of graphene moiré superlattices with pressure. *Nature*, *557*(7705), 404–408. https://doi.org/10.1038/s41586-018-0107-1

Yazyev, O. V., & Louie, S. G. (2010). Topological defects in graphene: Dislocations and grain boundaries. *Physical Review B - Condensed Matter and Materials Physics*, *81*(19). https://doi.org/10.1103/PhysRevB.81.195420

Yi, D., Luo, D., Wang, Z. J., Dong, J., Zhang, X., Willinger, M. G., Ruoff, R. S., & Ding, F. (2018). What Drives Metal-Surface Step Bunching in Graphene Chemical Vapor Deposition? *Physical Review Letters*, *120*(24), 246101. https://doi.org/10.1103/PhysRevLett.120.246101

Yulaev, A., Cheng, G., Hight Walker, A. R., Vlassiouk, I. V., Myers, A., Leite, M. S., & Kolmakov, A. (2016). Toward clean suspended CVD graphene. *RSC Advances*, *6*(87), 83954–83962. https://doi.org/10.1039/c6ra17360h

Zandiatashbar, A., Lee, G. H., An, S. J., Lee, S., Mathew, N., Terrones, M., Hayashi, T., Picu, C. R., Hone, J., & Koratkar, N. (2014a). Effect of defects on the intrinsic strength and stiffness of graphene. *Nature Communications*, *5*, 1–9. https://doi.org/10.1038/ncomms4186

Zandiatashbar, A., Lee, G. H., An, S. J., Lee, S., Mathew, N., Terrones, M., Hayashi, T., Picu, C. R., Hone, J., & Koratkar, N. (2014b). Effect of defects on the intrinsic strength and stiffness of graphene. *Nature Communications*, *5*. https://doi.org/10.1038/ncomms4186

Zhang, C., Lu, C., Pei, L., Li, J., Wang, R., & Tieu, K. (2019). The negative Poisson's ratio and strengthening mechanism of nanolayered graphene/Cu composites. *Carbon*, *143*, 125–137. https://doi.org/10.1016/j.carbon.2018.10.097

Zhang, H., Huang, J., Wang, Y., Liu, R., Huai, X., Jiang, J., & Anfuso, C. (2018). Atomic force microscopy for two-dimensional materials: A tutorial review. *Optics Communications*, *406*(May 2017), 3–17. https://doi.org/10.1016/j.optcom.2017.05.015

Zhang, J., & Zhao, J. (2013a). Mechanical properties of bilayer graphene with twist and grain boundaries. *Journal of Applied Physics*, *113*(4). https://doi.org/10.1063/1.4789594

Zhang, J., & Zhao, J. (2013b). Mechanical properties of bilayer graphene with twist and grain boundaries. *Journal of Applied Physics*, *113*(4). https://doi.org/10.1063/1.4789594

Zhang, J., Zhao, J., & Lu, J. (2012). Intrinsic strength and failure behaviors of graphene grain boundaries. *ACS Nano*, *6*(3), 2704–2711. https://doi.org/10.1021/nn3001356

Zhang, K., Feng, Y., Wang, F., Yang, Z., & Wang, J. (2017). Two dimensional hexagonal boron nitride (2D-hBN): Synthesis, properties and applications. *Journal of Materials Chemistry C*, *5*(46), 11992–12022. https://doi.org/10.1039/c7tc04300g

Zhang, P., Ma, L., Fan, F., Zeng, Z., Peng, C., Loya, P. E., Liu, Z., Gong, Y., Zhang, J., Zhang, X., Ajayan, P. M., Zhu, T., & Lou, J. (2014). Fracture toughness of graphene. *Nature Communications*, *5*, 1–7. https://doi.org/10.1038/ncomms4782

Zhang, R., Koutsos, V., & Cheung, R. (2016). Elastic properties of suspended multilayer WSe2. *Applied Physics Letters*, *108*(4). https://doi.org/10.1063/1.4940982

Zhang, W., Huang, J. K., Chen, C. H., Chang, Y. H., Cheng, Y. J., & Li, L. J. (2013). High-gain phototransistors based on a CVD MoS2 monolayer. *Advanced Materials*, *25*(25), 3456–3461. https://doi.org/10.1002/adma.201301244

Zhang, X. (2017). *Construction of Graphene-based Heterostructures via π - π Stacking Interaction and Surface Functionalization A thesis in fulfilment of the requirements for the degree of School of Chemistry*. *July*.

Zhang, Y. Y., Wang, C. M., Cheng, Y., & Xiang, Y. (2011). Mechanical properties of bilayer graphene sheets coupled by sp3 bonding. *Carbon*, *49*(13), 4511–4517. https://doi.org/10.1016/j.carbon.2011.06.058

Zhang, Yue, Yan, X., Yang, Y., Huang, Y., Liao, Q., & Qi, J. (2012). Scanning probe study on the piezotronic effect in ZnO nanomaterials and nanodevices. *Advanced Materials*, *24*(34), 4647–4655. https://doi.org/10.1002/adma.201104382

Zhang, Yupeng, & Pan, C. (2012a). Measurements of mechanical properties and number of layers of graphene from nano-indentation. *Diamond and Related Materials*, *24*, 1–5. https://doi.org/10.1016/j.diamond.2012.01.033

Zhang, Yupeng, & Pan, C. (2012b). Measurements of mechanical properties and number of layers of graphene from nano-indentation. *Diamond and Related Materials*, *24*, 1–5. https://doi.org/10.1016/j.diamond.2012.01.033

Zhao, H., Min, K., & Aluru, N. R. (2009). Size and chirality dependent elastic properties of graphene nanoribbons under uniaxial tension. *Nano Letters*, *9*(8), 3012–3015. https://doi.org/10.1021/nl901448z

Zhao, L., Guo, Q., Li, Z., Xiong, D. B., Osovski, S., Su, Y., & Zhang, D. (2019). Strengthening and deformation mechanisms in nanolaminated graphene-Al composite micro-pillars affected by graphene in-plane sizes. *International Journal of Plasticity*, *116*(January), 265–279. https://doi.org/10.1016/j.ijplas.2019.01.006

Zhao, X. J., Hou, H., Fan, X. T., Wang, Y., Liu, Y. M., Tang, C., Liu, S. H., Ding, P. P., Cheng, J., Lin, D. H., Wang, C., Yang, Y., & Tan, Y. Z. (2019). Molecular bilayer graphene. *Nature Communications*, *10*(1), 1–7. https://doi.org/10.1038/s41467-019-11098-9

Zhao, X., Zhang, Q., Chen, D., & Lu, P. (2010). Enhanced mechanical properties of graphene-based polyvinyl alcohol composites. *Macromolecules*, *43*(5), 2357–2363. https://doi.org/10.1021/ma902862u

Zheng, S., Cao, Q., Liu, S., & Peng, Q. (2018). Atomic Structure and Mechanical Properties of Twisted Bilayer Graphene. *Journal of Composites Science*, *3*(1), 2. https://doi.org/10.3390/jcs3010002

Zhi, C., Bando, Y., Tang, C., Kuwahara, H., & Golberg, D. (2009). Large-scale fabrication of boron nitride nanosheets and their utilization in polymeric composites with improved thermal and mechanical properties. *Advanced Materials*, *21*(28), 2889–2893. https://doi.org/10.1002/adma.200900323

Zhou, L., Wang, Y., & Cao, G. (2013). Boundary condition and pre-strain effects on the free standing indentation response of graphene monolayer. *Journal of Physics Condensed Matter*, *25*(47). https://doi.org/10.1088/0953-8984/25/47/475303

Zhou, L., Xue, J., Wang, Y., & Cao, G. (2013). Molecular mechanics simulations of the deformation mechanism of graphene monolayer under free standing indentation. *Carbon*, *63*, 117–124. https://doi.org/10.1016/j.carbon.2013.06.046

Zhu, H., Wang, Y., Xiao, J., Liu, M., Xiong, S., Wong, Z. J., Ye, Z., Ye, Y., Yin, X., & Zhang, X. (2015). Observation of piezoelectricity in free-standing monolayer MoS2. *Nature Nanotechnology*, *10*(2), 151–155. https://doi.org/10.1038/nnano.2014.309

Zhu, X., Zhao, Y., Ma, L., Zhang, G., Ren, W., Peng, X., Hu, N., Rintoul, L., Bell, J. M., & Yan, C. (2019). Graphene coating makes copper more resistant to plastic deformation. *Composites Communications*, *12*(November 2018), 106–111. https://doi.org/10.1016/j.coco.2019.01.006